공학박사 학위논문

Optimization and Stabilization of High Fidelity Multiphysics Simulation for Extended Applications Including VVERs

VVER을 포함한 광범위 적용을 위한 고신뢰도 다물리 해석의 최적화 및 안정화

2023년 2월

서울대학교 대학원

에너지시스템공학부

Gonzalez-Amoros Jorge

Optimization and Stabilization of High Fidelity Multiphysics Simulation for Extended Applications Including VVERs

VVER 을 포함한 광범위 적용을 위한 고신뢰도 다물리 해석의 최적화 및 안정화

지도 교수 심 형 진

이 논문을 공학박사 학위논문으로 제출함

2023년 1월

서울대학교 대학원

에너지시스템공학부

Gonzalez-Amoros Jorge

Gonzalez-Amoros Jorge의 공학박사 학위논문을 인준함

2023년 1월

위 원 장 _____ 조형규 _____ (인)

부위원장 _____ 심형진 _____ (인)

위 원 _____ 주한규 _____ (인)

위 원 _____ 윤한영 _____ (인)

위 원 _____ 조진영 _____ (인)

Abstract

The capability of the nTRACER direct whole core calculation code coupled with the ESCOT pin-level core thermal-hydraulics (T/H) code is extended and stabilized for extended applications including the high-fidelity multiphysics analysis of VVER cores. First of all, the calculation feature of ESCOT is extended to handle the hexagonal geometry cores of VVERs and its performance is assessed by a code-to-code comparison with COBRA-TF (CTF). The coupling of ESCOT with the nTRACER direct whole core calculation code is then enhanced to deal with the VVER cores. Secondly, the stability of the nTRACER calculation involving strong nonlinear feedback such as xenon and Doppler is stabilized by imposing the Anderson Acceleration (AA) to the neutron flux after Fourier analysis of the feedback effects.

In ESCOT, the lateral momentum terms, the turbulent mixing coefficient values, the fuel conduction solution and the parallelization algorithms are modified for the handling of hexagonal geometry. The newly implemented ESCOT features are verified by comparing the solution of the single assembly, minicore and full core steady-state standalone and coupled problems for the VVER-1000 benchmark X-2 with the CTF results. ESCOT and CTF results show differences within an acceptable range in both standalone and coupled calculations. The computing time superiority due to the use of the drift flux model (DFM) of ESCOT over the CTF two-fluid model is confirmed with a speed-up factor of 1.35. The use of the DFM together with the axial-radial parallelization capability of ESCOT makes ESCOT an ideal alternative to replace the simplified built-in T/H solver in nTRACER as the coupled simulation results demonstrate.

It is shown that the xenon feedback in nTRACER sometimes reveals a non-convergent oscillatory behavior, particularly in depletion calculations as the fissile material becomes scarce. A Fourier analysis is performed to a simplified 1G 1D problem with periodic boundary condition and variable cross sections to obtain an analytical expression relating the convergence degree of the Power Iteration (PI) that yields the smallest spectral radius for different feedback coefficients. Increasing problem complexity to a non-homogeneous problem makes it not feasible to obtain an analytical expression for realistic problems. Consequently, the AA is retrieved, modified and analyzed for multiphysics problems.

By systematically studying the sequential addition of xenon and boron to the neutronics-T/H 1G 1D problem, it is demonstrated that if the original fixed-point map of the AA applied only to the T/H variables is extended to include other physics by applying the AA to neutron flux, the oscillatory behavior is greatly suppressed. It turned out that the AA applied on the condensed two-group flux instead of on the original 47-group works well so that the increase in memory is trivial. The necessary average number of Fixed-Point Iterations (FPI) is reduced from about 15 to less than 10. The eigenvalue yielded also an error reduction from about 5 pcm to less than 0.5 pcm and it is highlighted that the AA applied to flux can achieve a convergence behavior similar to the quasi-optimal point.

The application of these findings to nTRACER solved the non-convergence issues in the depletion calculations for cores such as the APR1400 and the BEAVRS benchmark. In addition, the revision of the convergence criterion for the CMFD calculation is improved by adding the residual check to the original criterion of the residual ratio. This improvement saves the computing time by about an 11.5 % for the APR1400 quarter core depletion calculation.

Finally, a depletion calculation for the modified X-2 VVER benchmark is performed with nTRACER/ESCOT. The result show that the direct whole core depletion can be finished in 14 hours, among which only 11 % is spent for the ESCOT calculation and only 5 FPIs per depletion step are needed. This calculation demonstrates that stable high-fidelity depletion calculation for hexagonal geometry cores is possible in a competitive time span.

Keyword: nTRACER, ESCOT, hexagonal geometry core, xenon feedback, Fourier analysis, Anderson acceleration

Student Number: 2017-35073

Contents

List of Figures

List of Tables

Chapter 1. Introduction

High-fidelity simulation of the multiphysics phenomena occurring in nuclear reactors is of outmost importance for proper core design and accurate safety analysis. Traditionally, the integration of the multiphysics phenomena was done at very coarse levels due to the limitation of computing power. With the advent of computing technology, numerical solutions with higher resolution and higher fidelity have become more feasible in nuclear reactor analyses. Higher fidelity solutions can result in higher safety margins by decreasing the conservatism introduced by the higher uncertainties of the low fidelity solutions which in turn allows to curb the economic penalties during the nuclear power plant operation.

The direct whole core calculation (DWCC) has consequently gained potential in the last two decades. A group of high-fidelity neutronics codes based on the transport equation such as DeCART [1], nTRACER [2], and MPACT [3] have demonstrated their effectiveness. Although the initial T/H solver option implemented in these codes was a Computational Fluid Dynamics (CFD) code [4], its high computational cost led to its replacement with subchannel codes as they represent a sufficiently good alternative. Because of their speed and accuracy performance, many subchannel codes were coupled with numerous transport codes [5][6][7] and even with Monte Carlo codes [8].

COBRA-TF (CTF) [9] is currently the most widely used subchannel code. It employs the two-phase, three-field model which can cover all the possible flow regimes of Light Water Reactors (LWRs). Its well-established coupling interface makes its use for coupling with a neutronics code simple. For its part, Korea Atomic Energy Research Institute (KAERI) developed MATRA [10], a subchannel code which was the first to be coupled with DWCC codes [11] [12]. Its governing

equations are based on the Homogeneous Equilibrium Model (HEM) and the solution scheme exploits the axially dominant flow characteristics in PWRs so that the computing time is substantially shorter than CTF.

Despite having shown an acceptable performance in coupled calculations, the two subchannel codes still had room for improvement either on its speed or its accuracy, especially in the cases where the multiphysics code is run on massively parallel computing platforms. In this regard, Seoul National University Reactor Physics Laboratory (SNURPL), which is in a continuous development process of a forward-looking series of codes, carried out the development of a new subchannel scale T/H code called ESCOT (Efficient Simulator of COre Thermal-hydraulics) as an effort to provide efficient core T/H solutions to multiphysics analysis systems targeting high-performance parallel computing platforms [13].

ESCOT employs the Drift Flux Model (DFM) as it produces sufficiently accurate solutions for the typical core T/H conditions in pressurized water reactors (PWRs) and it is preferred over the two-fluid model in order to achieve high speed execution. Thus, the code is based on the four-equation DFM and the SIMPLEC (SIMPLE-Consistent) method. It is parallelized by employing both radial and axial domain decomposition with the Message Passing Interface (MPI) library. As its final aim is its employment as the T/H solver in multiphysics calculations, it has been coupled with several codes in the last few years [14][15][16].

Considering the expanding trend of the Water-Water Energetic Reactors (VVERs) worldwide in recent years, the Laboratory of Reactor Physics and Thermal-Hydraulics (LRT) of the Paul Scherrer Institute (PSI) developed a high-fidelity multi-physics code system for hexagonal geometry with sub-pin level resolution. Thus, the latest version of nTRACER, capable of VVER-1000 full core simulations

[16][18] (also referred as nTRACER-Fast or nTF in other publications), was coupled with CTF [19][20].

CTF had already been verified before for 3D VVER full core calculations on a coarse mesh [21]. However, its high-resolution hexagonal analysis had only been limited to single assembly calculations [22]. With this background, CTFv4.0 was used to build the LRT high-resolution core solver capable of 3D full core calculations and was verified with a coupled code system of similar capabilities (Serpent/SUBCHANFLOW) for the Hot Full Power (HFP) analysis of a VVER-1000 (X-2 benchmark) [23]. After the verification of nTRACER/CTF for single state-point simulations, the coupled code system was also expanded to full core cycle analysis and used to simulate the first cycle of the X-2 benchmark. The outcome of the LRT core solver is validated on the coarse mesh with experimental data [24]. The high-resolution depletion capabilities of nTRACER/CTF were also demonstrated in the cited publication together with the computational requirements of the novel code system for the full cycle calculation.

In these systems of coupled codes, the simulation of the various core physics is most frequently approached by the exchange of information between the algorithms which solve the different phenomena independently. This way to proceed is known as the Fixed-Point Iteration (FPI) and it allows an easy coupling of codes, especially when the code internals are not accessible.

These physical phenomena show, however, a nonlinear inter-dependency which can weaken the robustness of the FPI and definitely deteriorate the computation performance due to slow convergence [25]. The feedback mechanism and consequently the convergence rate depends on the problem characteristics such as its geometry, material composition, power level and the degree of feedback

increasing thereby the complexity of finding a straightforward solution to the nonlinearity [26][27].

The feedback-induced oscillations are caused by an excessive convergence of the Power Iteration (PI) whose output neutron flux is used to update the other physics. A common technique to alleviate this overconvergence and therefore reduce these oscillations is the adoption of a relaxation scheme. This scheme can be applied to any of the physical phenomena or even to all of them [28]. However, the relaxation of the neutronics calculation flux solution is preferred as the other physics (not only the T/H variables but also the xenon and critical boron concentrations, the core geometry change, etc.) are directly or indirectly dependent on it. In any case, the relaxation factor/s cannot be arbitrarily chosen since, as previously mentioned, the convergence behavior of the problem depends strongly on its characteristics. The factor/s must additionally be chosen to avoid causing excessive under-convergence as this will provoke convergence slow-down despite avoiding the oscillations.

A more effective method to resolve this convergence issue of the FPI is the Anderson Acceleration (AA). The idea behind the AA method is to determine the solution at the present iteration as a linear combination of the previous solution/s [29][30]. Therefore, the relaxation of the solution is obtained in a more problem-adaptative manner. At SNURPL, the AA method application has been the technique applied to the functionalization of the T/H variables [15][31]. But a better or more evolved technique needs to be defined and adopted for the problems that include the xenon and boron concentrations update which can make the problem enter in an oscillatory behavior, particularly in depleted cores [32].

A method recently developed determines the power iteration convergence degree as a function of the each individual FPI status and in accordance to the problem

characteristics [33][34]. This method approximates more optimally a perfect convergence behavior as it minimizes the oscillations (in both amount of oscillations and amplitude) and is more unlikely to incur in an excessive under-convergence. However, this method, despite being more analytically robust also possesses a certain degree of approximation for realistic applications (i.e. 3D problems with non-periodic boundary conditions).

1.1. Purpose and Scope of the Research

With the background introduced above, the purpose of this research is set to extend and optimize the capability of the ESCOT coupled nTRACER code for extended applications so that stabilized high-fidelity multiphysics simulation becomes possible for various pressurized water reactors (PWRs) including VVERs. For the extension of the capabilities of ESCOT for the applications to hexagonal geometry cores, various modifications of not only the geometry processor, but also some calculation algorithms [35] are necessary. In addition, the fuel conduction algorithms in ESCOT needs to be modified to deal with the hollow fuel pins typically employed in VVERs.

The algorithm modifications are verified, more specifically the lateral momentum equation, the mixing coefficient change including the turbulent mixing model and the parallelization scheme. To carry out this verification a code-to-code comparison with CTF results is performed. The model used for the verifications is based on the VVER-1000 benchmark X-2 [36][37].

As the second step, and besides the extension geometry, a series of more sophisticated models to better capture the effects induced by spacer grids are introduced in ESCOT. These effects are incorporated in the models for pressure loss,

heat transfer coefficient (HTC) enhancement and the increase of mixing. The models are directly adapted from CTF [38] and the correct implementation in ESCOT is verified by cross-comparison between the codes.

The third step taken in this work is the coupling of the hexagonal version of ESCOT with the neutronics solver capable of handling hexagonal geometry cores in the nTRACER DWCC code [39]. ESCOT will then replace the internal simplified one-dimensional T/H solver of nTRACER to generate more accurate results. The coupled nTRACER/ESCOT code is verified with the nTRACER/CTF system by analyzing single assembly, minicore and full core problems.

Prior to the depletion calculation for a problem based on the X-2 benchmark the instabilities in the multiphysics calculations are addressed by stabilizing and optimizing the convergence behavior in multiphysics at different reactor core states.

The first step consists of the characterization of the effects of the multiphysics-dependent cross sections on the FPI convergence behavior with the aim at explaining which are the aspects that affect the problem convergence the most. Starting from a simple one energy group (1G) and one-dimensional (1D) single pin problem with periodic boundary conditions, an analytical Fourier analysis [40][41][42] is performed to investigate the individual impact of the fuel and moderator temperature coefficients ($\widetilde{\mathrm{FTC}}$ and MTC respectively) on the convergence behavior and the definition of the optimal convergence point.

The subsequent step is the study of the feasibility of applying a new technique that allows the dynamic setting of the power iteration (PI) convergence degree in realistic problems so that the FPI approaches the most optimal convergence. The pessimistic output of this analysis led to retrieving the AA but extending its FPI map

from the current only T/H variables described in reference [31] to other physics (i.e. xenon and boron updates). The extended map of the AA is numerically analyzed for the simple problem.

Finally, the optimized extended FPI map is adapted to nTRACER by applying the acceleration after the CMFD calculation. The 47-group neutron flux is collapsed to 2 groups with memory saving purposes and reconstructed after the AA is completed. The changed FPI map usefulness is tested for checkerboard steady state and depletion problems. The modified AA method is then applied to the simulation of full core depletion problems that show problematic convergence behavior (APR1400 and BEAVRS). Ultimately, the first cycle of a fictitious core based on the X-2 benchmark is calculated with the improved nTRACER/ESCOT code.

1.2. Outline of the Thesis

In Chapter 2, ESCOT field equations as well as the constitutive relations are briefly reviewed together with the solution algorithms and the fuel conduction numerical method. Then, the modifications implemented to allow for the calculation of hexagonal geometries are presented along with the changes on the radial domain decomposition. The geometry and parallelization algorithm changes are verified for a series of single assembly, minicore and full core calculations by code-to-code comparison with CTF. Finally, the models to introduce the spacer grid effects on the T/H variables are described.

The neutronics-T/H coupling strategy of nTRACER/ESCOT for hexagonal problems is presented in Chapter 3. A series of single assembly, minicore and full core coupled calculations are performed and compared with the nTRACER/CTF system of codes with verification purposes.

The feasibility study of the extension of the neutronics-T/H calculations to other physics is presented in Chapter 4. It is shown that the neutron flux should be the target variable to be extrapolated by the AA, not the T/H variables. In Chapter 5, the effectiveness of the new stabilization feature in nTRACER is demonstrated with a series of Checkerboard and quarter core depletions calculations, including the APR1400 and BEAVRS cores, and an nTRACER/ESCOT VVER-1000 depletion calculation. Chapter 6 concludes the thesis.

Chapter 2. Description of the Pinwise Core Thermal-Hydraulics Code ESCOT

A general description of the pin-level nuclear reactor core T/H code ESCOT is presented. ESCOT adopts the four-equation DFM for two-phase calculations. The DFM simplifies the governing conservation equations by employing the mixture velocity in the momentum equation rather than using the gas and liquid velocities individually. Additionally, by solving only for the mixture energy and assuming the vapor in saturated conditions, the number of equations can further decrease to four in contrast to the six or nine equations in the two-fluid, three-field model. The DFM, unlike the HEM, allows the separation of the mixture velocity into each phase velocity by means of the two drift-flux parameters. The drift-flux parameters are determined experimentally, for this reason the DFM is considered a semi-empirical method.

The four equations of the DFM are solved applying the Finite Volume Method (FVM) and the Semi-Implicit Method for Pressure-Linked Equation (SIMPLE)-like algorithm in a staggered grid system. The FVM discretization is described with special emphasis on the modifications required for the analysis of VVERs. The empirical T/H data from VVER-like problems is scarce, therefore ESCOT solutions for VVER problems are verified by code-to-code comparison with CTF for steady state at normal operating conditions.

ESCOT aims at providing accurate yet fast core T/H solutions targeting massively parallel computing platforms. For highly parallelized execution, ESCOT is parallelized by a domain decomposition scheme that involves both radial and axial directions. This domain decomposition is described for hexagonal geometry problems and its effectiveness at speeding up the calculation of the T/H solutions at

core-scale level. The momentum and pressure systems are solved by using the Block Jacobi preconditioned Bi-Conjugate Gradient with Stabilization (BiCGStab) available inside the PETSc library [43].

2.1. Mixture Properties

The following mixture properties are needed in the DFM to formulate the conservation equations and the closure relations

Mixture density

$$\rho_m = \alpha\rho_v + (1-\alpha)\rho_l \tag{2.1}$$

Mixture velocity

$$\vec{u}_m = \frac{\alpha\rho_v\vec{u}_v + (1-\alpha)\rho_l\vec{u}_l}{\rho_m} \tag{2.2}$$

Mixture enthalpy

$$h_m = \frac{\alpha\rho_v h_v + (1-\alpha)\rho_l h_l}{\rho_m} \tag{2.3}$$

Thermodynamic quality

$$x_{th} = \frac{h_{l,fl} - h_{l,sat}}{h_{fg}}, \tag{2.4}$$

where

$$h_{l,fl} = \frac{\alpha\rho_v v_v h_v + (1-\alpha)\rho_l v_l h_l}{\alpha\rho_v v_v + (1-\alpha)\rho_l v_l} \tag{2.5}$$

Flow quality

$$x = \frac{\alpha\rho_v v_v}{\alpha\rho_v v_v + (1-\alpha)\rho_l v_l} \tag{2.6}$$

Here α is the void fraction and the subindexes m refers to the mixture variables, *v* to the vapor phase variable and *l* to the liquid one.

2.2. Field Equations of the Four-Equation Drift-Flux Model

In this section, the field equations of ESCOT are presented. ESCOT is based on four-equation drift-flux by assuming the saturated condition for vapor. The meaning of each term in the conservation equations is explained. Standard symbols and notations are used throughout the paper and extra definitions are included for those that may cause confusion. The detailed derivations of the generalized forms can be found in [44][45].

2.2.1. Mixture mass conservation equation

The mass conservation equation for mixture is given as

$$\frac{\partial \rho_m}{\partial t} + \nabla \cdot (\rho_m \vec{u}_m) = -\nabla \cdot \left(W_{tm}^{''} \right) \ , \tag{2.7}$$

where the term on the Right-Hand Side (RHS) is the mass transfer by turbulent mixing and void drift. As ESCOT is conceived to simulate steady state problems operating at nominal conditions or mild transients the dominant axial flow allows the use of a simple diffusion [46] as turbulent mixing model. This way the turbulent mixing is only considered to the lateral direction. The details of turbulent mixing and void drift model can be found in section 2.3.4.

2.2.2. Vapor mass conservation equation

The vapor mass conservation equation can be expressed as

$$\frac{\partial \left(\alpha \rho_v \right)}{\partial t} + \nabla \cdot \left(\alpha \rho_v \vec{u}_m \right) = \Gamma_v^{'''} - \nabla \cdot \left(\frac{\alpha \rho_l \rho_v}{\rho_m} \vec{V}_{gj}' \right) - \nabla \cdot \left(W_{tv}^{''} \right), \tag{2.8}$$

where the terms on the RHS are the volumetric vapor generation rate, the drift-flux parameter related divergence term, the vapor exchange due to turbulent mixing and

void drift.

2.2.3. Mixture momentum conservation equation

The mixture momentum conservation equation is formulated as

$$\frac{\partial}{\partial t}\left(\rho_m \vec{u}_m\right) + \nabla \cdot \left(\rho_m \vec{u}_m \vec{u}_m\right) = \rho_m \vec{g} - \nabla P + \nabla \cdot \boldsymbol{\tau}_m^{ij} - \nabla \cdot \vec{F}_{tm}'' - \nabla \cdot \left(\frac{\alpha}{1-\alpha} \frac{\rho_v \rho_l}{\rho_m} \vec{V}_{gj}' \vec{V}_{gj}' \right), \quad (2.9)$$

where the terms of the RHS are body force, force by pressure gradient, viscous shear stress, momentum transfer by turbulent mixing and void drift, and divergence term from the drift-flux model.

2.2.4. Mixture energy conservation equation

The energy conservation equation is written in terms of mixture enthalpy as

$$\frac{\partial}{\partial t}\left(\rho_m h_m\right) + \nabla \cdot \left(\rho_m h_m \vec{u}_m\right) = q_w''' + q_v''' - \nabla \cdot \vec{Q}_{tm}'' + \frac{\partial P}{\partial t} - \nabla \cdot \left(\frac{\alpha \rho_v \rho_l}{\rho_m} \left(h_v - h_l\right) \vec{V}_{gj}' \right). \quad (2.10)$$

where the terms on the RHS represent energy transfer rate from heated walls, volumetric heat generation in fluid, energy exchange due to turbulent mixing and void drift, work caused by pressure and divergence term by the drift-flux model.

2.3. Constitutive Relations for Subchannel-Scale Analysis

The RHS of the four conservation equations require several constitutive relations. Particularly, Equal-Volume exchange and Void Drift (EVVD) model, pressure drop model for friction and form loss, and vapor generation model are employed to simulate key phenomena in subchannel-scale analyses.

2.3.1. Equation of state

The solutions of the four-equation drift-flux model in section 2.2 consists of four primary variables: mixture velocity u_m, void fraction α, pressure P, and liquid enthalpy h_l. The other fluid variables, or secondary variables, are determined by using the Equation of State. In ESCOT, the steam properties are calculated by a set of functions and subroutines based on the IAPWS-IF97 steam tables/functions.

This way, the liquid temperature and density are obtained in terms of the pressure and the enthalpy as

$$\rho_l = \rho_l(P, h_l) \tag{2.11}$$

$$T_l = T_l(P, h_l). \tag{2.12}$$

Since the vapor phase is assumed to be saturation condition, the properties of vapor are calculated with only the pressure

$$\rho_v = \rho_{v,sat}(P) \tag{2.13}$$

$$T_v = T_{v,sat}(P) \tag{2.14}$$

$$h_v = h_{v,sat}(P). \tag{2.15}$$

2.3.2. Drift-flux parameters

The drift-flux parameters, namely the distribution parameter C_0 and gas drift velocity V_{gj}, are used to predict the gas and liquid velocities from the mixture velocity as described in Eqs. (2.26), (2.27) and (2.28). In ESCOT, two correlation models to obtain the drift-flux parameters are implemented: the Zuber and Findlay correlation [47] and the Chexal-Lellouche correlation [48].

The drift-flux parameters allow to obtain the phasic velocities. If the vapor velocity is defined as

$$u_v = j + (u_v - j)\,, \tag{2.16}$$

after performing area average after multiplying both side by void fraction, Eq. (2.16) becomes

$$\langle j_v \rangle = \langle \alpha j \rangle + \langle \alpha (u_v - j) \rangle\,, \tag{2.17}$$

where the operation $\langle \cdot \rangle$ represents the flow area averaging as

$$\langle \phi \rangle = \frac{1}{A} \int \phi dA\,. \tag{2.18}$$

Let us define the distribution parameter, C_0, and the gas drift velocity V_{gj} as

$$C_0 \equiv \frac{\langle \alpha j \rangle}{\langle \alpha \rangle \langle j \rangle} \quad \text{and} \tag{2.19}$$

$$V_{gj} \equiv \frac{\langle \alpha (u_g - j) \rangle}{\langle \alpha \rangle}\,, \tag{2.20}$$

thus, Eq. (2.16) becomes

$$\langle j_v \rangle = \langle \alpha \rangle \langle j \rangle C_0 + \langle \alpha \rangle V_{gj} \tag{2.21}$$

and

$$\langle u_v \rangle = \frac{\langle j_v \rangle}{\langle \alpha \rangle} = \langle j \rangle C_0 + V_{gj} \tag{2.22}$$

With the following definition for the volumetric flux

$$\langle j \rangle = \langle \alpha \rangle \langle u_v \rangle + \left(1 - \langle \alpha \rangle\right) \langle u_l \rangle \tag{2.23}$$

and the phasic relative (or slip) velocity

$$u_r = \langle u_v \rangle - \langle u_l \rangle\,, \tag{2.24}$$

the relation between the slip velocity and drift flux parameters can be derived from Eqs. (2.22), (2.23) and (2.24)

$$u_r = \frac{\langle j \rangle \left(C_0 - 1\right) + V_{gj}}{\left(1 - \langle \alpha \rangle\right)} = \frac{\langle u_v \rangle - \langle j \rangle}{\left(1 - \langle \alpha \rangle\right)} = \frac{V'_{gj}}{\left(1 - \langle \alpha \rangle\right)}\,. \tag{2.25}$$

From Eq. (2.2) and replacing each phase velocity with Eqs. (2.24) and (2.25), the following relations can be derived

$$u_l = u_m - \frac{\alpha}{1-\alpha}\frac{\rho_v}{\rho_m}V'_{gj}, \tag{2.26}$$

$$u_v = u_m + \frac{\rho_l}{\rho_m}V'_{gj}, \tag{2.27}$$

where from Eqs. (2.23), (2.25) and (2.27)

$$V'_{gj} = \frac{\rho_m V_{gj} + \rho_m (C_0 - 1)u_m}{\rho_m - (C_0 - 1)\alpha(\rho_l - \rho_g)} \tag{2.28}$$

2.3.3. Pressure drop model

The pressure drop models are implemented to incorporate friction and form loss as

$$\begin{aligned}\nabla \cdot \boldsymbol{\tau}_m^{ij} &= -\left(\left.\frac{dP}{dX}\right|_{friction} + \left.\frac{dP}{dX}\right|_{form} \right) \\ &= -\Phi\left(\sum_k \frac{f_k}{2D_h}\frac{G_k|G_k|}{\rho_k} + \frac{K_x}{2\Delta x}\rho_m u_m |u_m| + \frac{K_z}{2\Delta z}\rho_m w_m |w_m| \right)\end{aligned}, \tag{2.29}$$

where the subscript k indicates the phase, f is a friction factor, K is a form loss factor, and Φ is a two-phase multiplier for pressure drop. Besides, u is a lateral velocity, and w is an axial velocity.

First, the friction loss term is applied to the axial direction. It is calculated by a function of Reynolds number as follow:

$$f_k = a\,\mathrm{Re}_k^b + c \tag{2.30}$$

where the parameters depend on the Reynolds number as shown in Table 2-1.

Table 2-1. Friction factor parameters at different flow conditions

Flow condition	a	b	c	Range of Re
Laminar	64	-1	0	Re < 2,300
Transition	0.316	-0.25	0	2,300≤Re < 30,000
Turbulent	0.184	-0.20	0	30,000≤Re

The Reynolds number for each phase is defined [1] as below:

$$\mathrm{Re}_k = \frac{\alpha_k \rho_k u_k}{\mu_m}, \tag{2.31}$$

where the mixture viscosity is obtained as:

$$\mu_m = \left[\frac{1-x}{\mu_l} + \frac{x}{\mu_v} \right]^{-1}. \tag{2.32}$$

The form loss term would influence the flow which moves toward the axial and lateral directions. Generally, the axial form loss occurs due to the existence of spacer grids while the lateral form loss is caused by the flow passing through two rods.

In order to consider the effect of two-phase flow on pressure drop, the two-phase multiplier proposed by Armand [49]. As this work is limited to steady state at normal operating conditions $\Phi = 1$.

2.3.4. Turbulent mixing model

With the aim at reducing the computational burden subchannel codes employ a diffusion-like turbulent mixing model. The turbulent mixing is a driving force of mass, momentum, and energy exchange between neighboring channels in the lateral direction, which differs from the crossflow created by pressure gradient. This mixing phenomenon consists of two physics: turbulent mixing and void drift whose effects on the flow are in competition.

In the case of turbulent mixing, the flow gains in the variable (mass, momentum or energy) from the neighboring cells that have larger values, or it loses its quantity by being taken to neighboring cells that have smaller values. Thus, the turbulent mixing contributes to generating an even distribution of physical quantities of flows. The void drift, however, works in the opposite way. Small bubbles gather together and form larger bubbles so that the non-uniformity of the bubble distribution increases. The two phenomena are graphically depicted in Figure 2-1.

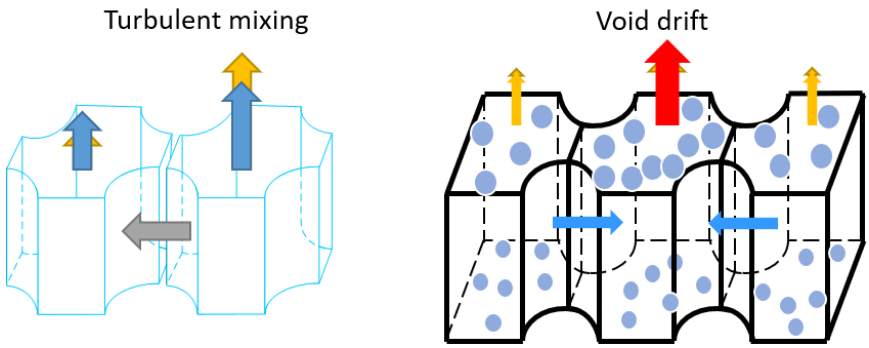

Figure 2-1. Simplified sketch of the turbulent mixing and void drift models

There are two models of turbulent mixing. In ESCOT in particular the Equal-Volume-exchange turbulent mixing and Void Drift (EVVD) model is implemented into the governing equations.

Mixture mass exchange:

$$\begin{aligned}\nabla \cdot \vec{W}''_{tm} &= \sum_j \frac{s_{ij}}{A_i}\left(W''^{TM}_{tm} + W''^{VD}_{tm}\right) \\ &= \sum_j \frac{s_{ij}}{A_i}\Theta_{ij}\frac{\varepsilon}{z^T_{ij}}\left[\left\{(\rho_m)_i - (\rho_m)_j\right\}\right. \\ &\qquad \left. -\left\{K_m \frac{G_i - G_j}{G_i + G_j}\left(\left[\alpha(\rho_v - \rho_l)\right]_i + \left[\alpha(\rho_v - \rho_l)\right]_j\right)\right\}\right]\end{aligned} \quad . \quad (2.33)$$

Vapor mass exchange:

$$\begin{aligned}\nabla\cdot\vec{W}''_{tm,v} &= \sum_j \frac{s_{ij}}{A_i}\left(W''^{TM}_{tm,v} + W''^{VD}_{tm,v}\right) \\ &= \sum_j \frac{s_{ij}}{A_i}\Theta_{ij}\frac{\varepsilon}{z^T_{ij}}\left[\left\{\left(\alpha\rho_v\right)_i - \left(\alpha\rho_v\right)_j\right\}\right. \\ &\qquad \left.-\left\{K_m\frac{G_i - G_j}{G_i + G_j}\left(\left(\alpha\rho_v\right)_i + \left(\alpha\rho_v\right)_j\right)\right\}\right]\end{aligned} \quad . \tag{2.34}$$

Momentum exchange:

$$\begin{aligned}\nabla\cdot\vec{F}''_{tm} &= \sum_j \frac{s_{ij}}{A_i}\left(F''^{TM}_{tm} + F''^{VD}_{tm}\right) \\ &= \sum_j \frac{s_{ij}}{A_i}\Theta_{ij}\frac{\varepsilon}{z^T_{ij}}\left[\left\{\left(\rho_m u_m\right)_i - \left(\rho_m u_m\right)_j\right\}\right. \\ &\qquad \left.-\left\{K_m\frac{G_i - G_j}{G_i + G_j}\left(\left[\alpha\left(\rho_v u_v - \rho_l u_l\right)\right]_i + \left[\alpha\left(\rho_v u_v - \rho_l u_l\right)\right]_j\right)\right\}\right]\end{aligned} \quad . \tag{2.35}$$

Energy exchange:

$$\begin{aligned}\nabla\cdot\vec{Q}''_{tm} &= \sum_j \frac{s_{ij}}{A_i}\left(Q''^{TM}_{tm} + Q''^{VD}_{tm}\right) \\ &= \sum_j \frac{s_{ij}}{A_i}\Theta_{ij}\frac{\varepsilon}{z^T_{ij}}\left[\left\{\left(\rho_m h_m\right)_i - \left(\rho_m h_m\right)_j\right\}\right. \\ &\qquad \left.-\left\{K_m\frac{G_i - G_j}{G_i + G_j}\left(\left[\alpha\left(\rho_v h_v - \rho_l h_l\right)\right]_i + \left[\alpha\left(\rho_v h_v - \rho_l h_l\right)\right]_j\right)\right\}\right]\end{aligned} \quad . \tag{2.36}$$

Here, ε is the eddy diffusivity, z_T the turbulent mixing length, K_m the scaling factor, s_{ij} is the gap (or slit) length between rods separating channels i and j, A_i is the flow area of channel i, Θ the turbulent mixing two-phase multiplier. The typical value of K_m is often suggested by 1.4. The mixing coefficient can be reformulated as a function of mass flux as

$$\frac{\varepsilon}{z^T_{ij}} = \frac{\beta\bar{G}}{\bar{\rho}} \tag{2.37}$$

The turbulent mixing coefficient β can be calculated by the Rogers&Rosehart

correlation [50], but mostly a constant value is assigned by users' input in subchannel codes. In case of the two-phase multiplier Θ, the model proposed by Beus [2] and is set to 1 in this work.

2.3.5. Vapor generation model

The vapor generation term Γ_v''' in Eq.(2.8) consists of two terms

$$\Gamma_v''' = \Gamma_w''' + \Gamma_{iv}''' , \tag{2.38}$$

where Γ_w''' is volumetric vapor generation rate by heated walls and Γ_{iv}''' is volumetric vapor exchange rate through an interface of two-phase. Both terms are implemented in ESCOT by using the models of RELAP5 [51].

Γ_w''' is calculated following correlations of Lahey [52]. For its part, Γ_{iv}''' is formulated under the saturated vapor condition and it depends on the interfacial heat transfer coefficient of liquid H_{il}. This depends on the flow regime map, which in ESCOT is the vertical volume flow regime map of RELAP5. The flows in steady-state PWRs are ESCOT target problems and consequently only unstratified and pre-Critical Heat Flux (CHF) regions are modeled.

2.4. Numerical Solution Method

The governing equations are spatially discretized by the Finite Volume Method (FVM) employing a staggered grid structure. The semi-implicit method is applied for temporal discretization. The pressure correction equation is derived by the SIMPLEC (SIMPLE-Consistent) scheme [53].

2.4.1. Discretization

The staggered grid structure in the radial direction employed in ESCOT is depicted in Figure 2-2. The scalar variables such as pressure, enthalpy, and density are defined at subchannel-centered scalar cells (Figure 2-2a) while the mixture velocity is defined at the gap-centered momentum cells (Figure 2-2b). The drift flux parameter V'_{gj} which is a function of C_0 and V_{gj} is also defined at the momentum cell because its characteristics are analogous to those of velocity. In the following descriptions, the subscripts I and J denote the radial and axial indices of the scalar cells, respectively, and the subscripts i and j are those of the momentum cells.

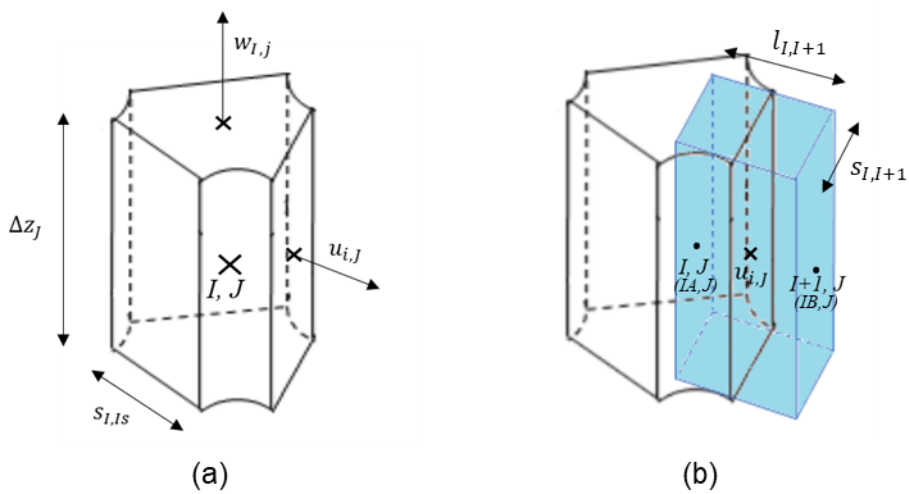

Figure 2-2. Schematic drawing of a scalar cell and momentum cell in staggered grid

The surface values of a control volume are determined by the donor cell scheme as

$$\phi_{i,J}^{\bar{n}} = \begin{cases} \phi_{I,J}^{n} & if\ u_{i,J}^{n} \geq 0 \\ \phi_{I+1,J}^{n} & if\ u_{i,J}^{n} < 0 \end{cases}, \tag{2.39}$$

where n is the time step index, and ϕ is an example variable. A weighted average is applied when the cell-centered values of surface quantities are necessary.

$$\phi_{I,j}^{n} = \frac{\Delta z_{J+1}\phi_{I,J}^{n} + \Delta z_{J}\phi_{I,J+1}^{n}}{\Delta z_{J} + \Delta z_{J+1}} \,. \tag{2.40}$$

The temporal discretization is based on the semi-implicit scheme. In this scheme, the sonic propagation and interphase exchange such as pressure and interfacial temperature are treated implicitly because their physical phenomena occur in a relatively short time. On the other hand, the terms related with fluid convection which would allow relatively larger time scales are treated explicitly.

By integrating the field equations over the control volume, the discretized forms of the conservation equations are derived. The notation in the discretized equations is: '*rnb*' denotes neighbors in radial direction and '*wnb*' means neighbors in both axial and radial directions. The detailed derivations can be found in [44][45].

Mixture mass continuity equation

$$\begin{aligned} &\frac{\rho_{m,I,J}^{n+1} - \rho_{m,I,J}^{n}}{\Delta t} A_{c,I,J}\Delta z_{J} + \sum_{ic=1}^{rnb}\left[\rho_{m}^{\bar{n}}\left(\vec{u}_{m}^{n+1}\cdot\vec{s}\right)_{ic}\Delta z_{J}\right]_{ic,J} \\ &\qquad + \left[\rho_{m}^{\bar{n}} w_{m}^{n+1} A_{c}\right]_{I,j} - \left[\rho_{m}^{\bar{n}} w_{m}^{n+1} A_{c}\right]_{I,j-1} = \sum_{ic=1}^{rnb}\left[TM_{m}\right]_{ic}^{n} \end{aligned} \,. \tag{2.41}$$

Vapor mass continuity equation

$$\begin{aligned} &\left[\alpha_{I,J}^{n}\frac{\rho_{v,I,J}^{n+1} - \rho_{v,I,J}^{n}}{\Delta t} + \rho_{v,I,J}^{n}\frac{\alpha_{I,J}^{n+1} - \alpha_{I,J}^{n}}{\Delta t}\right] A_{c,I,J}\Delta z_{J} \\ &+ \sum_{ic=1}^{rnb}\left[\left(\alpha\rho_{v}\right)^{\bar{n}}\left(\vec{u}_{m}^{n+1}\cdot\vec{s}\right)\Delta z_{J}\right]_{ic,J} + \left[\left(\alpha\rho_{v}\right)^{\bar{n}} w_{m}^{n+1} A_{c}\right]_{I,j} - \left[\left(\alpha\rho_{v}\right)^{\bar{n}} w_{m}^{n+1} A_{c}\right]_{I,j-1} \\ &\quad = \frac{H_{il}^{n}(T_{l}^{n+1} - T_{sat}^{n+1})}{h_{v,sat}^{n} - h_{li}^{n}} A_{c,I,J}\Delta z_{J} + \Gamma_{w}^{n} A_{c,I,J}\Delta z_{J} - \sum_{wnb}\left[CV\right]_{wnb}^{n} + \sum_{rnb}\left[TM_{v}\right]_{hnb}^{n} \end{aligned} \,. \tag{2.42}$$

Axial momentum equation

$$\begin{aligned} &a_{z,P} w_{m,I,j}^{n+1} - \sum_{ic=1}^{rnb} a_{z,ic} w_{m,\langle ic\rangle,j}^{n+1} - a_{z,DW} w_{m,I,j-1}^{n+1} - a_{z,UP} w_{m,I,j+1}^{n+1} \\ &\qquad = \left[P_{I,J-1}^{n+1} - P_{I,J}^{n+1}\right] A_{c,I,j} + S_{z,I,j} \end{aligned} \,. \tag{2.43}$$

Lateral momentum equation

$$a_{x,P}u_{m,i,J}^{n+1} - a_{x,W}u_{m,i-1,J}^{n+1} - a_{x,E}u_{m,i+1,J}^{n+1} - a_{x,DW}u_{m,i,J-1}^{n+1} - a_{x,UP}u_{m,i,J+1}^{n+1} = \left[P_{IA,J}^{n+1} - P_{IB,J}^{n+1}\right]s_i\Delta z_J + S_{x,i,J} \tag{2.44}$$

Mixture energy equation

$$\begin{aligned}&\frac{\left(\rho_m h_m\right)_{I,J}^{n+1} - \left(\rho_m h_m\right)_{I,J}^{n}}{\Delta t}A_{c,I,J}\Delta z_J + \sum_{ic=1}^{rnb}\left[\left(\rho_m h_m\right)^{\bar{n}}\left(\vec{u}_m^{n+1}\cdot\vec{s}\right)\Delta z_J\right]_{ic,J} \\ &+\left[\left(\rho_m h_m\right)^{\bar{n}}\left(w_m\right)^{n+1}A_c\right]_{I,j} - \left[\left(\rho_m h_m\right)^{\bar{n}}\left(w_m\right)^{n+1}A_c\right]_{I,j-1} \\ &= \sum_{rnb}\left[TM_{en}\right]_{rnb}^{n} + \frac{P_{I,J}^{n+1} - P_{I,J}^{n}}{\Delta t}A_{c,I,J}\Delta z_J + q_w''\xi_c\Delta z_J + q_v'''A_{c,I,J}\Delta z_J - \sum_{wnb}\left[CE\right]_{wnb}^{n}\end{aligned} \tag{2.45}$$

2.4.2. The pressure correction equation and solution with SIMPLE algorithm

The SIMPLEC algorithm is adopted to establish the pressure correction equation over the entire problem domain. The relation between the next time step velocity and pressure correction can be formulated in SIMPLEC as follow:

$$w_{m,I,j}^{n+1} = w_{m,I,j}^{*} + d_{I,j}\left[\left(P_{I,J}^{n+1} - P_{I,J}^{*}\right) - \left(P_{I,J+1}^{n+1} - P_{I,J+1}^{*}\right)\right], \tag{2.46}$$

where

$$d_{I,j} = \frac{A_{I,j}}{a_{z,P} - \sum_{nb} a_{z,nb}}$$

and $a_{z,P}$ and $a_{z,nb}$ are the diagonal and off-diagonal terms of discretized momentum equations, respectively. The superscript * denotes the intermediate solution variables. The relation in Eq. (2.46) must be coupled with scalar Eqs. (2.7), (2.8) and (2.10) to yield the pressure correction equation which would close the governing equations.

First, the secondary variables in scalar equations are linearized in terms of the primary variables as

$$\rho_v^{n+1} = \rho_v^n + \left(P^{n+1} - P^n\right)\left(\frac{\partial \rho_v}{\partial P}\right)^n \tag{2.47}$$

$$\begin{aligned}\rho_m^{n+1} = \rho_m^n &+ \left(\alpha^{n+1} - \alpha^n\right)\left(\rho_v^n - \rho_l^n\right) + \left(P^{n+1} - P^n\right)\left(\frac{\partial \rho_v}{\partial P}\right)^n \alpha^n \\ &+ \left[\left(P^{n+1} - P^n\right)\left(\frac{\partial \rho_l}{\partial P}\right)^n + \left(h_l^{n+1} - h_l^n\right)\left(\frac{\partial \rho_l}{\partial h_l}\right)^n\right]\left(1 - \alpha^n\right)\end{aligned} \tag{2.48}$$

$$T_l^{n+1} = T_l^n + \left(P^{n+1} - P^n\right)\left(\frac{\partial T_l}{\partial P}\right)^n + \left(h_l^{n+1} - h_l^n\right)\left(\frac{\partial T_l}{\partial h_l}\right)^n \tag{2.49}$$

$$T_{v,sat}^{n+1} = T_{v,sat}^n + \left(P^{n+1} - P^n\right)\left(\frac{\partial T_{v,sat}}{\partial P}\right)^n \tag{2.50}$$

$$\begin{aligned}\left(\rho_m h_m\right)^{n+1} = &\left(\rho_m h_m\right)^n + \delta\alpha\left(\left(\rho_v h_v\right)^n - \left(\rho_l h_l\right)^n\right) \\ &+ \left(\delta P\left(\frac{\partial \rho_l}{\partial P}\right)^n + \delta h_l\left(\frac{\partial \rho_l}{\partial h_l}\right)^n\right)\left(1 - \alpha^n\right)h_l^n + \delta P\left(\frac{\partial \rho_v}{\partial P}\right)^n \left(\alpha h_v\right)^n . \\ &+ \delta h_l\left(1 - \alpha^n\right)\rho_l^n + \delta P\left(\frac{\partial h_v}{\partial P}\right)^n \left(\alpha \rho_v\right)^n\end{aligned} \tag{2.51}$$

The combinations of the previous expressions with the scalar conservation equations lead to the following linear system for a certain scalar cell (*I,J*)

$$\begin{bmatrix} a_{11} & a_{12} & a_{13} \\ a_{21} & a_{22} & a_{23} \\ a_{31} & a_{32} & a_{33} \end{bmatrix}\begin{bmatrix} h_{l,I,J}^{n+1} \\ \alpha_{I,J}^{n+1} \\ P_{I,J}^{n+1} \end{bmatrix} = \begin{bmatrix} s_1 \\ s_2 \\ s_3 \end{bmatrix} - \begin{bmatrix} b_{11} & b_{12} & b_{13} & b_{14} & b_{15} & b_{16} \\ b_{21} & b_{22} & b_{23} & b_{24} & b_{25} & b_{26} \\ b_{31} & b_{32} & b_{33} & b_{23} & b_{35} & b_{36} \end{bmatrix}\begin{bmatrix} u_{ie,J}^{n+1} \\ -u_{iw,J}^{n+1} \\ v_{is,J}^{n+1} \\ -v_{in,J}^{n+1} \\ w_{I,j}^{n+1} \\ -w_{I,j-1}^{n+1} \end{bmatrix} . \tag{2.52}$$

By replacing the velocities of the new time step (*n*+1) in Eq. (2.52) with Eq. (2.46) and by inverting the 3x3 matrix on the LHS, the following linear system can be derived

$$\begin{bmatrix} h_{l,I,J}^{n+1} \\ \alpha_{I,J}^{n+1} \\ P_{I,J}^{n+1} \end{bmatrix} = \begin{bmatrix} s_1' \\ s_2' \\ s_3' \end{bmatrix} - \begin{bmatrix} b_{11}' & b_{12}' & b_{13}' & b_{14}' & b_{15}' & b_{16}' \\ b_{21}' & b_{22}' & b_{23}' & b_{24}' & b_{25}' & b_{26}' \\ b_{31}' & b_{32}' & b_{33}' & b_{23}' & b_{35}' & b_{36}' \end{bmatrix} \begin{bmatrix} d_{ie,J}\left[P_{I,J}^{n+1} - P_{IE,J}^{n+1}\right] \\ d_{iw,J}\left[P_{I,J}^{n+1} - P_{IW,J}^{n+1}\right] \\ d_{is,J}\left[P_{I,J}^{n+1} - P_{IS,J}^{n+1}\right] \\ d_{in,J}\left[P_{I,J}^{n+1} - P_{IN,J}^{n+1}\right] \\ d_{I,j}\left[P_{I,J}^{n+1} - P_{I,J+1}^{n+1}\right] \\ d_{I,j-1}\left[P_{I,J}^{n+1} - P_{I,J-1}^{n+1}\right] \end{bmatrix}. \quad (2.53)$$

Note that the linear system is changed to have neighbor coupling only in terms of pressure. The extraction of the 3rd row of the previous system yields the septa-diagonal linear system for the pressure equation

$$\left[1 + \sum_{nb} b_{nb}''\right] P_{I,J}^{n+1} - \sum_{nb} b_{nb}'' P_{nb}^{n+1} = s_3'. \quad (2.54)$$

The overall calculation procedure of SIMPLEC algorithm is illustrated in Figure 2-3 and the flowchart of ESCOT is given as well in Figure 2-4. At the beginning of a calculation, the flow regime maps in all computing cells are determined to set the appropriate correlations. The intermediate velocities are then obtained by solving linear systems of lateral and axial momentum equations, which are a penta-diagonal and a septa-diagonal matrix, respectively.

Next, the linear system of the pressure equation is solved, and the mixture velocity at the new time step is updated by the solution of the pressure equation. Although an iterative process might be recommended to achieve the converged solutions of velocities and pressure, performing only one outer iteration turned out to be enough in most cases as long as the time step size is sufficiently small.

The rest primary variables are determined by solving coupled system of Eq. (2.53) and the secondary variables are then updated through the steam table. The calculation is terminated when the convergence criteria are met or the simulation time reaches the end time.

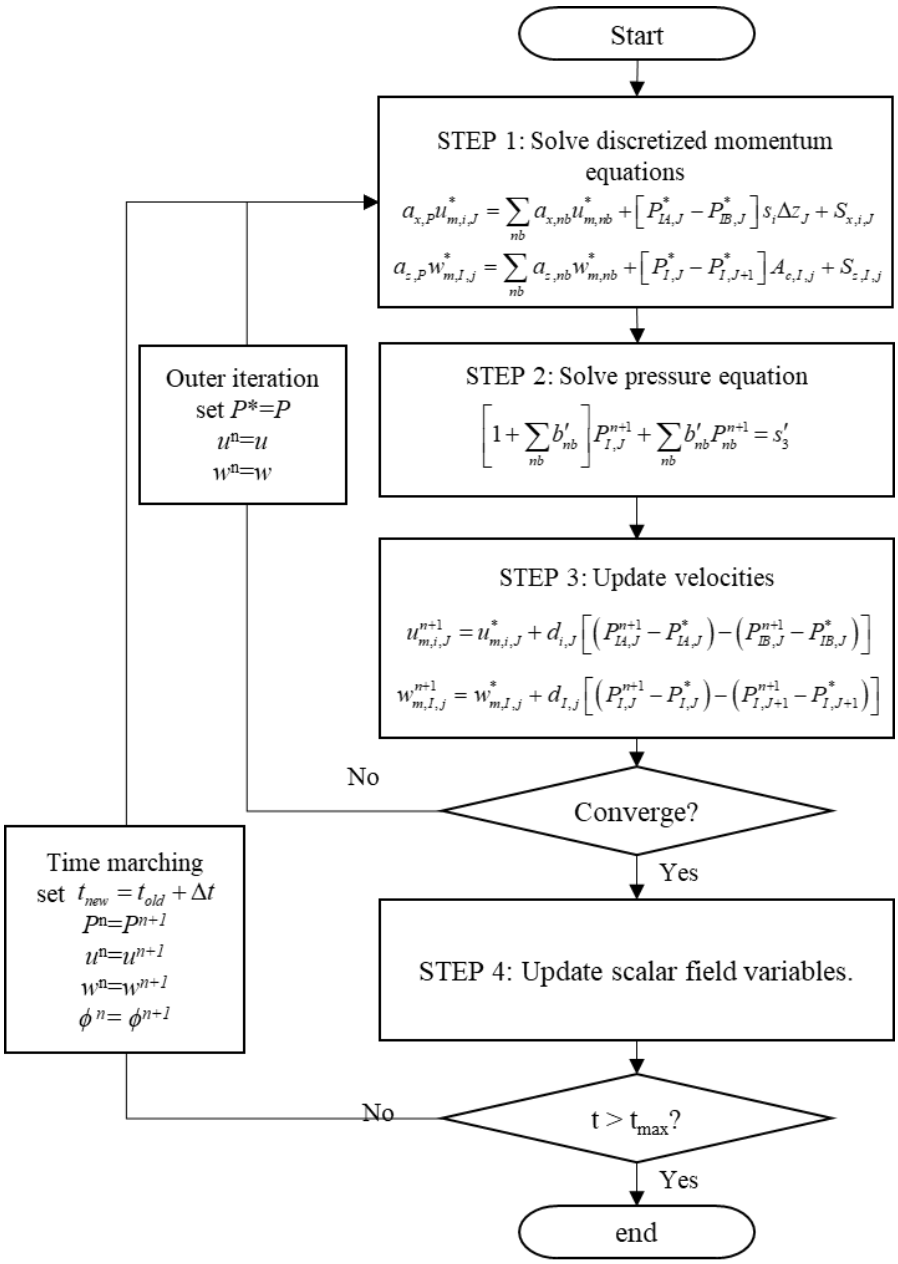

Figure 2-3. Flowchart of SIMPLEC algorithm

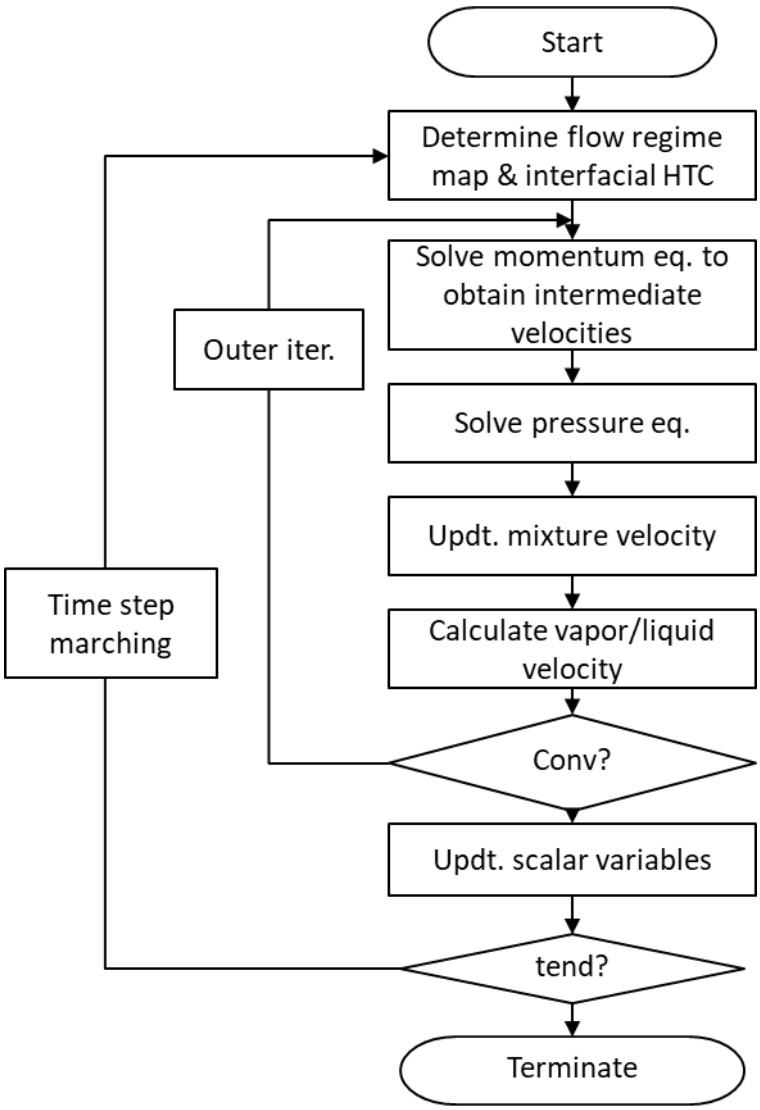

Figure 2-4. Flowchart of ESCOT based on the SIMPLEC algorithm

Four convergence criteria are monitored to determine whether a calculation reaches steady-state. The first criterion is the mass balance. It checks if the outlet and inlet mass flows are equal. It is defined as the difference between inlet and outlet mass flow rate divided by inlet mass flow rate as

$$M_{\text{balance}}(\%) = \frac{\dot{m}_{inlet} - \dot{m}_{outlet}}{\dot{m}_{inlet}} \cdot 100, \tag{2.55}$$

where

$$\dot{m}_{in} = \sum_{cell,in} \left(\rho v_m A\right)_{cell}.$$

The second parameter is the energy balance. It represents the energy conservation by checking output energy via outlet and the input energy via inlet and heated rod as

$$E_{balance}(\%) = \frac{\left(Q_{outlet} + Q_{drift}\right) - \left(Q_{rod} + Q_{inlet}\right)}{Q_{rod} + Q_{inlet}} \cdot 100, \tag{2.56}$$

where

$$Q_{in} = \sum_{cell,in} \left(\dot{m} h_m\right)_{cell}$$

and

$$Q_{drift} = \sum_{j=1}^{N_z} \left(\alpha \frac{\rho_l \rho_l}{\rho_m} \left(h_l - h_v\right) \vec{V}'_{gz} A_c \right)_j$$

The third parameter is the mass storage. It accounts for the mass stored in the system during the time step by comparing the difference between the present and the previous time step values of total mass. It is expressed as

$$\Delta M_{\text{mass storage}}(\%) = \frac{\Delta M_{fluid}}{\dot{m}_{inlet}} \cdot 100, \tag{2.57}$$

where

$$\Delta M_{fluid} = \sqrt{\sum_{cell}^{nell} \left[\left(\rho_{m,cell}^{n+1} - \rho_{m,cell}^{n} \right) \Delta V_{cell} \right]^2} \,/\, \Delta t.$$

The final parameter is the fluid energy storage. It accounts for energy stored in the fluid during the time step. Its expression is

$$\Delta E_{\text{fluid storage}} = \frac{\Delta E_{fluid}}{Q_{rod} + Q_{fluid}} \cdot 100 \quad , \tag{2.58}$$

where

$$\Delta E_{fluid} = \sqrt{\sum_{cell}^{nell} \left[\left(\left(\rho_m h_m \right)_{cell}^{n+1} - \left(\rho_m h_m \right)_{cell}^{n} \right) \Delta V_{cell} \right]^2} \, / \, \Delta t \quad .$$

2.5. Solution of the Conduction Equation

In the solution of coupled neutronics-T/H calculation, besides the moderator density and temperature, the temperature of clad, gap and fuel are necessary to solve the problem. For this reason, ESCOT includes the capability for fuel rods temperature distribution calculations.

2.5.1. The conduction equation

Departing from the heat balance equation for solids

$$\frac{\partial \left[e\left(\vec{r},t\right) \right]}{\partial t} + \nabla \cdot \left(\vec{q}^{\,''}\left(\vec{r},t\right) \right) = q^{'''}\left(\vec{r},t\right), \tag{2.59}$$

where the energy term is given by the product of three main terms:

$$e\left(\vec{r},t\right) = \rho\left(\vec{r},T\left(\vec{r},t\right)\right) c_p\left(\vec{r},T\left(\vec{r},t\right)\right) T\left(\vec{r},t\right), \tag{2.60}$$

while the convection terms can be substituted with the Fourier's wall conduction law:

$$\vec{q}^{\,''} = -k\left(\vec{r},T\left(\vec{r},t\right)\right) \nabla \left(T\left(\vec{r},t\right) \right). \tag{2.61}$$

Replacing Eq. (2.60) and (2.61) into Eq. (2.59) and simplifying the notation of the density ρ, the heat capacity at constant pressure c_p and the thermal conductivity k

$$\frac{\partial\left(\rho c_p T\right)}{\partial t}=\frac{\partial\rho}{\partial t}c_p T+\rho\frac{\partial c_p}{\partial t}T+\rho c_p\frac{\partial T}{\partial t}=\nabla\cdot\left(k\nabla T\left(\vec{r},t\right)\right)+q'''\left(\vec{r},t\right), \quad (2.62)$$

together with its boundary conditions

$$\begin{gathered} T\left(\vec{r},t_0\right)=T^*\left(\vec{r}\right) \\ \nabla T\left(\vec{r},t\right)=\nabla T\left(\vec{r}_0,t\right)\div T\left(\vec{r}_1,t\right)=T\left(\vec{r}_1,t\right) \end{gathered}, \quad (2.63)$$

and by applying the chain rule for partial derivatives to express the time dependency of ρ and c_p in temperature:

$$\frac{\partial\left(\rho c_p T\right)}{\partial t}=\left(\frac{\partial\rho}{\partial T}c_p T+\rho\frac{\partial c_p}{\partial T}T+\rho c_p\right)\frac{\partial T}{\partial t}, \quad (2.64)$$

the final equation heat balance equation can be formulated as:

$$\left(\frac{\partial\rho}{\partial T}c_p T\left(\vec{r},t\right)+\rho\frac{\partial c_p}{\partial T}T\left(\vec{r},t\right)+\rho c_p\right)\frac{\partial T\left(\vec{r},t\right)}{\partial t}=\nabla\cdot\left(k\nabla T\left(\vec{r},t\right)\right)+q'''\left(\vec{r},t\right). \quad (2.65)$$

In ESCOT the thermal conductivities and heat capacities are obtained from the FRAPCON correlations [55] for the fuel and clad materials respectively. The density of fuel and clad are considered constant in time $\frac{\partial\rho}{\partial t}=0$. For the gap conductance, however, the correlation employed is the one of BISON [56]

2.5.2. The solution strategy and implementation

ESCOT implements two main conduction solvers for the solution of Eq. (2.65), one for steady state and one for transient. Since this work is circumscribed to steady state problems only the former is described here. The conduction equation (Eq. (2.65)) for steady-state problems is simplified as

$$\nabla\cdot\left(k\nabla T\right)=q''' \quad (2.66)$$

with boundary conditions

$$k_{fuel}\nabla T(0)=0$$
$$T(r_{co})=T_w \quad , \tag{2.67}$$

where r_{co} is the outer radius of the fuel rod and T_w the outer surface temperature.

The continuity between fluid and wall has been established according to the convection equation

$$q'' = h(T_w - T_{bulk}), \tag{2.68}$$

where the wall heat transfer coefficient h is obtained from an empirical correlation which depends on the boiling regime. For the single liquid phase forced convection considered in this work ESCOT defines the wall heat transfer coefficient from the maximum between the Dittus-Boelter [57] and Sparrow [58] correlations

$$h = \max\left(0.023\frac{k_l}{D_h}\mathrm{Re}_l^{0.8}\,\mathrm{Pr}_l^{0.4}, 7.86\frac{k_l}{D_h}\right). \tag{2.69}$$

The equation has been integrated in the finite volume with the fuel pin discretization depicted in Figure 2-5.

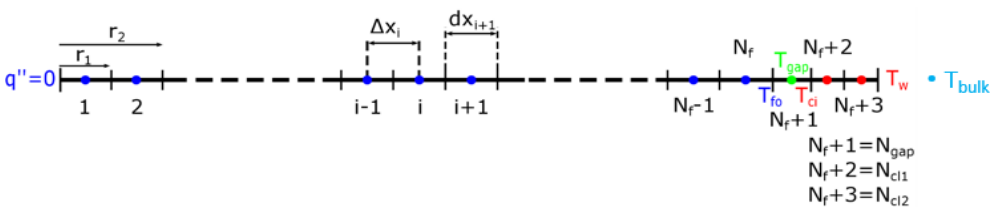

Figure 2-5. Radial discretization of the fuel pin for the conduction equation solution

This integration yields the following expression for the fuel pin

$$k_{fuel}^{i+\frac{1}{2}}(T_{i+1}-T_i) - k_{fuel}^{i-\frac{1}{2}}(T_i - T_{i-1}) + q_i'''\Delta V_i = 0\,, \tag{2.70}$$

where the temperature dependent inter-mesh conductivity coefficients in a cylindrical geometry are determined as

$$k_{fuel}^{i+\frac{1}{2}} = \frac{2\pi k_{fuel}^{i+1} k_{fuel}^{i}}{k_{fuel}^{i} \log\left(\frac{r_{i+1}}{r_{i+1/2}}\right) + k_{fuel}^{i+1} \log\left(\frac{r_{i+1/2}}{r_{i}}\right)}$$
$$k_{fuel}^{i-\frac{1}{2}} = \frac{2\pi k_{fuel}^{i} k_{fuel}^{i-1}}{k_{fuel}^{i-1} \log\left(\frac{r_{i}}{r_{i-1/2}}\right) + k_{fuel}^{i} \log\left(\frac{r_{i-1/2}}{r_{i-1}}\right)} \tag{2.71}$$

For the gap-clad the following continuity model is applied

$$2\pi R_{fo} h_{gap} \left(T_{fo} - T_{ci}\right) = k_{cl}^{N_f+2} \left(T_{ci} - T_{N_f+2}\right) \tag{2.72}$$

Since the thermal properties depend on the temperature an iterative process is needed to solve the system. Once the solution converges the center line temperature is obtained with a simple interpolation. A more detailed explanation is given in reference [59].

2.6. Hexagonal Geometry Extension

The DFM governing equations in hexagonal geometry as well as the solution algorithm flow do not vary from the ones in the cartesian case. However, due to the geometry change, the equations discretization and the geometry dependent coefficients need to be adapted. These modifications are addressed in the following.

2.6.1. Lateral momentum equation modifications

As previously described the lateral momentum balance is defined in the gap-centered cell. For its discretization the expression is integrated over the gap-centered Control Volume (CV) as shown in Eq. (2.73).

$$\int_{CV}\left[\frac{\partial\left(\rho_m\vec{u}_m\right)}{\partial t}+\nabla\cdot\left(\rho_m\vec{u}_m\vec{u}_m\right)\right]dV = \int_{CV}\left[\rho_m\vec{g}-\nabla P+\nabla\cdot\boldsymbol{\tau}_m^{ij}-\nabla\cdot\vec{F}_{tm}''-\nabla\cdot\left(\frac{\alpha}{1-\alpha}\frac{\rho_v\rho_l}{\rho_m}\vec{V}_{gj}'\vec{V}_{gj}'\right)\right]dV \quad . \quad (2.73)$$

The integration of the left-hand side (LHS) of the equation yields the following discretized expression:

$$\begin{aligned}\int_{CV}\nabla\cdot(\rho_m u_m\vec{u}_m)dV &= \int_s((\rho_m u_m)^n\vec{u}_m^{n+1})\cdot d\vec{S}\\ &=\left[(\rho_m u_m)^n s_i\Delta z_J u_m^{n+1}\right]_{IB,J}-\left[(\rho_m u_m)^n s_i\Delta z_J u_m^{n+1}\right]_{IA,J},\\ &\quad+\left[(\rho_m w_m)^n s_i l_i u_m^{n+1}\right]_{i,j}-\left[(\rho_m w_m)^n s_i l_i u_m^{n+1}\right]_{i,j-1}\end{aligned} \quad (2.74)$$

where s_i is the gap (distance between rods) dimension and Δz_J the height of the momentum cell. The subscripts IA,J and IB,J are the momentum control volume cell surface indices, which are equivalent to subchannel indices I,J and I+1,J in Figure 2-2.

Here the first two terms correspond to the radial component which considers the effect of the adjacent gap's radial velocities. The last two terms, analogously, account for the impact in the balance of the axial velocities for the CVs in the planes above and below of the CV of interest.

Although this balance can be straightforwardly adapted to the hexagonal geometry, the radial direction term presents some problems in form of instabilities and asymmetries when the adjacent velocities are projected onto the gap normal. As the radial velocity is several orders of magnitude smaller than the axial one and the contribution of this term is negligible compared to others present in the balance (such as the pressure differences), this component is eliminated as recommended in reference [54]. In CTF this term is optional and can be activated from the input file. In the case of being activated the radial velocities are considered provided they are

orthogonal to the gap of interest. In the hexagonal geometry case this only occurs for the few edge-to-edge channel connections and therefore this option has not been activated in this work.

Note that, in principle, this simplification can be applied provided the problem possesses an axial velocity dominance. Since ESCOT was primarily conceived as a code to be employed in (pseudo) steady state and mild transient cases, the axial velocity preponderance is inherent to the possible problems to be solved.

With the aim at verifying this assumption a cartesian geometry problem is simulated with and without the radial component. The results yielded for several primary and secondary variables are compared for different percentages of axial mass flow. The cartesian geometry problem chosen to carry out this assessment is a single assembly based on the APR1400 core geometry. Although ESCOT has the radial term activated by default only the velocities orthogonal to the gap of interest are considered in the CV momentum balance. Thus, the velocities parallel to the gap are neglected (like in CTF).

Figure 2-6 shows how the relative differences for the assessment variables stay within reasonable values despite the mass flow reduction, consequently the assumption is considered appropriate.

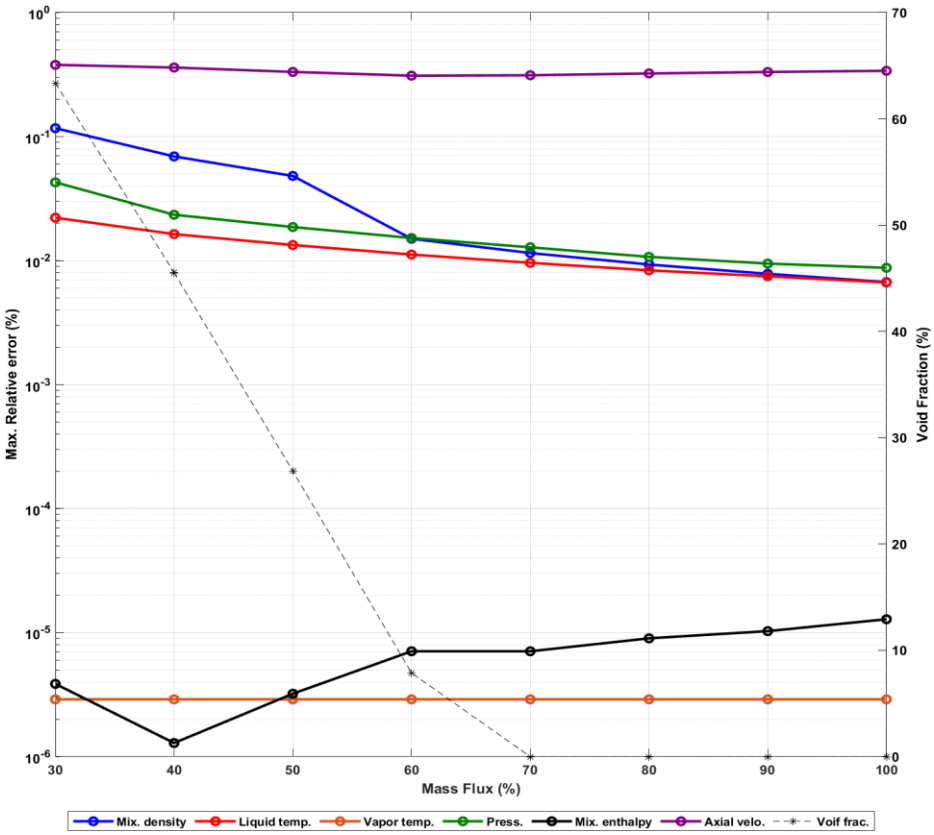

Figure 2-6. Impact of the radial term of the lateral momentum equation on the main variables for decreasing mass flux

2.6.2. Turbulent mixing coefficient in hexagonal problems

As explained in section 2.3.4, ESCOT applies the Equal-Volume-exchange turbulent mixing and Void Drift (EVVD) model. This model results in a set of four equations (one per DFM equation) that contain the term named mixing coefficient over turbulent length given in Eq. (2.37), which is retrieved here for convenience

$$\frac{\varepsilon}{z_{ij}^{T}} = \frac{\beta \bar{G}}{\bar{\rho}},$$

where the turbulent mixing parameter β is affected by the change of geometry. In ESCOT this coefficient, unlike in other codes, is not updated at every iteration and is fixed at a value of 0.05 in every channel for square fuel assembly problems.

Nevertheless, ESCOT takes as a reference for the mixing coefficient determination the Rogers & Rosehart correlation [50]:

$$\begin{aligned} \beta &= 0.5\lambda \,\mathrm{Re}^{-0.1}\left[1+\left(\frac{D_{h,j}}{D_{h,i}}\right)^{1.5}\right]\frac{D_{h,i}}{D_{rod}}, \quad \text{if } D_{h,i} < D_{h,j} \\ \beta &= 0.5\lambda \,\mathrm{Re}^{-0.1}\left[1+\left(\frac{D_{h,i}}{D_{h,j}}\right)^{1.5}\right]\frac{D_{h,j}}{D_{rod}}, \quad \text{if } D_{h,j} < D_{h,i} \end{aligned} \quad . \qquad (2.75)$$

Note that in this set of equations the parameter β depends on the hydraulic diameter (D_h). As the relation between hydraulic diameters for square and hexagonal geometries in the most typical type of channel in the core (inner channel) is approximately D_h^{hex} ~0.6 D_h^{sq} , the recommended mixing coefficient for the simulation of VVERs is β = 0.03.

In order to verify the mixing model as well as the fixed value for the turbulent mixing coefficient a simple model based on a VVER-1000 single assembly geometry is employed. With the aim at keeping the symmetry the guide tubes are replaced with fuel pins.

In this model a radial gradient of the relative power is imposed. In the simple sketch of Figure 2-7 the fuel pins under the blue area have a relative power of 1.5, the yellow one of 0.5 and the red one of 1.0. The axial power distribution for its part is uniform from top to bottom.

Then the coolant temperature at the indicated subchannels are compared for different mixing coefficients with ESCOT and CTF. The mixing coefficients are namely no mixing (NM), turbulent mixing coefficient of 0.03 and turbulent mixing coefficient obtained with the Rogers & Rosehart correlation (only for CTF).

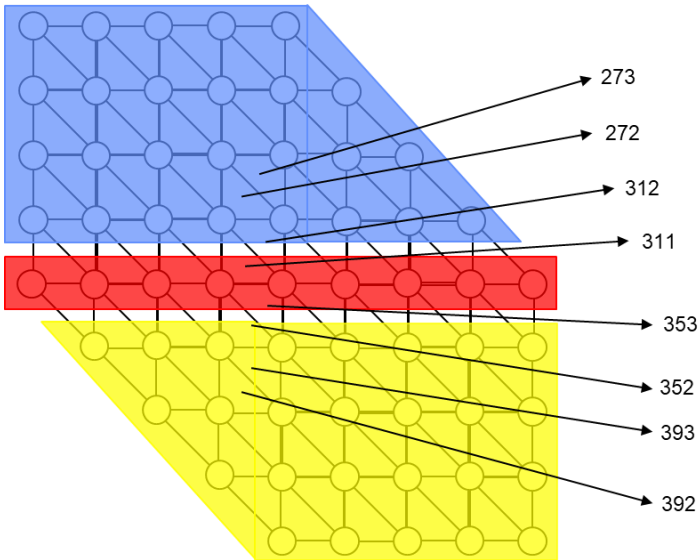

Figure 2-7. Sketch of the simplified VVER-1000 single assembly model indicating the relative power radial distribution and the channels observed in the analysis

The results depicted in Figure 2-8 allow to conclude that, due to the small difference between ESCOT and CTF values, the mixing model is appropriate and properly implemented in ESCOT. On the other hand, the comparison of the temperature values yielded by the fixed-value and the ones by the correlation-dependent coefficient make clear that 0.03 slightly exacerbates the mixing in the problem. However, the differences are not excessively large (3-5 °C) given the extreme conditions applied in this problem. Thus, the proposed fixed value should not induce erroneous results in realistic problems.

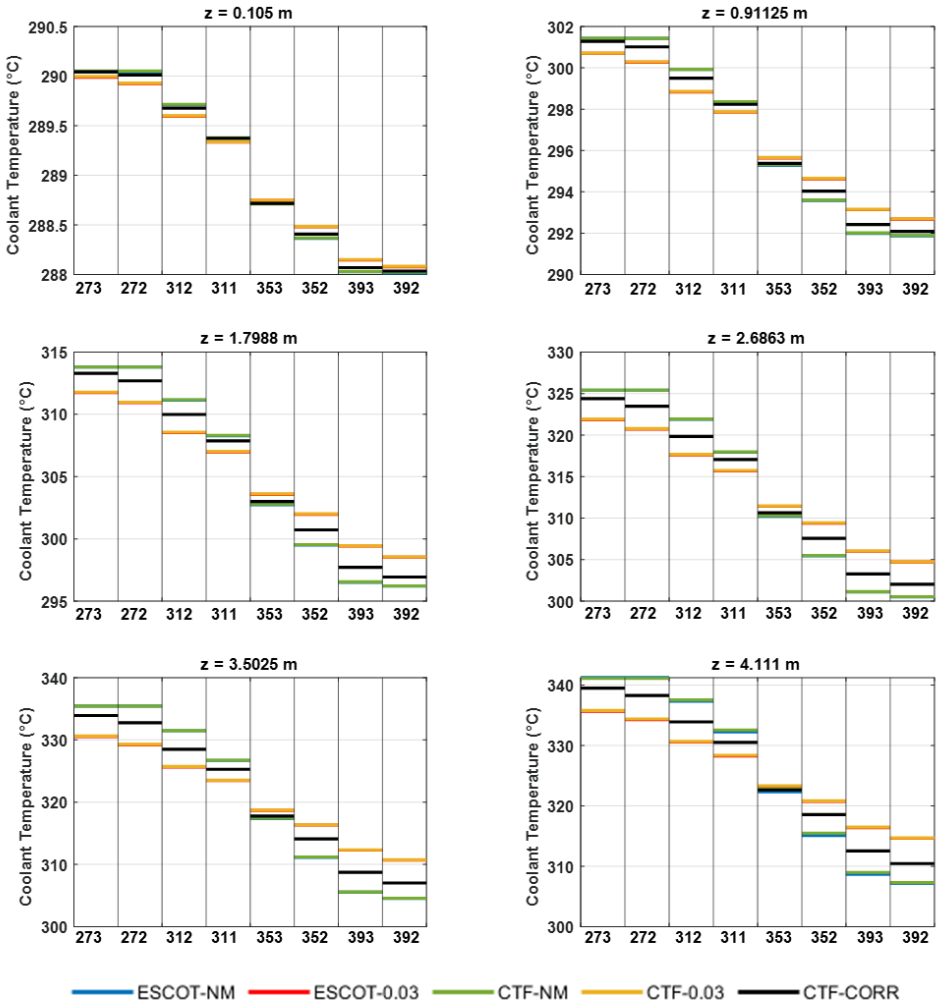

Figure 2-8. ESCOT and CTF coolant temperature results at different channels and elevations for diverse turbulent mixing coefficient values

2.6.3. Fuel conduction in hollow pins

The fuel pins in VVER cores are hollow, this is with a hole at its center. The fuel conduction solver needs to be adapted to contemplate this peculiarity. For this the solid conduction is solved within the solid excluding the gas in the central hole.

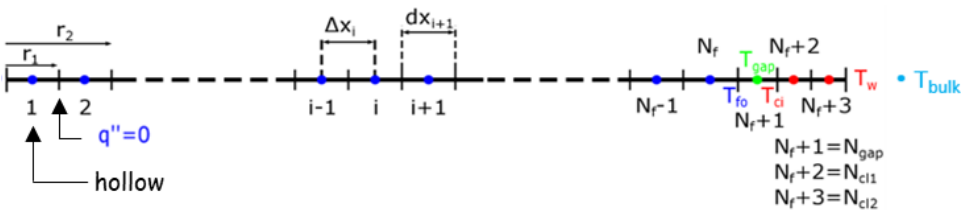

Figure 2-9. Radial discretization of the hollow fuel pin for the conduction equation solution

Once the fuel temperature has reached convergence the temperature at the inner rim is calculated by extrapolation. Then the temperature in the whole, including the central line, is assumed to be the same as in the inner hole surface. Figure 2-10 shows the fuel temperature radial distribution for a hollow pin obtained numerically and analytically, while Figure 2-11 shows the error between both solutions. Since the maximum difference is lower than 1 °C, which corresponds to a relative error of 0.1 %, the solution and the assumptions for the hollow pin are considered valid.

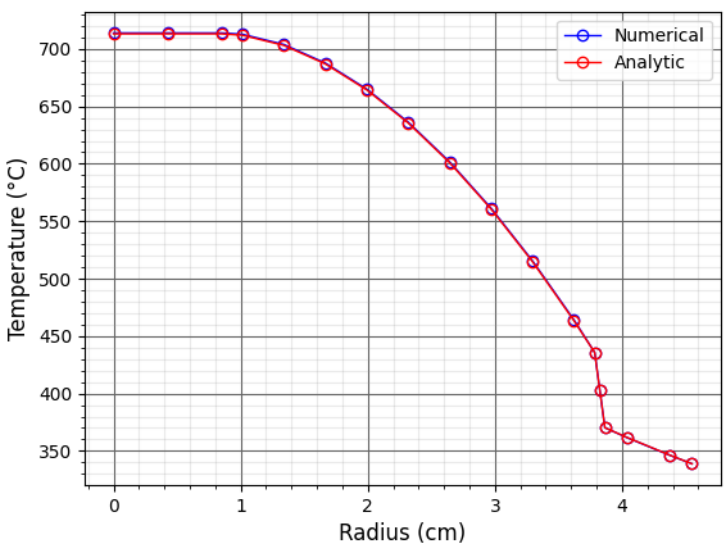

Figure 2-10. Fuel rod temperature analytic and numerical solutions radial distribution

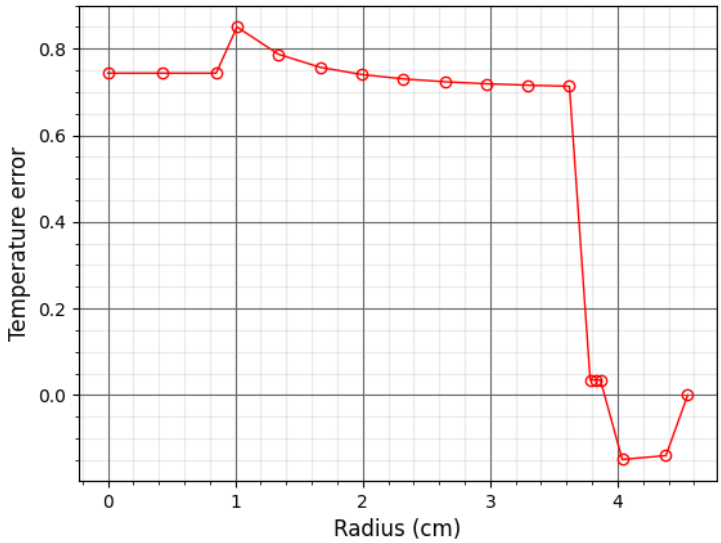

Figure 2-11. Fuel rod temperature error radial distribution

2.7. Hexagonal Geometry Radial Domain Decomposition

ESCOT applies a bidirectional (axial and radial) domain decomposition in order to achieve massive parallelization aiming at multinode and multicore platforms employing for it the MPI internode communication tool. Thus, each assembly is assigned to a different process. For the case of bordering elements (namely channels and gaps) the dominant process is determined from left to right and top to bottom as illustrated in Figure 2-12.

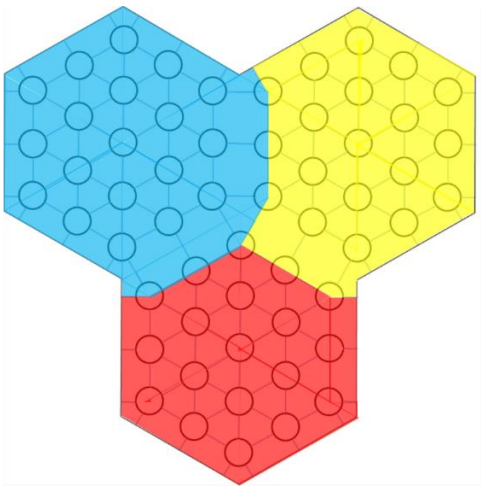

Figure 2-12. Radial domain elements process assignment

The cell elements at the boundaries of each domain might require the data of other domains running in other processes so that their linear systems can be solved. To enable this, auxiliary cells (or ghost cells) representing these missing cells are defined at the boundaries as shown in Figure 2-13. After each iteration real cells pass their data to their equivalent ghost cells in other processes so that they can be employed in the next iteration.

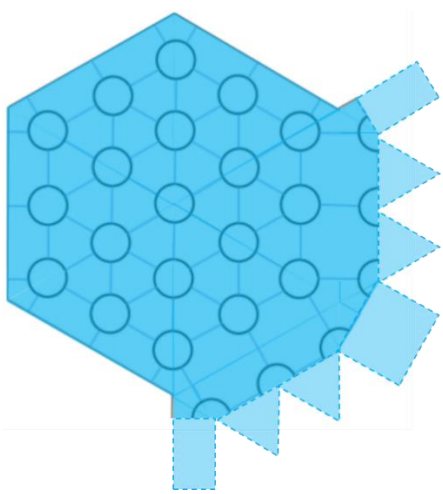

Figure 2-13. Radial domain ghost cell definition

2.8. Code-to-Code ESCOT Hexagonal Verification with CTF

The standalone comparison aims at assessing the modifications implemented in ESCOT to compute hexagonal geometry problems by comparing its results with CTF. In order to do so three different problems are computed, one consisting of a single assembly to inspect the T/H variables accuracy, a second one which is a full core problem to evaluate the solution time performance and a third one is a minicore to assess the parallelization schemes in ESCOT.

The reactor model employed for the assessment is the VVER-1000 reactor benchmark X-2 [36][37]. The operating conditions for the Hot Full Power (HFP) state. are a fuel assembly average power of 18.40491 MW, an inlet temperature of 287 °C, a pressure at the core outlet of 15.7 MPa and a mass flow of 109.8 kg/s.

The absolute differences for the variables results are determined by subtracting the ESCOT values from the CTF ones, as for the relative ones the previous result is divided by the CTF values.

All the calculations are performed on a 10-node cluster in which each node is equipped with two 26 core CPUs of Intel Xeon Gold 6230 R with 2.10 GHz clocks and with 540 GB RAM.

2.8.1. Solution accuracy assessment with single assembly problem

The single assembly calculation is performed employing a single core. The stopping criteria for both codes is 0.01 for the balance variables and 0.1 for the storage ones. The analysis of the T/H variables consists of the comparison of the axial distribution of the coolant density, temperature and pressure for two channels

at different assembly locations. The two locations are the central channel at the assembly edge (edge channel) and at one of the channels surrounding the assembly central instrumentation tube (inner channel).

The distributions are shown in Figure 2-14 together with the relative differences between CTF and ESCOT results. These differences remain below a maximum of 0.01 %, obtained for the coolant temperature at the inner channel outlet, which is a negligible value given the differences in the governing equations.

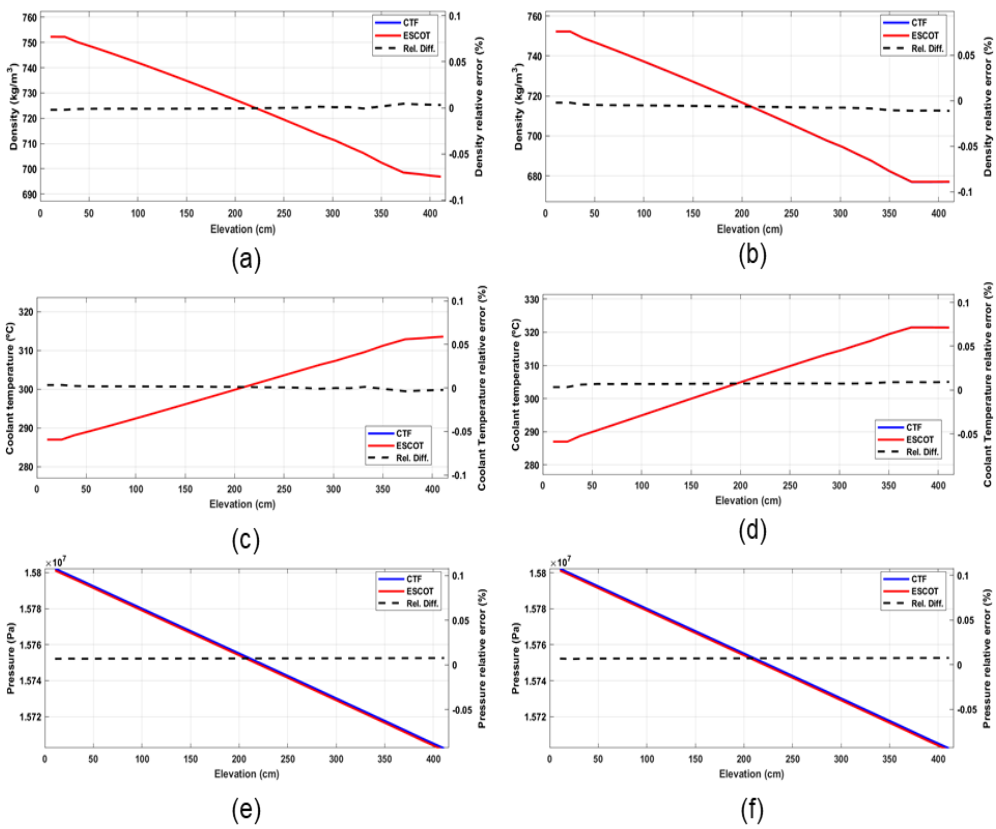

Figure 2-14. Coolant density, temperature and Pressure axial distributions and relative differences for edge (a, c and e) and central (b, d and f) channels

Both CTF and ESCOT give the option of calculating the fuel temperature distribution by solving the conduction equation in the pins once the T/H variables

reach convergence. For the comparison of the fuel temperature here the fuel pin is discretized with 10 concentric rings.

Note that in the case of VVERs the pins have a hole at the center and therefore there is an extra central ring for which the temperature is not determined with the linear system solution. Thus, the central temperature of the pin needs to be set once the linear problem is converged. For the setting of this temperature CTF and ESCOT follow the same approach. They determine the inner hole rim temperature by adjusting it with a quadratic approximation and the central temperature is assumed to have the same magnitude as this rim value as described in section 2.6.3.

Figure 2-15 depicts the radial distribution fuel temperatures at three different axial locations (active height bottom, middle and top) for the central fuel pin at the assembly edge and at a pin surrounding the central instrumentation tube. CTF output gives the temperatures at the clad outer and inner surfaces and fuel pin surface and central line. The differences are smaller than 0.1 °C for the almost every point and goes up to slightly above 0.1 ºC for the center line temperature for the outer pin at top elevation.

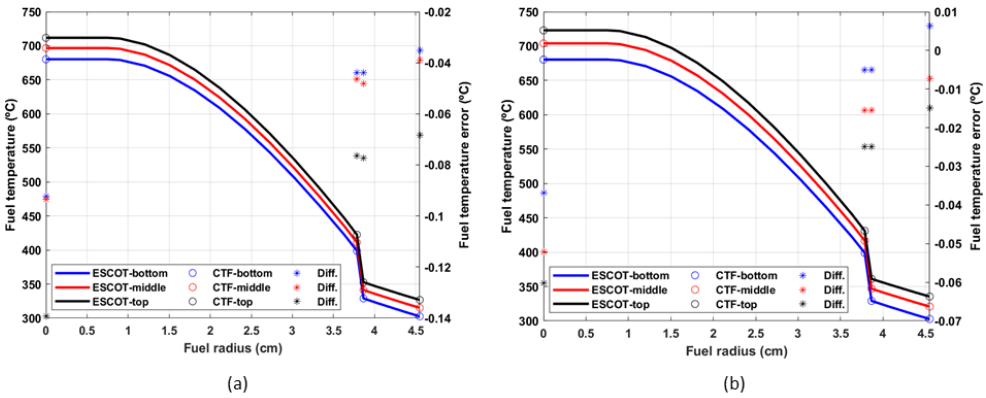

Figure 2-15. Fuel pin temperature radial distributions and differences at the edge central pin (a) and assembly central pin (b) at three different elevations

2.8.2. Drift-flux model time performance assessment with full core problem

The computing time performance of the codes is inspected by simulating the full core problem. The objective with these calculations is to demonstrate the superiority of the DFM over the two-fluid approach by comparing the momentum equations computing time. The comparison is performed applying radial parallelization for which one core is assigned to each assembly, what makes a total of 163 computing cores.

The main solution steps and the total computing time are summarized in Table 2-2. The comparison of computing times for CTF and ESCOT employing the same parallelization confirms the advantage of the simplified DFM as the solution of the momentum and pressure linear systems is faster in ESCOT by a factor of about 1.57 and 1.76, respectively. The only solution step for which CTF is faster than ESCOT is the next time step variables update. This step consists mainly in the use of steam tables and this result makes clear the inefficiency of the IAPWS tables implemented in ESCOT and it implies and aspect of potential improvement in ESCOT. It turns out that ESCOT is 1.35 times faster than CTF to compute the full core problem in terms

of the total computing time even though CTF requires a lower number of iterations to converge.

Table 2-2. CTF and ESCOT time performance comparison for a full core calculation

	CTF	ESCOT
Initialization (s)	19.6	16.9
Momentum eq. solution (s)	96.9	61.7
Pressure eq. solution (s)	315.1	178.7
Scalar variables solution (s)	23.1	21.0
Next time step update (s)	5.2	35.8
Total time (s)	524.6	389.2
Number of iterations	274	340

2.8.3. Parallelization assessment with minicore problem

For the assessment of the radial and radial-axial parallelization schemes in ESCOT a minicore consisting of nineteen assemblies (see Figure 2-16) is simulated with an increasing number of cores. The radial parallelization is carried out by assigning one core per assembly, seven in this case. The radial-axial parallelization is performed by assigning a number of cores that is multiple of the number of assemblies.

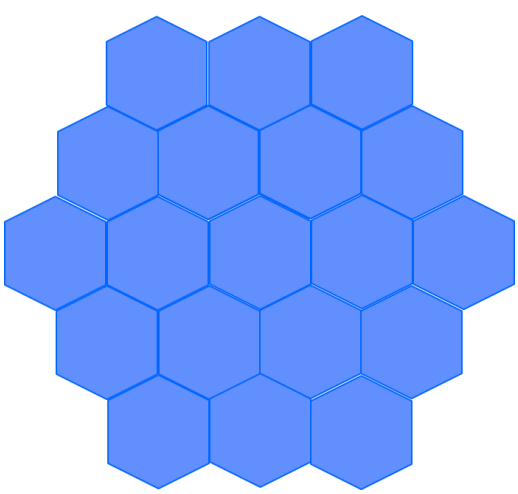

Figure 2-16. Minicore radial configuration

Table 2-3 contains the computing time for each process and for the entire simulation for several number of employed cores as well as the speed-up (in brackets) reached at each simulation. The momentum equation process includes the axial and radial momenta and set-up and solution. The same applies to the pressure equation.

The radial parallelization in ESCOT for the full core yields a speedup of a factor 4.5 with respect to the single processor calculation. By only doubling the number of processors in a radial-axial parallelization the calculation becomes 7.7 times faster than the single processor one. Although the increase of processors beyond this point reaches even greater speed-up factors this is hindered by the increasing communication time (see Figure 2-17).

Table 2-3. ESCOT processes parallelization time performance and speed-up

# Cores	**1**	**19**	**38**	**76**	**152**
Initialization (s)	2.2	4.5	4.9	5.9	9.2
Momentum equation (s)	549.7	41.4 (13.3)	21.6 (25.4)	17.1 (32.2)	16.2 (34.0)
Pressure equation (s)	1439.3	103.1 (14.0)	62.0 (23.2)	44.7 (32.2)	39.3 (36.6)
Scalar variables solution (s)	35.5	11.2 (3.2)	5.4 (6.5)	8.0 (4.5)	9.6 (3.7)
Next time step update (s)	386.4	24.3 (15.9)	13.7 (28.2)	7.9 (48.8)	6.2 (62.0)
Comm. (s)	-	19.9	9.4	15.0	19.0
Total time (s)	2449.7	192.7 (12.7)	115.1 (21.3)	90.7 (27.0)	88.9 (27.5)

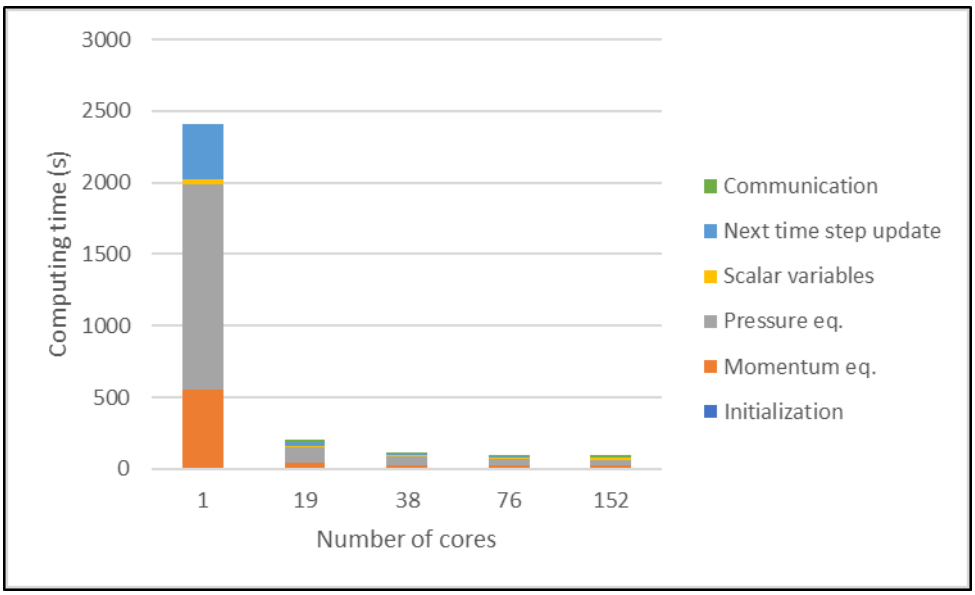

Figure 2-17. ESCOT parallelization time performance with several number of cores

2.9. Spacer Grids Models in ESCOT

Spacer grids are used in nuclear reactors to maintain the structural integrity of the fuel assemblies, this is to keep the fuel rods' position during operation. The introduction of spacer grids entails a series of side-effects in the reactor physics, such as an increased fluid motion, which in turn enhances cooling effects, or an increased axial pressure loss, which needs to be compensated by the main coolant pump at the core inlet.

Accounting for the grid-induced effects in the simulation in detail requires precise knowledge of their geometry. Depending on the type of grid, the range of effects or their intensity may vary. For example, the type of springs that keep the rod in place or the presence of mixing vanes and their characteristics.

The scale of these localized effects makes them difficult to place into subchannel codes and their predictions are generally better with CFD simulations. Subchannel

codes, such as CTF, contain correlations and approximations to account for this spacer grid effects [38]. At the present moment, ESCOT only allows for the introduction of a fixed form loss value corresponding to K_z in Eq. (2.29) which induces an extra axial pressure loss. The objective in this section is introducing a more sophisticated model for pressure loss coefficient calculation as well as the necessary correlations for HTC and turbulent mixing enhancement due to the presence of the grids.

Since detailed parameters of the VVER spacer grids are not available, the newly introduced correlations in ESCOT are verified with their counterparts in CTF by employing the same parameters in both subchannel codes. Ideally, these parameters should be obtained from empirical results, or at least from CFD simulations, if the detailed geometry of the grids was known.

2.9.1. Spacer grid form loss coefficient for pressure drop

The current strategy in ESCOT to account for the pressure drop due to the presence of spacer grids is via the form loss coefficient as

$$\Delta P_{SG} = -\Phi \frac{K_z}{2\Delta z} \rho_m w_m \left| w_m \right|, \tag{2.76}$$

CTF also offers the possibility of using the user-dependent form loss coefficient and therefore it can be compared right away. However, because of the lack of VVER spacer grid manufacturer data, a wide range of form loss coefficient values are evaluated. The problem model is based on the X-2 VVER single assembly in which the guide tubes have been replaced with fuel pins to prevent any asymmetry. The power is set uniform radially and axially. Figure 2-18 shows that, despite an increased relative error at the spacer grid locations, the error is still very small.

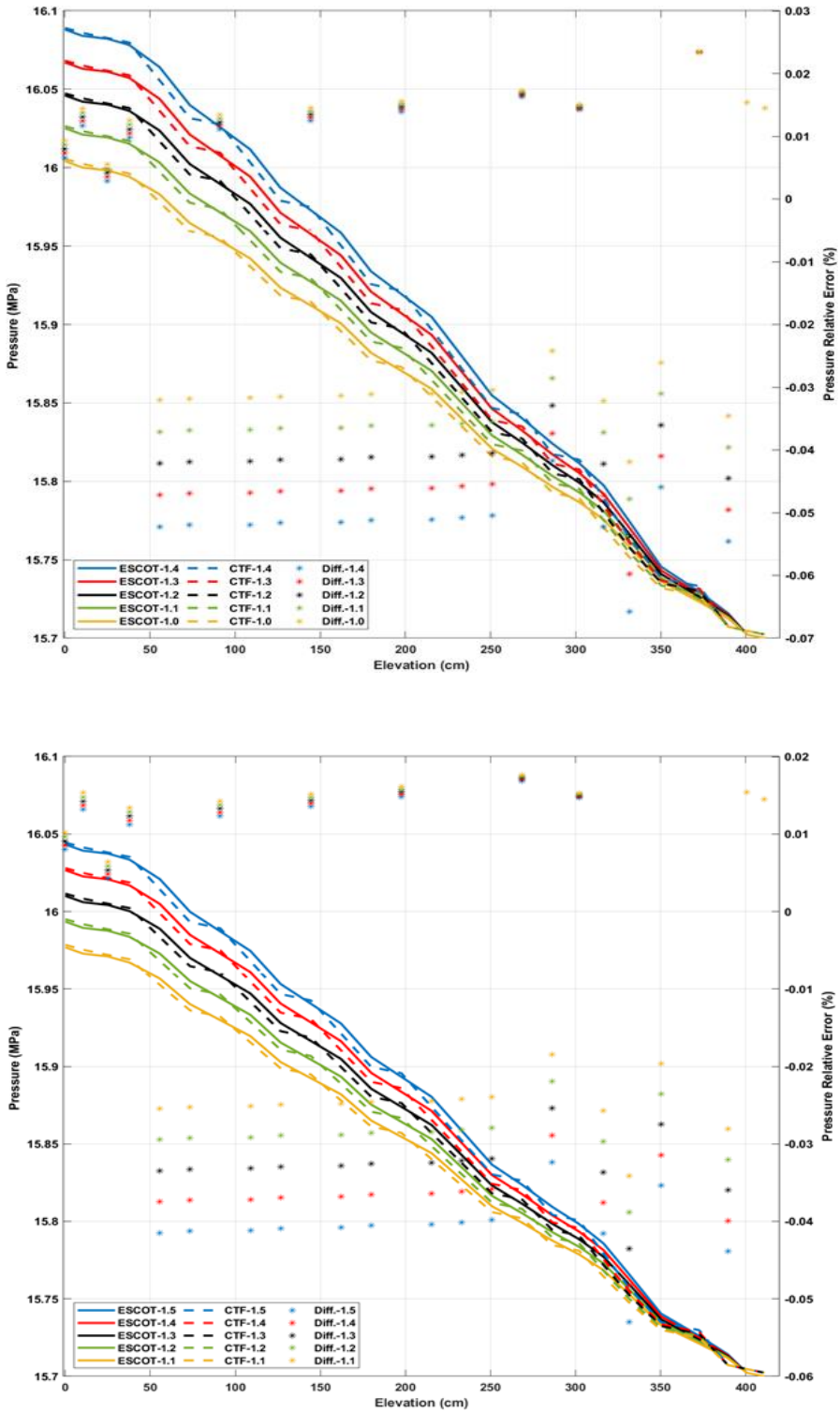

Figure 2-18. ESCOT and CTF radially averaged pressure curves for different form loss coefficients

The pressure loss depends on the area reduction due to the presence of the spacer grid itself, its restraint mechanisms such as springs and the mixing vanes. In order to make the form loss coefficient depend on this area reduction the following expression is employed.

$$K_z = \begin{cases} \min\left\{20{,}196\,\mathrm{Re}_m^{-0.333}\right\} f_{loss} A_{SG,block}^2, & if\ \mathrm{Re}_m \le 10^4 \\ \max\left\{6.5{,}41\,\mathrm{Re}_m^{-0.16}\right\} f_{loss} A_{SG,block}^2, & if\ \mathrm{Re}_m > 10^4 \end{cases}, \tag{2.77}$$

Note that Eq. (2.77) also depend on input values. The pressure loss coefficient multiplier f_{loss} is set within the CTF recommended values (1.0-1.4). As for the area blockage ratio $A_{SG,block,}$ it is set to 0.441, following Rehme's value for honey-comb spacer grid [60].

Figure 2-19 shows the radially averaged pressure curves for the suggested range loss coefficient multipliers. As for the fixed-value form loss coefficients the error increases at the spacer grid locations but well below 0.1 % which allows to conclude that the correlation has been properly implemented in ESCOT. A better alternative to the correlation in Eq. (2.77) would be the calculation of the form loss coefficient with a higher-resolution code (such a CFD code) employing for it the detail geometry of the spacer grid.

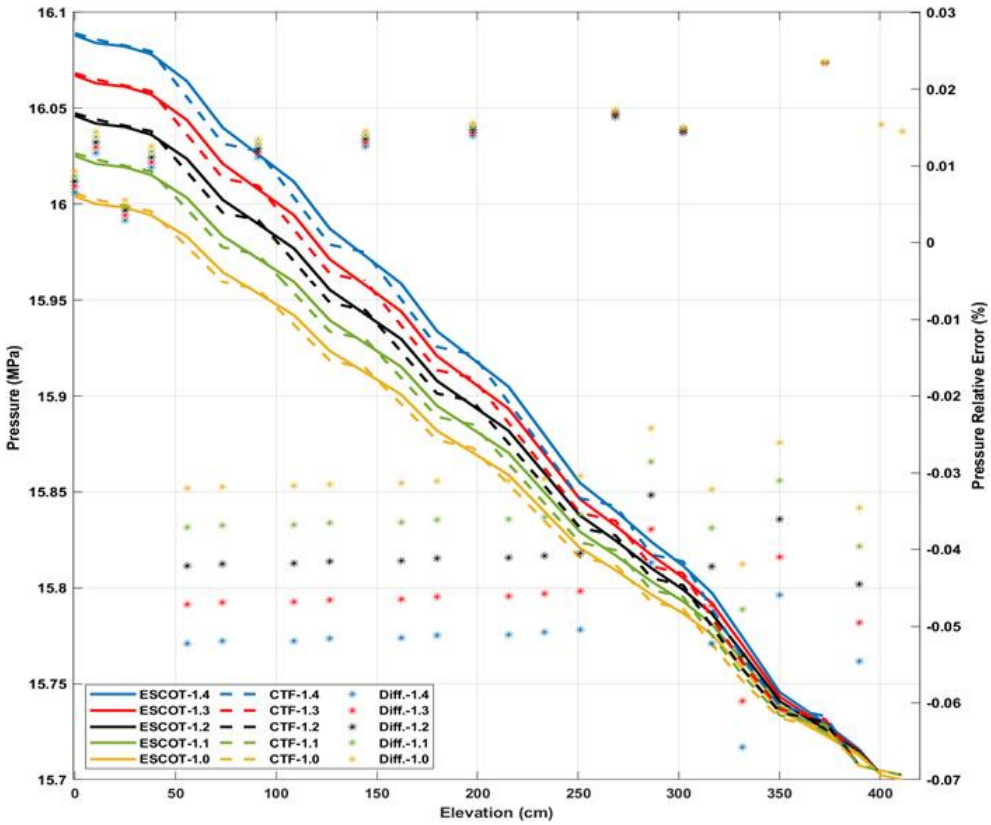

Figure 2-19. ESCOT and CTF radially averaged pressure curves for different loss coefficient multipliers

2.9.2. Spacer grid HTC enhancement

The spacer grids induce a fluid acceleration due to the flow area restriction, additionally they cause the destruction of the developed flow and increase the turbulence degree of the fluid. These phenomena enhance the heat transfer from the fuel rods to the fluid by allowing for a greater thermal gradient across the fluid and consequently a greater heat transfer from the rod surface.

The HTC (Eq. (2.69)) can be calculated by multiplying the dimensionless Nusselt by the thermal conduction coefficient k and divide it by the hydraulic diameter D_h. The Nusselt number is expressed in ESCOT as

$$Nu = \max\left(0.023\,\mathrm{Re}_l^{0.8}\,\mathrm{Pr}_l^{0.4}, 7.86\right), \tag{2.78}$$

where the Reynolds is given in Eq. (2.31) which is retrieved here

$$\mathrm{Re}_k = \frac{\alpha_k \rho_k u_k}{\mu_m},$$

and the Prandtl number, is a measure of the fluid's momentum diffusion rate compared to its energy diffusion rate

$$\mathrm{Pr} = \frac{C_p \mu}{k}. \tag{2.79}$$

As this research is limited to single-phase water coolant at normal operating conditions, its variation is not large but it changes enough to have an effect on the heat transfer coefficient.

With the aim at considering the effect of the spacer grids on the HTC, CTF employs the Yao-Hochreiter-Leech (YHL) model. The YHL formula augments the dimensionless Nusselt number as

$$\frac{Nu}{Nu_0} = \left[1 + 5.55 A_{SG,block}^2 \exp\left(-0.13 \frac{z}{D_h}\right)\right], \tag{2.80}$$

where the subscript 0 on the Nusselt number refers to the bare subchannel geometry. Here $A_{SG,block}$ is the blockage ratio and z/D_h is a dimensionless downstream distance.

The YHL correlation also contains a second term which accounts for the mixing vanes. This is achieved by defining A as the projected area of the grid onto the subchannel and Φ the mixing vane angle in Eq. (2.81). However, CTF user manual indicates that this second term is inappropriate for the prediction of the HTC enhancement factor and therefore it is better to avoid including this term and limit the expression to Eq. (2.80).

$$\frac{Nu}{Nu_0} = \left[1 + 5.55 A_{SG,block}^2 \exp\left(-0.13 \frac{z}{D_h}\right)\right] \left[1 + A^2 \tan^2(\Phi) \exp\left(-0.034 \frac{z}{D_h}\right)\right]^{0.4}, \tag{2.81}$$

Figure 2-20 shows the wall temperature at two fuel rods at two different locations in the assembly, one at the assembly edge and one at the center. The results are obtained by applying the YHL correlation to the problem proposed in the previous subsection, which is based on a modified X-2 benchmark assembly. The results show relative differences between ESCOT and CTF much lower than 0.1 %. Consequently, the correlation has been properly implemented in ESCOT.

The YHL correlation recommends a series of experimentally set coefficients, specifically 5.55 and 0.13. Besides it only represents the HTC changes downstream of the spacer grid but not within the grid height or its vicinity. For these reasons, and like for the pressure loss case, obtaining the HTC enhancement factor from a CFD calculation should increase the accuracy of the simulations.

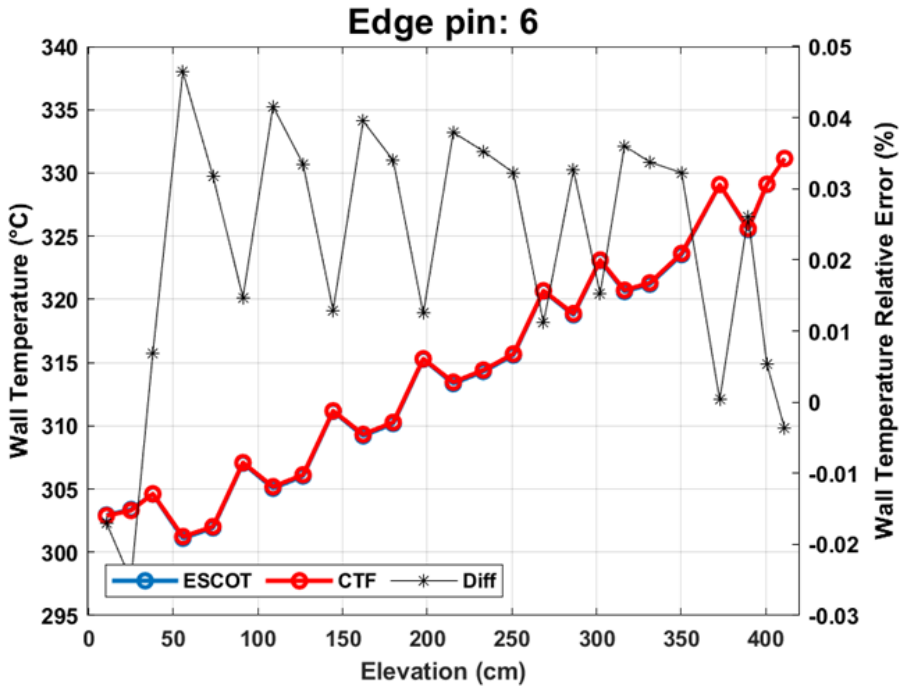

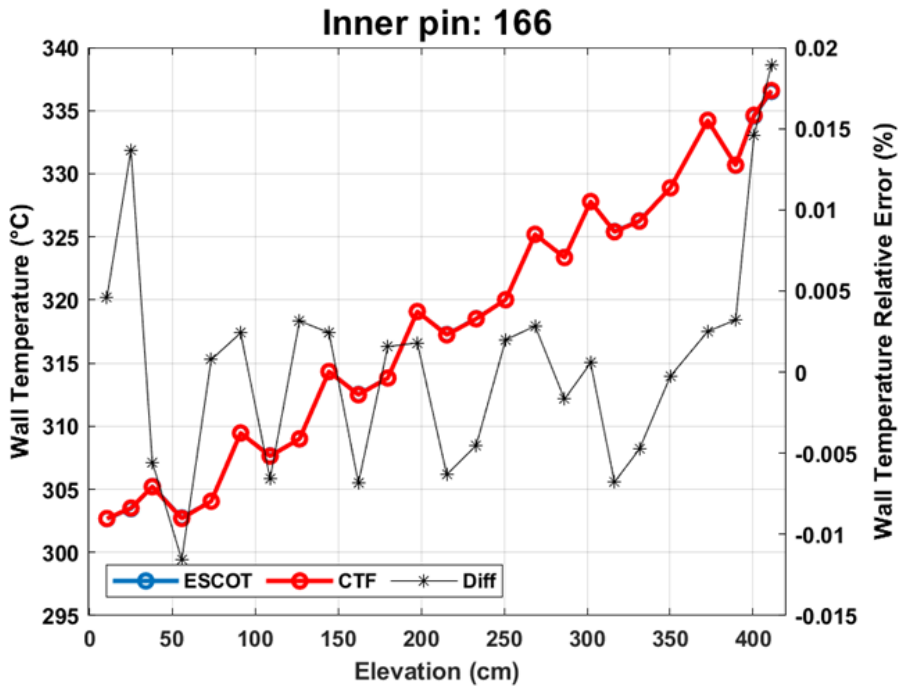

Figure 2-20. Comparison between ESCOT and CTF of the wall temperature at two fuel pin locations

2.9.3. Spacer grid turbulent mixing enhancement

The turbulent mixing model described in section 2.3.4 is characterized by the turbulent mixing coefficient β. The presence of spacer grids increases the mixing rate around the grid location.

$$\beta_{SG} = \beta_{bare} f \tag{2.82}$$

Eq. (2.82) represents the modified mixing coefficient obtained by multiplying the base coefficient β_{bare} (set in this work to 0.03) by the enhancement coefficient f. This enhancement coefficient is obtained by interpolating the input values given for different angles and elevations.

In order to verify the implementation in ESCOT the problem employed in section 2.6.2 is retrieved and the spacer grids are inserted. The angle set for the vanes is 10°. Thus, the enhancement coefficient is calculated by interpolating the values given in Table 2-4 for the input angle value and the axial momentum cells elevation.

Table 2-4. Mixing coefficient enhancement factor for different angles and axial elevations

	Degree (°)			**Degree (°)**	
Elevation (m)	0.00	15.00	**Elevation (m)**	0.00	15.00
0.000	1.00	1.00	2.288	1.00	2.30
0.208	1.00	1.00	2.496	1.00	2.20
0.416	1.00	1.00	2.704	1.00	2.10
0.624	1.00	1.10	2.912	1.00	2.00
0.832	1.00	1.30	3.120	1.00	1.90
1.040	1.00	1.50	3.328	1.00	1.70
1.248	1.00	1.70	3.536	1.00	1.50
1.456	1.00	1.90	3.744	1.00	1.30
1.664	1.00	2.00	3.952	1.00	1.20
1.872	1.00	2.10	4.160	1.00	1.10
2.080	1.00	2.20			

Figure 2-21 shows the results for the problem with and without spacer grids for which the bare mixing coefficient is set at 0.03. The results for CTF and ESCOT depict a nearly perfect match for the channels analyzed at the different problem elevations. Note that the enhancement factors in Table 2-4 are artificial although realistic. To better determine these factors, they should be obtained from a CFD calculation by simulating the problem with a detailed spacer grid geometry and the mixing vane angle obtained from the manufacturer specifications for the grid.

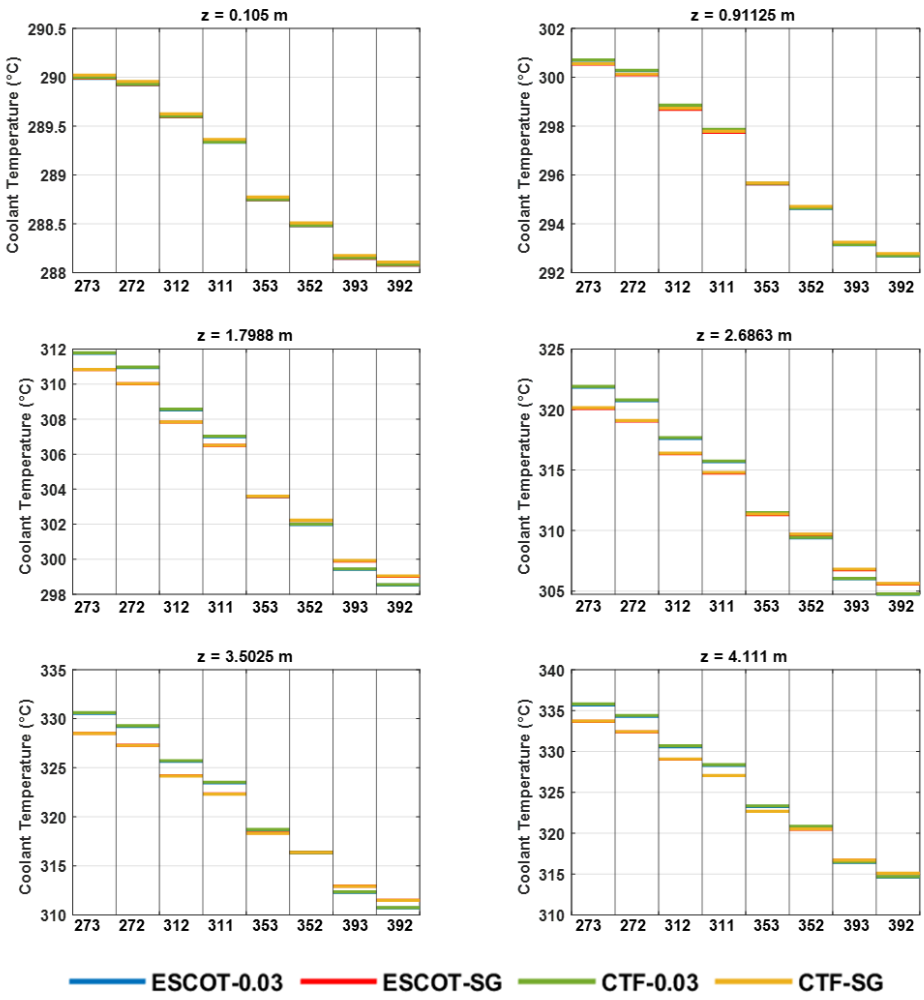

Figure 2-21. ESCOT and CTF coolant temperature results at different channels and elevations for problems with and without spacer grids

Chapter 3. nTRACER/ESCOT Coupled Calculations for Hexagonal Geometry

The ultimate objective is to replace the simplified internal T/H solver of the neutronics DWCC code nTRACER with a more sophisticated T/H algorithm (ESCOT) in hexagonal geometry applications. In the case presented in this research the neutronics and T/H algorithms are treated as independent codes and they need to follow a coupling strategy. This strategy is described here together with the coupling methods defined by PSI developers for nTRACER/CTF systems of codes as it will serve as a reference for verification.

The comparison of the standalone versions of ESCOT and CTF was already presented in section 2.8 along with their computing time performances and ESCOT's bi-directional parallelization approach. In this chapter, however, the impact due to ESCOT and CTF differences on the neutronics are analyzed by performing a series of coupled calculations as well as what portion of the calculation is taken by each T/H solver.

The reactor model employed for the assessment is the VVER-1000 reactor benchmark X-2, whose description and modeling are explained in this section prior to the results presentation. All the calculations were performed on the same 10 node cluster employed for the standalone verification.

3.1. nTRACER/ESCOT Coupling Strategy

The two sets of governing equations (T/H and neutronics) are nonlinearly coupled and their decoupling is obtained by a modification of the Gauss Seidel-Fixed Point (or Picard) Iteration scheme for two field variables. The Picard based

calculation flow of the neutronics and the T/H problems is depicted in Figure 3-1. After each neutronics iteration, the T/H module is executed to provide the new distributions of coolant density and temperature (ρ_{cool}, T_{cool}) and fuel temperature (T_{fuel}) which are then used to update the cross sections for the next neutronics calculation.

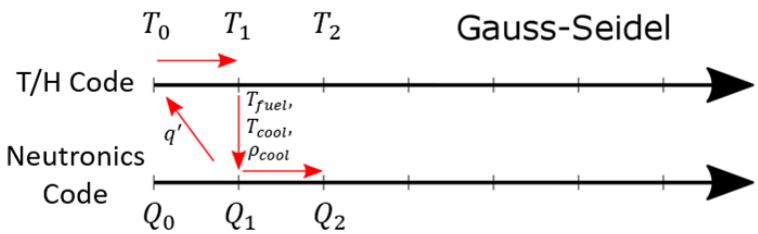

Figure 3-1. Gauss-Seidel approach for the neutronics-T/H coupling scheme

ESCOT and nTRACER have different parallelization schemes, bidirectional and axial respectively. Consequently, if a direct coupling of the codes is set, this is the parent code is nTRACER and ESCOT is used as a library, then the number of cores assigned to ESCOT is the same as to nTRACER, namely the number of axial planes of the problem. Therefore, the direct coupling limits enormously the time performance of ESCOT.

Aiming at obtaining their best performances, a wrapping system was developed. The wrapper code (the parent process in this case) uses the MPI capability of spawning two child processes and manages the exchange of information between the two codes by creating three sub-communicators: two parent-child communicators and one child-child inter-communicator, Figure 3-2 schematizes the communication system.

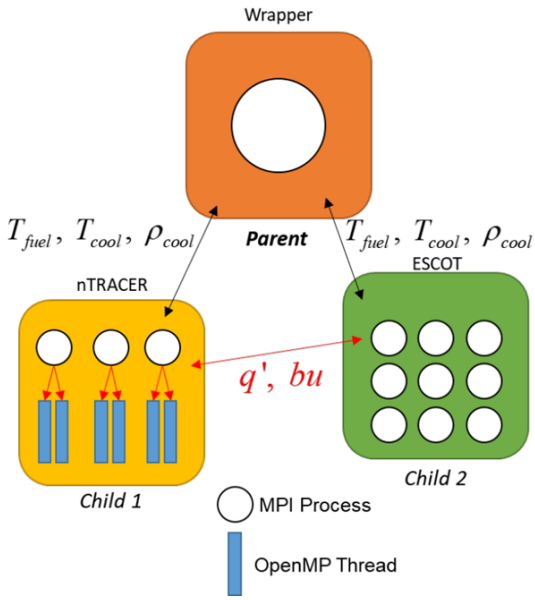

Figure 3-2. nTRACER/ESCOT wrapping system

First, the parent process initializes nTRACER and ESCOT; then the nTRACER code starts its calculation while ESCOT stands by. When the neutronics simulation reaches the T/H calculation point, nTRACER sends directly the power and burnup to ESCOT through the inter-communicator and waits in standby for the T/H variables. With the updated power ESCOT proceeds and calculates the T/H fields; once ESCOT has converged, the new distributions of ρ_{cool}, T_{cool}, T_{fuel} are sent to the wrapper which sends them back to nTRACER.

This communication scheme has been inherited from the cartesian geometry case. In the cartesian geometry the fuel pin numbering in nTRACER and ESCOT are different and, while nTRACER re-orders the fuel pin power (and the Burnup) numbering to match the one in ESCOT before communicating it, for the T/H variables ESCOT leaves this re-ordering task to the Wrapper.

Thus, although in the hexagonal geometry case the numbering is equivalent in both codes, and re-ordering is therefore unnecessary, the same communication

scheme is kept. This mapping is depicted in Figure 3-3 along with the channel and gap numbering of ESCOT.

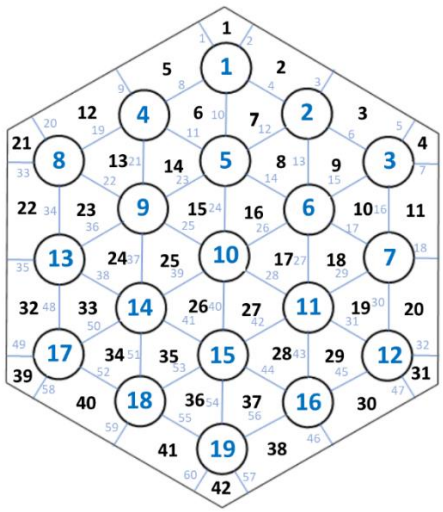

Figure 3-3. nTRACER/ESCOT assembly elements numbering

3.1.1. nTRACER/CTF coupling characteristics

Since the nTRACER/CTF system of codes is the reference for verification of nTRACER/ESCOT, let us give a few details of the coupling performed by the PSI team. The first characteristic of this coupling is that in this case the coupling is direct and therefore the number of cores available in CTF is the same as in nTRACER. Since CTF, unlike ESCOT, has a radial-only domain decomposition, the fuel assemblies need to be evenly lumped in a number of clusters equal to the number of axial planes in nTRACER.

The second difference is the assembly computational mesh for full core calculations (for single assembly and minicore the mesh matches ESCOT's). This is characterized by the simplification of the corner channels which reduces the total number of cells at the expense of degrading the accuracy of the result. Figure 3-4 shows the computational mesh and numbering in nTRACER/CTF.

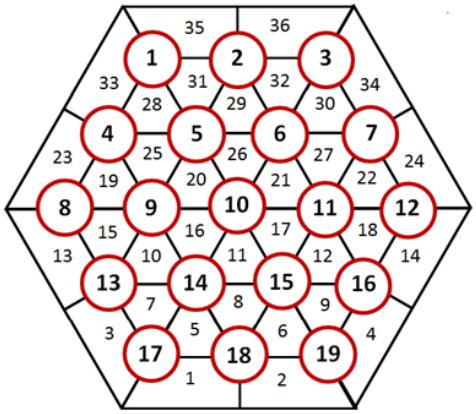

Figure 3-4. nTRACER/CTF assembly elements numbering

A minor difference but worth describing is that while nTRACER communicates the gadolinia fraction present in the burnable absorber containing to ESCOT, in the case of the nTRACER/CTF this fraction is not shared. Therefore, CTF cannot take it into account to calculate temperature distribution in these pins.

The final discrepancy is the definition of the inter-assembly channels in the full core calculation. While in ESCOT a common entity is defined, matching thereby the reality more closely, CTF considers two separate channels. Figure 3-5 presents this definition difference.

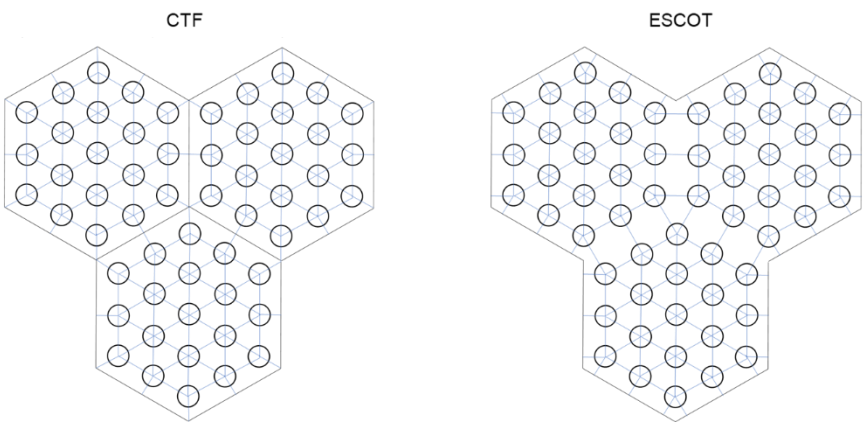

Figure 3-5. nTRACER/CTF and nTRACER/ESCOT inter-assembly channels definition

3.2. X-2 benchmark modeling

The X-2 benchmark was already employed in the previous standalone calculations but it is described in more detailed here as it is more relevant for the neutronics calculations. The benchmark is based on the operational data of the second unit of the VVER-1000 Khmelnitsky Nuclear Power Plant (NPP) located in Ukraine. The aim of this benchmark is to develop a VVER-1000 data platform for the verification and validation of reactor simulation tools. X-2 consists of three stages including Hot Zero Power (HZP) experiments, cycle depletion and several transients, which occurred at the unit during the first cycles of operation.

An effort to revise the X-2 benchmark was initiated with an updated and refined publication of the HZP experiments. The new specifications include detailed geometry models of the active core and the heavy reflector, as well as updated material compositions for the critical HZP state and corresponding operational data. Figure 3-6 presents the layout for the fresh core and the structure of the heavy reflector and Figure 3-7 the fuel axial composition as depicted in the benchmark specifications. Other material and geometry relevant information can be found in the references.

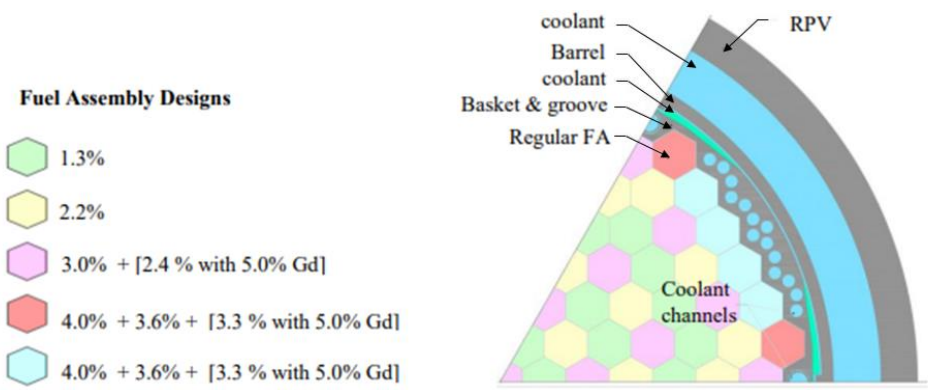

Figure 3-6. Fuel designs and core layout for the X-2 benchmark

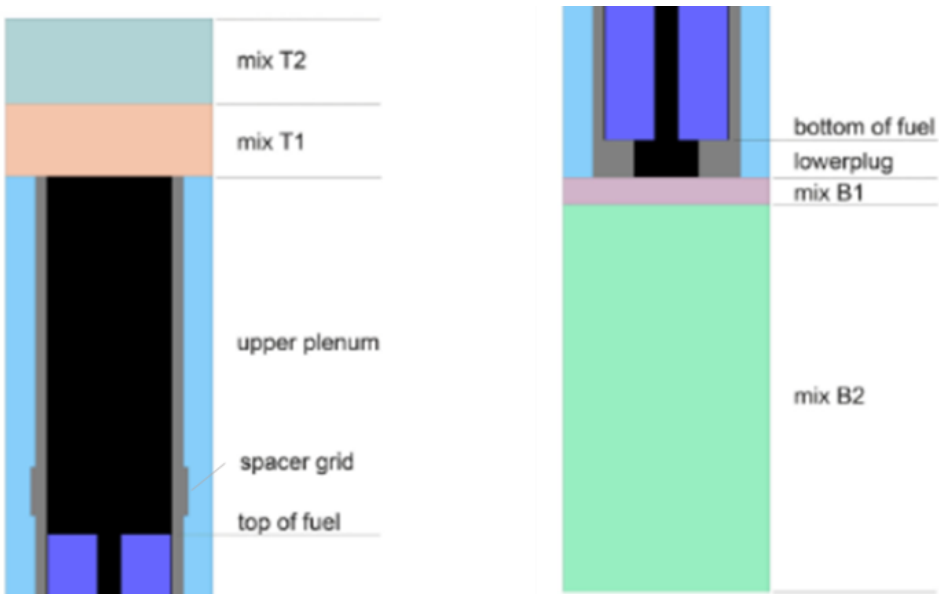

Figure 3-7. Axial layout of the fuel pin model in the X-2 benchmark

Although there is still no data for other reactor states besides HZP, the team in charge of the X-2 benchmark provided the author with the operating conditions for the Hot Full Power (HFP) state. This way the operational data used in this work are a fuel assembly average power of 18.40491 MW, inlet temperature of 287 °C, pressure at the core outlet of 15.7 MPa and a mass flow of 109.8 kg/s.

The X-2 models used in this work are based on the HZP geometry and material definitions and the operating conditions are those of the HFP as previously stated. This being said, a series of simplifications and approximations need to be assumed according to nTRACER modelling limitations. To begin with, although this benchmark problem presents a 120° symmetry, the full 360° core is simulated here as the current version of nTRACER is not capable of computing this degree of symmetry.

In nTRACER, the groove region (Figure 3-6) is modeled as a homogeneous mixture of coolant and steel, equivalent to the real geometry at the edge of the core

basket, which is cylindrical with horizontal grooves. The spacer grids are modeled as an added layer of homogenized steel and water around the fuel cladding (see Figure 3-8a), in order to avoid axial nodes of small dimensions (2 cm in this case) can cause instabilities. In CTF and ESCOT the effect of spacer grids is neglected.

The reference model of the axial top and bottom reflectors is built with several mixtures of homogeneous materials of specific height [178]. The axial reflectors are further homogenized in nTRACER, given the small thickness of the layers of the reference model. The two segments forming the top reflector are homogenized into a single region (see Figure 3-8a). The bottom reflector is divided in two segments. The lower segment is built with the material (B2), suggested in the benchmark specifications. The top segment consists of a homogeneous mixture of the lower plenum, the first homogeneous region of the reference model (B1) and part of the second homogeneous region of the reference model (B2) (see Figure 3-8b). The axial reflectors are defined in ESCOT and CTF as additional axial layers of the active core with zero power.

nTRACER models corner stiffeners semi-explicitly. The latest version of the code allows to define an integer number of gap cells, starting from the assembly corners, with the corner stiffener material. This means that the length of the corner stiffener can only be approximated by a multiplier of the pincell size. Nonetheless, there is small difference between the actual length of the corner stiffener and the model. Corner stiffeners are not considered in the T/H codes ESCOT and CTF for now.

The radius of the central guide tube is reduced in the nTRACER model since it exceeds the size of the pincell (flat-to-flat is 1.275 cm).

Concerning the heavy reflector, nTRACER reproduces the water holes, the water liner between the core basket and barrel, the downcomer and the groove with homogeneous pincells of water and steel that map approximately their shape in the reflector assemblies (see Figure 3-8d). nTRACER is also capable of reproducing the water gap between the active core and the basket explicitly, except the corner cell (Figure 3-8c). ESCOT and CTF do not model the heavy reflector. The 3 mm water gap surrounding the active core is also neglected from the T/H model.

Although in a real VVER core the coolant flow is not the same in every assembly the mass flow is kept steady as there is not available information about the mass flow distribution at the core inlet for X-2.

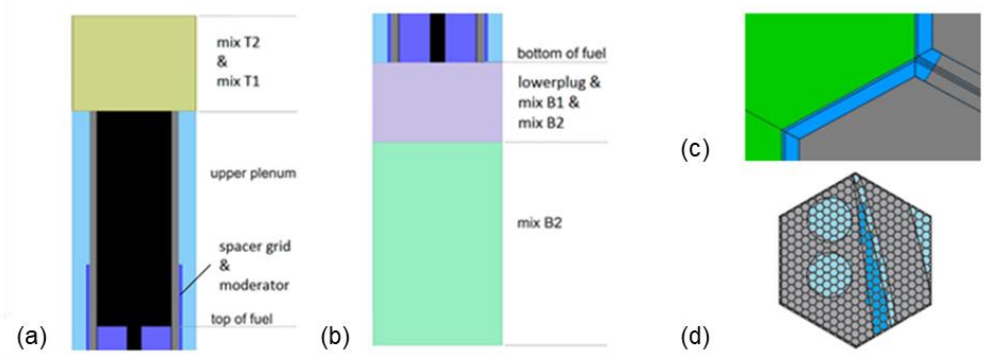

Figure 3-8. nTRACER approximations for the X-2 model

3.3. ESCOT-CTF coupled case comparison

During a multiphysics calculation, the T/H variables are updated recursively during the iterative process as their values are used to update the temperature and density dependent macroscopic cross sections. With this background, in this subsection the accuracy at coolant and fuel temperatures and coolant density determination of CTF and ESCOT in coupled calculations is compared. Besides, as the intention is to replace the very fast but rough nTRACER 1D simple T/H, the speed of the two subchannel codes and the portion of time they take in the coupled calculation is analyzed. For this comparison single assembly, minicore and full core problems are considered.

3.3.1. Single assembly calculations

For the single assembly case two types of assemblies are simulated, one not containing any burnable absorber (22AU, yellow in Figure 3-6) and the other one containing (30AV5, pink in Figure 3-6). Only one computing node is used in the single assembly cases, since each node contains 52 cores nTRACER employs in some of its algorithms, such as the ray tracing or the subgroup calculation, while ESCOT only uses one core. The coupling between neutronics and T/H is performed in a direct manner being nTRACER the parent code that calls CTF or ESCOT when the T/H update is necessary.

The calculation results are given in Table 3-1 for assembly 22AU. The multiplication factor k_{eff} difference is a direct consequence of the relatively high difference in fuel temperatures (see Table 3-2).

Figure 3-10e shows that CTF yields a slightly lower coolant temperature but the difference is negligible. CTF also gives a lower fuel average temperature but as the standalone calculations showed the difference is not remarkable and always below 0.1 % as shown in Table 3-2.

As for the simulation time taken by the T/H solver in the coupled calculation, this is considerably smaller in ESCOT case due to the greater simplicity of its governing equations as seen in the previous subsection. The calculation time as well as the portion of time are given in Table 3-1. Figure 3-9 shows the computing time required by each calculation type in the coupled calculations.

Table 3-1. CTF and ESCOT X2 single assembly 22AU performance comparison

	k_{eff}	# FPI	T/H time (s)	% of total time
CTF	1.24516	6	541.39	44.60
ESCOT	1.24514	6	146.51	17.20

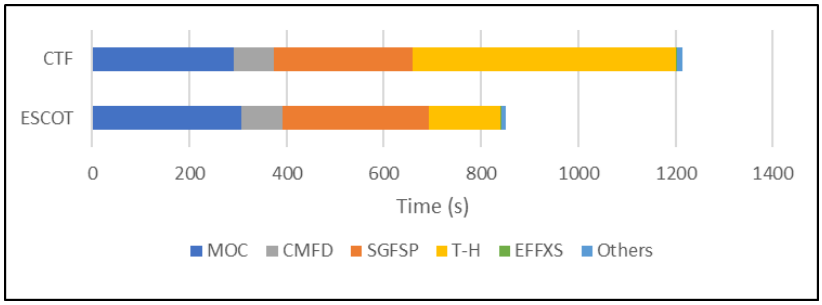

Figure 3-9. CTF and ESCOT coupled calculations computing times for assembly 22AU

The small differences in fuel and coolant temperature are enough to cause a k_{eff} value discrepancy (2 pcm), the power distribution, however, is not dramatically affected as summarized in Table 3-2 through somewhat different axial distributions shown in Figure 3-10. The differences noted in k_{eff} and axial profiles are insignificant.

Table 3-2. CTF and ESCOT X2 single assembly 22AU radial and axial relative differences

	Radial Power (%)	Radial T_{fuel} (%)	Radial T_{cool} (%)
MAX	0.01	0.02	0.03
RMS	0.00	0.01	0.01
	Axial Power (%)	**Axial T_{fuel} (%)**	**Axial T_{cool} (%)**
MAX	0.08	0.05	0.02
RMS	0.04	0.02	0.01

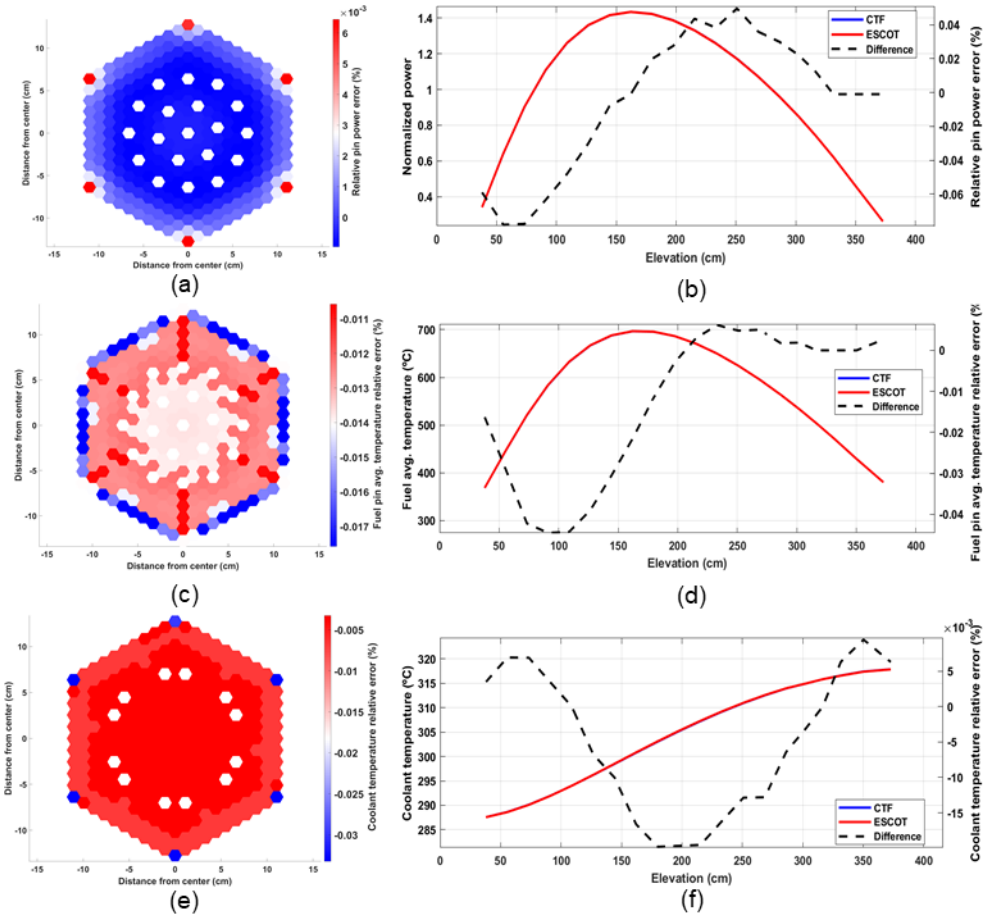

Figure 3-10. Axially averaged (a, c and e) and radially averaged (b, d and f) power distribution and fuel and coolant temperature relative differences for assembly 22AU

In the case of the gadolinia-containing assembly (30AV5) for which the results are given in Table 3-3 and Table 3-4, the general conclusions are quite similar to the unpoisoned case. The only difference is noted at the burnable absorber pins. This difference is also due to the difference in the fuel temperature calculation scheme between ESCOT and CTF. As previously described in section 3.1.1, although CTF includes algorithms to compute the fuel conduction coefficients with gadolinia content, the gadolinia composition information is not transferred to CTF from nTRACER in the current coupling scheme while in the nTRACER/ESCOT coupling this information is communicated. Because the pin power and temperature of gadolinia pins are low, this difference is also not very significant.

Table 3-3. CTF and ESCOT X2 single assembly 30AV5 performance comparison

	k_{eff}	# FPI	T/H time (s)	% of total time
CTF	1.20283	7	632.79	45.50
ESCOT	1.20288	6	150.08	18.16

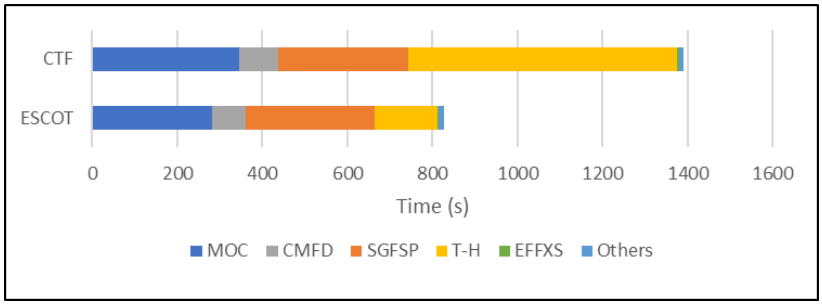

Figure 3-11. CTF and ESCOT coupled calculations computing times for assembly 30AV5

This magnified difference is clearly observed in the power and fuel temperature axially integrated radial distributions in Table 3-4 and Figure 3-12. As for the coolant temperature the gadolinia has a minor effect and the corner patterns can still be seen.

Table 3-4. CTF and ESCOT X2 single assembly 30AV5 radial and axial relative differences

	Radial Power (%)	Radial T_{fuel} (%)	Radial T_{cool} (%)
MAX	0.02	0.03	0.04
RMS	0.00	0.02	0.02
	Axial Power (%)	**Axial T_{fuel} (%)**	**Axial T_{cool} (%)**
MAX	0.19	0.09	0.05
RMS	0.10	0.04	0.03

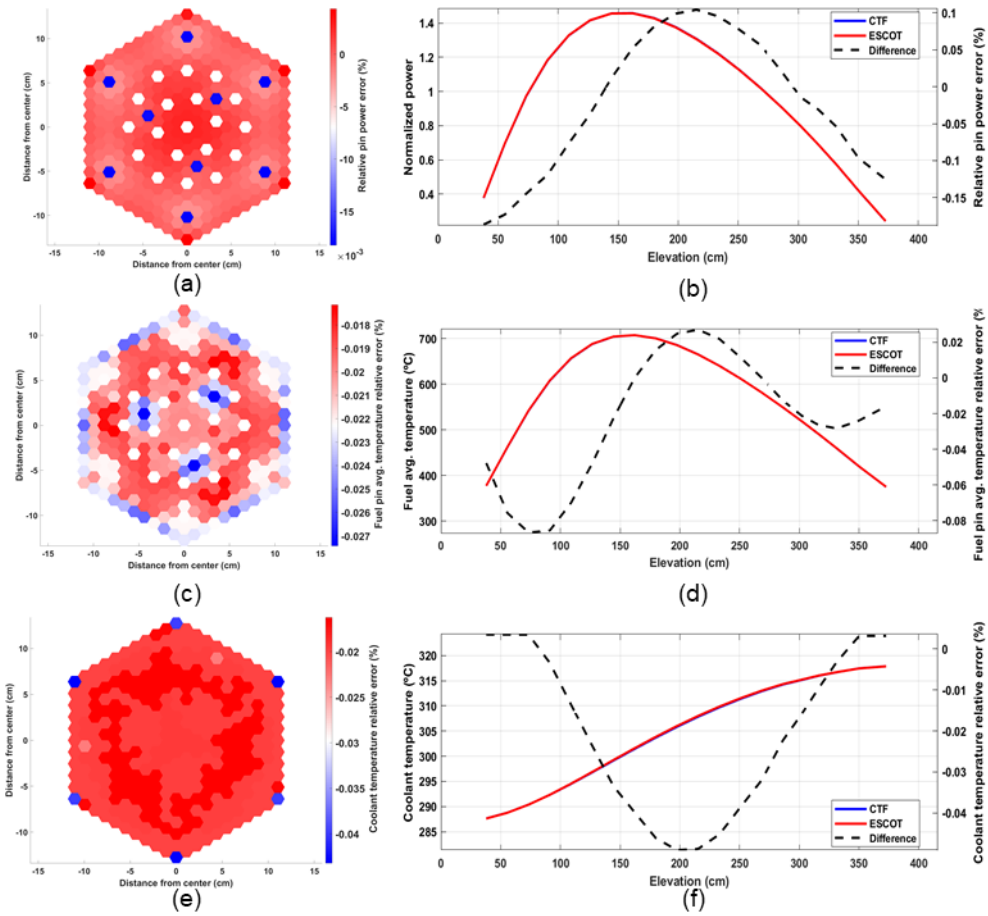

Figure 3-12. Axially averaged (a, c and e) and radially averaged (b, d and f) power distribution and fuel and coolant temperature relative differences for assembly 30AV5

3.3.2. Minicore calculation

With the aim at observing the differences arising from the distinct coupling performed for each T/H code a minicore is simulated. The minicore is formed by a central 13AU assembly (green in Figure 3-6) and three 22AU and three 30AV5 assemblies arranged alternatively at the periphery. The minicore is surrounded by a line of reflector assemblies. In order to isolate the aforementioned discrepancies effects the calculation is performed in single computational node like in the single assembly cases.

The k_{eff} and computing time of the full core calculations are compared in Table 3-5. The k_{eff} of the two calculations matches very well while the ESCOT computing time is between 1/5 and 1/7 of CTF's as shown in Table 3-5 and Figure 3-13. This significant reduction is due to the DFM simplicity. The differences in core characteristic parameters shown in Table 3-6 within an acceptable range, being the maximum fuel temperature difference somehow larger at the highest power region.

Table 3-5. CTF and ESCOT X2 minicore performance comparison

	k_{eff}	# FPI	T/H time (s)	% of total time
CTF	0.97931	7	5,080.96	41.81
ESCOT	0.97934	7	1,726.27	18.81

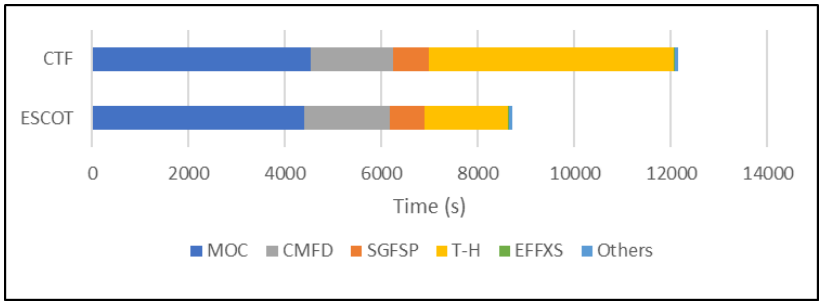

Figure 3-13. CTF and ESCOT coupled calculations computing times for minicore

Table 3-6. CTF and ESCOT X2 minicore radial and axial relative differences

	Radial Power (%)	Radial T_{fuel} (%)	Radial T_{cool} (%)
MAX	0.06	0.75	0.21
RMS	0.02	0.12	0.04
	Axial Power (%)	**Axial T_{fuel} (%)**	**Axial T_{cool} (%)**
MAX	0.43	0.12	0.02
RMS	0.20	0.08	0.02

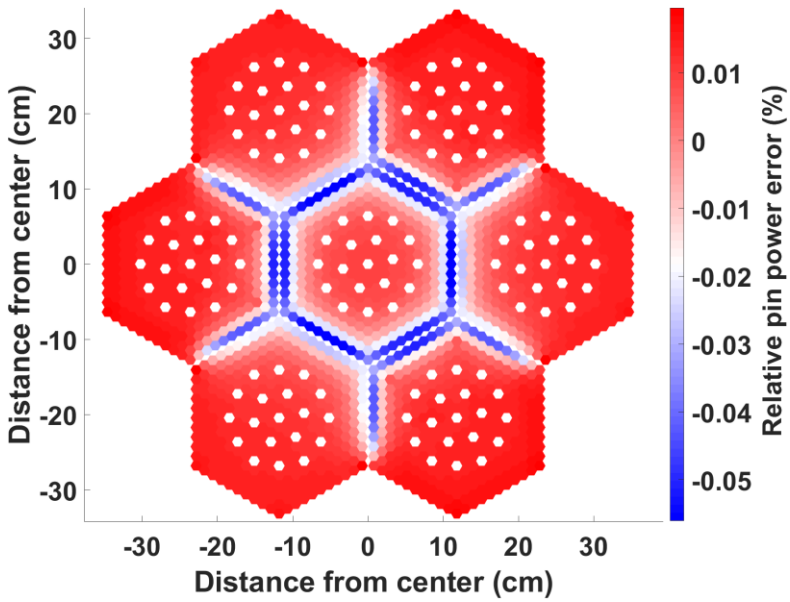

Figure 3-14. Axially averaged power distribution relative differences for minicore

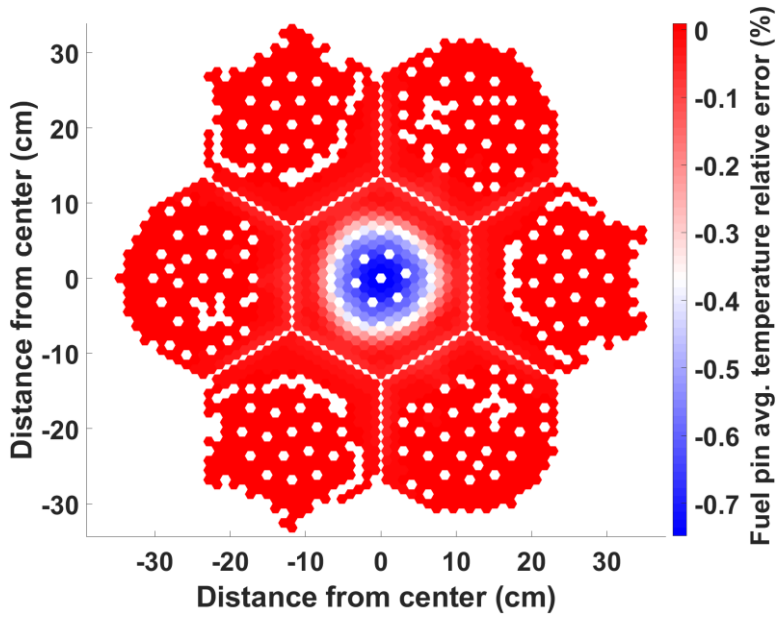

Figure 3-15. Axially averaged average fuel temperature relative differences for minicore

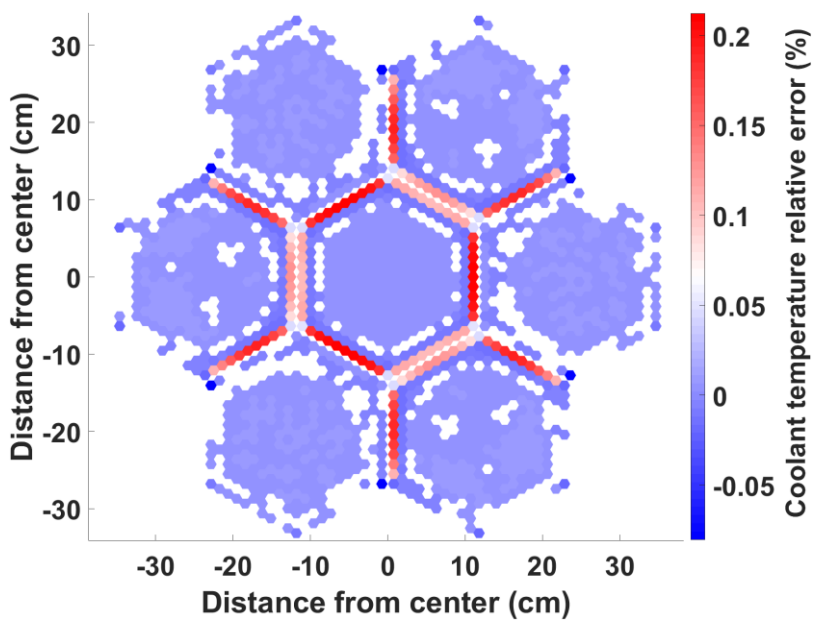

Figure 3-16. Axially averaged coolant temperature relative differences for minicore

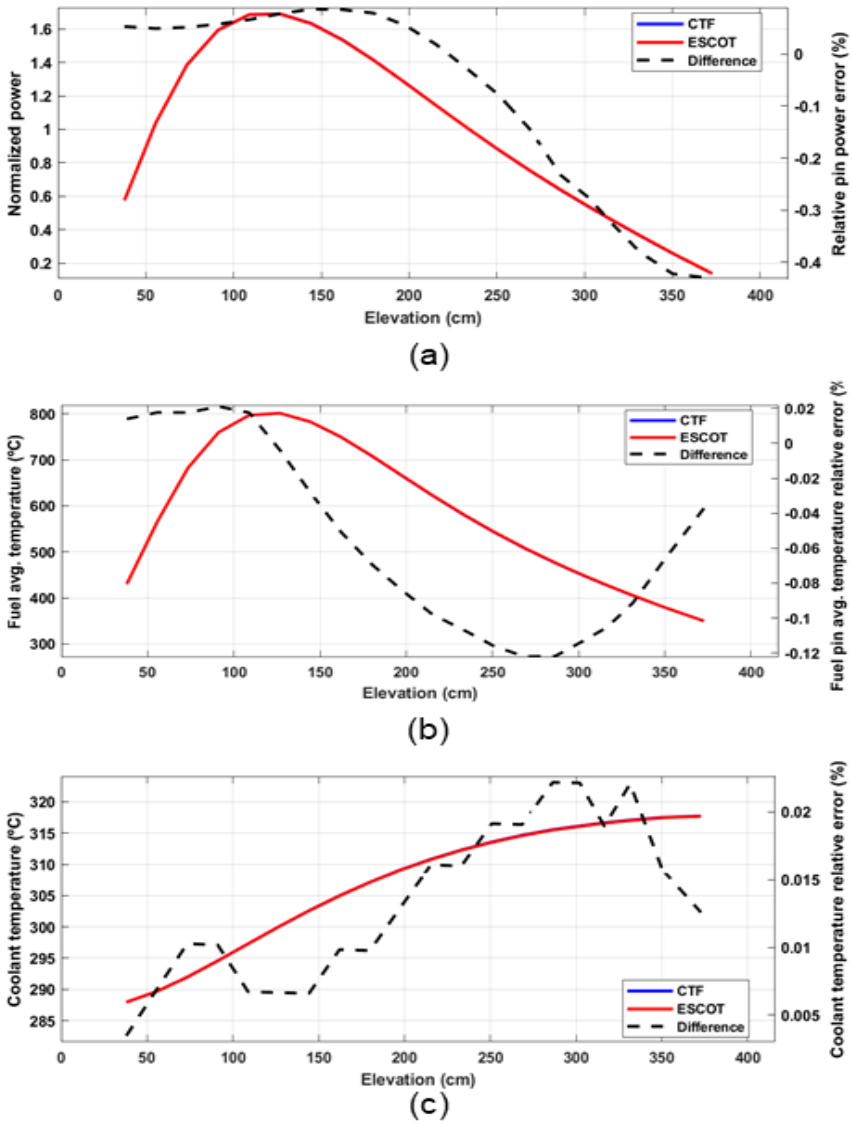

Figure 3-17. Radially averaged power distribution and fuel and coolant temperature relative differences for assembly minicore

3.3.3. Full core calculation

For the full core case, and like in the standalone calculation, no symmetry is applied. Note that, as explained in section 3.1.1, the parallelization schemes in CTF and ESCOT are different. While for CTF nTRACER acts as the parent code and consequently the number of computing processes is limited to those of nTRACER (25 in this case as the number of planes in nTRACER model of X-2 is 25), in the ESCOT case a wrapper code sets up the number of independent processes for neutronics and T/H, and this way while nTRACER is given 468 cores (=9 computing nodes x 52 cores/computing node), ESCOT is assigned to 326 for a double axial-radial decomposition (=163 assemblies x 2 axial domain decomposition).

The k_{eff} and computing time of the full core calculations are compared in Table 3-7 and Figure 3-18.The k_{eff} of the two calculations is consistent with the previous single assembly and minicore calculations. As for the computing time ESCOT is about seven times faster than CTF, the time required by the MOC calculation, however, is slightly higher in the nTRACER/ESCOT case in about 15 minutes due to the MPI spawn function that allows the assignment of a different number of cores for each code, but that in exchange is slightly detrimental on the planar MOC performance.

Table 3-7. CTF and ESCOT X2 full core performance comparison

	k_{eff}	# FPI	T/H time (s)	% of total time
CTF	1.15692	5	9,429.74	35.05
ESCOT	1.15696	5	1,478.13	7.07

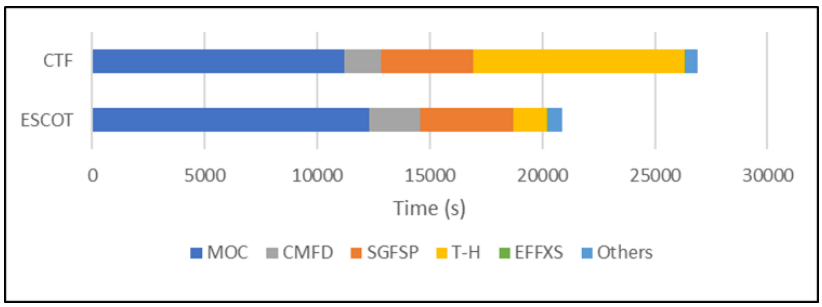

Figure 3-18. CTF and ESCOT coupled calculations computing times for full core

The differences in core characteristic parameters shown in Table 3-8 are of the same magnitude as in the minicore case. Therefore, the reasons behind these discrepancies are valid also in this case together with the difference in the interassemby channels treatment and the difference in the corner channels definition.

Table 3-8. CTF and ESCOT X2 full core radial and axial relative differences

	Radial Power (%)	**Radial T_{fuel} (%)**	**Radial T_{cool} (%)**
MAX	0.08	0.11	0.33
RMS	0.02	0.02	0.05
	Axial Power (%)	**Axial T_{fuel} (%)**	**Axial T_{cool} (%)**
MAX	0.19	0.07	0.03
RMS	0.11	0.04	0.02

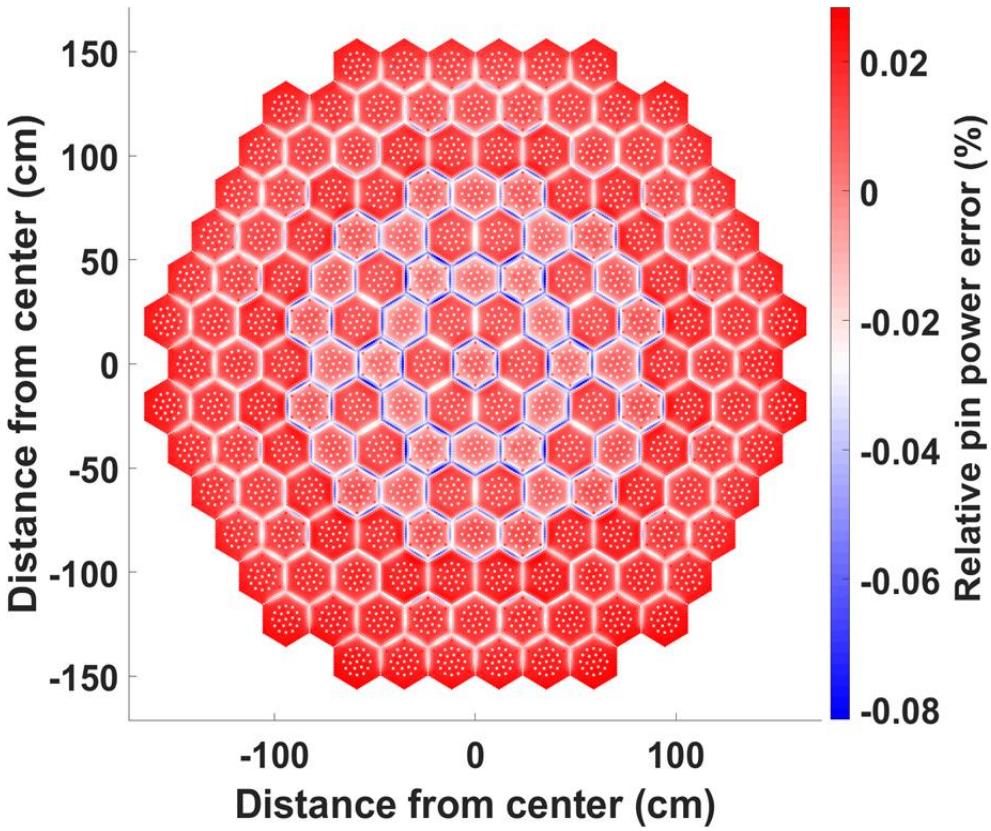

Figure 3-19. Axially averaged power distribution relative differences for full core

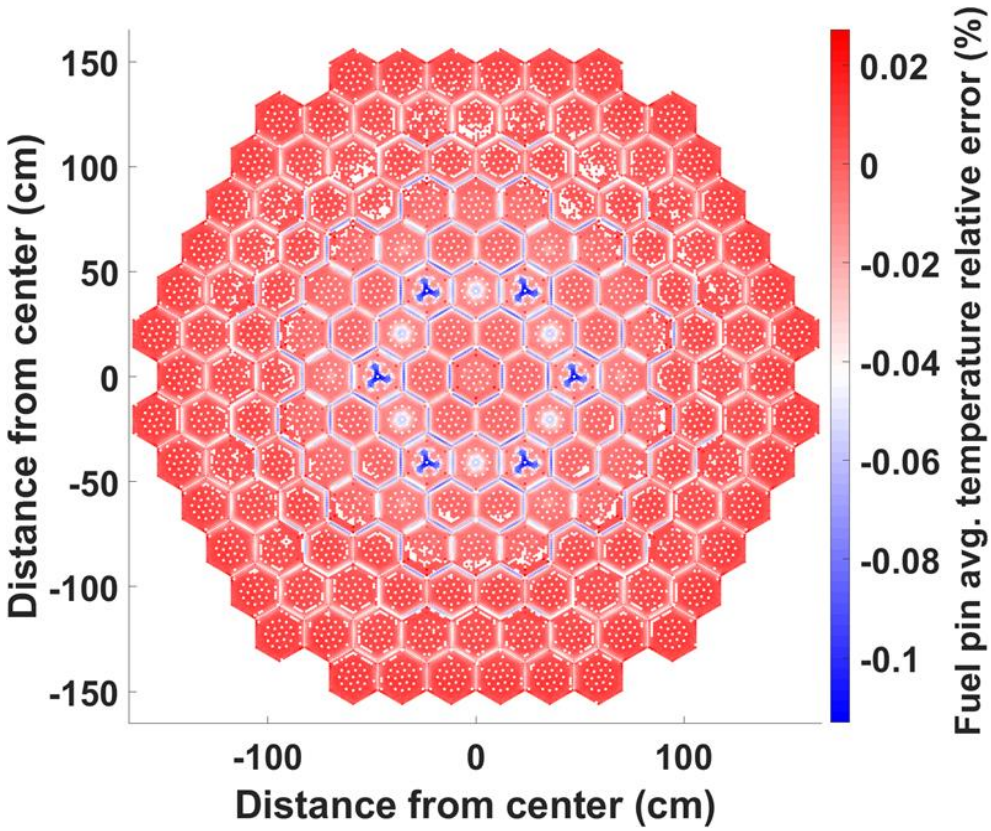

Figure 3-20. Axially averaged fuel average temperature relative differences for full core

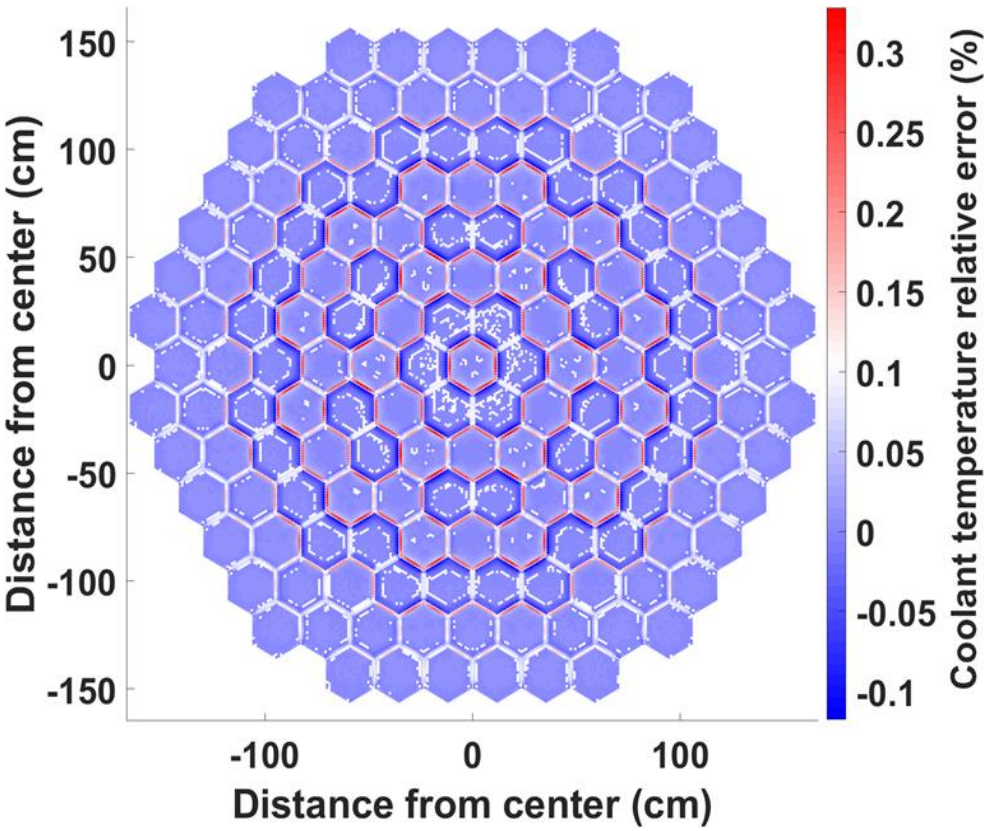

Figure 3-21. Axially averaged coolant temperature relative differences for full core

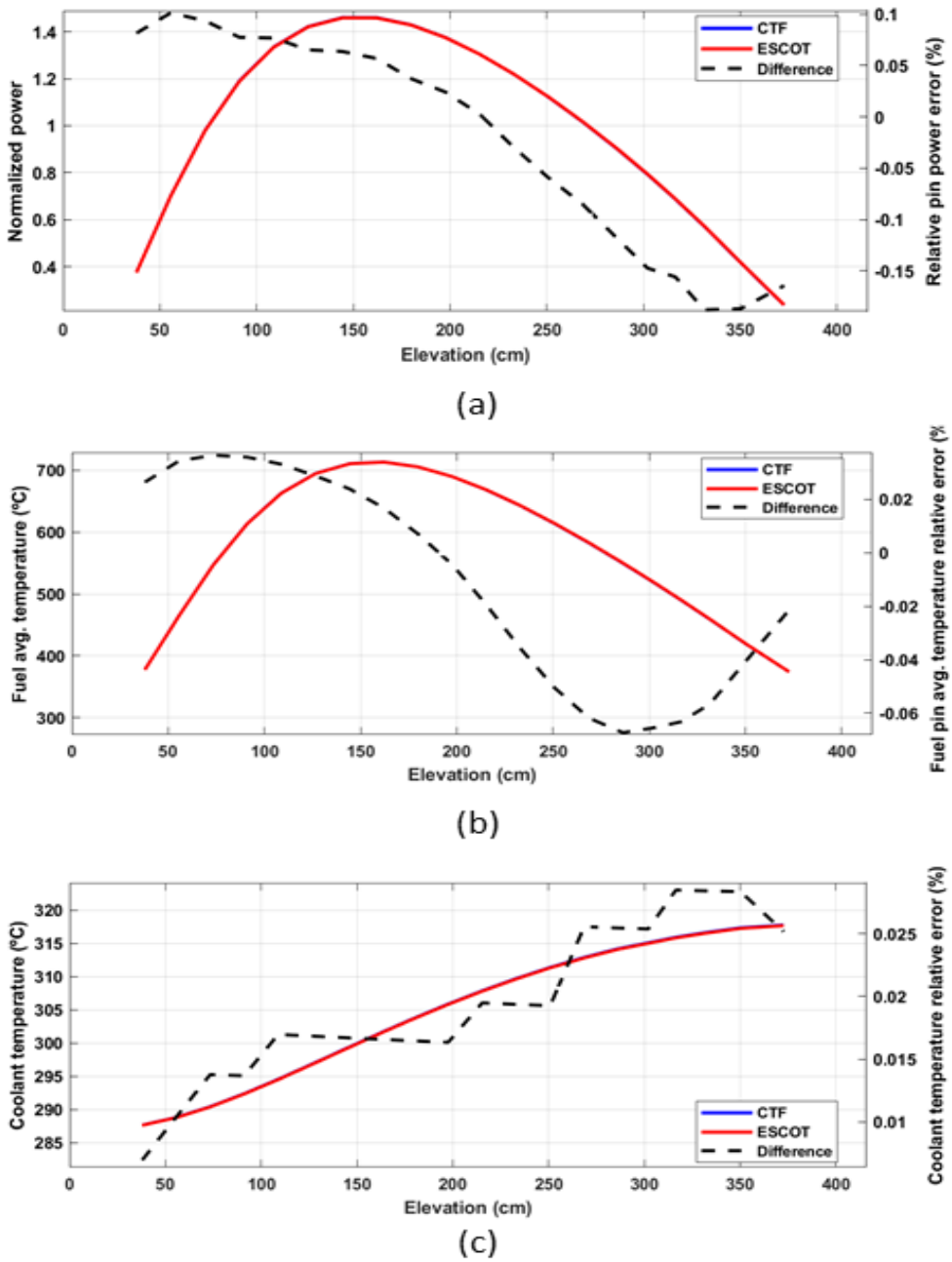

Figure 3-22. Radially averaged power distribution and fuel and coolant temperature relative differences for assembly full core

Chapter 4. Study and Optimization of the Multiphysics Calculation

The most practical manner to couple a neutronics calculation with other reactor physics is the Fixed-Point Iteration (FPI), particularly if these physics are calculated in other codes whose internals are not accessible, because it can be done by just establishing an interface to exchange the variables of interest among the codes. However, its poor convergence and instability has been pointed out. This undesirable performance is due to the nonlinear inter-dependency of the physical phenomena which causes an oscillatory behavior induced by an excessive convergence of the PI whose output flux is used to update the other physics.

Hence, the AA was introduced to mathematically optimize the convergence of neutronics-T/H calculations on FPI. The AA improved the coupled calculations, especially when the physics are limited to neutronics-T/H. Nonetheless, when the physics are extended to incorporate xenon and boron the performance becomes poorer, particularly as the fissile material becomes scarce in depletion calculations.

Thus, the work presented in this section focuses first on characterizing the effects of the problem multiphysics-dependent cross sections on the FPI convergence. Departing from a simple 1G 1D single pin problem a Fourier analysis is performed to study the individual impact of $\widetilde{FTC}$ and MTC on the convergence behavior. Then the impracticability of analytically finding the optimal PI convergence degree in realistic problems is demonstrated. Finally, the AA is retrieved and its FPI map extended to include the physics other than the T/H ones. The superiority of this extended map is demonstrated numerically by employing the simple 1G 1D problem.

4.1. Fourier Analysis of the Multiphysics Problem

In this section a Fourier analysis is performed so that an analytical expression that relates the FPI problem spectral radius with the PI convergence degree for several combinations of $\widetilde{FTC}$ and MTC values is obtained. This expression would allow for a study of the conditions that entail the most challenging convergence behavior. For it the 1G 1D homogeneous problem is employed and periodic boundary conditions are imposed.

4.1.1. Review of the Fixed-Point Iteration

The FPI is an iterative method to find roots of nonlinear equations. For a single nonlinear equation, the following scalar function is defined

$$f(x) = 0\,, \tag{4.1}$$

it can be rewritten as

$$x = g(x)\,. \tag{4.2}$$

In the FPI, the Eq.(4.2) is iteratively solved until the unique point x^* is found:

$$x^{(k+1)} = g(x^{(k)}) \;\; until \;\; x^{(k+1)} \to x^*, \quad k = 0,1,2,\ldots. \tag{4.3}$$

Even though this iterative method is simple to implement, its convergence is conditional. The true error for k-th iteration is

$$e^{(k)} = x^{(k)} - x^* \tag{4.4}$$

The relation between the true error at the current and the previous iteration can be derived as

$$
\begin{aligned}
e^{(k)} &= x^{(k)} - x^* = g(x^{(k-1)}) - g(x^*) = \frac{g(x^{(k-1)}) - g(x^*)}{x^{(k-1)} - x^*}\left(x^{(k-1)} - x^*\right) \\
&= g'\left(\xi^{(k-1)}\right)\left(x^{(k-1)} - x^*\right), \qquad \xi^{(k-1)} \in [x^*, x^{(k-1)}] \ \because \text{Mean value theorem} \qquad (4.5) \\
&= g'\left(\xi^{(k-1)}\right) e^{(k-1)}
\end{aligned}
$$

Thus, the error reduction factor of the FPI can be defined as:

$$\rho = \frac{e^{(k)}}{e^{(k-1)}} = g'(\xi^{(k-1)}). \tag{4.6}$$

The iteration can convergence only if the absolute error reduction factor is less than one. Therefore, the convergence criteria of the FPI can be expressed as

$$\max_{x \in [a,b]} \left| g'(x) \right| < 1. \tag{4.7}$$

The FPI can be applied to solve a system of nonlinear equations such as

$$\mathbf{f}(\mathbf{x}) = 0, \tag{4.8}$$

where $\mathbf{f} = [\, f_1, f_2, \cdots, f_n \,]^T$ is a n-dimensional vector of scalar functions and $\mathbf{x} = [x_1, x_2, \cdots, x_n]^T$ is a n-dimensional solution vector. The equivalent system of Eq.(4.8) can be constructed for the FPI as

$$\mathbf{x} = \mathbf{g}(\mathbf{x}), \tag{4.9}$$

which can be re-expressed as

$$
\begin{aligned}
x_1 &= g_1(x_1, x_2, \cdots, x_n) \\
x_2 &= g_2(x_1, x_2, \cdots, x_n) \\
&\vdots \\
x_n &= g_n(x_1, x_2, \cdots, x_n)
\end{aligned}
. \tag{4.10}
$$

If the above system is simplified to a system of two nonlinear equations for an easier understanding

$$x_1 = g_1(x_1, x_2)$$
$$x_2 = g_2(x_1, x_2) \tag{4.11}$$

The above equation can be solved by the FPI

$$x_1^{(k+1)} = g_1(x_1^{(k)}, x_2^{(k)})$$
$$x_2^{(k+1)} = g_2(x_1^{(m)}, x_2^{(k)}) \tag{4.12}$$

For the solution of the system in Eq. (4.12) two approaches are applicable depending on how the subscript m is treated. If m=k, all depending variables $x_1$and x_2 in the fixed-point map, g_1 and g_2, are the ones of the last iteration, so each system is decoupled or independent. This method is so-called the Jacobi scheme. Because the Jacobi scheme is naturally parallelizable, it has a strength to apply the tandem approach in multiphysics where multiple codes are coupled.

On the other hand, when m=k+1, it becomes the Gauss-Seidel (G-S) scheme for which the solution of x_2 is calculated with the updated variable x_1. It is a reasonable presumption that the solution of G-S scheme would converge faster than the Jacobi one as it uses a more updated solution. Although this statement does not have a general character, it was demonstrated in reference [45] that it holds for our purpose and consequently this is the default scheme in this work.

4.1.2. Problem description and cross sections change functionalization

The 1G 1D neutronics problem is based on the diffusion equation which is solved with the Finite Differences Method (FDM). The cross sections are made dependent on the feedback coefficients so that the FPI convergence behavior in terms on the feedback mechanism can be investigated. The coefficients are limited here to the thermal $\widetilde{FTC}$s and MTCs for practicality, the conclusions, however, can be extended also to the xenon and boron feedback mechanisms. With the aim at facilitating the

study the following relation is derived to estimate the fission and absorption cross section variation for a given feedback coefficient.

$$\partial\rho \approx \frac{\Sigma_{a0}}{\nu\Sigma_{f0}}\frac{\Delta\nu\Sigma_f}{\nu\Sigma_{f0}} - \frac{\Delta\Sigma_a}{\nu\Sigma_{f0}} . \tag{4.13}$$

With the derived relation, the cross sections change ($\Delta\Sigma_a, \Delta\nu\Sigma_f$) can be readily estimated for a given specific reactivity change ($\partial\rho$) from the reference stage ($\Sigma_{a0}, \nu\Sigma_{f0}$). Note that the changes only affect the absorption and nu-fission cross sections while the diffusion cross section remains constant as it is weakly affected as shown in reference [45].

Now, a set of problems in a broad range of MTC and $\widetilde{FTC}$ values is constructed. The calculations are limited to negative $\widetilde{FTC}$s and MTCs corresponding to the LWR operating conditions under normal circumstances. The following equidistant 17 reactivity coefficients for $\widetilde{FTC}$ and MTC are selected as below:

$$\begin{aligned} \frac{\partial\rho}{\partial\sqrt{T_f}}(\text{pcm}/\sqrt{\text{K}}) &= \left[-192, -180, \cdots, -12, 0\right] \ \textit{for}\ \text{FTC} \\ \frac{\partial\rho}{\partial T_c}(\text{pcm/K}) &= \left[-96, -90, \cdots, -6, 0\right] \ \textit{for}\ \text{MTC} \end{aligned} , \tag{4.14}$$

that sufficiently covers the practical range of $\widetilde{FTC}$ and MTC. Thus, 289 (17x17) problems with different $\widetilde{FTC}$s and MTCs are configured.

The nested iteration (outer-FPI and inner-PI) algorithm in a discretized form can be summarized as in Table 4-1. In it, *L* and *K* are the FPI and PI maximum number of iterations respectively. *N* is the number of meshes in which the problem is subdivided. Eqs. (4.15) and (4.16) represent the feedback-induced cross section changes for which the initial $\Delta\Sigma_{a,n}^{(0)}$ and $\Delta\nu\Sigma_{f,n}^{(0)}$ are equal to zero and updated at each FPI. Eqs. (4.17), (4.18), (4.21) and (4.22) represent the variable coupling between FPI and PI, where ϕ_0 is the flux at convergence.

Table 4-1. Algorithm of discretized FPI with variable absorption and nu-fission cross sections

do l=1, L

$$\Sigma_{a,n}^{(l-1)} = \Sigma_{a,0} + \Delta\Sigma_{a,n}^{(l-1)} \tag{4.15}$$

$$\nu\Sigma_{f,n}^{(l-1)} = \nu\Sigma_{f,0} + \Delta\nu\Sigma_{f,n}^{(l-1)} \tag{4.16}$$

$$\phi_n^{(l-1,0)} = \phi_n^{(l-1)} \tag{4.17}$$

$$k_{eff}^{(l-1,0)} = k_{eff}^{(l-1)} \tag{4.18}$$

do k=1, K

$$-\frac{D}{h^2}\left(\phi_{n-1}^{(l-1,k)} - 2\phi_n^{(l-1,k)} + \phi_{n+1}^{(l-1,k)}\right) + \Sigma_{a,n}^{(l-1)}\phi_n^{(l-1,k)} = \frac{\nu\Sigma_{f,n}^{(l-1)}}{k_{eff}^{(l-1,k-1)}}\phi_n^{(l-1,k-1)} \tag{4.19}$$

$$k_{eff}^{(l-1,k)} = k_{eff}^{(l-1,k-1)} \frac{\sum_{n'=0}^{N-1} \nu\Sigma_f \phi_{n'}^{(l-1,k)} \nu\Sigma_f \phi_{n'}^{(l-1,k)}}{\sum_{n'=0}^{N-1} \nu\Sigma_f \phi_{n'}^{(l-1,k)} \nu\Sigma_f \phi_{n'}^{(l-1,k-1)}} \tag{4.20}$$

end do

$$\phi_n^{(l)} = \phi_0 \frac{\phi_n^{(l-1,K)}}{\sum_{n'=0}^{N-1} \phi_{n'}^{(l-1,K)} \Big/ N} \tag{4.21}$$

$$k_{eff}^{(l)} = k_{eff}^{(l-1,K)} \tag{4.22}$$

end do

From Eq. (4.13) the MTCs and $\widetilde{FTC}$s can be expressed in the following manner:

$$MTC = \frac{\partial\rho}{\partial T_c} \approx \frac{\Sigma_{a0}}{\left(\nu\Sigma_{f0}\right)^2}\frac{\Delta\nu\Sigma_f}{\Delta T_c} - \frac{1}{\nu\Sigma_{f0}}\frac{\Delta\Sigma_a}{\Delta T_c}, \tag{4.23}$$

$$FTC = \frac{\partial\rho}{\partial\sqrt{T_f}} \approx \frac{\Sigma_{a0}}{\left(\nu\Sigma_{f0}\right)^2}\frac{\Delta\nu\Sigma_f}{\Delta\sqrt{T_f}} - \frac{1}{\nu\Sigma_{f0}}\frac{\Delta\Sigma_a}{\Delta\sqrt{T_f}}, \tag{4.24}$$

The cross-section changes are expressed as:

$$\Delta\Sigma_a = \Delta\sqrt{T_f}\,\frac{\Delta\Sigma_a}{\Delta\sqrt{T_f}} + \Delta T_c\,\frac{\Delta\Sigma_a}{\Delta T_c}, \tag{4.25}$$

$$\Delta\nu\Sigma_f = \Delta\sqrt{T_f}\,\frac{\Delta\nu\Sigma_f}{\Delta\sqrt{T_f}} + \Delta T_c\,\frac{\Delta\nu\Sigma_f}{\Delta T_c} \tag{4.26}$$

From Eqs. (4.23) and (4.24), and assuming that one of the temperature dependent cross-section changes (absorption in this case) is fixed the following expressions are obtained.

$$\frac{\Delta\nu\Sigma_f}{\Delta T_c} = \frac{\left(\nu\Sigma_{f0}\right)^2}{\Sigma_{a0}}\left(MTC + \frac{1}{\nu\Sigma_{f0}}\frac{\Delta\Sigma_a}{\Delta T_c}\right), \tag{4.27}$$

$$\frac{\Delta\nu\Sigma_f}{\Delta\sqrt{T_f}} = \frac{\left(\nu\Sigma_{f0}\right)^2}{\Sigma_{a0}}\left(FTC + \frac{1}{\nu\Sigma_{f0}}\frac{\Delta\Sigma_a}{\Delta\sqrt{T_f}}\right) \tag{4.28}$$

Plugging these expressions into Eq. (4.26) then Eqs. (4.25) and (4.26) can be expressed as a function of the Temperature Coefficients as

$$\Delta\Sigma_a = \left(\sqrt{T_f} - \sqrt{T_{f,0}}\right)\frac{\Delta\Sigma_a}{\Delta\sqrt{T_f}} + \left(T_c - T_{c,0}\right)\frac{\Delta\Sigma_a}{\Delta T_c}, \tag{4.29}$$

$$\begin{aligned}\Delta\nu\Sigma_f = \frac{\left(\nu\Sigma_{f0}\right)^2}{\Sigma_{a0}}\Bigg[&\left(\sqrt{T_f} - \sqrt{T_{f,0}}\right)\left(FTC + \frac{1}{\nu\Sigma_{f0}}\frac{\Delta\Sigma_a}{\Delta\sqrt{T_f}}\right)\\ &+\left(T_c - T_{c,0}\right)\left(MTC + \frac{1}{\nu\Sigma_{f0}}\frac{\Delta\Sigma_a}{\Delta T_c}\right)\Bigg]\end{aligned} \tag{4.30}$$

Since the moderator and fuel temperatures depend on the flux the cross-section changes can be re-expressed as

$$\Delta\Sigma_a = \alpha_f\phi\frac{\Delta\Sigma_a}{\Delta\sqrt{T_f}} + \alpha_c\phi\frac{\Delta\Sigma_a}{\Delta T_c}, \tag{4.31}$$

$$\Delta\nu\Sigma_f = \frac{\left(\nu\Sigma_{f0}\right)^2}{\Sigma_{a0}}\left[\alpha_f\phi\left(FTC + \frac{1}{\nu\Sigma_{f0}}\frac{\Delta\Sigma_a}{\Delta\sqrt{T_f}}\right) + \alpha_c\phi\left(MTC + \frac{1}{\nu\Sigma_{f0}}\frac{\Delta\Sigma_a}{\Delta T_c}\right)\right], \tag{4.32}$$

where α_f and α_c represent the flux-dependent temperature change.

4.1.3. Fourier analysis of the multiphysics homogeneous problem

The Fourier analysis is a useful technique to examine the asymptotic convergence rate of iteration scheme involving differential equations. It allows, after some algebraic manipulation, the expression of the eigenvalues in terms of the Fourier wave number. The largest eigenvalue is the spectral radius of the iterative process. This way the study of the PI convergence degree effect (maximum number of PI, K here) on the FPI convergence rate for a problem with iteration dependent cross sections can be carried out.

The first step of the Fourier analysis consists in the linearization of the problem. The following flux and multiplication factor linearizations are introduced in the algorithm:

$$\phi_n^{(l)} = \left(\phi_0 + \phi_0 \epsilon \xi_n^{(l)}\right), \tag{4.33}$$

$$\frac{1}{k_{eff}^{(l)}} = \left(\frac{1}{k_\infty} + \frac{1}{k_\infty}\epsilon\delta^{(l)}\right), \tag{4.34}$$

$$\phi_n^{(l,k)} = \left(\phi_0 + \phi_0 \epsilon \xi_n^{(l,k)}\right), \tag{4.35}$$

$$\frac{1}{k_{eff}^{(l,k)}} = \left(\frac{1}{k_\infty} + \frac{1}{k_\infty}\epsilon\delta^{(l,k)}\right), \tag{4.36}$$

where ϵ is a very small number. The multiplication factor at convergence is $k_\infty = \nu\Sigma_{f1}/\Sigma_{a1}$, which expressed with dependence on the temperature coefficients results in

$$k_\infty = \left\{\nu\Sigma_{f,0} + \frac{\nu\Sigma_{f0}}{\Sigma_{a0}}\left[\alpha_f\phi_0\left(\nu\Sigma_{f0}FTC + \frac{\Delta\Sigma_a}{\Delta\sqrt{T_f}}\right) + \alpha_c\phi_0\left(\nu\Sigma_{f0}MTC + \frac{\Delta\Sigma_a}{\Delta T_c}\right)\right]\right\} \Bigg/ \left[\Sigma_{a,0} + \alpha_f\phi_0\frac{\Delta\Sigma_a}{\Delta\sqrt{T_f}} + \alpha_c\phi_0\frac{\Delta\Sigma_a}{\Delta T_c}\right] \tag{4.37}$$

The PI diffusion equation and multiplication factor linearization, for which only the first order error terms are kept, results in

$$
\begin{aligned}
&-\frac{D\left(\xi_{n-1}^{(l-1,k)}-2\xi_{n}^{(l-1,k)}+\xi_{n+1}^{(l-1,k)}\right)}{\left(\Sigma_{a,0}+\alpha_f\phi_0\dfrac{\Delta\Sigma_a}{\Delta\sqrt{T_f}}+\alpha_c\phi_0\dfrac{\Delta\Sigma_a}{\Delta T_c}\right)h^2} \\
&+\xi_n^{(l-1,k)}+\frac{\phi_0\alpha_f\dfrac{\Delta\Sigma_a}{\Delta\sqrt{T_f}}+\phi_0\alpha_c\dfrac{\Delta\Sigma_a}{\Delta T_c}}{\Sigma_{a,0}+\alpha_f\phi_0\dfrac{\Delta\Sigma_a}{\Delta\sqrt{T_f}}+\alpha_c\phi_0\dfrac{\Delta\Sigma_a}{\Delta T_c}}\xi_n^{(l-1)} \\
&=\delta^{(l-1,k-1)}+\xi_n^{(l-1,k-1)} \\
&+\frac{\phi_0\alpha_f\left(\nu\Sigma_{f0}FTC+\dfrac{\Delta\Sigma_{a,0}}{\Delta\sqrt{T_f}}\right)+\phi_0\alpha_c\left(\nu\Sigma_{f0}MTC+\dfrac{\Delta\Sigma_{a,0}}{\Delta T_c}\right)}{\Sigma_{a0}+\alpha_f\phi_0\left(\nu\Sigma_{f0}FTC+\dfrac{\Delta\Sigma_a}{\Delta\sqrt{T_f}}\right)+\alpha_c\phi_0\left(\nu\Sigma_{f0}MTC+\dfrac{\Delta\Sigma_a}{\Delta T_c}\right)}\xi_n^{(l-1)}
\end{aligned}
\tag{4.38}
$$

$$
\delta^{(l-1,k)}+\frac{1}{N}\sum_{n'=0}^{N-1}\xi_{n'}^{(l-1,k)}=\delta^{(l-1,k-1)}+\frac{1}{N}\sum_{n'=0}^{N-1}\xi_{n'}^{(l-1,k-1)} \tag{4.39}
$$

For its part the FPI-PI coupling expressions are

$$
\xi_n^{(l-1,0)}=\xi_n^{(l-1)} \tag{4.40}
$$

$$
\delta^{(l-1,0)}=\delta^{(l-1)} \tag{4.41}
$$

$$
\xi_n^{(l)}+\sum_{n'=0}^{N-1}\xi_{n'}^{(l-1,K)}=\xi_n^{(l-1,K)} \tag{4.42}
$$

$$
\delta^{(l)}=\delta^{(l-1,K)} \tag{4.43}
$$

The second step is the Fourier ansatzes introduction, which are

$$
\xi_n^{(l)}=a_m\omega_m^l e^{i\lambda_m(n+1/2)h}, \tag{4.44}
$$

$$
\xi_n^{(l,k)}=b_m^n\omega_m^l e^{i\lambda_m(n+1/2)h}, \tag{4.45}
$$

$$
\delta^{(l)}=c\omega_0^l, \tag{4.46}
$$

$$
\delta^{(l,k)}=d^k\omega_0^l, \tag{4.47}
$$

where a_m, b_m, c and d are the errors at the first iteration, ω_m is the Fourier eigenvalue and λ_m the Fourier frequency.

And the equations are re-expressed as

$$
\begin{aligned}
&-\frac{D\left(e^{i\lambda_m(n-1+1/2)h}-2e^{i\lambda_m(n+1/2)h}+e^{i\lambda_m(n+1+1/2)h}\right)}{\left(\Sigma_{a,0}+\alpha_f\phi_0\frac{\Delta\Sigma_a}{\Delta\sqrt{T_f}}+\alpha_c\phi_0\frac{\Delta\Sigma_a}{\Delta T_c}\right)h^2}b_m^k\omega_m^{(l-1)} \\
&+b_m^k\omega_m^{(l-1)}e^{i\lambda_m(n+1/2)h}+\frac{\phi_0\alpha_f\frac{\Delta\Sigma_a}{\Delta\sqrt{T_f}}+\phi_0\alpha_c\frac{\Delta\Sigma_a}{\Delta T_c}}{\Sigma_{a,0}+\alpha_f\phi_0\frac{\Delta\Sigma_a}{\Delta\sqrt{T_f}}+\alpha_c\phi_0\frac{\Delta\Sigma_a}{\Delta T_c}}a_m\omega_m^{(l-1)}e^{i\lambda_m(n+1/2)h} \\
&=d^{(k-1)}\omega_0^{(l-1)}+b_m^{(k-1)}\omega_m^{(l-1)}e^{i\lambda_m(n+1/2)h} \\
&+\frac{\phi_0\alpha_f\left(\nu\Sigma_{f0}FTC+\frac{\Delta\Sigma_{a,0}}{\Delta\sqrt{T_f}}\right)+\phi_0\alpha_c\left(\nu\Sigma_{f0}MTC+\frac{\Delta\Sigma_{a,0}}{\Delta T_c}\right)}{\Sigma_{a0}+\alpha_f\phi_0\left(\nu\Sigma_{f0}FTC+\frac{\Delta\Sigma_a}{\Delta\sqrt{T_f}}\right)+\alpha_c\phi_0\left(\nu\Sigma_{f0}MTC+\frac{\Delta\Sigma_a}{\Delta T_c}\right)}a_m\omega_m^{(l-1)}e^{i\lambda_m(n+1/2)h}
\end{aligned}
\tag{4.48}
$$

$$
\begin{aligned}
&d^k\omega_0^{(l-1)}+\frac{1}{N}\sum_{n'=0}^{N-1}b_m^k\omega_m^{(l-1)}e^{i\lambda_m(n'+1/2)h} \\
&=d^{(k-1)}\omega_0^{(l-1)}+\frac{1}{N}\sum_{n'=0}^{N-1}b_m^{(k-1)}\omega_m^{(l-1)}e^{i\lambda_m(n'+1/2)h}
\end{aligned}
\tag{4.49}
$$

The coupling expressions result in

$$b_m^0=a_m \tag{4.50}$$

$$d^0=c \tag{4.51}$$

$$a_m\omega_m=b_m^K \tag{4.52}$$

$$c\omega_0=d^K \tag{4.53}$$

For the fundamental mode, *m=0* case ($\lambda_0 = 0$), the equations are simplified as

$$b_0^k + \frac{\phi_0\alpha_f \dfrac{\Delta\Sigma_a}{\Delta\sqrt{T_f}} + \phi_0\alpha_c \dfrac{\Delta\Sigma_a}{\Delta T_c}}{\Sigma_{a,0} + \alpha_f\phi_0 \dfrac{\Delta\Sigma_a}{\Delta\sqrt{T_f}} + \alpha_c\phi_0 \dfrac{\Delta\Sigma_a}{\Delta T_c}} a_0$$

$$= d^{(k-1)} + b_0^{(k-1)} \tag{4.54}$$

$$+ \frac{\phi_0\alpha_f \left(\nu\Sigma_{f0} FTC + \dfrac{\Delta\Sigma_{a,0}}{\Delta\sqrt{T_f}} \right) + \phi_0\alpha_c \left(\nu\Sigma_{f0} MTC + \dfrac{\Delta\Sigma_{a,0}}{\Delta T_c} \right)}{\Sigma_{a0} + \alpha_f\phi_0 \left(\nu\Sigma_{f0} FTC + \dfrac{\Delta\Sigma_a}{\Delta\sqrt{T_f}} \right) + \alpha_c\phi_0 \left(\nu\Sigma_{f0} MTC + \dfrac{\Delta\Sigma_a}{\Delta T_c} \right)} a_0$$

$$d^k + b_0^k = d^{(k-1)} + b_0^{(k-1)} \tag{4.55}$$

And the coupling expressions

$$b_0^0 = a_0 \tag{4.56}$$

$$d^0 = c \tag{4.57}$$

$$a_0\omega_0 = b_0^K \tag{4.58}$$

$$c\omega_0 = d^K \tag{4.59}$$

By combining the equations above

$$\omega_0 = 0 \tag{4.60}$$

As for the other eigenmodes, $m>0$

$$b_m^k = \frac{1}{\left[1-\frac{2D\left(\cos\left(\lambda_m h\right)-1\right)}{\left(\Sigma_{a,0}+\alpha_f\phi_0\frac{\Delta\Sigma_a}{\Delta\sqrt{T_f}}+\alpha_c\phi_0\frac{\Delta\Sigma_a}{\Delta T_c}\right)h^2}\right]} b_m^{(k-1)}$$

$$+\left[\frac{\phi_0\alpha_f\left(\nu\Sigma_{f0}FTC+\frac{\Delta\Sigma_{a,0}}{\Delta\sqrt{T_f}}\right)+\phi_0\alpha_c\left(\nu\Sigma_{f0}MTC+\frac{\Delta\Sigma_{a,0}}{\Delta T_c}\right)}{\Sigma_{a0}+\alpha_f\phi_0\left(\nu\Sigma_{f0}FTC+\frac{\Delta\Sigma_a}{\Delta\sqrt{T_f}}\right)+\alpha_c\phi_0\left(\nu\Sigma_{f0}MTC+\frac{\Delta\Sigma_a}{\Delta T_c}\right)}\right.$$

$$\left.-\frac{\phi_0\alpha_f\frac{\Delta\Sigma_a}{\Delta\sqrt{T_f}}+\phi_0\alpha_c\frac{\Delta\Sigma_a}{\Delta T_c}}{\Sigma_{a,0}+\alpha_f\phi_0\frac{\Delta\Sigma_a}{\Delta\sqrt{T_f}}+\alpha_c\phi_0\frac{\Delta\Sigma_a}{\Delta T_c}}\right]$$

$$\Big/\left[1-\frac{2D\left(\cos\left(\lambda_m h\right)-1\right)}{\left(\Sigma_{a,0}+\alpha_f\phi_0\frac{\Delta\Sigma_a}{\Delta\sqrt{T_f}}+\alpha_c\phi_0\frac{\Delta\Sigma_a}{\Delta T_c}\right)h^2}\right]a_m \tag{4.61}$$

And the coupling expressions

$$b_m^0 = a_m \tag{4.62}$$

$$d^0 = c \tag{4.63}$$

$$a_m\omega_m = b_m^K \tag{4.64}$$

$$c\omega_0 = d^K \tag{4.65}$$

Inserting Eq. (4.62) into (4.61) and re-expressing the big expressions with A and B

$$b_m^k = Ab_m^{(k-1)} + Bb_m^0, \tag{4.66}$$

which gives the following recurrent relation

$$b_m^K = \frac{\left(A+B-1\right)A^K - B}{A-1} b_m^0 \tag{4.67}$$

With Eqs. (4.62) and (4.64)

$$a_m \omega_m = \frac{(A+B-1)A^K - B}{A-1} a_m \tag{4.68}$$

Simplifying

$$\omega_m = \frac{(A+B-1)}{A-1} A^K - \frac{B}{A-1}, \tag{4.69}$$

with the eigenmodes different from 0 expressed as

$$\lambda_m h = \frac{2\pi m}{N}, \qquad m = 1, \ldots, N-1 \tag{4.70}$$

and the spectral radius being by definition

$$\rho = \max\left(|\omega_m|\right) \tag{4.71}$$

The simple problem for this analytical convergence analysis has a single pin configuration with 3.80 m of axial height. The size of each computational mesh is 15.2 cm, which yields 25 axial meshes. The base cross-section values at T_c = 600 K, T_f = 600 K are: $D_0 = 1.2605$ cm, $\Sigma_{a0} = 0.0216\ \mathrm{cm}^{-1}$, $\nu\Sigma_{f0} = 0.0267\ \mathrm{cm}^{-1}$, $\kappa\Sigma_{f0} = 0.353 \cdot 10^{-12}\ \mathrm{cm}^{-1}$.

The linear power density is 17.5 kW/m with a constant pressure of 15.513 MPa and 0.360 kg/s mass flow rate. The fuel geometry is given by r_f = 4.2 mm and r_{co}= 4.8 mm. The thermal properties assigned are k_f= 5.0 W/(m·K), k_c = 16.0 W/(m·K) and h_w = 36,000 W/(m2·K). With these T/H characteristics the flux-temperature coefficients are set at α_c = 0.5766 K, α_f= 3.4192 $\sqrt{K}$.

For the absorption feedback parameters, $1\ \mathrm{pcm/K}$ and $1\ \mathrm{pcm}/\sqrt{\mathrm{K}}$ are fixed for moderator and fuel respectively. Different $\widetilde{FTC}$ and MTC combinations results are represented in Figure 4-1. Along with the analytical values the numerically obtained spectral radii are presented. The numerical results are obtained by the flux error reduction rate near convergence ($\rho \approx \|\phi^{(l)} - \phi^{(l-1)}\| / \|\phi^{(l-1)} - \phi^{(l-2)}\|$).

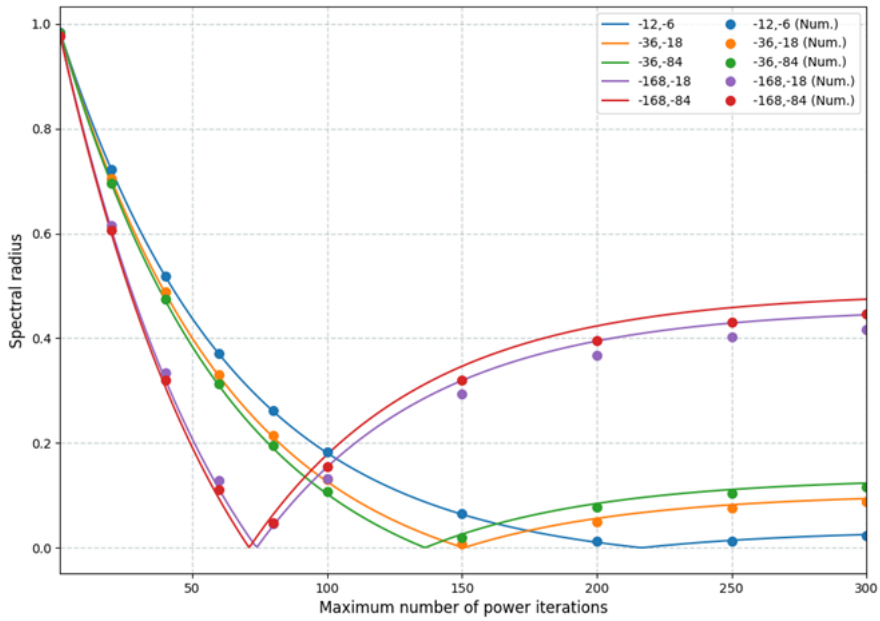

Figure 4-1. Analytical and numerical Power Iteration dependent spectral radius results for different combinations of $\widetilde{FTC}$ and MTC

For each $\widetilde{FTC}$ and MTC combination the minimum spectral radius is obtained by a different maximum number of PIs, *K*. Or, in other words, a different degree of PI convergence. This number which yields the minimum spectral radius can be analytically determined by equating Eq. (4.69) to zero.

$$\frac{(A+B-1)}{A-1}A^K - \frac{B}{A-1} = 0, \tag{4.72}$$

and this number results in

$$K = \frac{\log(|B|) - \log(|A+B-1|)}{\log(|A|)} \tag{4.73}$$

This equation yields the optimal number of PIs for different combinations of $\widetilde{FTC}$ and MTC as shown in Table 4-2.

Table 4-2. Number of PI that yields the optimal number of FPI for diverse combinations of $\widehat{FTC}$ and MTC

$\widehat{FTC}$, MTC	K
-12, -6	217
-36, -18	151
-168, -84	71
-168, -18	74
-36, -84	136

4.1.4. Fourier analysis of the multiphysics non-homogeneous problem

The analytical expression for the optimal number of PI obtained in the previous analysis cannot be directly employed in more complex and realistic problems. This is, multi-dimensional and multi-group problems with more realistic boundary conditions. And more complex codes, such as nTRACER, which solves a 2D/1D fine mesh MOC solution with CMFD acceleration.

Thus, ideally, the Fourier analysis should incorporate all the characteristics of the target problem and code (in this case nTRACER). The first intended modification on the simplified problem that is implemented is the zero flux boundary conditions. While in the problem with periodic boundary conditions the flux at convergence has a constant homogeneous shape, in this case the final flux has a sine-like shape and therefore the cross sections, which depend on the flux level, also have a non-uniform shape.

The discretized flux solution with these new boundary conditions is

$$\phi_n = \phi_0 \frac{\int_{x_{n-1}}^{x_n} \sin\left(\frac{\pi x}{Nh}\right) dx \Big/ h}{\int_0^{Nh} \sin\left(\frac{\pi x}{Nh}\right) dx \Big/ Nh} = \phi_0 \frac{N}{2}\left[\cos\left(\frac{\pi x_{n-1}}{Nh}\right) - \cos\left(\frac{\pi x_n}{Nh}\right)\right] \tag{4.74}$$

The introduction of such a complex flux solution in the linearized Eq. (4.38)-(4.43) makes the Fourier analysis impractical and consequently prevents the calculation of the optimal number of PIs. In Figure 4-2 the numerical solution of the spectral radius for the zero-flux boundary conditions is shown along with the analytical and numerical solutions for periodic boundary conditions. It can be observed that the optimal point is shifted enough so that using the homogeneous solution in the heterogeneous solution would have an impact negative enough as to discard this option.

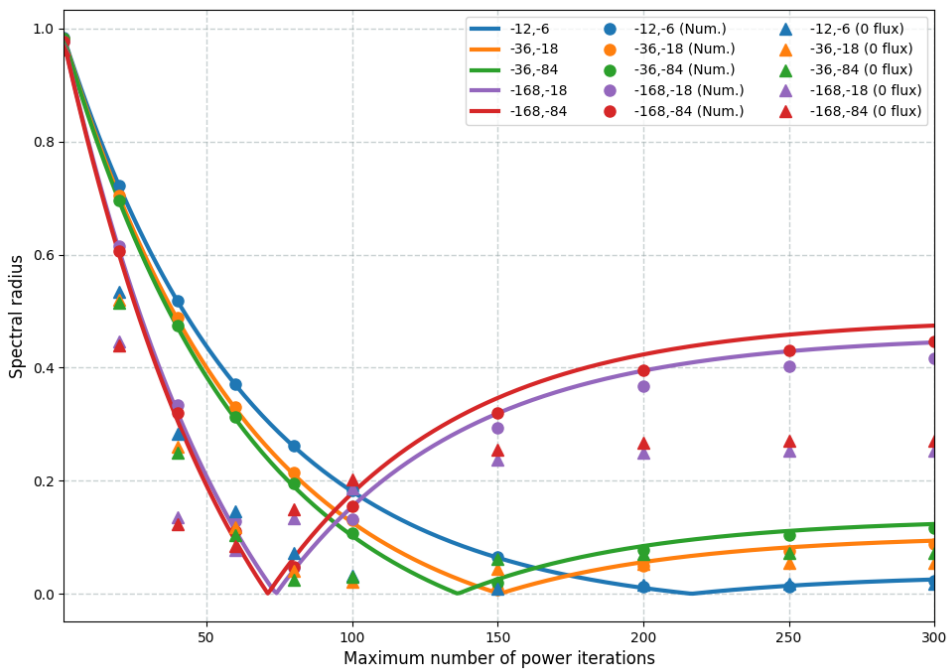

Figure 4-2. Analytical and numerical Power Iteration dependent spectral radius results for different combinations of $\widetilde{FTC}$ and MTC for periodic and zero-flux boundary conditions

This being said, the optimal number of PIs could be somehow corrected to get closer to the shifted value. However, this estimation would make the method to lose part of its efficacy as the correction is not independent from the problem characteristics. Additionally, note that the A and B factors in Eq. (4.73) can be expressed as

$$A = \frac{1}{1 + 2\frac{D}{\left(\Sigma_{a,0} + \Delta\Sigma_a\right)h^2}\left(\cos\left(\lambda_m h\right) - 1\right)} \tag{4.75}$$

$$B = \frac{\frac{\Sigma_{a,0}}{\Sigma_{a,0} + \Delta\Sigma_a} - \frac{\nu\Sigma_{f,0}}{\nu\Sigma_{f,0} + \Delta\nu\Sigma_f}}{1 + 2\frac{D}{\left(\Sigma_{a,0} + \Delta\Sigma_a\right)h^2}\left(\cos\left(\lambda_m h\right) - 1\right)} \tag{4.76}$$

which means that to predict the optimal number of PIs one would need to foresee the cross-section changes, which also depends on the problem characteristics, and would imply that additional calculations are necessary to estimate these changes.

Alternatively, and since it had yielded good results for the neutronics-T/H case, the AA method is retrieved and its study extended to improve its potential to stabilize and optimize the non-linear iteration to multiphysics problems.

4.2. Numerical Analysis of the Anderson Acceleration for Multiphysics Problems

With the previous results, the AA is reconsidered as an option to find a better and stable optimal. The AA application to the T/H variables yielded satisfactory results for the neutronics-T/H coupling but it has been demonstrated as insufficient when other physics are considered (i.e. xenon and boron updates). In this section the AA to solve nonlinear equations are briefly reviewed. Then, a numerical analysis focusing on how to adapt the AA to better treat the multiphysics FPI is carried out.

4.2.1. Review of the Anderson Acceleration

The AA can be applied to accelerate the convergence rate of the FPI of a system of nonlinear equations [61][62]. Thus, for a system of nonlinear equations that follows Eq.(4.8) and (4.9) the unconstrained least squares AA algorithm can be

written as in Table 4-3. The idea of this method is to determine the solution at (k+1)-th iteration as a linear combination of solution history **g** whose coefficients are determined by minimizing the norm of the residual vectors **f**. There is a parameter m, the storage depth of the AA, that determines how many histories will be stored. The AA with a specific m becomes AAm.

Table 4-3. Algorithm of the unconstrained least squares Anderson Acceleration

Given $\mathbf{x}^{(0)}$ and $m \geq 1$.
Set $\mathbf{x}^{(1)} = \mathbf{g}(\mathbf{x}^{(0)})$.
for k=1, 2, ... **do**
Set $m_k = \min[m, k]$.
Compute $\mathbf{g}(\mathbf{x}^{(k)})$ and let $\mathbf{f}^{(k)} = \mathbf{g}^{(k)}(\mathbf{x}^{(k)}) - \mathbf{x}^{(k)}$.
Compute $\Delta\mathbf{f}^{(i)} = \mathbf{f}^{(i+1)} - \mathbf{f}^{(i)}$ and $\Delta\mathbf{g}^{(i)} = \mathbf{g}\left(\mathbf{x}^{(i+1)}\right) - \mathbf{g}\left(\mathbf{x}^{(i)}\right),\ i = k - m_k, \ldots, k-1$
Set $\tilde{\mathbf{F}}^{(k)} = \left[\Delta\mathbf{f}^{(k-m_k)}, \ldots, \Delta\mathbf{f}^{(k-1)}\right]$ and $\tilde{\mathbf{G}}^{(k)} = \left[\Delta\mathbf{g}^{(k-m_k)}, \ldots, \Delta\mathbf{g}^{(k-1)}\right]$
Determine $\boldsymbol{\gamma}^{(k)} = [\gamma_0^{(k)}, \ldots, \gamma_{m_k-1}^{(k)}]^T$ which solves $\min_{\boldsymbol{\gamma}=[\gamma_0,\ldots,\gamma_{m_k-1}]^T} \left\|\mathbf{f}^{(k)} - \tilde{\mathbf{F}}^{(k)}\boldsymbol{\gamma}^{(k)}\right\|_2$ (4.77)
Set $\mathbf{x}^{(k+1)} = \mathbf{g}\left(\mathbf{x}^{(k)}\right) - \tilde{\mathbf{G}}^{(k)}\boldsymbol{\gamma}^{(k)}$.
end for

The least-squares problem of Eq. (4.77) can be solved by a QR decomposition. The matrix $\tilde{\mathbf{F}}^{(k)}$, which is a set of differences of residual vectors, can be decomposed by the QR factorization as

$$\tilde{\mathbf{F}}^{(k)} = \mathbf{Q}^{(k)}\mathbf{R}^{(k)} = \begin{bmatrix} \hat{\mathbf{Q}}^{(k)} & \bar{\mathbf{Q}}^{(k)} \end{bmatrix} \begin{bmatrix} \hat{\mathbf{R}}^{(k)} \\ 0 \end{bmatrix}, \tag{4.78}$$

where $\tilde{\mathbf{F}}^{(k)} \in \mathbb{R}^{n\times m_k}$, $\mathbf{Q}^{(k)} \in \mathbb{R}^{n\times n}$, $\mathbf{R}^{(k)} \in \mathbb{R}^{n\times m_k}$, $\hat{\mathbf{Q}}^{(k)} \in \mathbb{R}^{n\times m_k}$, $\hat{\mathbf{R}}^{(k)} \in \mathbb{R}^{m_k\times m_k}$, $\bar{\mathbf{Q}}^{(k)} \in \mathbb{R}^{n\times(n-m_k)}$, and n is the dimension of a solution vector **x**, m_k is the order of the AA. Then the least square problem can be rewritten as

$$\begin{aligned} \boldsymbol{\gamma} &= \min_{\gamma} \left\|\mathbf{f} - \tilde{\mathbf{F}}\boldsymbol{\gamma}\right\|_2 = \min_{\gamma} \left\|\mathbf{f} - \mathbf{Q}\mathbf{R}\boldsymbol{\gamma}\right\|_2 = \min_{\gamma} \left\|\mathbf{Q}^T\mathbf{f} - \mathbf{R}\boldsymbol{\gamma}\right\|_2 \\ &= \min_{\gamma} \left\| \begin{pmatrix} \hat{\mathbf{Q}}^T \\ \bar{\mathbf{Q}}^T \end{pmatrix} \mathbf{f} - \begin{pmatrix} \hat{\mathbf{R}} \\ 0 \end{pmatrix} \boldsymbol{\gamma} \right\|_2 = \min_{\gamma} \left\| \begin{pmatrix} \hat{\mathbf{Q}}^T\mathbf{f} - \hat{\mathbf{R}}\boldsymbol{\gamma} \\ \bar{\mathbf{Q}}^T\mathbf{f} \end{pmatrix} \right\|_2 = \min_{\gamma} \left\|\hat{\mathbf{Q}}^T\mathbf{f} - \hat{\mathbf{R}}\boldsymbol{\gamma}\right\|_2 \end{aligned} \tag{4.79}$$

For simplicity, the notation k for the FPI index is omitted in the equation above. In the end, the solution of the least square problem is obtained by solving a $m_k \times m_k$ triangular system, $\hat{\mathbf{R}}\boldsymbol{\gamma} = \hat{\mathbf{Q}}^T\mathbf{f}$, which can be solved with a thin QR factorization. More details about the calculation process can be found in [63].

4.2.2. The physical model

The physical model employed here is the same as the one in reference [31], for this reason only a brief description of the equations employed is offered here. The model is a simplified neutronics-T/H coupled system that holds the interdependency between neutron flux distribution and temperature distributions of fuel and coolant as well as xenon and boron densities. The neutronics is governed by a 1G 1D homogenous diffusion equation. For the T/H 1D heat conduction and convection are assumed for fuel and coolant temperatures calculation. The xenon is updated by means of the xenon equilibrium model and the boron concentration with the problem multiplication factor k_{eff}. The geometry of the model is a single fuel pin in PWRs. All the analyses in this work are performed under the steady state assumption.

Neutron Diffusion Equation

The 1G and 1D diffusion equation expressed in the Finite Difference Method (FDM) with N meshes can be written in the following linear system form:

$$\mathbf{M}\phi = \lambda\mathbf{F}\phi, \tag{4.80}$$

where $\mathbf{M}$ is a tridiagonal matrix, $\mathbf{F}$ is a diagonal matrix, $\phi = [\phi_1, \cdots, \phi_N]$ is the solution vector of neutron flux, and λ (the system fundamental mode eigenvalue) is the inverse of the multiplication factor k_{eff}. Here, the matrices coefficients (which are the diffusion equation cross sections) depend on the temperatures of the fuel (T_f) and

the coolant (T_c) and the number densities of xenon (N_{Xe}) and boron (N_B). This dependence can be expressed as

$$\phi = NT(\mathbf{T_f}, \mathbf{T_c}, \mathbf{N_{Xe}}, \mathbf{N_B}), \tag{4.81}$$

$$k_{eff} = EIG(\phi), \tag{4.82}$$

if the neutronics *NT* and the eigenvalue *EIG* operations are adopted and where $\boldsymbol{T_f}$, $\boldsymbol{T_c}$, $\boldsymbol{N_{Xe}}$ and $\boldsymbol{N_B}$ are the solution vector of fuel and coolant temperatures and xenon and boron number densities for discretized nodes.

Heat Conduction Equation for Fuel Temperature

The fuel heat conduction is limited to the radial direction and azimuthal and centerline symmetries are assumed as well as constant thermal properties of the fuel materials. The problem geometry is reduced to a simple fuel pellet surrounded by cladding material with no separation between them. For the heat transfer from the cladding to the coolant bulk the Newton's law is employed. With all these assumptions and equations, the volumetric average fuel temperature can be derived as

$$T_{f,avg} = \frac{\int_0^{r_f} rT(r)dr}{\int_0^{r_f} rdr} = \frac{q'_f}{\pi}\left(\frac{1}{8k_f} + \frac{1}{2k_c}\ln\frac{r_{co}}{r_f} + \frac{1}{2r_{co}h_w}\right) + T_{c,bulk}, \tag{4.83}$$

where r_f is the radius of the fuel pellet and r_{co} the cladding outer one, k_f and k_c for their part indicate the thermal conductivity of fuel and cladding respectively and h_w is the heat transfer coefficient of the wall (cladding outer surface). q'_f is the linear heat generation rate of the fuel that is calculated from the normalized scalar flux (ϕ) and T_{fbulk} is the coolant bulk temperature.

The above derivation can be re-expressed with the thermal conduction operation, *FC*, as follows:

$$\mathbf{T_f} = FC(\phi, \boldsymbol{T_c}), \tag{4.84}$$

which shows the dependency on the neutron flux and coolant temperature.

Heat Convection Equation for Coolant Temperature

The fluid conservation equations are simplified by assuming a constant mass flow rate given by the mass continuity equation at steady-state. Besides, the constant pressure is assumed over a problem domain, so the momentum equation is not considered. Then, by energy conservation, the enthalpy at the *n*-th node can be calculated with the following expressions

$$h_{n,out} = \frac{q_n' \Delta x_n}{\dot{m}_0} + h_{n,in}, \tag{4.85}$$

$$\bar{h}_n = \frac{1}{2}\left(h_{n,out} + h_{n,in}\right), \tag{4.86}$$

where $\dot{m}_0$ is the mass flow rate, Δx is the node length, h is the specific enthalpy at the node boundaries (indicated by the *in* and *out* subscripts) or at the node center. With the specific enthalpy value, h_i, and the presumed pressure the temperature of the coolant can be calculated employing steam tables.

The thermal-hydraulic operator, *TH*, which corresponds to the above procedure, allows the expression of the coolant temperature calculation as

$$\mathbf{T_c} = TH(\phi). \tag{4.87}$$

Xenon equilibrium

The Xenon concentration is updated assuming it has reached its equilibrium

$$N_{Xe} = \frac{\left(\gamma_{Xe} + \gamma_I\right)\Sigma_f \phi}{\lambda_{Xe} + \sigma_{a,Xe}\phi}, \tag{4.88}$$

where γ_{Xe} and γ_I are the Xenon and Iodine yields respectively, Σ_f is the fission cross section, λ_{Xe} is the decay constant of Xenon and $\sigma_{a,Xe}$ the absorption microscopic cross section.

This operation can be re-expressed with the Xenon operator *XE* as

$$\mathbf{N_{Xe}} = XE(\phi) \tag{4.89}$$

Boron update

The Boron update is performed until the problem eigenvalue λ reaches the value of 1. This is achieved by employing the following linear functionalization

$$N_B^{(l+1)} = \left(1-\lambda^{(l+1)}\right)\frac{N_B^{(l-1)} - N_B^{(l)}}{\lambda^{(l)} - \lambda^{(l+1)}} + N_B^{(l)}, \tag{4.90}$$

where l is the outer iteration (or FPI) number.

This operation can be re-expressed with the Boron operator *B* as

$$\mathbf{N_B} = B(k_{eff}) \tag{4.91}$$

Iterative solution of the coupled system

The physical models can be summarized in the following systems that need to be solved:

$$\phi = NT(\mathbf{T_f}, \mathbf{T_c}, \mathbf{N_{Xe}}, \mathbf{N_B}), \tag{4.92}$$

$$k_{eff} = EIG(\phi), \tag{4.93}$$

$$\mathbf{T_c} = TH(\phi), \tag{4.94}$$

$$\mathbf{T_f} = FC(\phi, \boldsymbol{T_c}), \tag{4.95}$$

$$\mathbf{N_{Xe}} = XE(\phi), \tag{4.96}$$

$$\mathbf{N_B} = B(k_{eff}) \tag{4.97}$$

with two equations for neutronics and two T/H and one for xenon and boron updates. The solution algorithm of the FPI defined by the above nonlinear equations is depicted in Table 4-4.

Table 4-4. FPI scheme for 1D simplified coupled system

Given ϕ^0, $\mathbf{T_c^0}$, $\mathbf{T_f^0}$, $\mathbf{N_{Xe}^0}$, $\mathbf{N_B^0}$.
for l=0, 1, ... **do**
Update $\Sigma(\mathbf{T_f^{(l)}}, \mathbf{T_c^{(l)}}, \mathbf{N_{Xe}^{(l)}}, \mathbf{N_B^{(l)}})$.
Solve $\phi^{(l+1)} = NT(\mathbf{T_f^{(l)}}, \mathbf{T_c^{(l)}}, \mathbf{N_{Xe}^{(l)}}, \mathbf{N_B^{(l)}})$ and $k_{eff}^{(l+1)} = EIG(\phi^{(l+1)})$
Solve $\mathbf{T_c^{(l+1)}} = TH(\phi^{(l+1)})$
Solve $\mathbf{T_f^{(l+1)}} = FC(\phi^{(l+1)}, \mathbf{T_c^{(l+1)}})$
Solve $\mathbf{N_{Xe}^{(l+1)}} = XE(\phi^{(l+1)})$
Solve $\mathbf{N_B^{(l+1)}} = B(k_{eff}^{(l+1)}, k_{eff}^{(l)}, \mathbf{N_B^{(l)}}, \mathbf{N_B^{(l-1)}})$
end for

For the 1-D neutronics-T/H coupled system given in Eq. (4.92)-(4.95) with a Gauss-Seidel solution scheme, the AA fixed-point map when only the T/H variables are considered can be expressed as

$$\begin{bmatrix} \mathbf{T_c} \\ \mathbf{T_f} \end{bmatrix}^{(l+1)} = \mathbf{g}_{gs}\left(\begin{bmatrix} \mathbf{T_c} \\ \mathbf{T_f} \end{bmatrix}^{(l)}\right) = \begin{bmatrix} TH\left(NT\left(\mathbf{T_f}, \mathbf{T_c}\right)\right) \\ FC\left(\mathbf{T_c}, NT\left(\mathbf{T_f}, \mathbf{T_c}\right)\right) \end{bmatrix}^{(l)} \tag{4.98}$$

Nonetheless, when other physics are introduced the previous the previous AA fixed-point map must be re-written as

$$\begin{bmatrix} \mathbf{T_c} \\ \mathbf{T_f} \end{bmatrix}^{(l+1)} = \mathbf{g}_{gs}\left(\begin{bmatrix} \mathbf{T_c} \\ \mathbf{T_f} \end{bmatrix}^{(l)}\right) = \begin{bmatrix} TH\left(NT\left(\mathbf{T_f}, \mathbf{T_c}, \mathbf{N_{Xe}}, \mathbf{N_B}\right)\right) \\ FC\left(\mathbf{T_c}, NT\left(\mathbf{T_f}, \mathbf{T_c}, \mathbf{N_{Xe}}, \mathbf{N_B}\right)\right) \end{bmatrix}^{(l)} \tag{4.99}$$

As shown in realistic calculations in more complex codes this map is inappropriate to obtain a stable and reasonably optimized convergence. Consequently, the system in Eq. (4.99) is proposed to be extended to

$$\begin{bmatrix} \mathbf{T_c} \\ \mathbf{T_f} \\ \mathbf{N_{Xe}} \\ \mathbf{N_B} \end{bmatrix}^{(l+1)} = \mathbf{g}_{gs}\left(\begin{bmatrix} \mathbf{T_c} \\ \mathbf{T_f} \\ \mathbf{N_{Xe}} \\ \mathbf{N_B} \end{bmatrix}^{(l)}\right) = \begin{bmatrix} TH\left(NT\left(\mathbf{T_f},\mathbf{T_c},\mathbf{N_{Xe}},\mathbf{N_B}\right)\right) \\ FC\left(\mathbf{T_c},NT\left(\mathbf{T_f},\mathbf{T_c},\mathbf{N_{Xe}},\mathbf{N_B}\right)\right) \\ XE\left(NT\left(\mathbf{T_f},\mathbf{T_c},\mathbf{N_{Xe}},\mathbf{N_B}\right)\right) \\ B\left(EIG\left(NT\left(\mathbf{T_f},\mathbf{T_c},\mathbf{N_{Xe}},\mathbf{N_B}\right)\right)\right) \end{bmatrix}^{(l)} \tag{4.100}$$

This fixed-point map can be, however, very memory demanding and even too complex to implement. Alternatively, and since all the other physics depend on the flux distribution the map can be transformed into

$$[\phi]^{(l+1)} = \mathbf{g}_{gs}\left([\phi]^{(l)}\right) = \begin{bmatrix} NT\begin{pmatrix} FC(\phi,TH(\phi)), \\ TH(\phi), \\ XE(\phi), \\ B(EIG(\phi)) \end{pmatrix} \end{bmatrix}^{(l)}, \tag{4.101}$$

which is effectively a partial convergence of the PI flux solution, possibly less optimal than the analytical convergence point but more sophisticated than the user-dependent relaxation factors. In the following the performance of this new map is compared to the solution without AA and with the AA(TH) currently applied.

4.2.3. Problem specifications

The simple problem for the convergence analyses has a single pin configuration with 3.81 m of axial height. The size of each computational mesh is 1 cm, which yields 381 axial meshes. The typical geometry and boundary conditions of a PWR at Hot Full Power (HFP) are applied: 15.513 MPa outlet pressure, 295 °C inlet temperature, 0.360 kg/s mass flow rate, 17.5 kW/m linear power density, r_f = 4.2 mm, and r_{co}= 4.8 mm. The thermal properties assigned are k_f = 5.0 W/(m·K), k_c = 16.0 W/(m·K), and h_w = 36,000 W/(m^2·K). The zero-flux boundary condition is applied

for the neutronics system.

The cross sections generation conditions are T_c = 600 K, T_f = 600 K, and 1000 ppm boron concentration. The base cross section values result: $D_0 = 1.2605$ cm, $\Sigma_{a0} = 0.0216\ \mathrm{cm}^{-1}$, $\nu\Sigma_{f0} = 0.0267\ \mathrm{cm}^{-1}$, $\kappa\Sigma_{f0} = 0.353 \cdot 10^{-12}\ \mathrm{cm}^{-1}$.

With the generated cross-sections, the multiphysics calculations are performed. The problems are solved by the Gauss-Seidel (G-S) type FPI. The iteration is terminated when the following fission source pseudo error and multiplication factor convergence criteria are satisfied:

$$\varepsilon_{\psi}^{(l)} = \frac{\left\| \boldsymbol{\psi}^{(l)} - \boldsymbol{\psi}^{(l-1)} \right\|_2}{\left\| \boldsymbol{\psi}^{(l)} \right\|_2} \leq 5 \times 10^{-6} \tag{4.102}$$

and

$$\varepsilon_{eig}^{(l)} = \frac{\left| k_{eff}^{(l)} - k_{eff}^{(l-1)} \right|}{k_{eff}^{(l)}} \leq 5 \times 10^{-6}, \tag{4.103}$$

where $\boldsymbol{\psi}$ is the fission source vector ($\mathbf{F}\phi$) and the superscript l is the iteration number notation of FPI. The neutronics problem solution is obtained with the PI for which the same convergence criteria as in Eqs. (4.102) and (4.103) but with values of $2 \cdot 10^{-6}$ and $1 \cdot 10^{-6}$ respectively with a maximum of 1000 of PIs.

4.2.4. Numerical analysis of neutronics-T/H problems

In this section the 1G single pin homogeneous problem is systematically studied for the combinations of $\widetilde{FTC}$ and MTC values described in section 4.1.2. At first only the T/H variables are considered and the xenon and boron concentrations are added sequentially so that the effect of each feedback can be assessed in an isolated manner. The AA*m*() notation refers to Anderson Acceleration with depth (number of histories) *m* and within brackets the variables it is applied to the T/H variables or the

neutron flux ϕ.

Table 4-5 shows the comparison between the solution without AA, the AA(TH), which is the currently implemented in nTRACER and AA(ϕ) which is the one proposed in this research. The comparison consists of the average number of FPIs needed to converge all the $\widetilde{FTC}$-MTC problems and the maximum k_{eff} deviation from the reference result (the problem without AA application).

Table 4-5. Average number of required FPIs and k_{eff} errors for different AA solutions

	w/o AA	AA1 (TH)	AA2 (TH)	AA1 (ϕ)	AA2 (ϕ)
Average # FPI	9.29	7.56	7.09	7.06	6.80
keff diff. (pcm)	-	0.39	0.34	0.29	0.30

As the comparison shows, the application of AA reduces the number of required FPIs. Since the problem only considers the neutronics and T/H variables AA(TH) and AA(ϕ) result in a very similar convergence behavior as the fixed-point map is equivalent. This can be corroborated in a more visual manner in Figure 4-3, where there are certain combinations of $\widetilde{FTC}$ and MTC values more challenging to be converged than others if no "relaxation" is applied as shown analytically with the Fourier analysis.

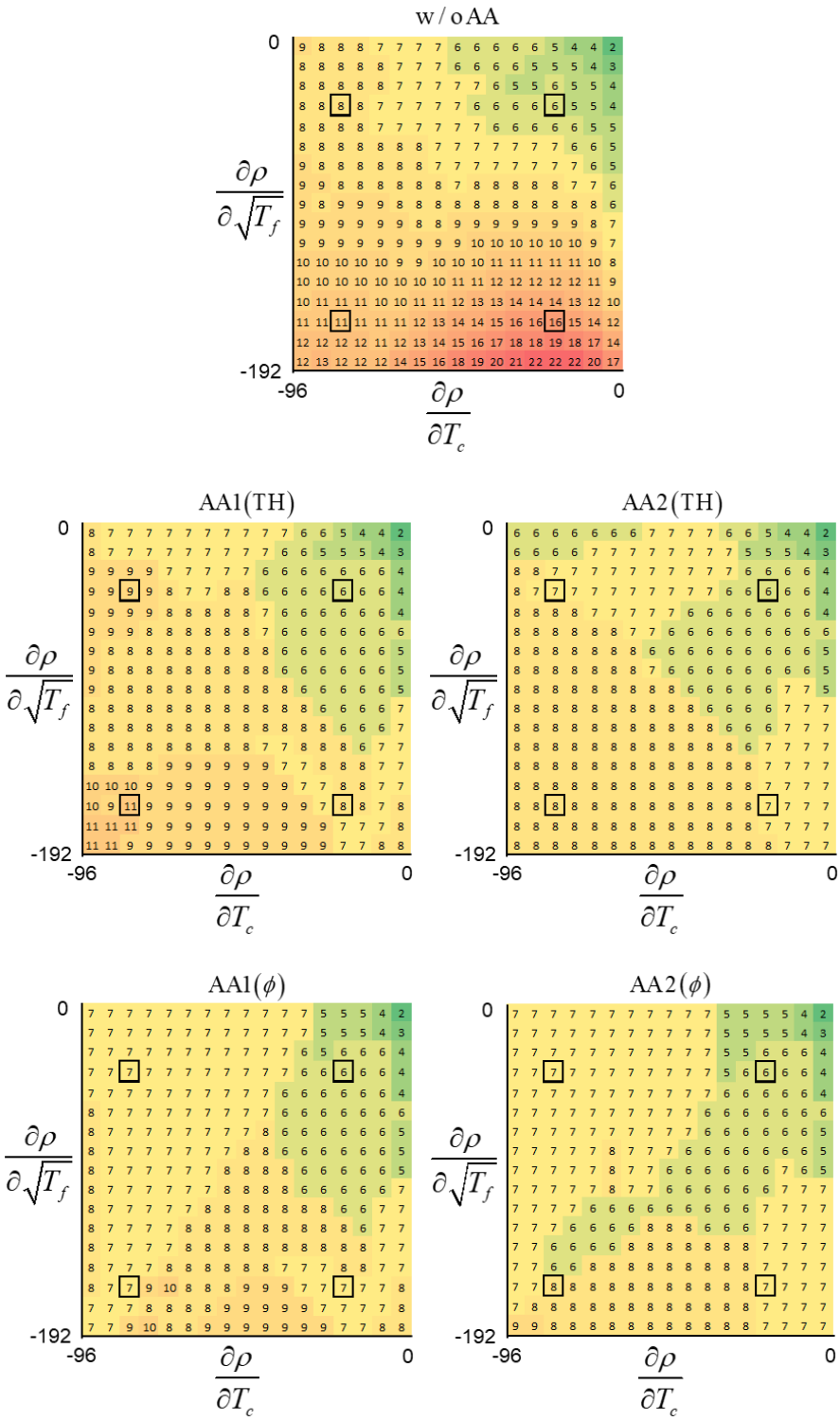

Figure 4-3. Number of FPIs required for different combinations of $\widetilde{FTC}$ and MTC employing diverse AA solutions

In Figure 4-4 the FPI fission source pseudo error (Eq. (4.102)) convergence behavior is shown for a various combinations of $\widetilde{FTC}$ and MTC, which cover sufficiently the cases depicted in Figure 4-3. These comparisons reinforce the data showed in Figure 4-3, this is there is no big changes with the variable switch between from T/H to ϕ. It also demonstrates the effectiveness improvement of applying the AA, particularly in strong $\widetilde{FTC}$ scenarios.

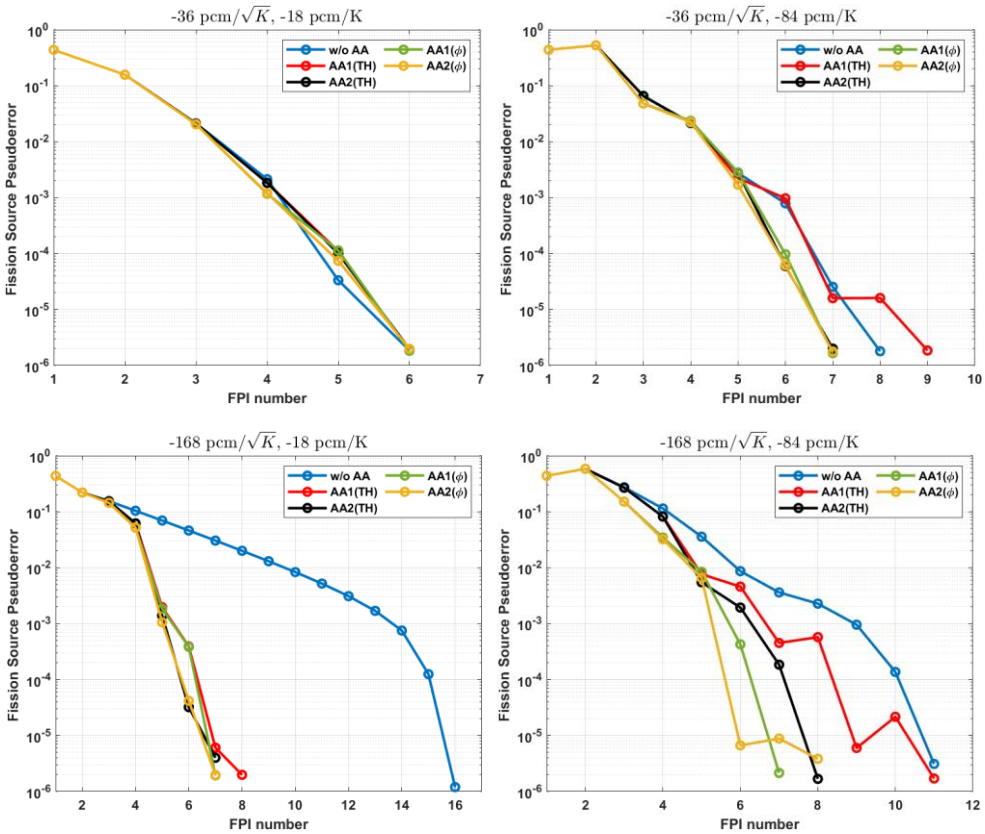

Figure 4-4. Fission source pseudo error convergence behavior for various $\widetilde{FTC}$ and MTC combinations

In Figure 4-5 the fission source value at a problem elevation of 110 cm is represented. In these plots a clear difference between using AA on ϕ instead of on the T/H variables is observed. In the strong $\widetilde{FTC}$ figures a smaller oscillation is shown in the case of AA(ϕ), this is due to the change that the AA produces in the

next FPI initial source. This effect is not tremendously relevant in this case as the PI convergence is monitored by the fission source and eigenvalue convergence, but it can have a greater impact if the next neutronics solution geometry and energy sweeps number is fixed. For example, in nTRACER the MOC sweeps have a fixed number, therefore the initial source determines the solution obtained.

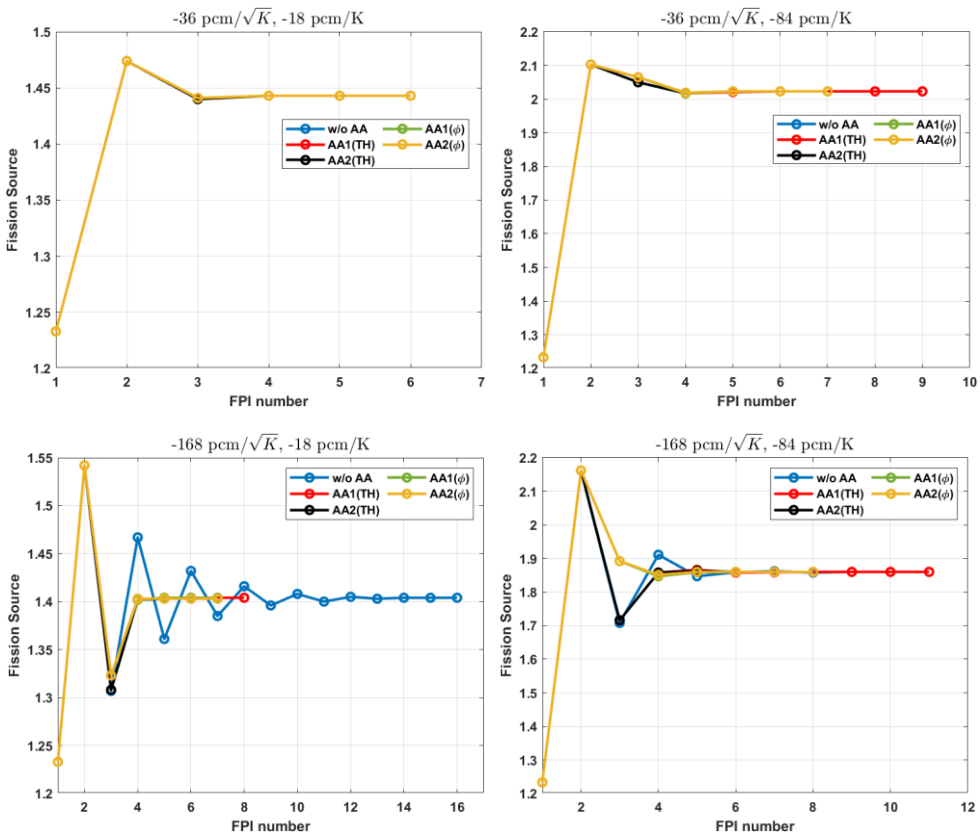

Figure 4-5. Fission source value convergence behavior at a problem elevation of 110 cm for various $\widetilde{FTC}$ and MTC combinations

By capping the number of maximum PIs for the problem without AA a quasi-optimal convergence point (lowest number of FPIs required for problem convergence) can be obtained. Figure 4-6 shows how a fully converged problem can yield a number of FPIs very close to the optimal one provided AA is applied. Although, in some cases, AA(ϕ) yields a better behavior than AA(TH), it does not

seem to be a very relevant difference.

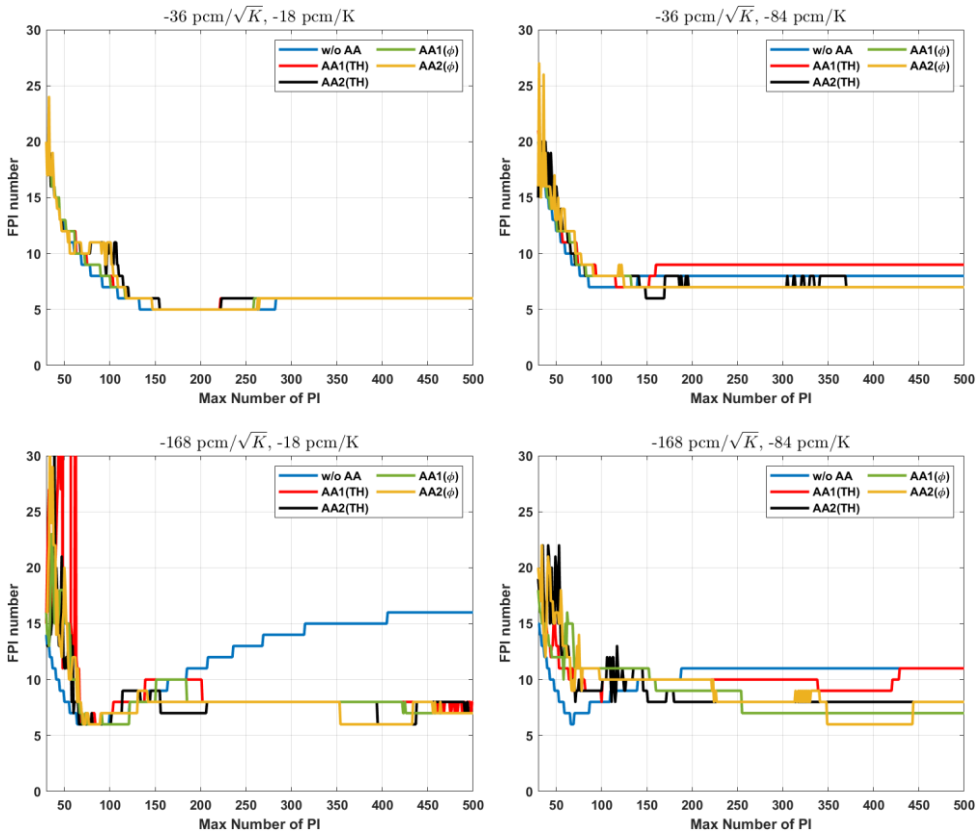

Figure 4-6. Number of FPIs required to converge given a fixed number of PIs for various $\widetilde{FTC}$ and MTC combinations

Figure 4-7 to Figure 4-10 depict the fission source shapes for the first six iterations for the problems without and with AA. It is clear how the oscillatory behavior is drastically reduced with the application of AA. Also the effect of AA(ϕ) on the next FPI initial source is observed in the strong $\widetilde{FTC}$ cases, especially in Figure 4-10.

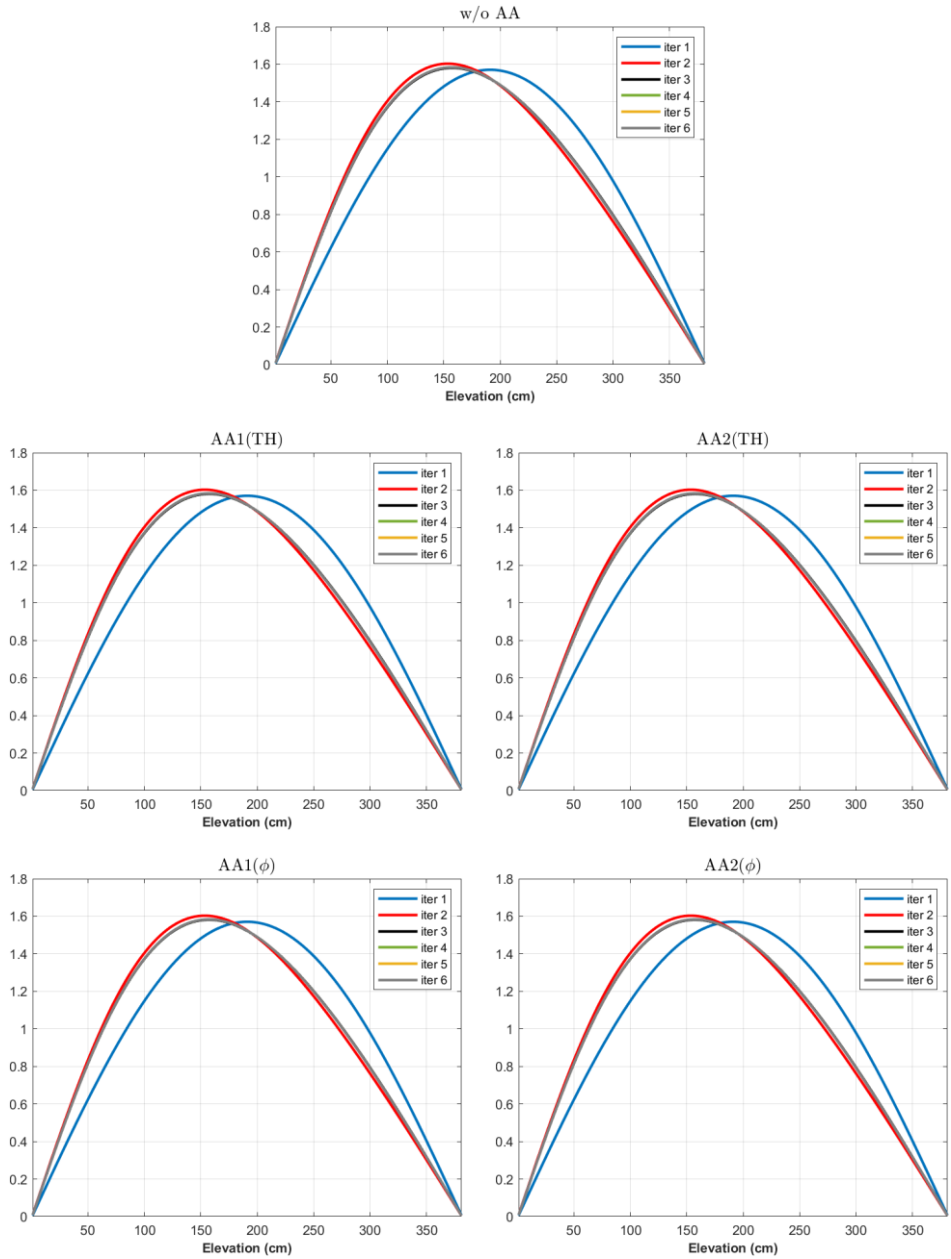

Figure 4-7. Fission source shapes for the six first iterations for $\widetilde{FTC} = -36\ pcm/\sqrt{K}$ and MTC = -18 pcm/K

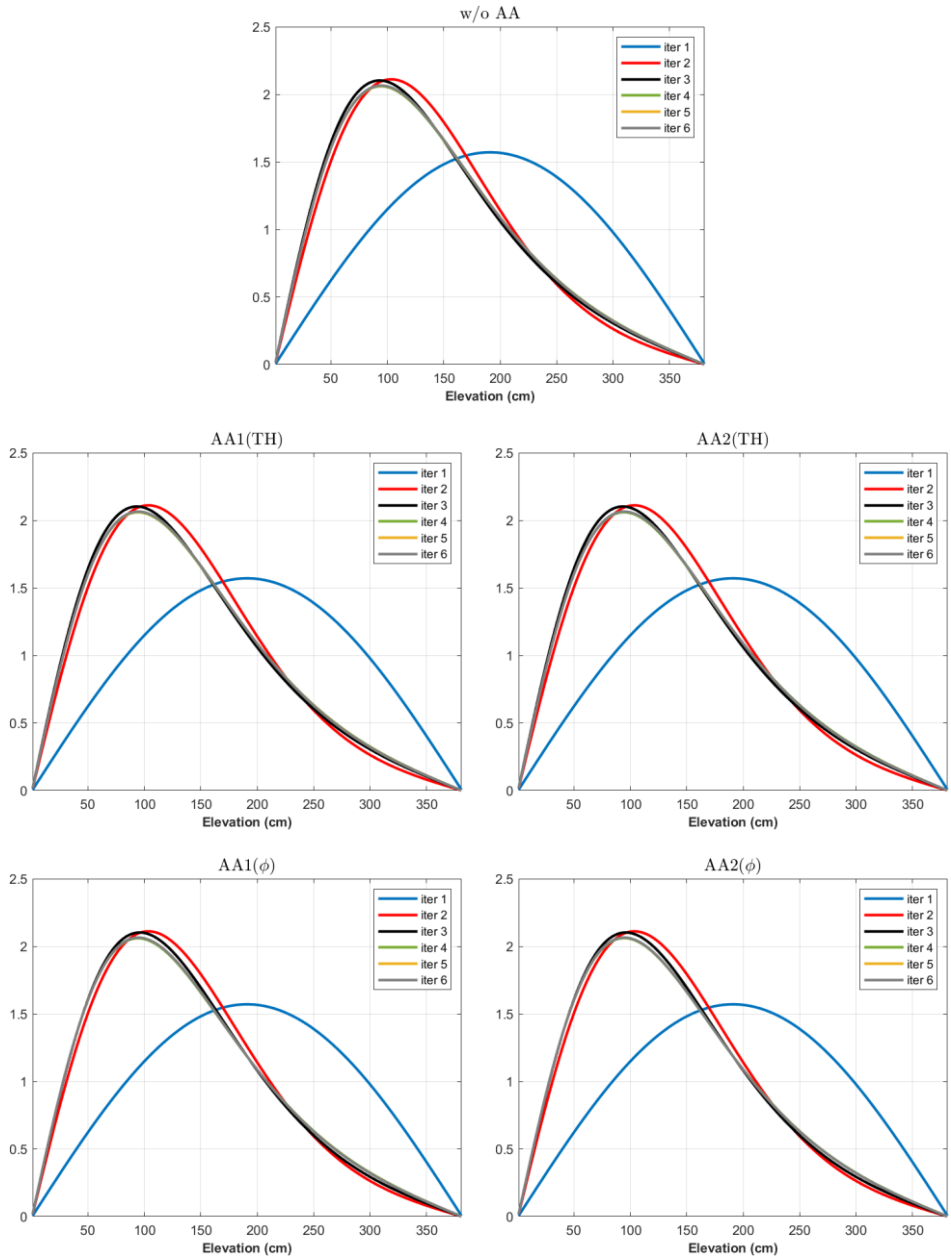

Figure 4-8. Fission source shapes for the six first iterations for $\widetilde{FTC} = -36\ pcm/\sqrt{K}$ and MTC = -84 pcm/K

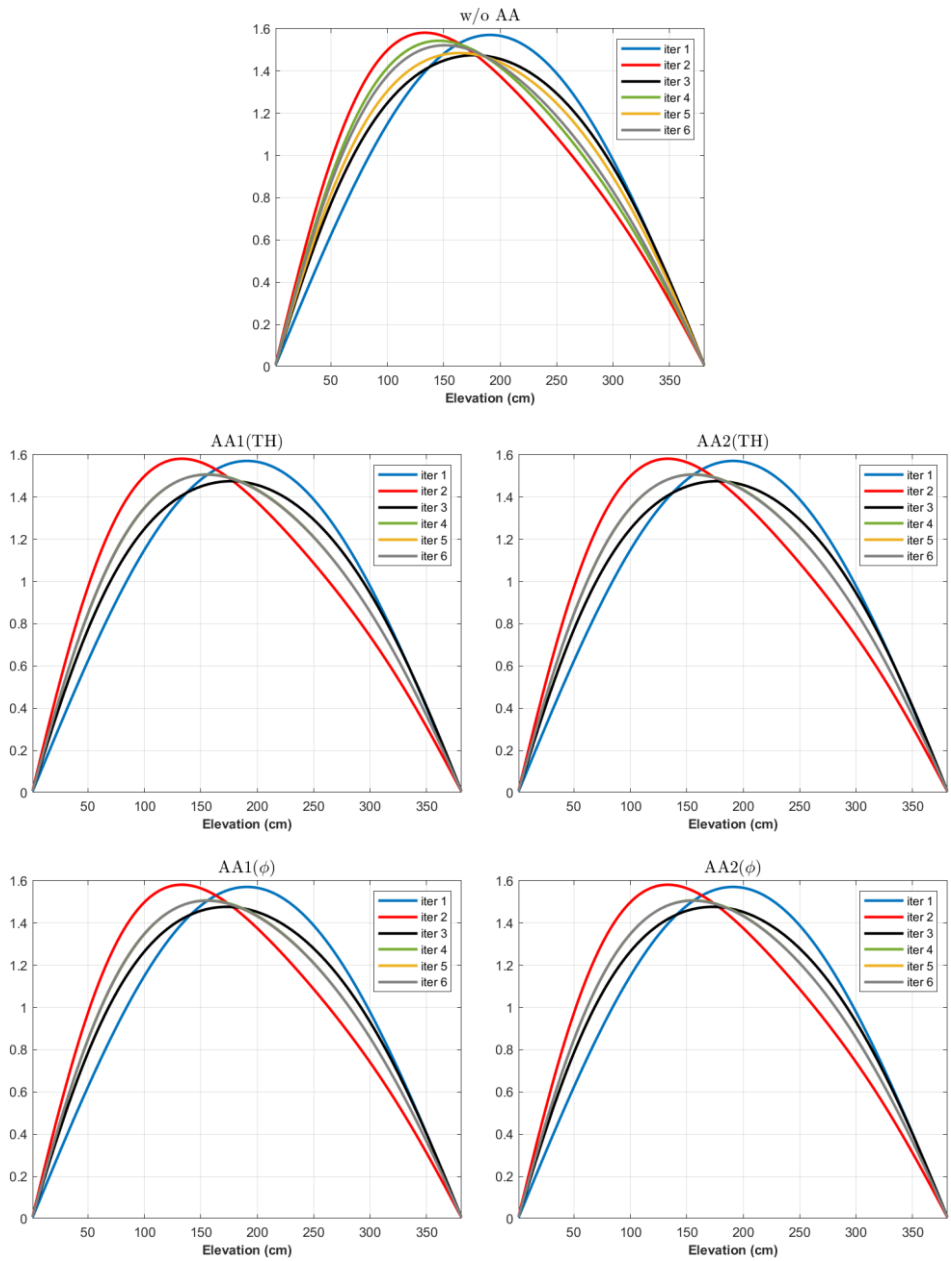

Figure 4-9. Fission source shapes for the six first iterations for $\widetilde{FTC} = -168\ pcm/\sqrt{K}$ and MTC = -18 pcm/K

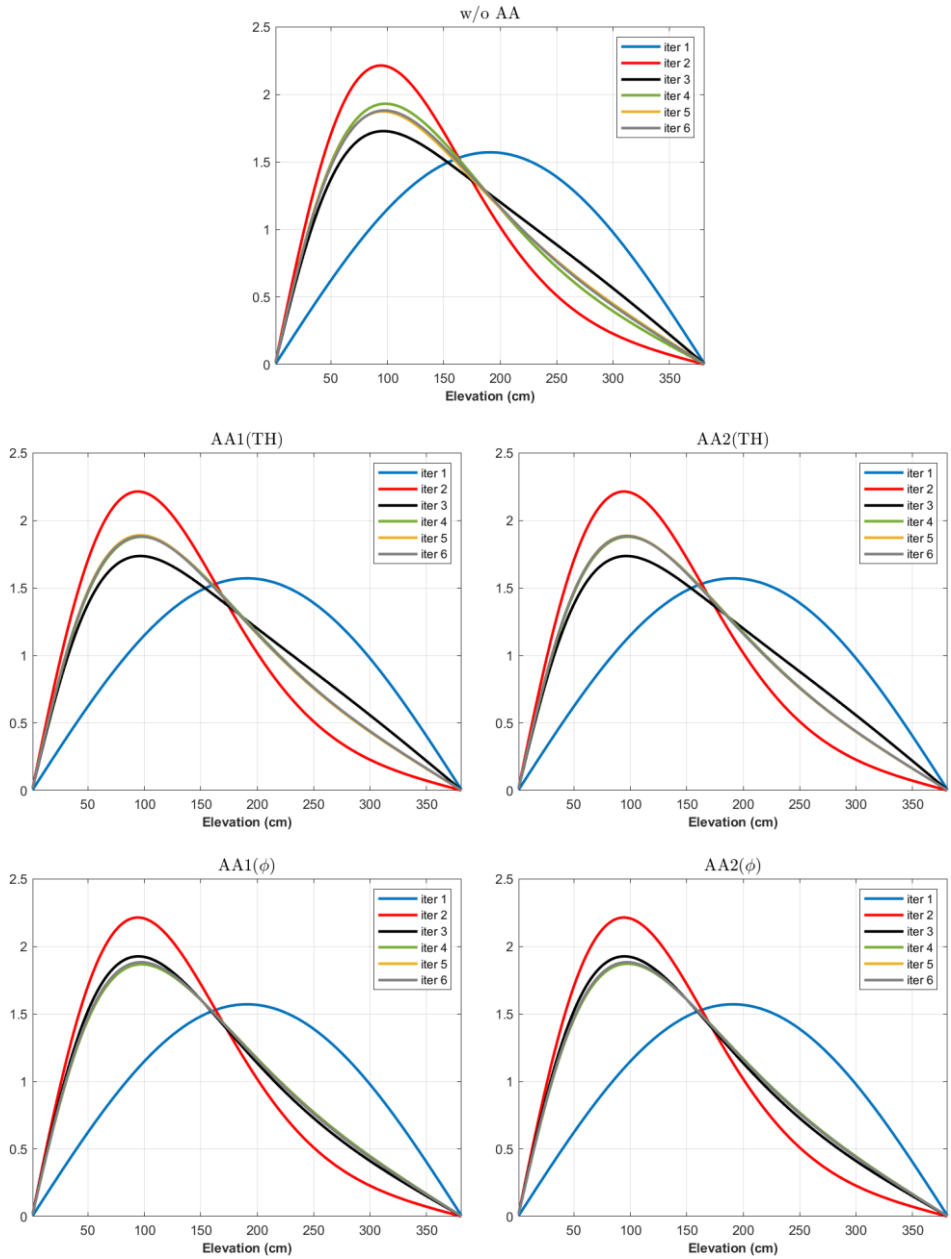

Figure 4-10. Fission source shapes for the six first iterations for $\widetilde{FTC} = -168\ pcm/\sqrt{K}$ and MTC = -84 pcm/K

4.2.5. Numerical analysis of neutronics-T/H-xenon problems

Table 4-6 gathers the results of the comparison between the solution without AA, the AA(TH) and AA(ϕ) when the xenon density update is added to the thermal feedbacks studied in the previous section. Now the comparison makes clear that in the presence of the xenon feedback the application of AA to only the T/H variables is insufficient and that by applying it to the neutron flux the problems converge on average considerably faster. Additionally, the errors in k_{eff} are much smaller.

Table 4-6. Average number of required FPIs and k_{eff} errors for different AA solutions for problems with xenon update

	w/o AA	AA1 (TH)	AA2 (TH)	AA1 (ϕ)	AA2 (ϕ)
Average # FPI	div.	14.22	14.07	9.22	7.76
keff diff. (pcm)	-	4.33	3.21	0.26	0.21

Figure 4-11 supports this conclusion, this is particularly notable in the feedback regions presenting the most challenging conditions. While it is true that AA(TH) allows to converge those problems that did not manage to reach convergence without the AA application, its performance was far from optimal if compared with the AA(ϕ) results.

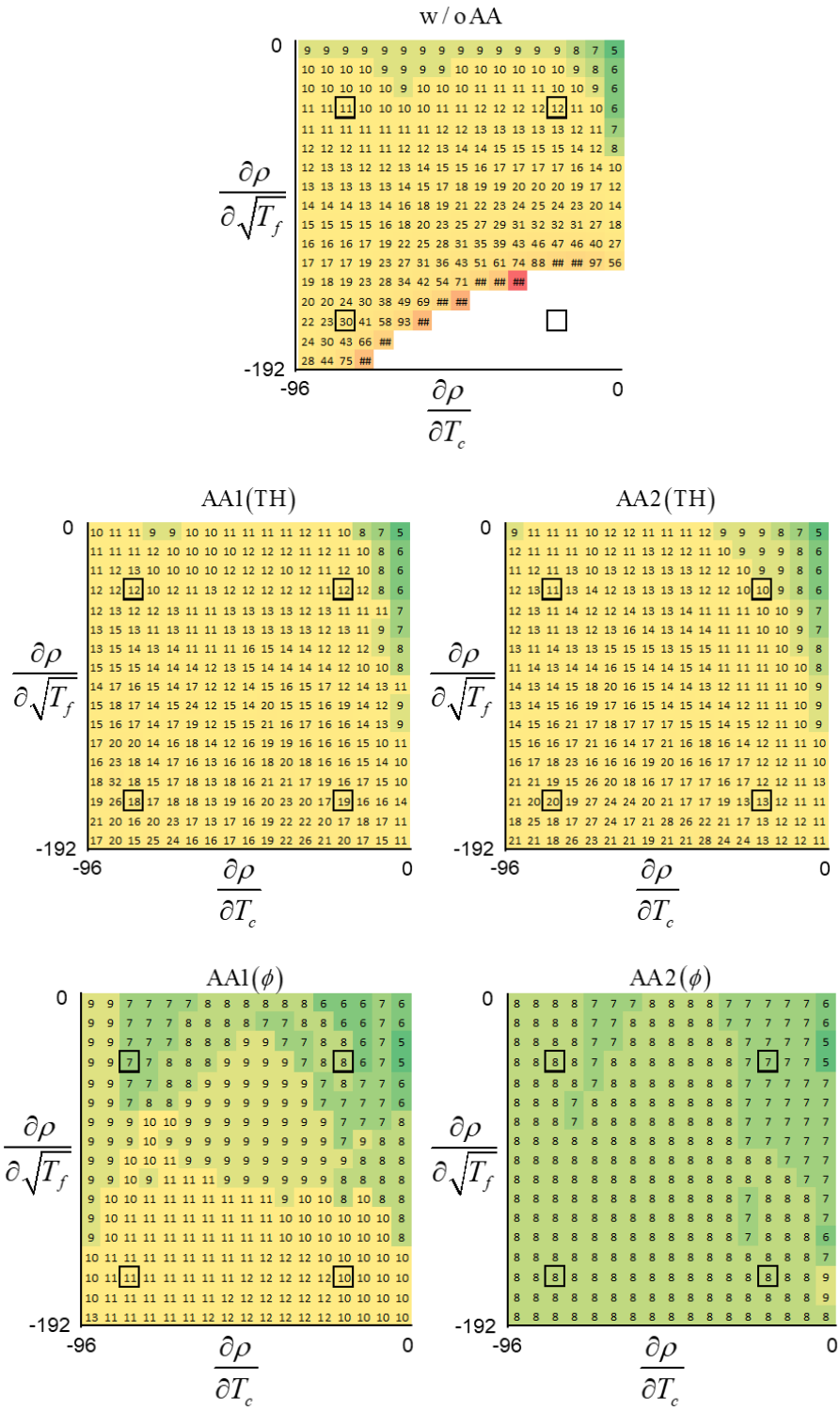

Figure 4-11. Number of FPIs required for different combinations of $\widetilde{FTC}$ and MTC and xenon update employing diverse AA solutions

The fission source pseudo error and the fission source value at a problem elevation of 110 cm for the combinations of $\widetilde{FTC}$ and MTC of interest in Figure 4-12 shows the superiority of the application of AA to ϕ at reducing the oscillations and consequently reducing the error at faster rates even in the cases with a weak $\widetilde{FTC}$.

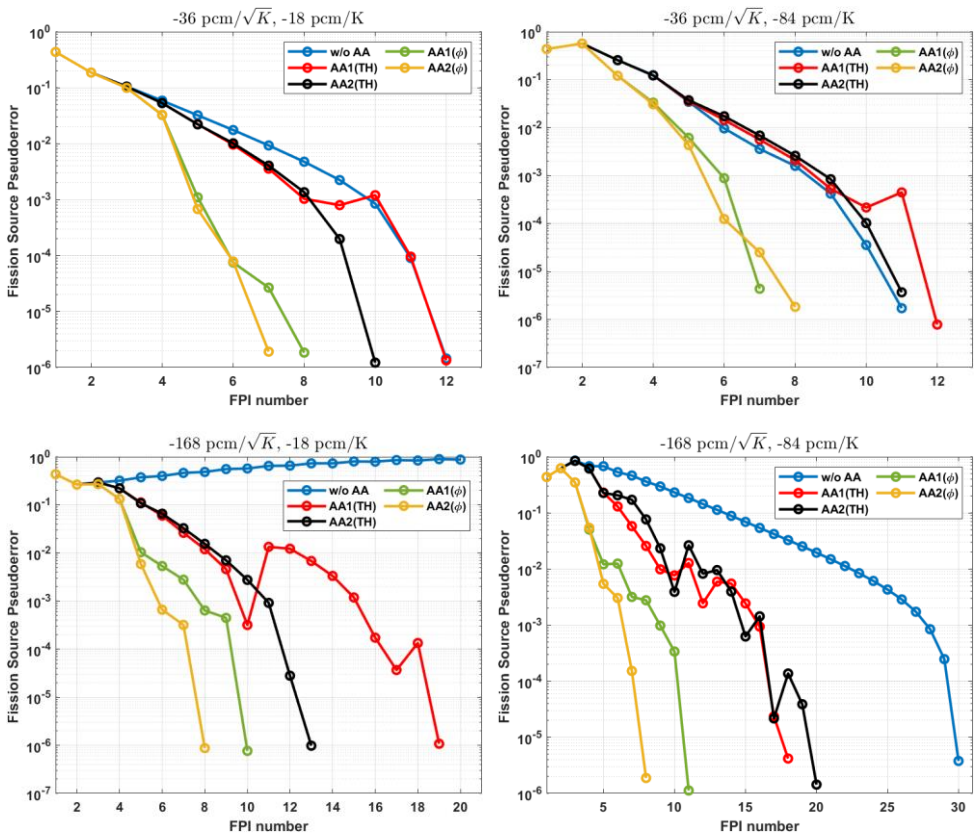

Figure 4-12. Fission source pseudo error convergence behavior for various $\widetilde{FTC}$ and MTC combinations and xenon update

In Figure 4-13 the fission source value at a problem elevation of 110 cm is represented. In these plots not only the advantage of using the AA to increase the convergence chances is shown, but also the greater effect of AA(ϕ) at suppressing the oscillations and consequently improving the convergence rate.

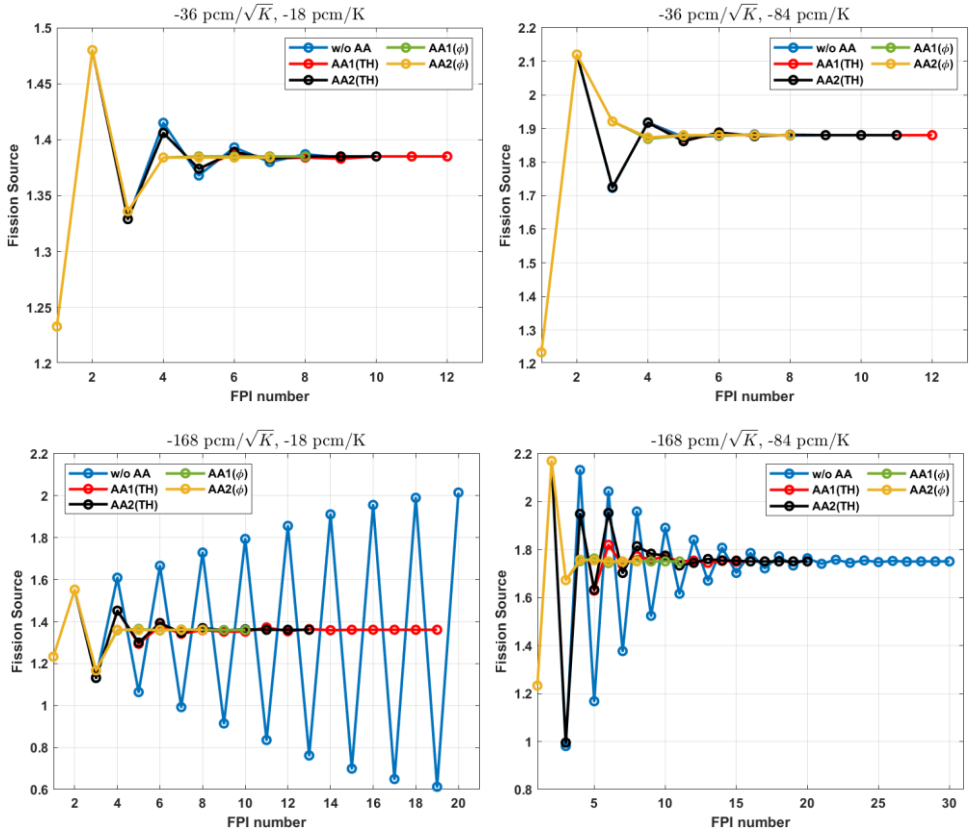

Figure 4-13. Fission source value convergence behavior at a problem elevation of 110 cm for various $\widetilde{FTC}$ and MTC combinations and xenon update

Figure 4-14 shows the number of FPIs needed to converge for a given fixed number of PIs. The application of AA(ϕ) at full convergence gives a similar number of FPIs to the optimal minimum. On the other hand, the AA(TH) cannot reach the numbers of AA(ϕ) and even becomes chaotic under certain circumstances, such as at strong $\widetilde{FTC}$ problems. Thus, since the optimal convergence point is difficult to be found analytically, AA(ϕ) can be considered an optimal alternative.

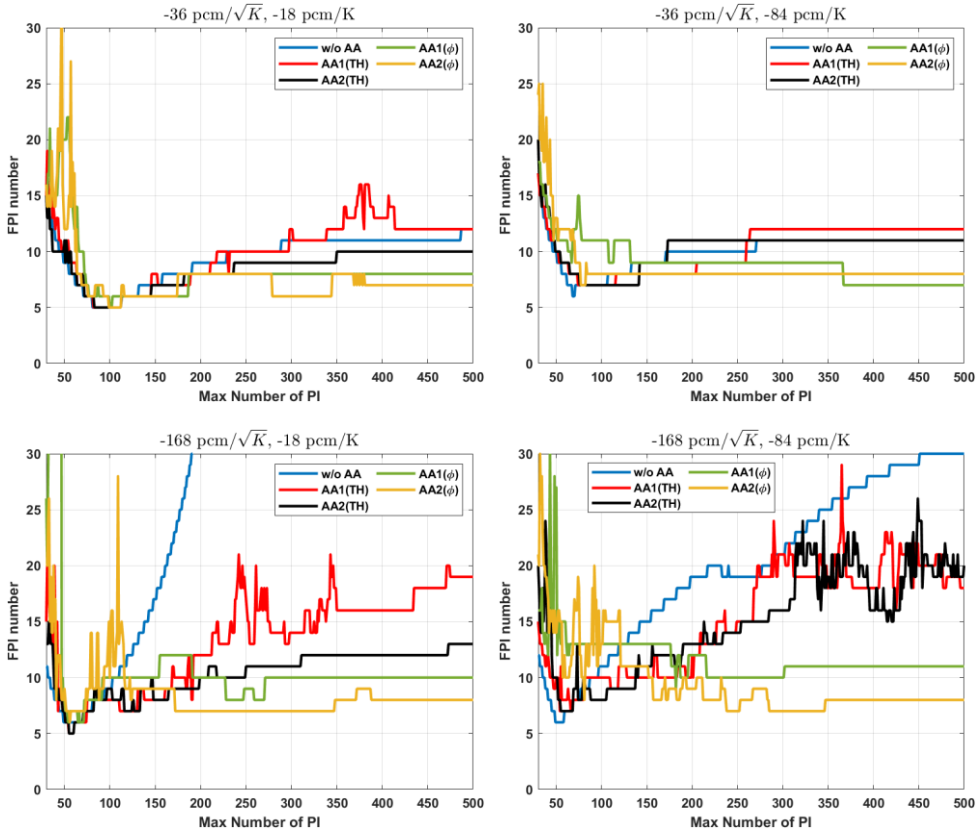

Figure 4-14. Number of FPIs required to converge given a fixed number of PIs for various $\widetilde{FTC}$ and MTC combinations and xenon update

The oscillatory behavior of the first six iteration fission source from Figure 4-15 to Figure 4-18 confirms how AA(ϕ) suppresses more effectively the feedback-induced oscillations.

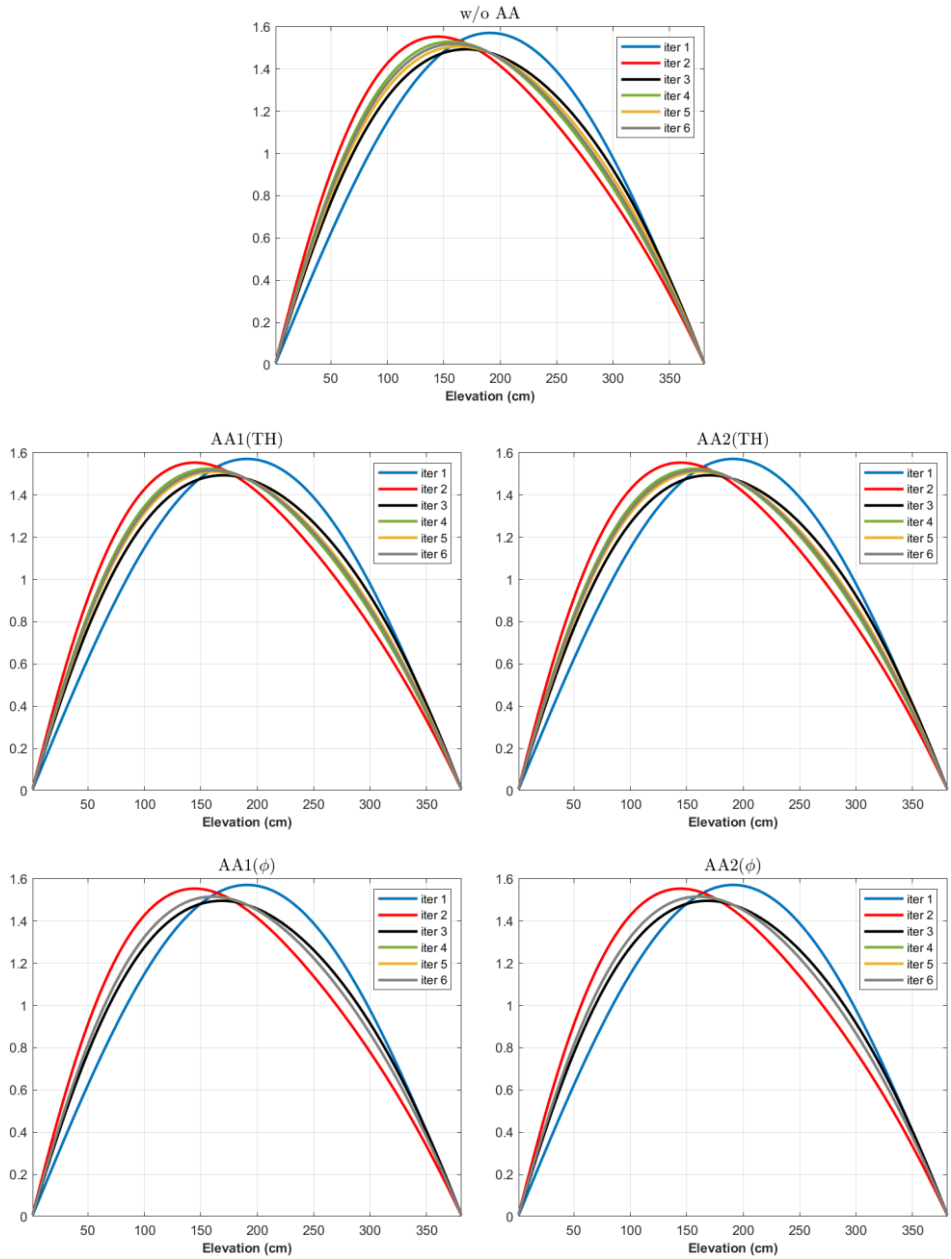

Figure 4-15. Fission source shapes for the six first iterations for $\widetilde{FTC} = -36\ pcm/\sqrt{K}$ and MTC = -18 pcm/K and xenon update

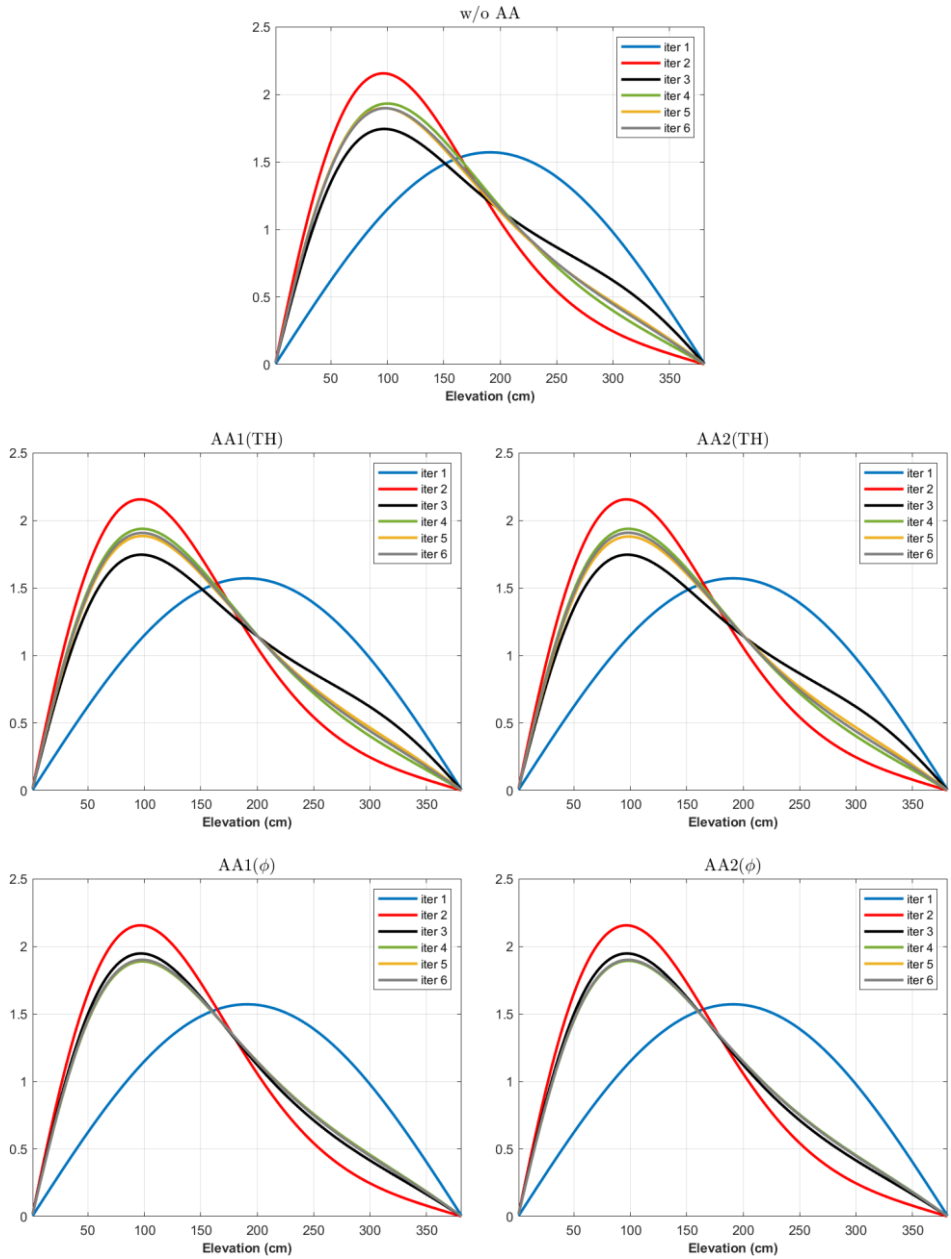

Figure 4-16. Fission source shapes for the six first iterations for $\widetilde{FTC} = -36\ pcm/\sqrt{K}$ and MTC = -84 pcm/K and xenon update

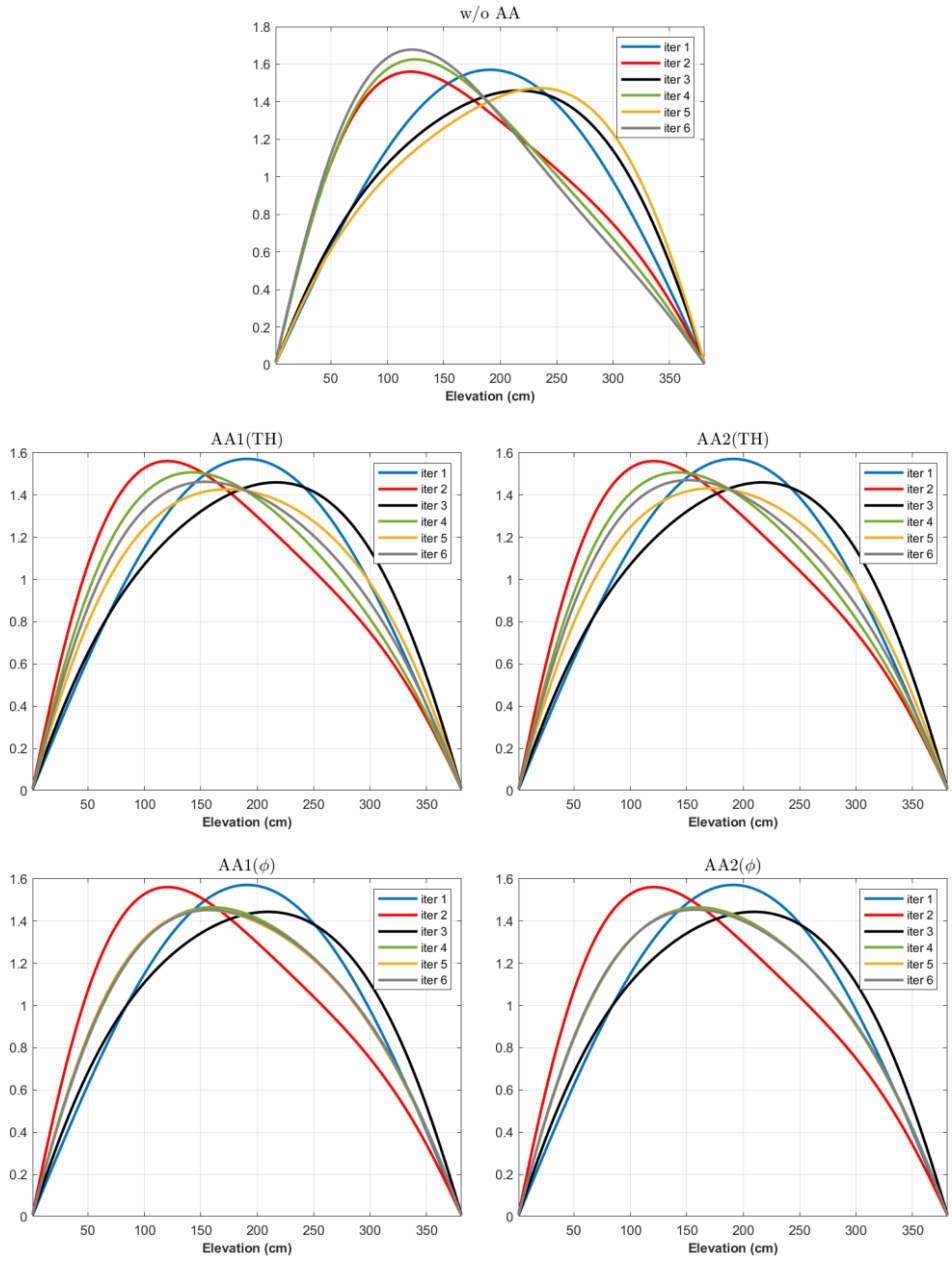

Figure 4-17. Fission source shapes for the six first iterations for $\widetilde{FTC} = -168\ pcm/\sqrt{K}$ and MTC = -18 pcm/K and xenon update

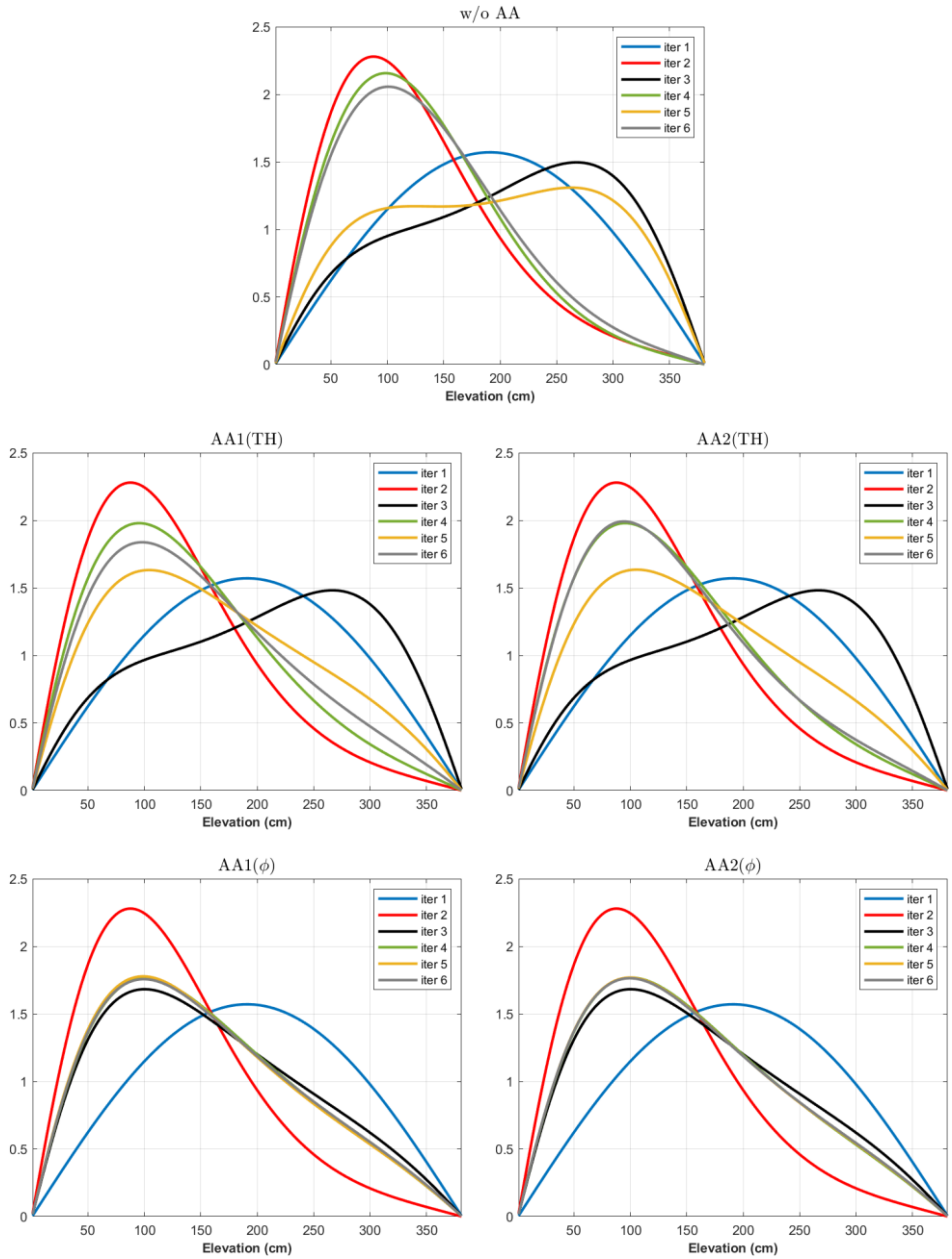

Figure 4-18. Fission source shapes for the six first iterations for $\widetilde{FTC} = -168\ pcm/\sqrt{K}$ and MTC = -84 pcm/K and xenon update

4.2.6. Numerical analysis of neutronics-T/H-xenon-boron problems

The critical boron concentration (CBC) update is introduced to the problem presented in the previous section. Table 4-7 shows the reduction in the average number of FPIs needed to reach convergence when AA(TH) is replaced with AA(ϕ).

Table 4-7. Average number of required FPIs and CBC errors for different AA solutions for problems with xenon and boron updates

	w/o AA	AA1 (TH)	AA2 (TH)	AA1 (ϕ)	AA2 (ϕ)
Average # FPI	div.	15.56	15.04	9.90	9.51
CBC diff. (ppm)	-	0.10	0.28	0.10	0.09

Figure 4-19 shows that the area of no convergence when AA is not applied becomes larger respect to the previous section problems as the feedback conditions become more hostile. In addition, the application of AA(ϕ) instead of AA(TH) allows for the convergence with single digits FPI numbers when it originally needed over twenty FPIs.

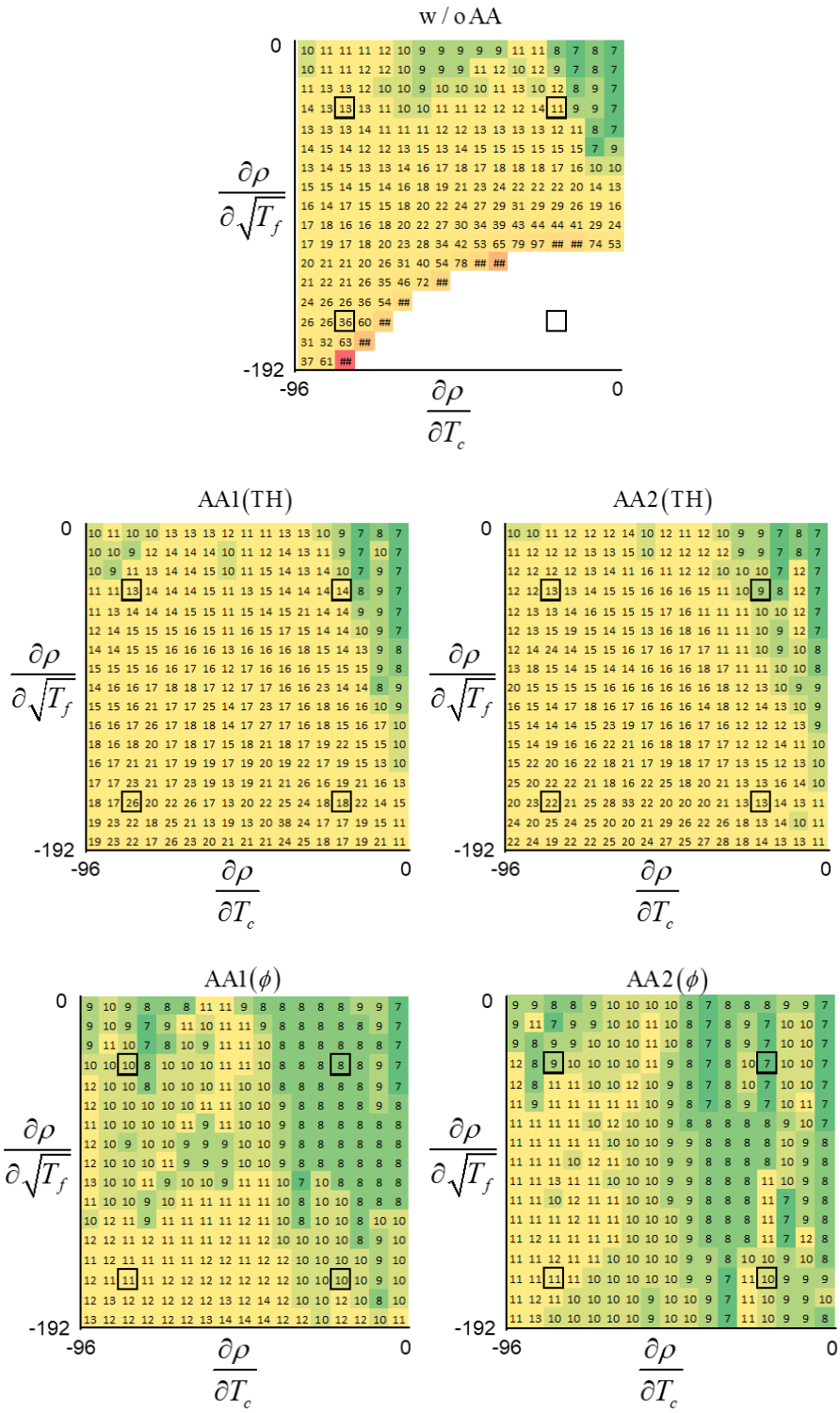

Figure 4-19. Number of FPIs required for different combinations of $\widetilde{FTC}$ and MTC and xenon and boron updates employing diverse AA solutions

The same conclusions are drawn observing Figure 4-20. Here the fission source pseudo error is presented in Figure 4-20. And the application of AA(ϕ) allows for a greater error reduction rate.

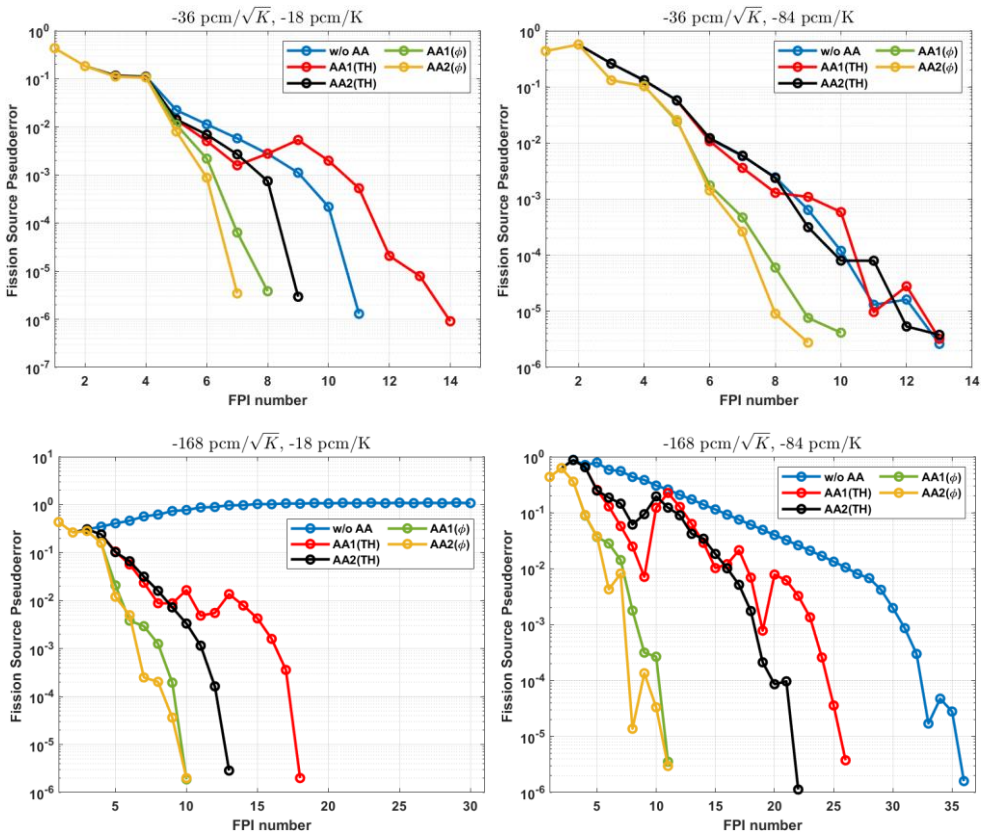

Figure 4-20. Fission source pseudo error convergence behavior for various $\widetilde{FTC}$ and MTC combinations and xenon and boron updates

As for the fission source value at a problem elevation of 110 cm presented Figure 4-21, the application of AA(ϕ) reduces the oscillations and guarantees the problem convergence in every case.

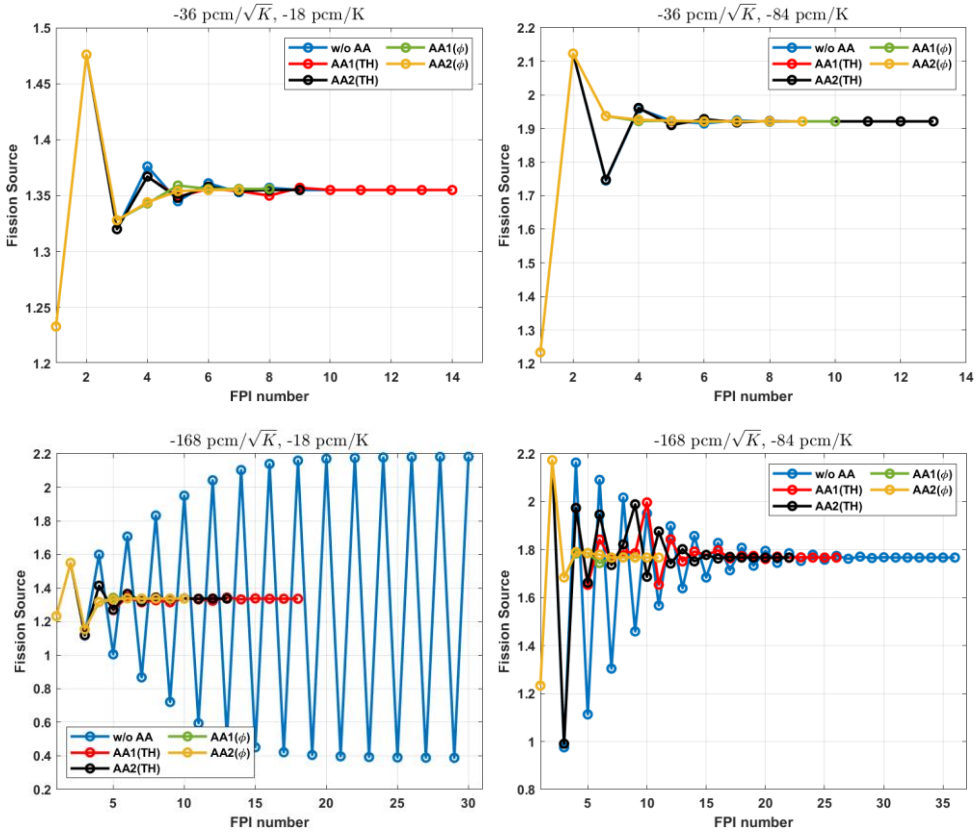

Figure 4-21. Fission source value convergence behavior at a problem elevation of 110 cm for various $\widetilde{FTC}$ and MTC combinations and xenon and boron updates

Analogously to the T/H-xenon case the AA(ϕ) at full convergence yields a number of FPIs similar to the numerically obtained optimal as shown in Figure 4-22. The AA(TH), however, shows a dangerous behavior as it becomes unpredictable at a distance from the optimal minimum.

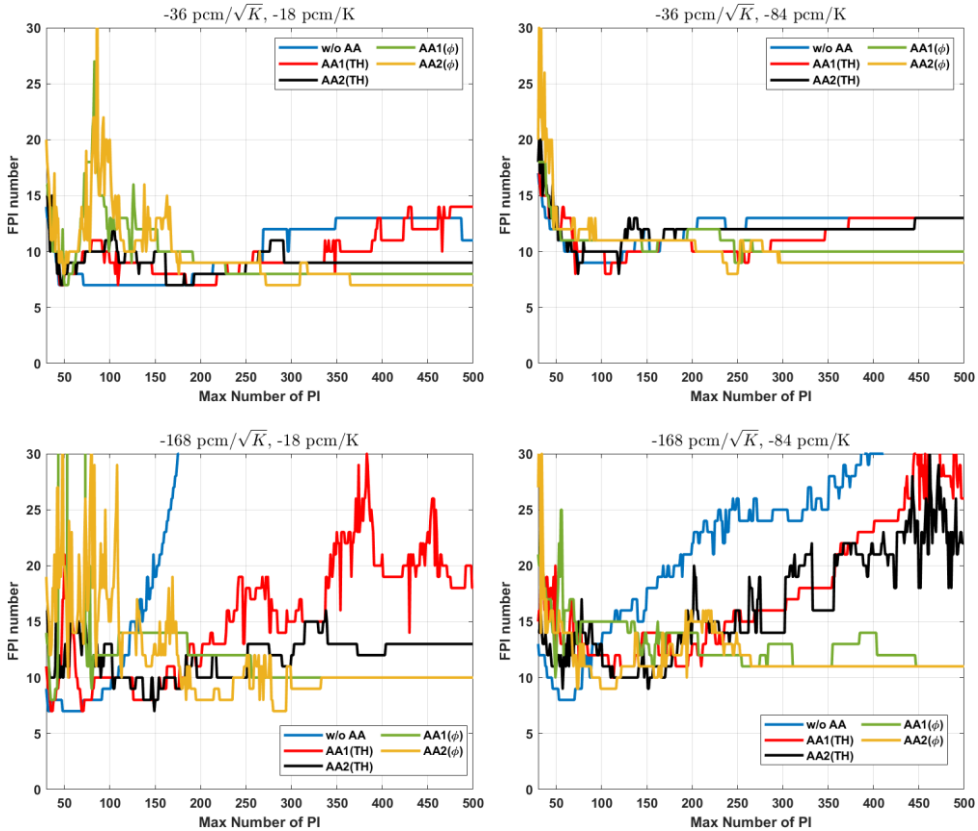

Figure 4-22. Number of FPIs required to converge given a fixed number of PIs for various $\widetilde{FTC}$ and MTC combinations and xenon update and boron updates

The oscillatory behavior of the first six iteration fission source for the four points of interest are presented from Figure 4-23 to Figure 4-26. Compared to the T/H-xenon case, the oscillations become more aggressive, and only the application of AA(ϕ) can get them under an effective control.

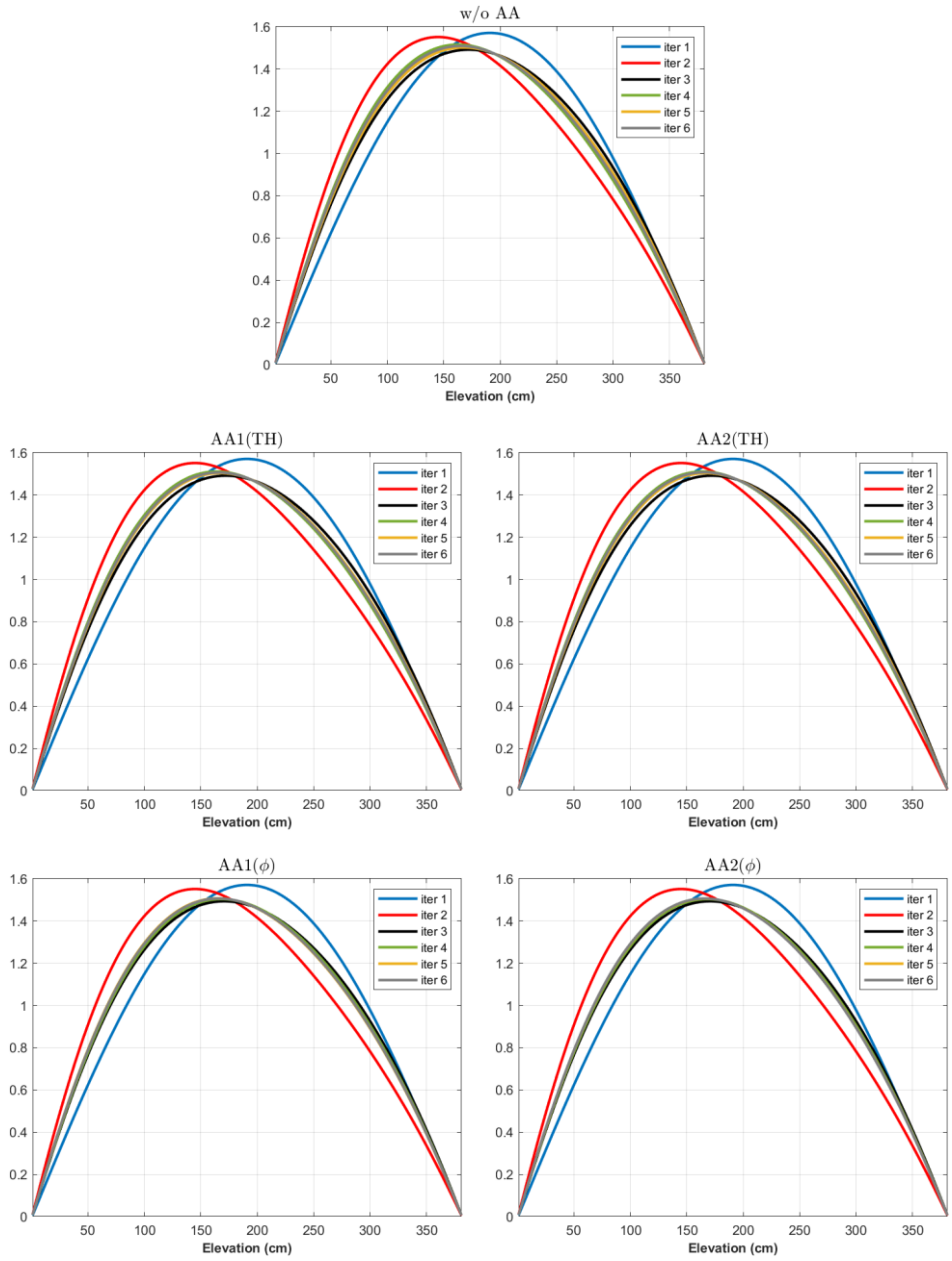

Figure 4-23. Fission source shapes for the six first iterations for $\widetilde{FTC} = -36\ pcm/\sqrt{K}$ and MTC = -18 pcm/K and xenon and boron updates

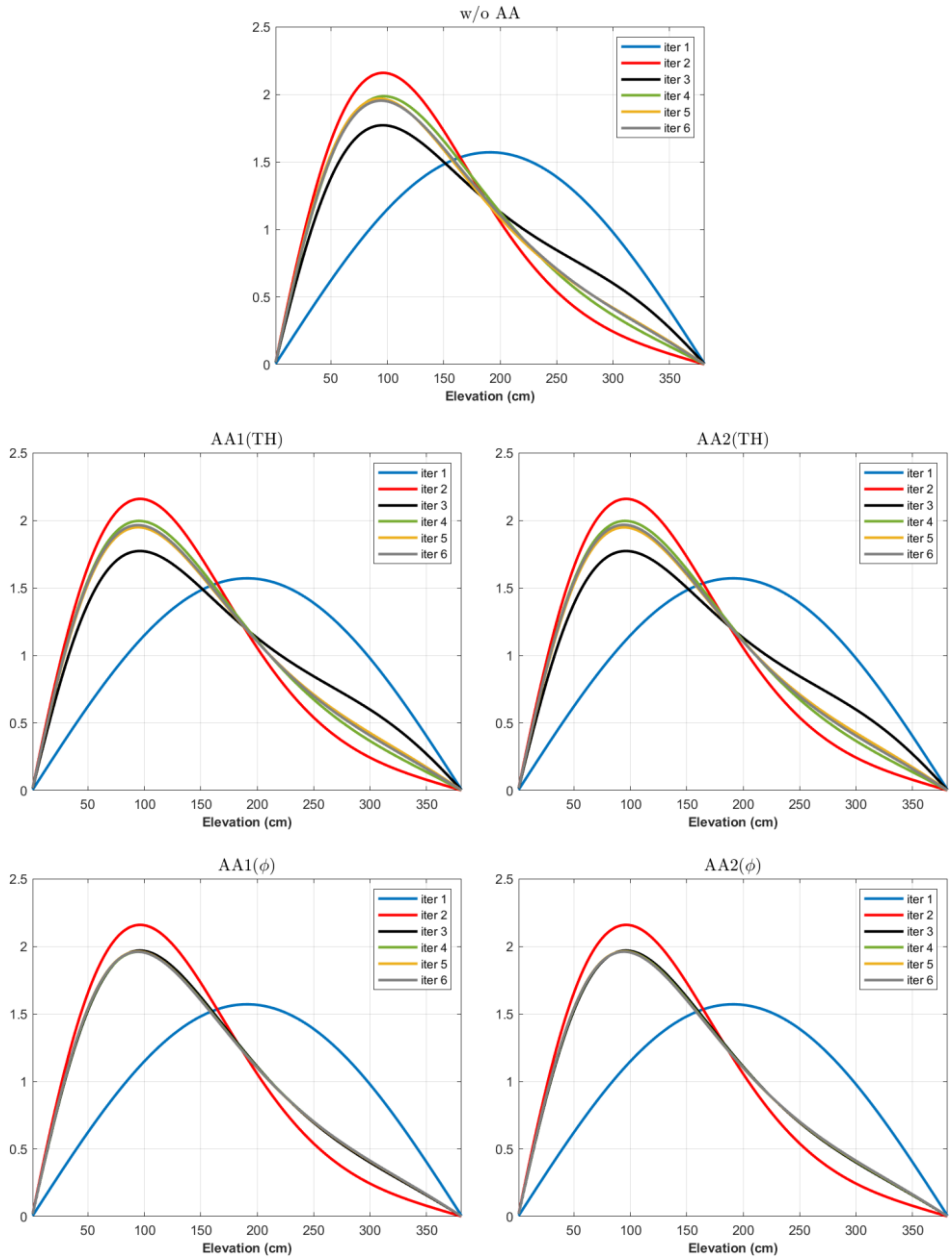

Figure 4-24. Fission source shapes for the six first iterations for $\widetilde{FTC} = -36\ pcm/\sqrt{K}$ and MTC = -84 pcm/K and xenon and boron updates

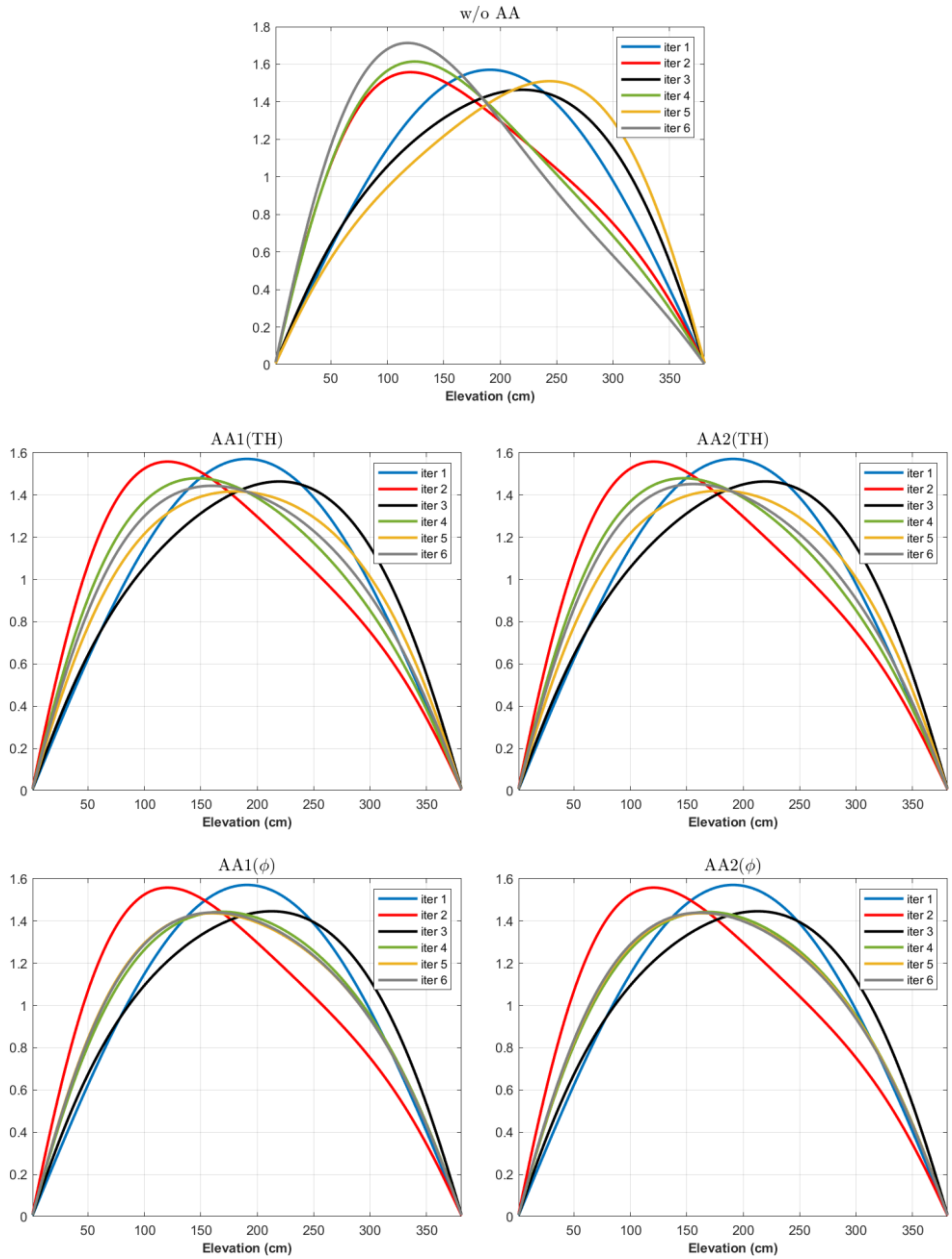

Figure 4-25. Fission source shapes for the six first iterations for $\widetilde{FTC} = -168\ pcm/\sqrt{K}$ and MTC = -18 pcm/K and xenon and boron updates

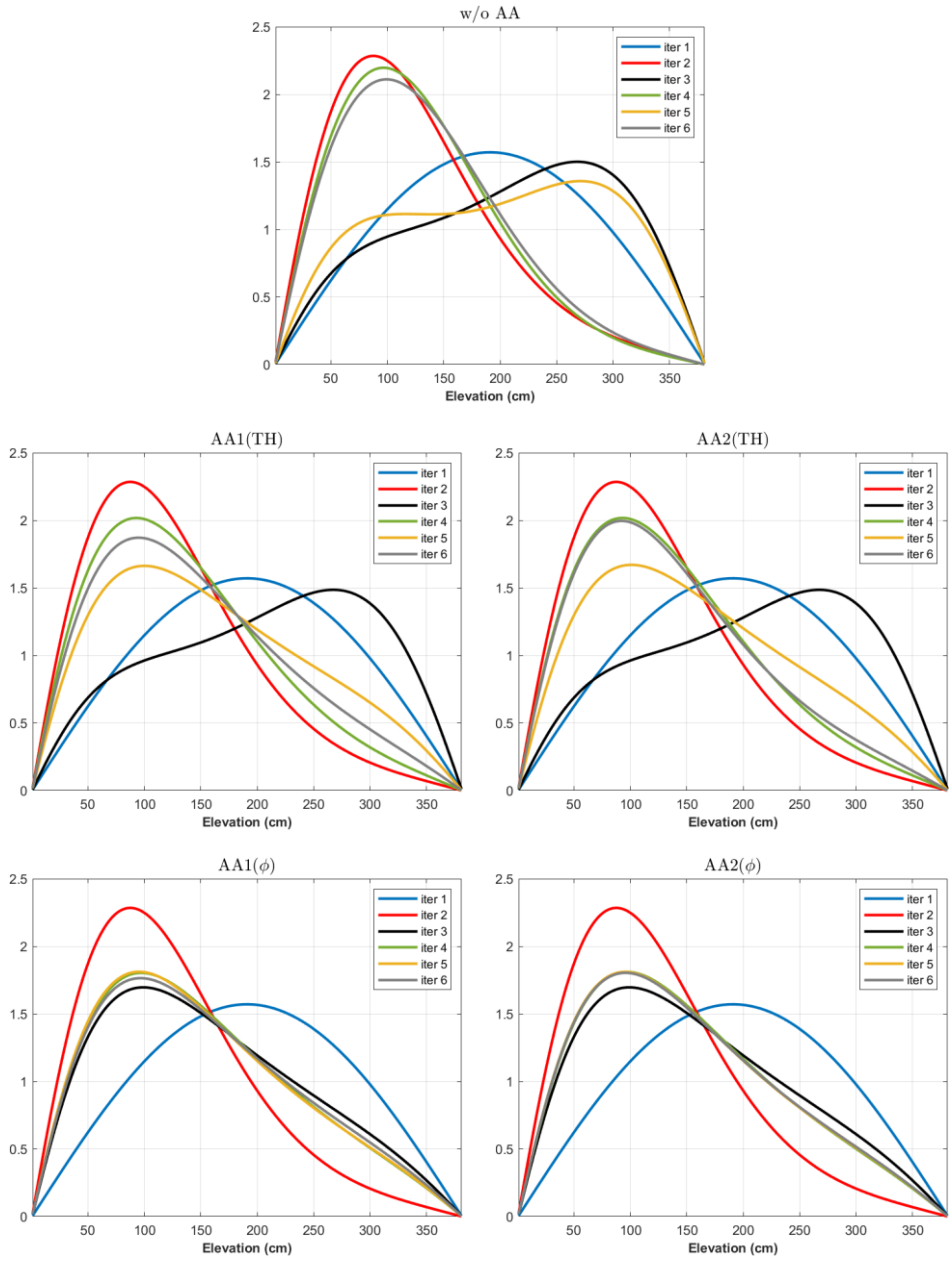

Figure 4-26. Fission source shapes for the six first iterations for $\widetilde{FTC} = -168\ pcm/\sqrt{K}$ and MTC = -84 pcm/K and xenon and boron updates

Since the calculation of the CBC does not depend directly on the flux but via the problem eigenvalue, it is interesting to check its behavior with the different AA solutions. Figure 4-27 shows this behavior for the four T/H feedback points. Here the linear increase in early iterations has been suppressed for readability. With AA(ϕ) the CBC search shows a less erratic trend avoiding big oscillations and consequently reaching the converged value faster.

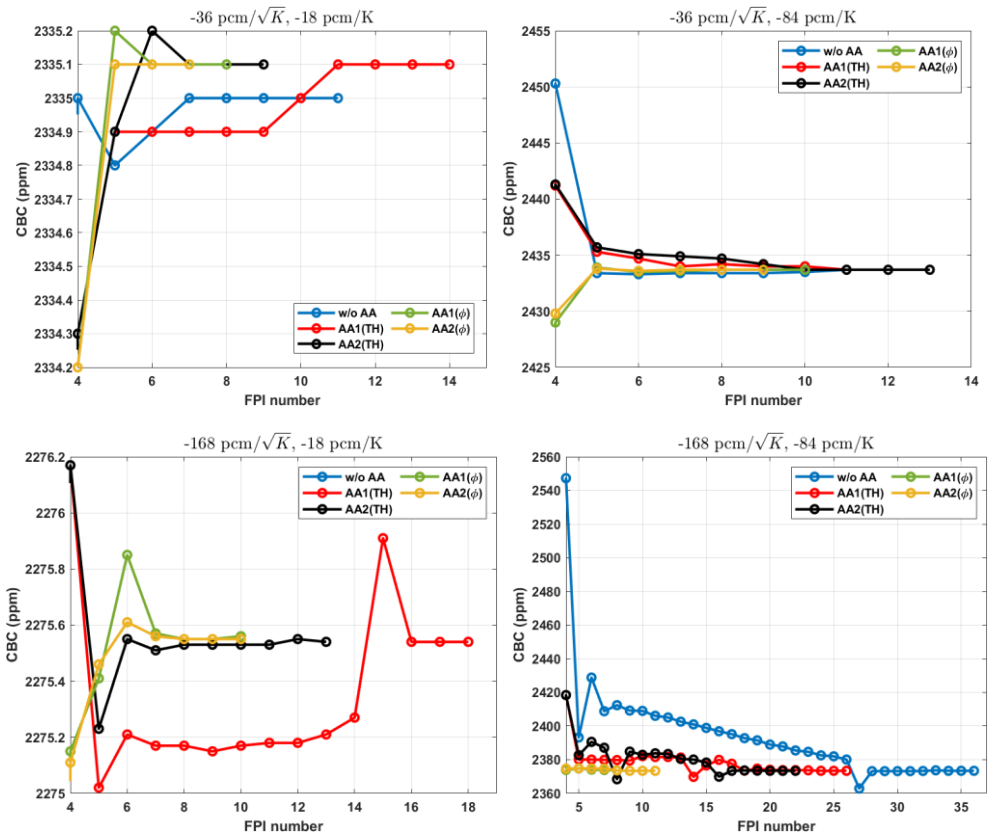

Figure 4-27. Critical Boron Concentration evolution for various $\widetilde{FTC}$ and MTC combinations and xenon and boron updates

Chapter 5. Anderson Acceleration in nTRACER

The transference of the conclusions drawn in the previous section cannot be performed straightforwardly into nTRACER. The code structure in nTRACER is much more complex than the 1G 1D problem, it includes a pin resolved MOC neutron solver with a 2D/1D strategy, a pinwise CMFD acceleration, in addition to a 47-energy group structure. The code algorithm for a steady state calculation with T/H, xenon and boron updates is given in Figure 5-1. With these considerations the application of AA(ϕ) to nTRACER is studied in this chapter by introducing the reactor physics gradually to understand how the AA change affects the calculation as it gets more complicated as the number of physics phenomena increases. Thus, first only the T/H feedbacks are applied to later introduce the xenon update and finally the boron update. The problem to carry out this study is a Checkerboard (CB56) consisting of the assemblies B3 and C0 of the APR1400 core.

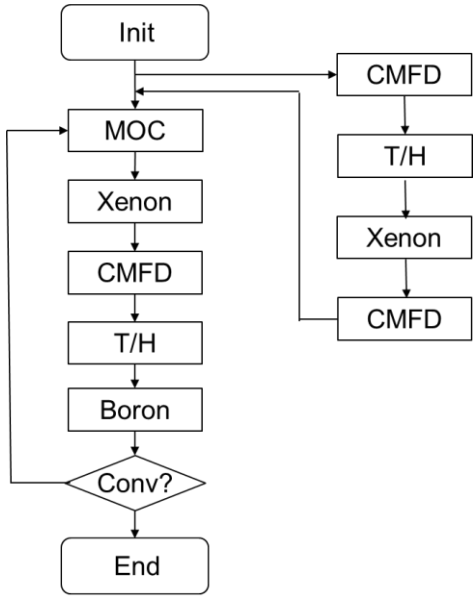

Figure 5-1. Steady state with multiphysics updates algorithm in nTRACER

After the introduction of AA(ϕ) to steady state calculations, a series of depletion calculations are simulated to test if the new AA can resolve the depletion calculation instabilities. These depletion calculations are first limited to the CB56 problem before testing it with the depletion of the APR1400 quarter core.

Then the convergence criteria of the PI in nTRACER (CMFD acceleration) is studied to optimize it. The AA(ϕ) with the newly optimized PI is tested with the APR1400 and BEAVRS benchmark depletion calculations. Finally, the modified X-2 core depletion is calculated with the nTRACER/ESCOT system of codes and the AA(ϕ) with the optimized PI to show its competitiveness to perform a VVER depletion calculation.

5.1. Checkerboard Calculations

In this section the AA(ϕ) is applied to a CB56 neutronics-T/H (-xenon-boron) problem and the results compared with the original AA(TH). The calculations consist of a series of steady state and depletion problems. The flux group structure is also analyzed to reduce the memory needs for the application and storage of the AA(ϕ).

5.1.1. Checkerboard steady state calculations

Table 5-1 contains the results for Steady State calculations of the CB56 problem with only the T/H update, they demonstrate that the AA(TH) and AA(ϕ) yield similar results as expected in this case. Note that, as pointed out with the 1G 1D problem, the application of AA(ϕ) do not affect only the power with which the T/H variables are calculated but also affects the initial source at the next FPI MOC calculation. As the MOC sweep is performed for a fixed number of iterations in nTRACER, the flux solution after the MOC calculation is also altered.

Table 5-1. Average number of required FPIs and k_{eff} errors for different AA solutions for the CB56 problem with T/H update

	w/o AA	AA1 (TH)	AA2 (TH)	AA1 (ϕ)	AA2 (ϕ)
# FPI	7	8	6	6	6
keff	1.10604	1.10606	1.10605	1.10610	1.10606
dkeff (pcm)	-	-2	-1	-6	-2

Table 5-2 shows the number of FPIs required for the CB56 problem to converge when both T/H and xenon updates are included. Note that the algorithm structure of nTRACER (see Figure 5-1) offers a "natural" protection against flux oscillations in these multiphysics problems. Since the xenon equilibrium is applied between the MOC and the CMFD solutions, the flux output from the PI (with which the T/H calculation is performed) is already soften. This way, the xenon and fuel temperature distributions tend to compensate each other. This, nonetheless, is not enough to suppress the oscillatory behavior in every case as will be shown later.

Table 5-2. Average number of required FPIs and k_{eff} errors (from the average value) for different AA solutions for the CB56 problem with T/H and xenon updates

	w/o AA	AA1 (TH)	AA2 (TH)	AA1 (ϕ)	AA2 (ϕ)
# FPI	div	7	7	7	7
keff	-	1.07405	1.07405	1.07402	1.07406
dkeff (pcm)	-	1.36	1.36	4.36	0.36

In Table 5-3 the results when the CBC search is included in the multiphysics problem are given. Although the necessary number of FPIs with AA(ϕ) is inferior to the AA(TH) case, the reduction is not remarkable as the xenon-fuel temperature is a dominant effect and the code structure together with AA(TH) is enough to offer a reasonably good performance.

Table 5-3. Average number of required FPIs and CBC errors for different AA solutions for the CB56 problem with T/H, xenon and boron updates

	w/o AA	AA1 (TH)	AA2 (TH)	AA1 (ϕ)	AA2 (ϕ)
# FPI	19	9	10	8	9
CBC	1815.58	1815.52	1815.56	1815.47	1815.63
CBC (ppm)	-	0.06	0.02	0.11	-0.05

Prior to the tests with depletion calculations the number of energy groups of the neutron flux that undergoes the AA needs to be addressed. The 47 energy groups structure is reasonable for small problems like a CB but for full core calculations the memory requirements are too demanding, especially if the AA depth is greater than one. For this reason, a group condensation to 2 groups and 1 group are proposed for the AA application. Thus, after the CMFD problem is finished the flux is collapsed to a few-group structure. Once the AA(ϕ) is completed, the 47-group flux is reconstructed.

Table 5-4, Table 5-5 and Table 5-6 show that the results with the few-groups energy structure hold their respective 47-group counterparts of Table 5-1, Table 5-2 and Table 5-3 with little to no difference in either the number of FPIs or eigenvalue (or CBC) results.

This being said, the two-group structure is preferred over the one group as it possesses a greater physical meaning. On the one hand, the fast-to-thermal ratio is about 3.5 in thermal reactors and, therefore, it makes sense to treat the thermal and fast fluxes independently and not in a lumped manner. On the other hand, the impact of the feedback physics is greater, generally, in the thermal region. These two arguments are backed by the thermal and fast fluxes depicted in Figure 5-2. The two-group structure is employed from this point on.

Table 5-4. Average number of required FPIs and k_{eff} errors for different AA solutions applied to a few group fluxes for the CB56 problem with T/H update

	AA1 (ϕ)-1G	AA2 (ϕ)-1G	AA1 (ϕ)-2G	AA2 (ϕ)-2G
# FPI	7 (+1)	6 (0)	7 (+1)	6 (0)
keff	1.1061	1.10605	1.1061	1.10606
dkeff (pcm)	-6	-1	-6	-2

Table 5-5. Average number of required FPIs and k_{eff} errors for different AA solutions applied to a few group fluxes for the CB56 problem with T/H and xenon updates

	AA1 (ϕ)-1G	AA2 (ϕ)-1G	AA1 (ϕ)-2G	AA2 (ϕ)-2G
# FPI	9 (+2)	7 (0)	7 (0)	7 (0)
keff	1.07408	1.07405	1.07402	1.07406
dkeff (pcm)	-1.64	1.36	4.36	0.36

Table 5-6. Average number of required FPIs and CBC errors for different AA solutions applied to a few group fluxes for the CB problem with T/H, xenon and boron updates

	AA1 (ϕ)-1G	AA2 (ϕ)-1G	AA1 (ϕ)-2G	AA2 (ϕ)-2G
# FPI	8 (0)	8 (-1)	8 (0)	8 (-1)
CBC	1815.67	1815.53	1815.5	1815.62
CBC (ppm)	-0.09	0.05	0.08	-0.04

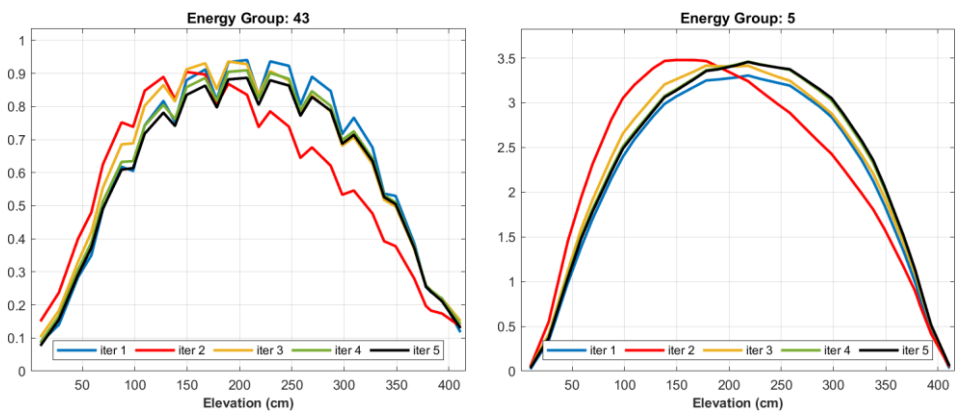

Figure 5-2. Flux axial distribution after the first five PIs for a thermal (43) and fast (5) energy groups in the CB56 multiphysics problem

The AA(ϕ) does not show a significant improvement with respect to AA(TH) performance for the steady state cases studied so far. The consequent step is the comparison for depletion calculations, for which the AA(TH) has been demonstrated to not be enough to solve the convergence issues.

5.1.2. Checkerboard depletion calculations

The CB56 problem depletion calculation is performed. At each step (including the initial steady state calculation) the CBC search is performed together with the T/H and xenon equilibrium updates. The AA(TH) and AA(ϕ) are compared for depths one and two.

Figure 5-3 and Figure 5-4 show that AA1(TH) and AA2(TH) fail to converge at 14 MWd/kgHM and 13 MWd/kgHM, respectively. AA(ϕ), however, manages to converge for both of the AA storage depths studied. This being said a depth of one yields a better performance overall. The AA(ϕ) is effectively able to stabilize the calculations by guaranteeing the convergence of every burnup step.

Giving a closer look at the power axial behavior at 14 MWd/kgHM burn-up step for AA1(TH) and AA1(ϕ), which are given in Figure 5-5, it is corroborated how AA1(ϕ) reduces the oscillatory significantly and at a greater rate than AA1(TH). It can be seen how the axial power change between iterations four, five and six is negligible for AA1(ϕ) while it is persistent for AA1(TH). This difference in the oscillatory behavior transforms into a faster fission source pseudoerror reduction as shown in Figure 5-6.

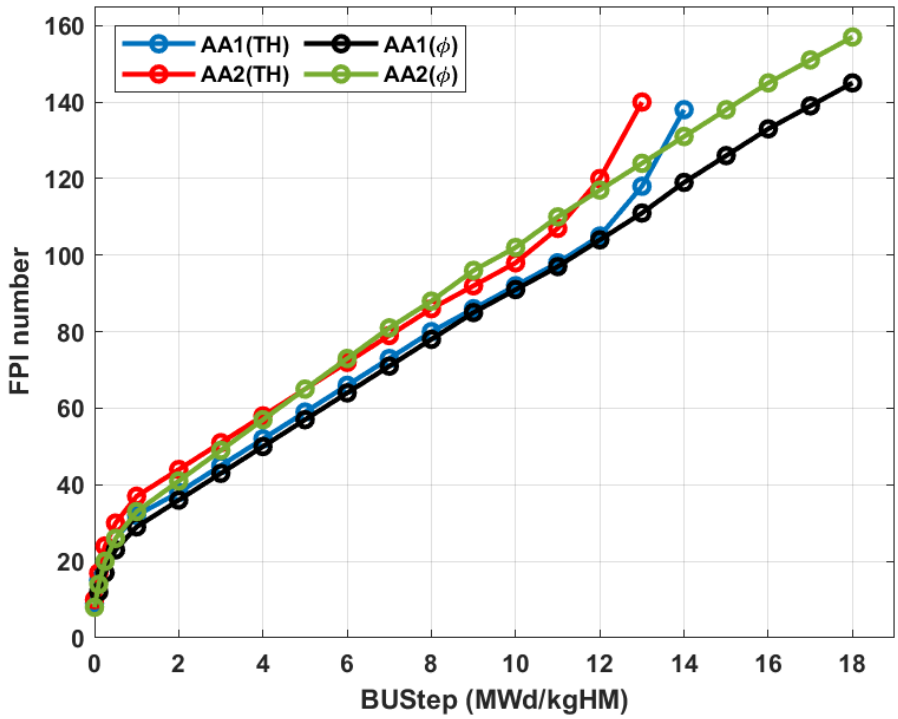

Figure 5-3. Cumulative number of FPIs for the APR1400 based CB56 depletion calculation with AA(TH) and AA(ϕ)

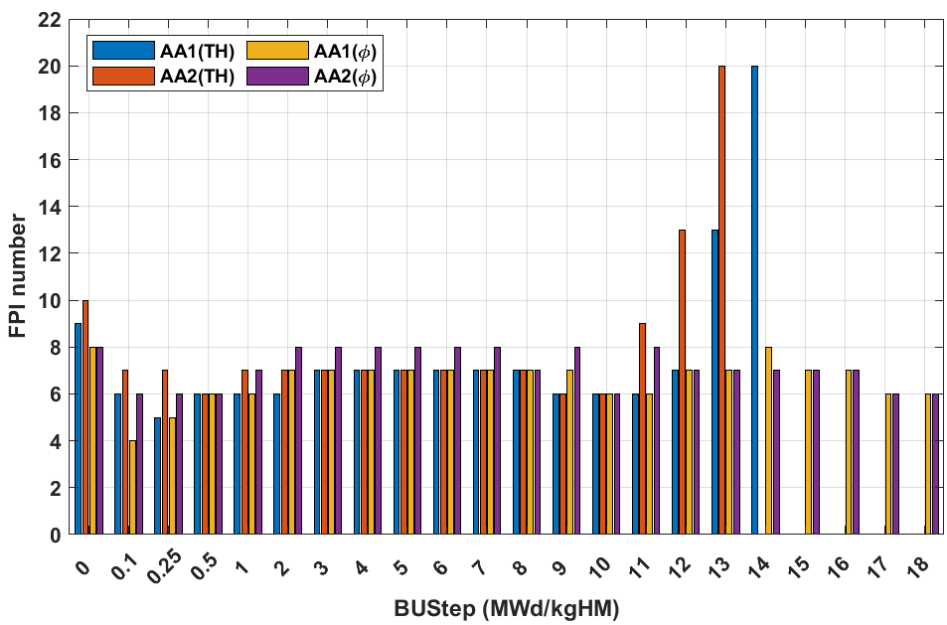

Figure 5-4. Burn-up stepwise number of FPIs for the APR1400 based CB56 depletion calculation with AA(TH) and AA(ϕ)

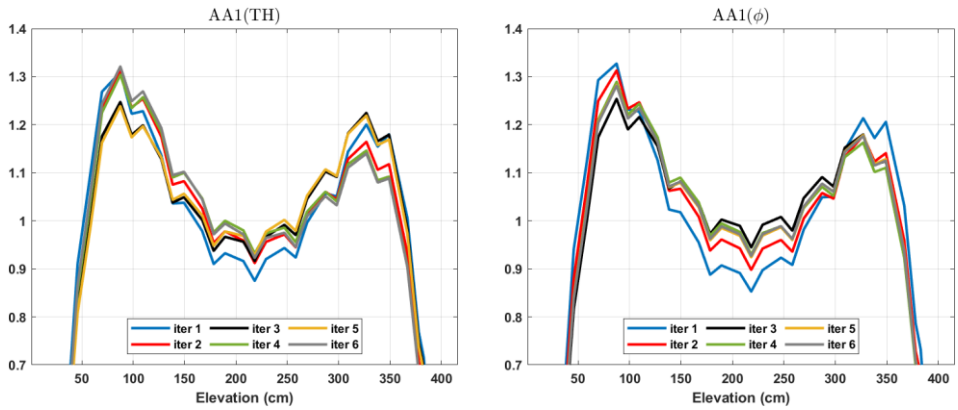

Figure 5-5. Power axial distributions at the first six FPIs for the CB56 problem at the burn-up step 14 MWd/kgHM for AA1(TH) and AA1(ϕ)

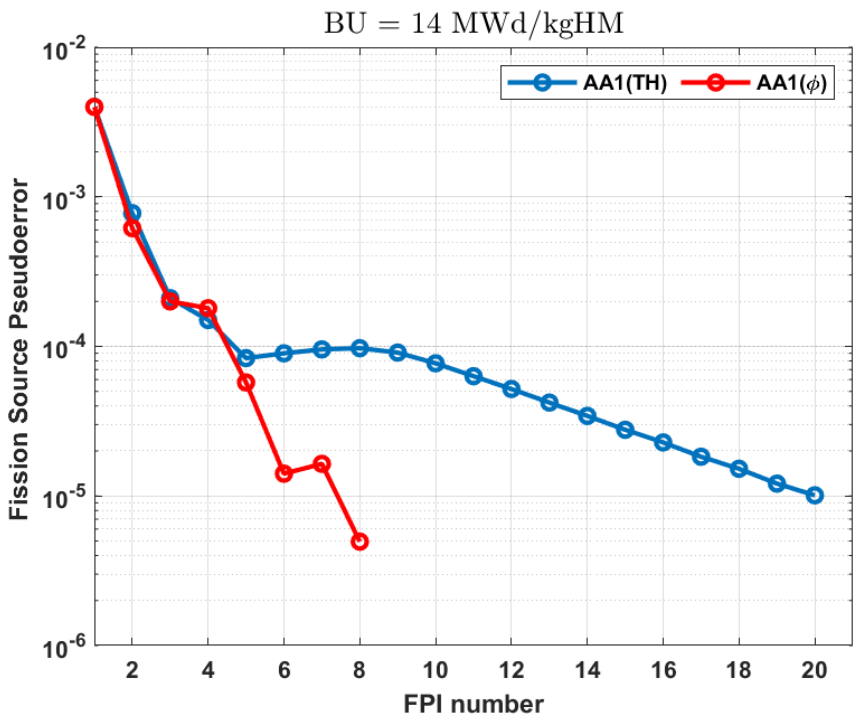

Figure 5-6. FPI fission source pseudoerror for the CB56 problem at the burn-Up step 14 MWd/kgHM for AA(TH) and AA(ϕ)

The non-convergence calculation at 14 MWd/kgHM could be avoided by reducing the burn-up step size. Thus, Figure 5-7 and Figure 5-8 show the calculation between 13 and 14 MWd/kgHM steps with the original 1 MWd/kgHM size and a shorter one with 0.1 MWd/kgHM. With the shorter step size every step manages to converge, nevertheless the cumulative number of required FPIs makes it prohibitive to employ such a short step and consequently the newly proposed AA(ϕ) is indispensable.

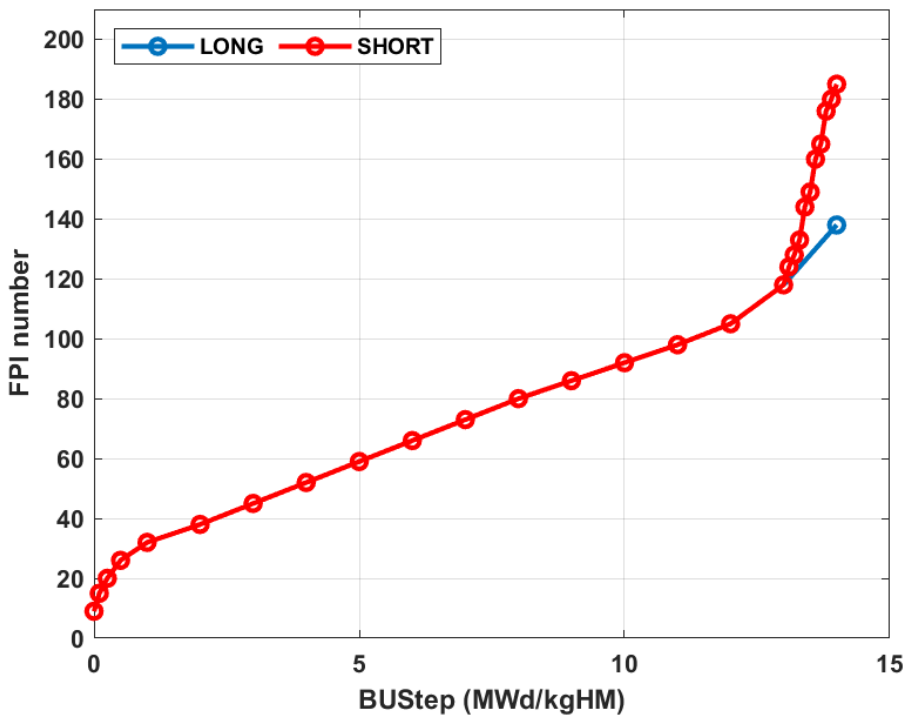

Figure 5-7. Cumulative number of FPIs for the APR1400 based CB56 depletion calculation with long and short burn-up step sizes from 13 to 14 MWd/kgHM

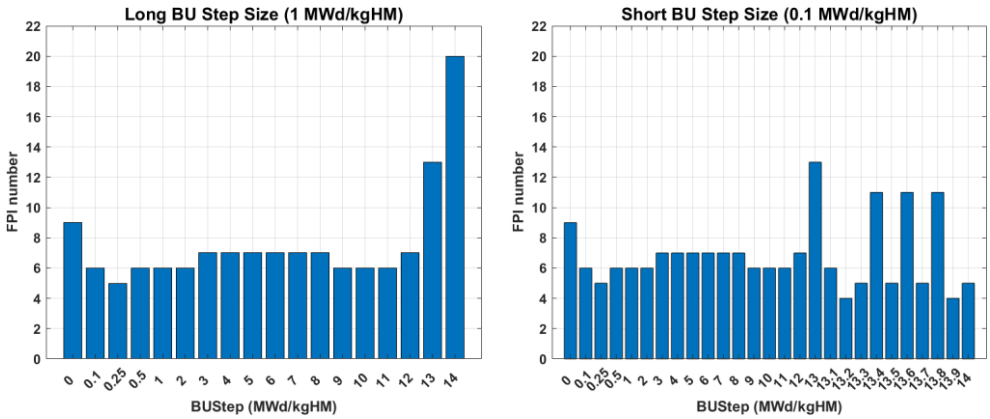

Figure 5-8. Burn-up stepwise number of FPIs for the APR1400 based CB56 depletion calculation with long and short burn-up step sizes from 13 to 14 MWd/kgHM

Figure 5-9 shows a comparative of the fission power axial distributions at different burn-up steps. It is obvious that the shape evolution in the short step case is much more gradual. This gradualism allows the convergence because the initial and final distributions are closer. The convergence, however, should be reached independently of the initial distribution.

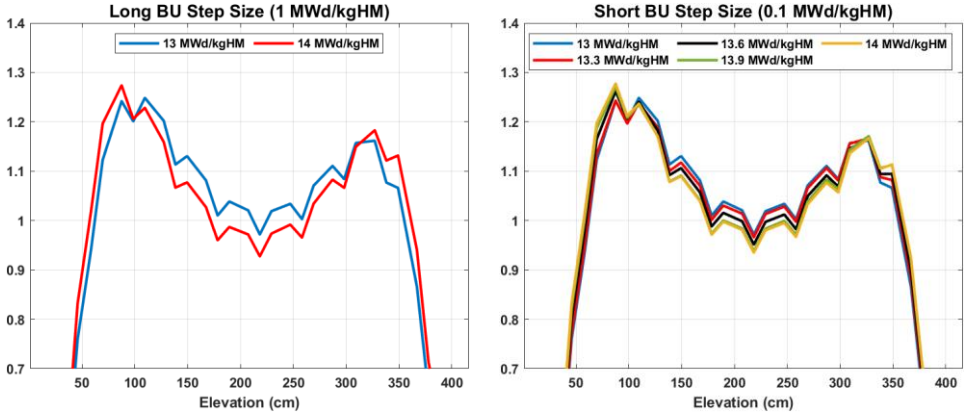

Figure 5-9. Power axial distributions at different burn-up steps with long and short burn-up step sizes from 13 to 14 MWd/kgHM

Figure 5-10, for its part, depicts the different power axial distributions reached with the two step sizes at 14 MWd/kgHM. The use of coarse step sizes allows a faster

calculation at the expense of a poorer accuracy, so I balance between time-accuracy is needed.

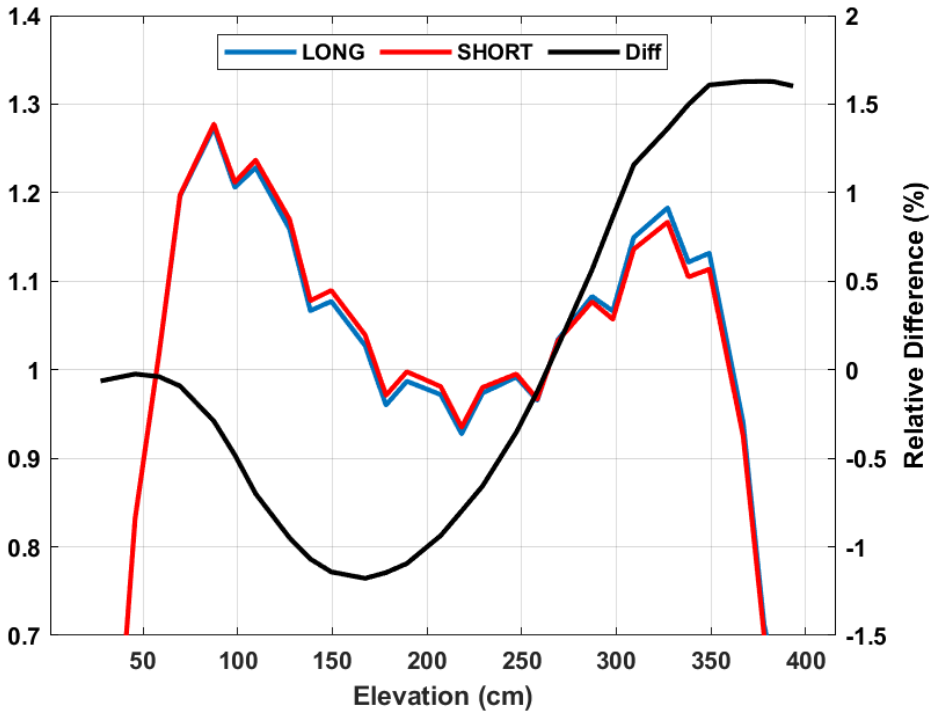

Figure 5-10. Power axial distributions for the CB56 problem at 14 MWd/kgHM for calculations with long and short burn-up step sizes from 13 to 14 MWd/kgHM

5.2. Optimization of the Core Depletion

The AA(ϕ) is finally applied to the APR1400 core depletion calculation in this section. Besides, intrinsic disadvantage of the convergence criterion set for the PI convergence in nTRACER (the residual reduction ratio) is presented and an alternative is presented to improve the overall convergence behavior of the calculation.

5.2.1. Core depletion calculation

Figure 5-11 shows how the new AA(ϕ) manages to avoid the non-convergent behavior of the AA(TH). As a matter of fact, it can complete the depletion cycle with a fairly constant number for the necessary FPIs per state point, as shown Figure 5-12.

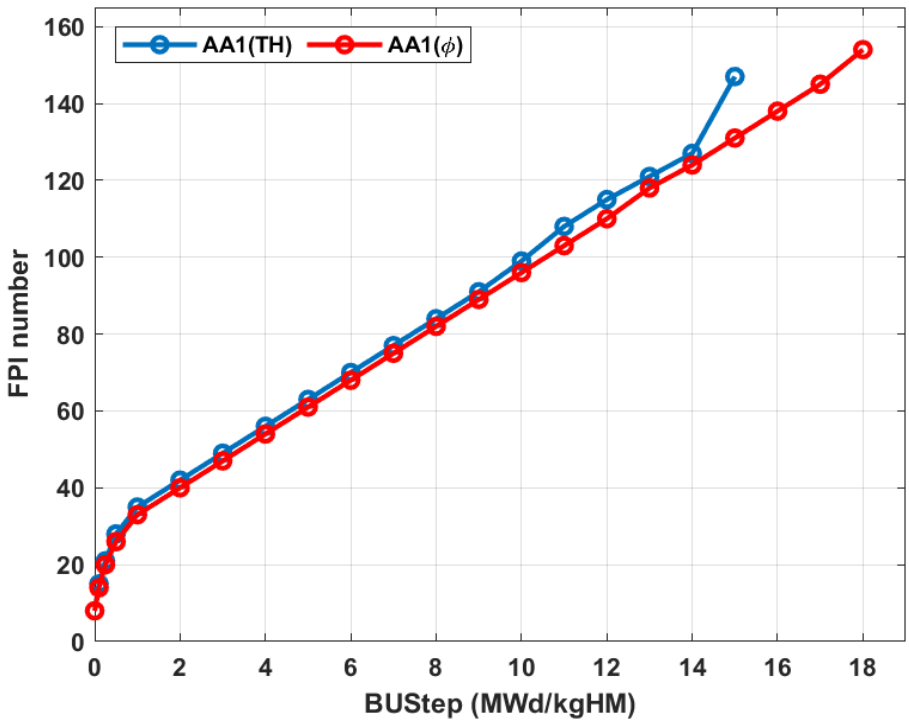

Figure 5-11. Cumulative number of FPIs for the APR1400 quarter core depletion calculation with AA(TH) and AA(ϕ)

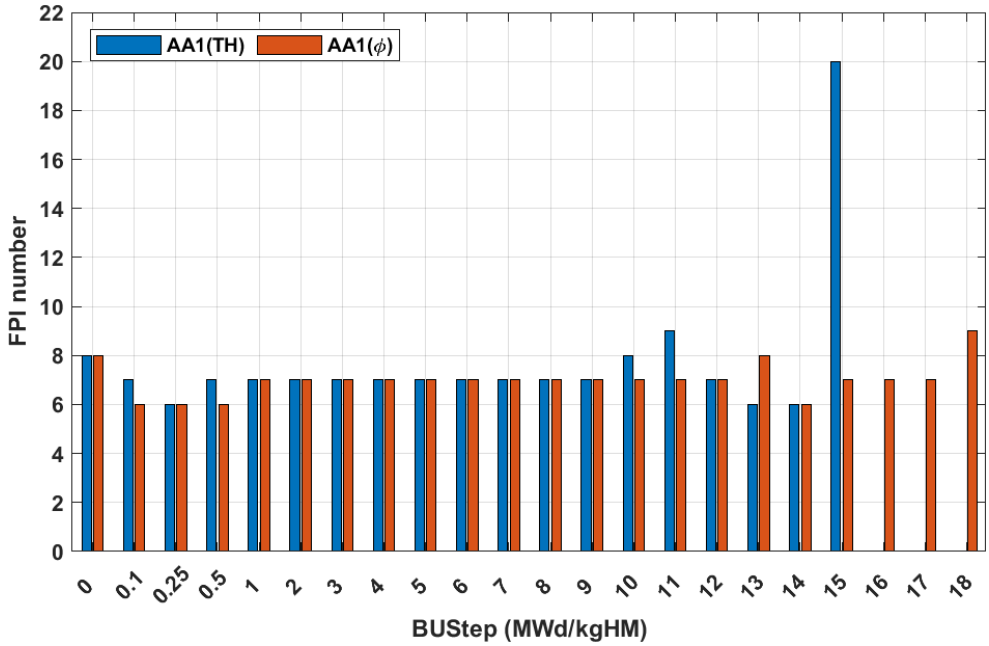

Figure 5-12. Burn-Up stepwise number of FPIs for the APR1400 full core depletion calculation with AA(TH) and AA(ϕ)

Note that in general terms the AA(TH) does not show a great difference when compared to AA(ϕ) in the number of FPIs (in the state points for which AA(TH) reaches convergence). This indicates that, for certain core configurations, and given the algorithm structure in nTRACER, the use of AA(TH) is quite competent at offering a reasonably good convergence. This being said, it is also obvious that AA(TH) is not trustworthy in every case and thereby AA(ϕ) must be adopted.

5.2.2. Study of the power iteration convergence criteria in nTRACER

The convergence criterion imposed in nTRACER to monitor the convergence of the CMFD acceleration calculation is the reduction of the residual ratio, which is the ratio between the residual at the present iteration and the initial residual at the first iteration and is expressed as

$$\varepsilon_r = \frac{r_k}{r_0}, \tag{5.1}$$

where r_k is the residual value at the present iteration, r_0 at the initial iteration and ε default value in nTRACER is 0.1.

The residual reduction ratio has an intrinsic limitation. While it guarantees a rapid convergence at early stages of the calculation when the solution is far from convergence, it really complicates the PI escape at late FPIs. In other words, it forces the problem sweep for a greater number of PIs when the solution is converged and the change between iterations is almost nonexistent and consequently the residual reduction ratio barely changes. This implies a greater number of CMFD calculations, which in a depletion calculation constitute a good portion of calculation time.

In order to inspect the effect of the convergence criterion employed to monitor the PI convergence, the 1G 1D of the previous chapter is retrieved here. In it only the T/H feedbacks, $\widetilde{FTC} = -168\, pcm/\sqrt{K}$ and MTC = -84 pcm/K , are employed and no AA is applied. The problem is simulated with different PI convergence criteria, namely the residual reduction set at 2 10^{-6}, the residual reduction ratio set at 0.05, the fission source pseudoerror reduction defined as

$$\tilde{\varepsilon}_\psi = \frac{\|\psi_k - \psi_{k-1}\|}{\|\psi_k\|}, \tag{5.2}$$

set at 2 10^{-6} and the fission source pseudoerror reduction ratio given

$$\varepsilon_\psi = \frac{\tilde{\varepsilon}_{\psi,k}}{\tilde{\varepsilon}_{\psi,0}}, \tag{5.3}$$

set at 0.05.

Figure 5-13a shows the fission source value at an elevation of 110 cm. It can be observed how the use of reduction ratios, especially in the case of the residual ratio,

reduces the oscillation at early FPIs when the problem is far from convergence. Besides, at these early stages the AA does any effect on the result as there is no information stored yet. In addition, Figure 5-13b shows that the ratios required less iterations at early FPIs while the error and residual reduction required PIs plummet at later PI calls.

This behavior is coherent with Figure 5-13c and Figure 5-13e. As previously explained, at late iterative steps the ratios have more difficulties to converge because the residual and the fission source pseudo error barely change (changes below 10^{-6} for most of the calculation), this means that the PI keeps updating the result although it is already clearly converged.

Figure 5-13d and Figure 5-13f in contrast show that the ratios yield a very tight value at early FPIs but suffer a sharp increase at late FPIs if the residual and the pseudoerror are employed as a convergence criterion.

This way a change in the nTRACER CMFD convergence criterion is proposed to avoid these late FPIs waste of iterations. With this purpose a combination of the residual reduction ratio at early iterations and of the residual at late FPIs is intended. Thus, the residual ratio at 0.1 is kept but his is combined with a maximum residual value of 10^{-5}. Note that the objective pursued with this change is not the reduction of FPIs but the save of unnecessary CMFD iterations.

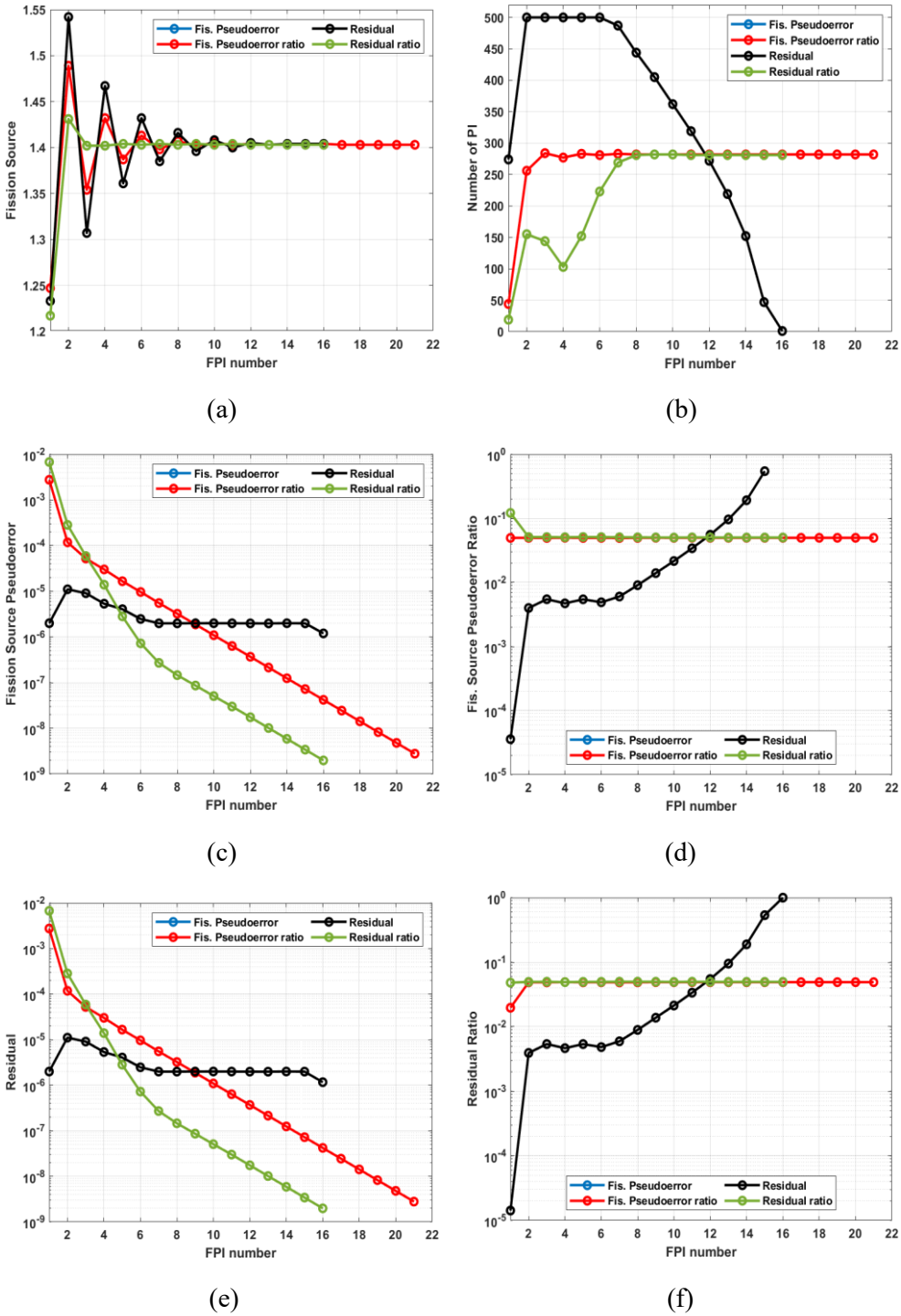

Figure 5-13. FPI evolution of diverse PI variables for different PI convergence criteria for the 1G 1D neutronics-T/H problem w/o AA and $\widetilde{FTC} = -168\ pcm/\sqrt{K}$ and MTC = -84 pcm/K

Before applying the converge criterion change, this is studied with the 1G 1D problem for the multiphysics calculations of the previous chapter with the different AA applications. The results summarized in Table 5-7 allows to draw a series of conclusions for the criterion change. First, for the case without AA application, the new convergence criterion yields the best convergence. The same applies for the AA(TH) case, particularly as the physics of the problem become more complex.

For AA(ϕ), however, no improvement is observed with the new criterion, although it does not show a worsening with respect to the original residual criterion (equivalent to the fission source pseudoerror as shown in Figure 5-13) either and still improves the results of AA(TH). In any case, although the AA(ϕ) does not see its results improved, the aim of the change was mainly the reduction of PIs and therefore it represents the best option for the PI criterion.

Table 5-7. Average number of required FPIs for different physics and convergence PI criteria for the 1G 1D problem

	T/H			T/H-xenon			T/H-xenon-boron		
	ε_r	r	ε_r+r	ε_r	r	ε_r+r	ε_r	r	ε_r+r
w/o AA	11.6	9.3	8.5	38.2	28.1	23.4	39.0	28.8	22.6
AA1(TH)	8.9	7.6	7.5	17.7	14.2	12.2	18.1	15.6	13.7
AA2(TH)	8.4	7.1	7.0	16.9	14.1	11.9	17.0	15.0	13.2
AA1(ϕ)	8.8	7.1	7.3	11.3	9.2	9.0	12.1	9.9	10.0
AA2(ϕ)	8.3	6.8	7.2	9.5	7.8	7.7	11.1	9.5	9.8

The convergence criterion change is now applied to nTRACER and the APR1400 quarter core depletion calculation is performed. Figure 5-14 shows that the new criterion manages to reduce the number of total FPIs substantially. Figure 5-15 reflects how the reduction of FPIs takes place mainly in the late state points. Figure 5-16 shows that the total time has decreased, although percentagewise the FPI time remains fairly constant while the CMFD time has experienced a reduction from 24 % to 21 %.

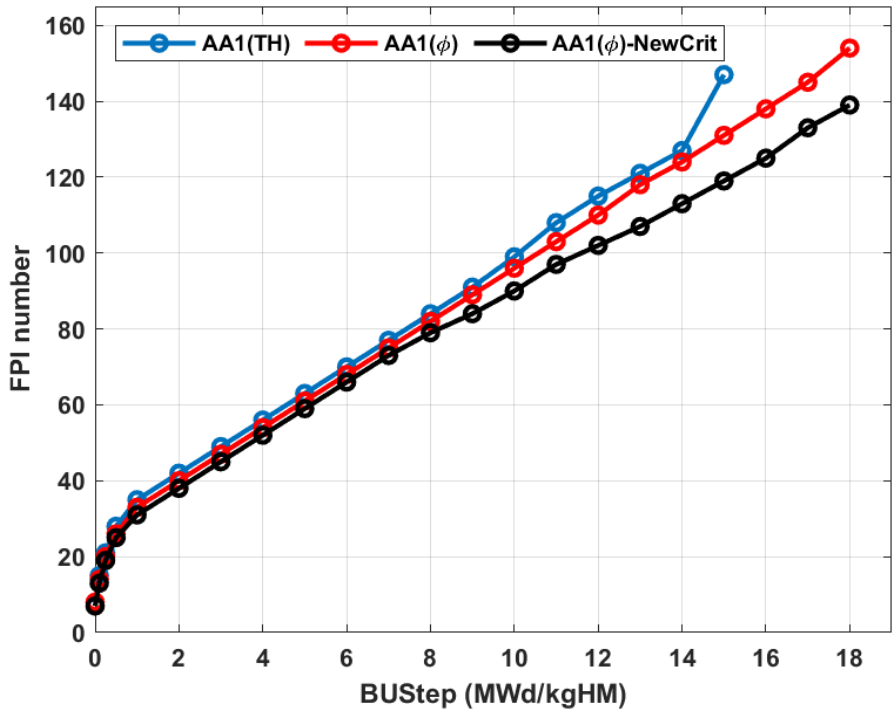

Figure 5-14. Cumulative FPIs for the APR1400 full core depletion calculation with AA(TH) and AA(ϕ) with the old and the new PI convergence criteria

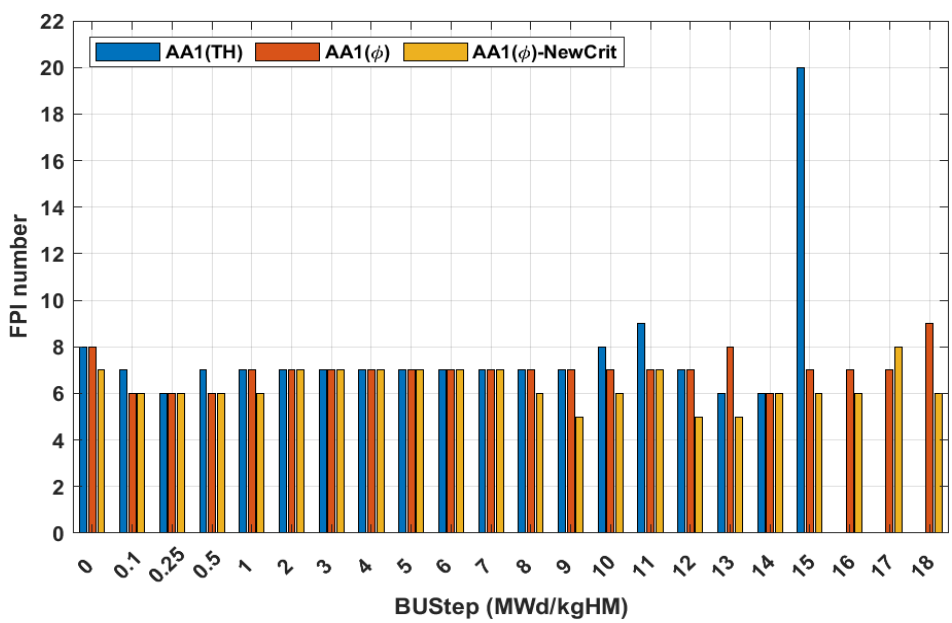

Figure 5-15. Burn-Up stepwise number of FPIs for the APR1400 full core depletion calculation with AA(TH) and AA(ϕ) with the old and the new PI convergence criteria

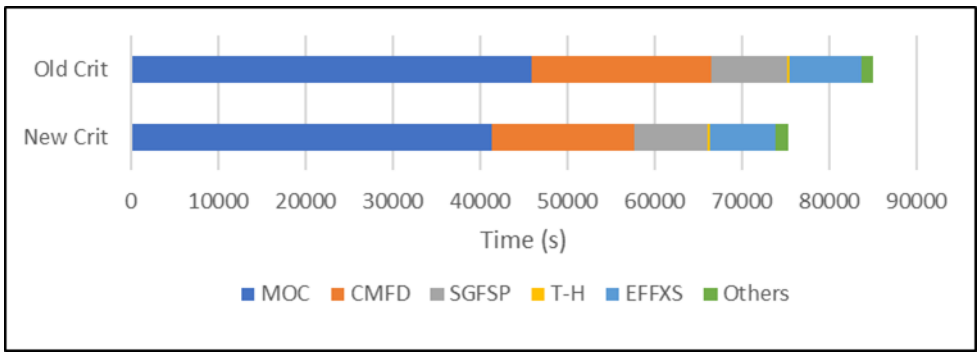

Figure 5-16. Computing time required by each calculation process for the old and new PI criteria for the AA(ϕ) application to the APR1400 quarter core depletion calculation

The new changes are tested with a different problem. For this, the BEAVRS benchmark quarter core model is considered. As shown in Figure 5-17 and Figure 5-18, the AA1(TH) with the old criterion can barely solve beyond the first three burn-up steps. The AA1(ϕ) with the new criterion can successfully complete the cycle.

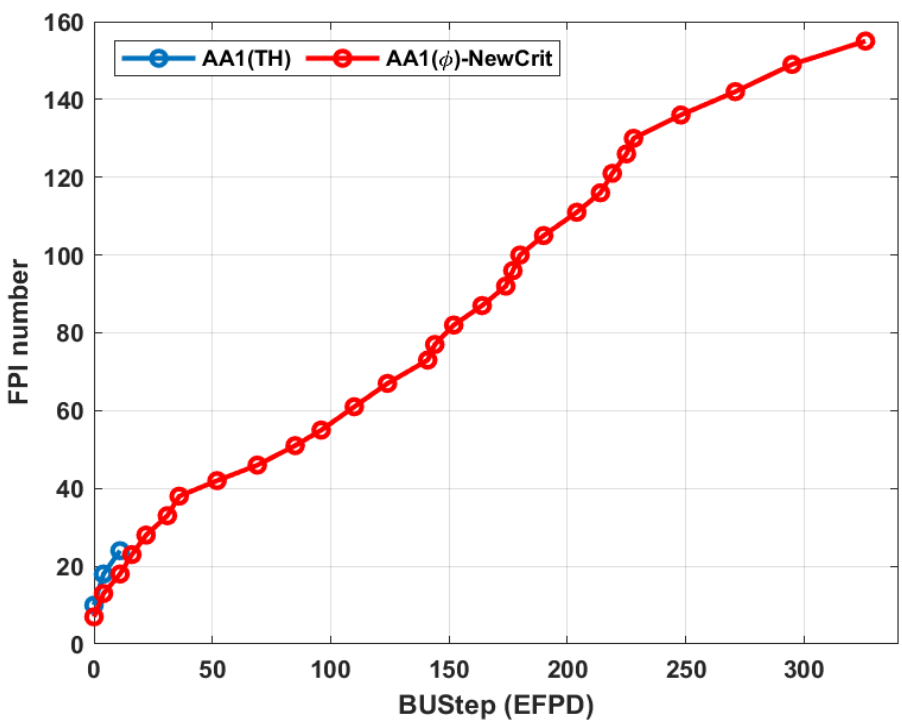

Figure 5-17. Cumulative number of FPIs for the BEAVRS quarter core depletion calculation with the AA(TH) and AA(ϕ) with the new PI convergence criteria

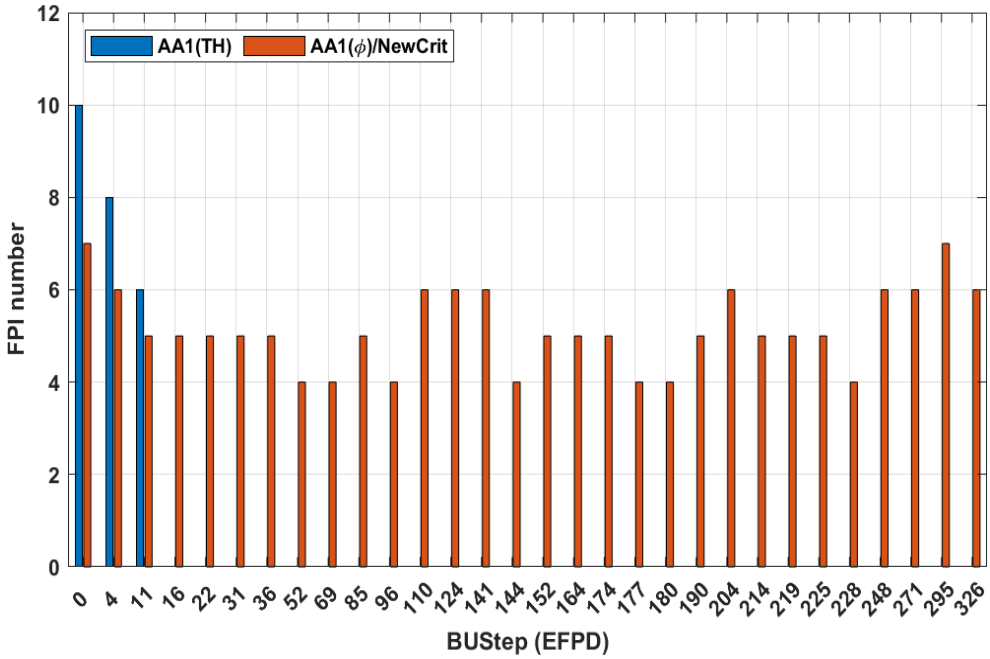

Figure 5-18. Burn-Up stepwise number of FPIs for the BEAVRS quarter core depletion calculation with the AA(TH) and AA(ϕ) with the new PI convergence criteria

5.3. nTRACER/ESCOT VVER Depletion Calculation

The research presented in this work is put together in this section by simulating a depletion calculation of a VVER problem which includes the changes in the AA together with new the new PI convergence criterion. This depletion is performed with the newly developed system of codes nTRACER/ESCOT capable of handling hexagonal core geometries.

The problem simulated is based on the X-2 benchmark geometry, however, due to computing capacity limitations, the problem is simplified here. Thus, the modification and its implications are explained prior to presenting the calculation results.

5.3.1. Core model simplification

The current computing capabilities at SNURPL does not allow the simulation of a full core depletion calculation coupled with the subchannel code ESCOT. Note that the single state point in section 3.3.3 required nine nodes for more than five hours. This way a minimal typical depletion cycle would need around four days of almost full server exclusivity.

With the aim at avoiding this, the core is simplified by applying a 60 degrees symmetry which would modify the geometry, more specifically the burnable absorbers location in the assembly 30AV5 as highlighted in red in Figure 5-19. This small change, however, is not extremely relevant for the objective of this calculation, which is demonstrating the capability of the nTRACER/ESCOT system of codes of carrying out a depletion calculation of a VVER core.

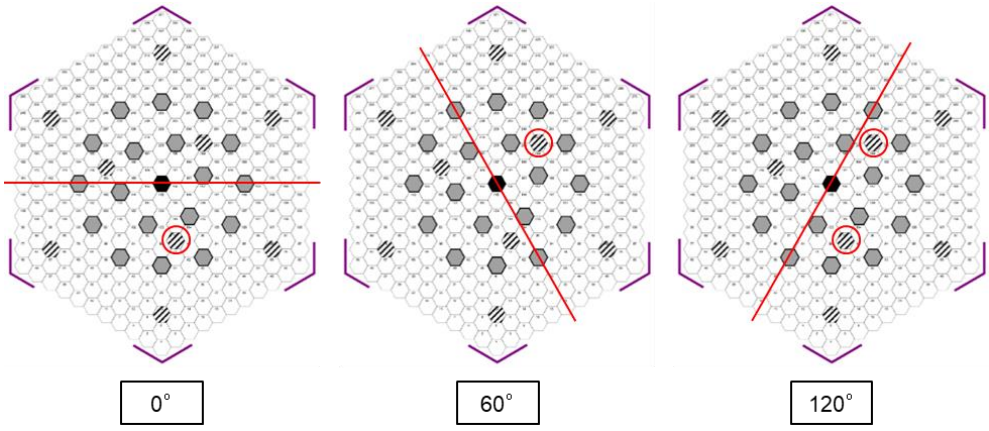

Figure 5-19. X-2 benchmark 30AV5 fuel assembly burnable absorber layout for different symmetry options

5.3.2. Depletion calculation results

Figure 5-20 shows the cumulative number of FPIs required to complete a standard core fuel cycle. It shows the stability of the calculation. Figure 5-21, for its part shows the number of FPIs per burn-up step, which is fairly constant, demonstrating that the calculation is quite close to the optimal given that it contains the search of the CBC together with the T/H and xenon updates. Figure 5-22 gives the amount of time required by each of the principal calculation steps in the nTRACER/ESCOT system of codes. Note that the time taken by ESCOT is around 11 %, this portion would be remarkably smaller if the internal simple T/H solver was employed, the accuracy and reality representation would also be quite poorer too. All in all, it is demonstrated that the system of codes proposed is ready to carry out a VVER depletion calculation in a stable and rather optimized manner.

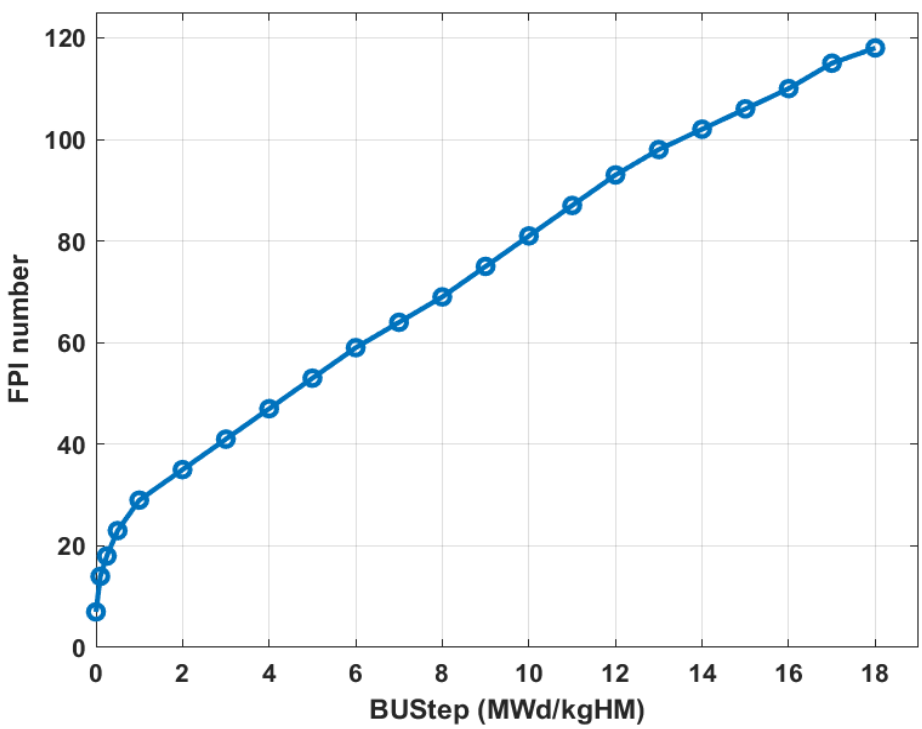

Figure 5-20. Cumulative number of FPIs for the X-2 sixth core depletion calculation with the AA(ϕ) with the new PI convergence criteria performed with nTRACER/ESCOT

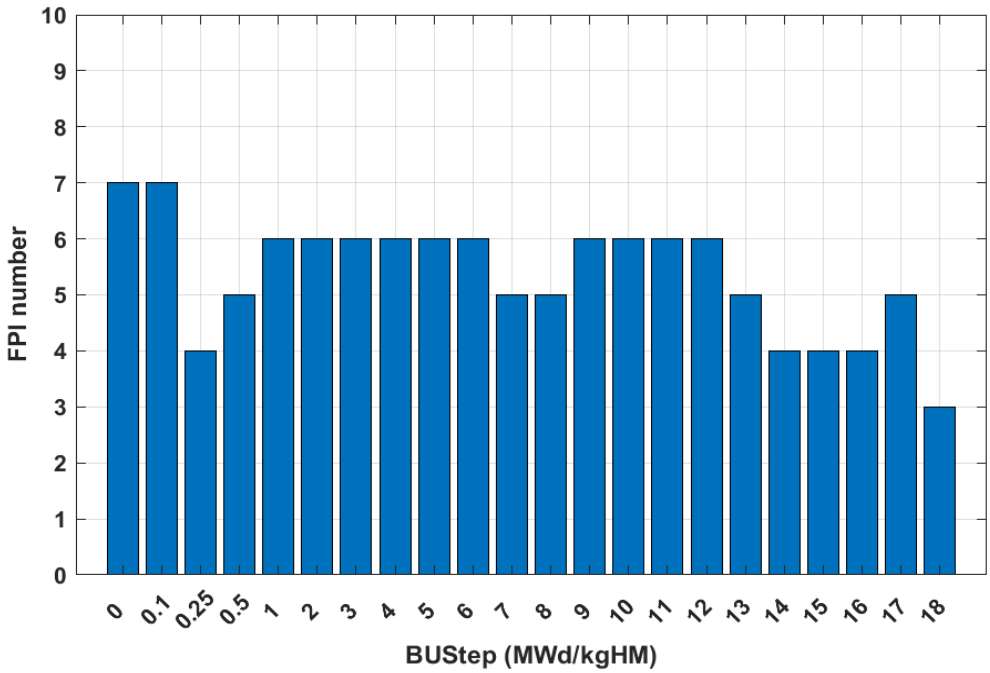

Figure 5-21. Burn-Up stepwise number of FPIs for the X-2 sixth core depletion calculation with the AA(ϕ) with the new PI convergence criteria performed with nTRACER/ESCOT

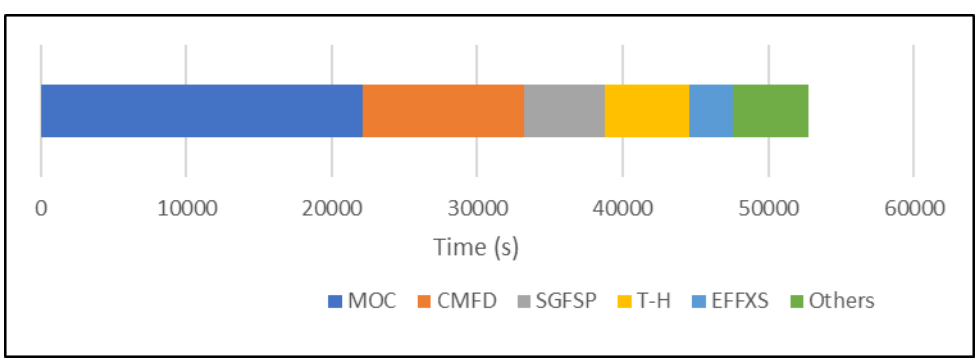

Figure 5-22. Computing time required by each calculation process for the the X-2 sixth core depletion calculation with the AA(ϕ) with the new PI convergence criteria performed with nTRACER/ESCOT

Chapter 6. Summary and Conclusions

The pinwise core T/H analysis subchannel code ESCOT was extended to deal with hexagonal geometry cores, in particular the VVER cores. The ESCOT preprocessor was updated to produce the channels, gaps and pin relations in hexagonal geometry. Its algorithms were adapted to the new geometry type, more specifically the radial term of the lateral momentum was eliminated, the turbulent mixing coefficient fixed-value was recalculated and the fuel pin conduction solution was adapted to compute hollow pins. More sophisticated correlation models were implemented to introduce the spacer grid effects on the axial pressure loss, the HTC enhancement and the turbulent mixing increase. The bidirectional domain decomposition schemes for parallel execution were adapted too: extension of the ghost cells definition and the process assignment of the problem elements. ESCOT was coupled with the hexagonal solver in the DWCC neutronics code nTRACER. Both standalone and coupled results were compared with CTF results. The reference results of the coupled calculations were obtained with the PSI developed nTRACER/CTF system of codes.

Then, the study of the FPI coupled system with extended physics beyond T/H variables, this is xenon and boron updates, was carried out in the 1G 1D simplified problem. Due to the impracticality of obtaining an analytical expression for the optimal partial convergence of the Power Iteration (PI), it was demonstrated that the modification of the AA application from the T/H variables to the neutron flux obtained in the PI improved the FPI convergence behavior notably by effectively suppressing the excessive oscillatory behavior. The modified AA was transferred to nTRACER and its capability to stabilize depletion calculations was demonstrated. The PI in nTRACER (CMFD acceleration) convergence criteria was assessed to avoid unnecessary CMFD iterations. Lastly, and to compile the research and

calculation improvements performed in this work, a VVER depletion calculation with the nTRACER/ESCOT system of codes was executed.

In the following the main conclusions of this research are presented. The changes implemented in ESCOT were verified. The neglect of the radial term of the lateral momentum equation following the philosophy of other subchannel codes such as CTF was determined to be correct as it does not cause major differences (< 0.1 %) in the problem main variables in a cartesian geometry problem when the axial dominance is weakened. The change in the turbulent mixing coefficient was verified against the CTF results employing the turbulent mixing correlation with a maximum difference below 4 °C in an extreme problem. Finally, the fuel conduction in the hollow pins was validated with a maximum error of less than 1 °C if compared with the analytical solution. As for the spacer grid correlations, their implementation was verified by comparing single assembly results from ESCOT and CTF.

For the single assembly standalone calculations ESCOT showed virtually no difference with CTF for coolant density, temperature and pressure and a fuel temperature deviation smaller than 0.2 °C at the pin center line. To assess the time performance of the DFM compared to the three-field model of CTF a full core VVER problem was simulated. The results show that ESCOT is 1.35 faster than CTF due to mainly the time reduction in the momentum and pressure equations solution, there is, however, room for improvement in the steam table implementation. The scalability of the bidirectional domain decomposition was tested with a minicore problem consisting of seven assemblies. The radial only decomposition results in a speedup of 4.5 with respect to the single node calculation. The radial-axial decomposition increased notably the acceleration of the calculation, for example with the employment of 56 cores allowed a 11.5 factor speedup with respect to the single node calculation. This performance increase is due to mainly the time

reduction of the momenta and pressure systems solution while the communication time does not experience much increase.

nTRACER/ESCOT coupled calculations were assessed with single assembly and minicore calculations for the direct coupling and with the full core for via wrapper coupling. No remarkable differences were observed in the fuel or coolant temperatures or in the power distribution. As for the time performance, ESCOT is around 3.5 faster than CTF in direct coupling calculations running in a single node, while the factor increases to about 7 in the full core wrapper-assisted calculation for which ESCOT employed 326 cores in contrast with the 25 assigned to CTF.

The instabilities produced by multiphysics (T/H, xenon and boron) problems were studied with a Fourier analysis. This analysis showed that the stability and optimization depend on the convergence degree of the PI. It also made clear that the definition of an analytical expression to define the optimal convergence point for realistic problems was not possible and eventually approximations would be necessary. Alternatively, the extension of the AA fixed-point map from the original T/H variables to include the other physics was proposed. The convenience of this extension was studied numerically with the 1G 1D problem and the following conclusions were drawn in each multiphysics analysis:

- In the neutronics-T/H problem the average number of FPIs remained almost the same. The number of FPIs with the new AA map yielded a slightly lower number of FPIs and eigenvalue error, also a small reduction in the oscillations was observed. This small change can be explained because the next FPI initial source is modified due to the application of AA on the neutron flux. More important is the observation that the application of AA at full convergence PI yielded a similar number of FPIs as the numerically

obtained optimal convergence point.

- The introduction of xenon allowed to observe the real potential of the application of AA to the flux. The average number of FPIs is reduced from the original 14 to around 8 and the k_{eff} error is reduced from about 3.5 pcm to less than 0.3 pcm. The oscillatory behavior is also greatly reduced and it is demonstrated that the number of needed FPIs is similar to the numerically optimal point while the original AA(TH) enters a chaotic region if fully converged PI is imposed.
- When the boron update is included in the calculation the new AA applied on the flux offered similar numbers to the previous calculation. The average number of FPIs passed from more than 15 to less than 10. The oscillatory behavior also improved drastically and a reduction of the oscillation in the CBC calculation observed as well.

The simple problem conclusions were adapted to nTRACER. Although good results were already obtained in nTRACER for steady state calculations due to the code structure and the application of AA(TH), it showed instabilities in depletion calculations that resulted in no convergence. With the new AA applied on the flux obtained in the nTRACER's PI, this is the CMFD acceleration, the stability of depletion calculations was guaranteed. With the aim at saving memory, the original 47 energy groups flux was collapsed to 2 groups before the AA application and subsequent reconstruction with memory saving purposes for the calculation of core problems. Besides, the convergence criteria of the CMFD calculation was modified from the original residual ratio to residual ratio and residual. This small change allowed for the save of a relevant number of CMFD iterations that reduced the total computing time by an 11.5 % in depletion calculations.

Finally, the nTRACER/ESCOT depletion calculation of modified VVER-1000

full core problem based on the X-2 benchmark was performed. This calculation demonstrated that stable high-fidelity depletion calculation for hexagonal geometry cores is possible in a competitive time span.

For future works the following is proposed. The ESCOT modelling sophistication can be increased by introducing the assembly stiffeners, this would reduce the interassembly exchange and mixing of coolant at the assembly corners and would bring the simulation closer to the reality. The introduction of spacer grids in coupled calculations would also have a relevant impact in the results, for this a correct characterization of the spacer grids and their models' factors for pressure loss, HTC increase and mixing enhancement would be necessary. As explained in this work, this could be performed by CFD calculations. With the regards its validation, the scarcity of experimental data complicates this process but it is a pending task. For the time being the coupled nTRACER/ESCOT code can be validated with the benchmark data once the computational resources are appropriate.

Regarding the neutronics calculations, the 2D/1D MOC should be overcome with the aim at removing the nonlinearities that induce instabilities if the definition of thin planes is necessary (i.e. spacer grids of less than 3 cm height). The current CMFD acceleration also introduces nonlinearities in the calculation and the problem might result unstable if fluxes close to zero exist.

Acknowledgements

I would like to start by thanking professor Joo Han Gyu for giving me the chance of carrying out my doctoral studies at the Reactor Physics Laboratory. His guidance and tutoring made me become a better professional and achieve the objectives I had set for myself.

Then, I would like to thank the committee members of the defense process: professor Shim Hyung Jin and professor Cho Hyoung kyu as well as Dr. Yoon Han Young and Dr. Cho Jinyoung. I appreciate your effort and dedication to the review of my research thesis and your valuable comments and corrections.

My lab mates have also played a determinant role in my PhD research success. Thus, I would like to thank both present and former members. I would like to mention the present members as they had a bigger impact in this last stretch: Lee Han Gyu, Kim Kyung Min, Im Jaeuk, Jeon Seoyoon, Kwon Sung Joon, Kim Seongchan and Jae Seunguk.

I would also like to have some words for those in my personal sphere. To my friends, the ones from home and the ones I made in Korea, for their emotional support and for the good times spent together. And last but not least, I would like to thank my family for their support and their understanding despite the long distance and time.

Jorge Gonzalez Amoros

2023-01-16

References

[1] Joo, Han Gyu, et al. "Methods and performance of a three-dimensional whole-core transport code DeCART." (2004).

[2] Jung, Yeon Sang, et al. "Practical numerical reactor employing direct whole core neutron transport and subchannel thermal/hydraulic solvers." Annals of Nuclear Energy 62 (2013): 357-374.

[3] MPACT TEAM, "MPACT Theory Manual v2.0.0.," Consortium for Advanced Simulation of Light Water Reactors, CASL-U-2015-0078-000, Oak Ridge, NT, USA, 2015.

[4] Thomas, J. W., et al. "The Coupling of the STAR-CD software to a whole-core neutron transport code DeCART for PWR Applications." (2003).

[5] Kochunas, Brendan, et al. "VERA core simulator methodology for pressurized water reactor cycle depletion." Nuclear Science and Engineering 185.1 (2017): 217-231.

[6] Christienne, M., et al. "Coupled Tort-TD/CTF Capability for high-fidelity LWR core calculations-321." (2010).

[7] Lee, Jaejin, et al. "nTRACER/COBRA-TF coupling and initial assessment." Korea 151 (2015): 742.

[8] Yu, Jiankai, et al. "MCS based neutronics/thermal-hydraulics/fuel-performance coupling with CTF and FRAPCON." Computer Physics Communications 238 (2019): 1-18.

[9] Salko, Robert K., and Maria N. Avramova. "COBRA-TF Subchannel Thermal-Hydraulics Code (CTF) Theory Manual–Revision 0." The Pennsylvania State University (2015).

[10] Kwon, H., et al. "Validation of a Subchannel Analysis Code MATRA Version 1.1." KAERI/TR-5581/2014 (2014).

[11] Kim, Seong-Jin, et al. "Preliminary coupling of MATRA code for multi-physics analysis." Transactions of the Korean Nuclear Society Spring Meeting, Jeju, Korea. 2014.

[12] Shim, C. B., Y. S. Jung, and H. G. Joo. "Cross flow modeling in direct whole core transport calculation with a subchannel solver." Proc. ICAPP. 2013.

[13] Lee, Jaejin, Alberto Facchini, and Han Gyu Joo. "Development of a drift-flux model based core thermal-hydraulics code for efficient high-fidelity multiphysics calculation." Nuclear Engineering and Technology 51.6 (2019): 1487-1503.

[14] Lee, Jaejin, Han Gyu Joo, and Jin Young Cho. Initial assessment of Anderson acceleration on pinwise coupled neutronics/thermal-hydraulics code

nTER/ESCOT. No. KURNS-EKR--5. 2020.
[15] Facchini, Alberto, Jaejin Lee, and Han Gyu Joo. "Investigation of Anderson acceleration in neutronics-thermal hydraulics coupled direct whole core calculation." Annals of Nuclear Energy 153 (2021): 108042.
[16] Kim, Kyung Min, et al. "Performance Assessment of GPU-Based nTRACER/ESCOT Coupled Simulations." (2020).
[17] Kim, S. C., et al. "Verification of the Hexagonal Ray Tracing Module and the CMFD Acceleration in nTRACER." Transactions of the Korean Nuclear Society Autumn Meeting, Gyeongju, Korea, October. 2017.
[18] Kim, Seongchan, and G. H. Joo. "nTRACER Solutions of the Two-Dimensional VVER Benchmark Problems." Proceedings of the Transactions of the Korean Nuclear Society Virtual Spring Meeting, Virtual. 2020.
[19] Papadionysiou, Marianna, et al. "Coupling of nTRACER to Cobra-Tf for High-Fidelity Analysis of VVERs." EPJ Web of Conferences. Vol. 247. EDP Sciences, 2021.
[20] Papadionysiou, Marianna, et al. "Verification and validation of the high-resolution code nTF with VVER-1000 hot zero power monte carlo calculations and experimental data." Annals of Nuclear Energy 178 (2022): 109385.
[21] Spasov, Ivan, Plamen Ivanov, and Nikola Kolev. "Simulation of a rod ejection transient in VVER-1000 with COBAYA4-CTF." Comptes rendus de l'Académie bulgare des Sciences 71.3 (2018).
[22] Jimenez, J. "Testing of SUBCHANFLOW and COBRA-TF models for a VVER fuel assembly, " 2015.
[23] Papadionysiou, Marianna, et al. "Verification of nTRACER / COBRA-TF with Serpent2 / SUBCHANFLOW for Full Core High Fidelity High-Resolution Analysis of VVERs." 2022.
[24] Papadionysiou, Marianna, et al. "Validation of the novel core solver nTRACER/COBRA-TF for full core high fidelity cycle analysis of VVERs." Nuclear Engineering and Design 398 (2022): 111946.
[25] Wang, Jincheng, Qin Wang, and Ming Ding. "Review on neutronic/thermal-hydraulic coupling simulation methods for nuclear reactor analysis." Annals of Nuclear Energy 137 (2020): 107165.
[26] Gill, Daniel F., David P. Griesheimer, and David L. Aumiller. "Numerical methods in coupled Monte Carlo and thermal-hydraulic calculations." Nuclear Science and Engineering 185.1 (2017): 194-205.
[27] Toth, Alex, et al. Analysis of Anderson acceleration on a simplified neutronics/thermal hydraulics system. Oak Ridge National Lab.(ORNL), Oak Ridge, TN (United States). Consortium for Advanced Simulation of LWRs (CASL), 2015.

[28] Choi, Sooyoung, et al. "Development of high-fidelity neutron transport code STREAM." Computer Physics Communications 264 (2021): 107915.

[29] Anderson, Donald G. "Iterative procedures for nonlinear integral equations." Journal of the ACM (JACM) 12.4 (1965): 547-560.

[30] Toth, Alexander Raymond. "A Theoretical Analysis of Anderson Acceleration and Its Application in Multiphysics Simulation for Light-Water Reactors." (2016).

[31] Lee, Jaejin, and Han Gyu Joo. "Convergence analysis of fixed-point iteration with Anderson Acceleration on a simplified neutronics/thermal-hydraulics system." Nuclear Engineering and Technology 54.2 (2022): 532-545.

[32] Lee, Hangyu, et al. “High-Speed Direct Whole-Core Cycle Depletion on Heterogeneous Computing Architectures”, Annals of Nuclear Energy, vol. 124, no. 1, pp. 559-562, (2021).

[33] Shen, Qicang, Sooyoung Choi, and Brendan Kochunas. "A Robust, Relaxation-Free Multiphysics Iteration Scheme for CMFD-Accelerated Neutron Transport k-Eigenvalue Calculations—I: Theory." Nuclear Science and Engineering 195.11 (2021): 1202-1235.

[34] Shen, Qicang, Sooyoung Choi, and Brendan Kochunas. "A Robust, Relaxation-Free Multiphysics Iteration Scheme for CMFD-Accelerated Neutron Transport k-Eigenvalue Calculations—II: Numerical Results." Nuclear Science and Engineering 195.11 (2021): 1202-1235.

[35] Gonzalez-Amoros, Jorge, et al. “Extension of the high-resolution thermal-hydraulics code ESCOT to Hexagonal core geometries for multi-physics calculations.” International Conference on Physics of Reactors 2022 (PHYSOR 2022). Pittsburgh, PA, May 15-20, 2022. Pages 784-793.

[36] Lötsch, T., et al. "The X2 benchmark for VVER-1000 reactor calculations. Overview and current status." Proceedings of the 26th AER Symposium on VVER Reactor Physics and Reactor Safety, Helsinki, Finland. 2016.

[37] Bilodid, Yuri, Emil Fridman, and Thomas Lötsch. "X2 VVER-1000 benchmark revision: Fresh HZP core state and the reference Monte Carlo solution." Annals of Nuclear Energy 144 (2020): 107558.

[38] Blyth, Taylor Scott. "Development and Implementation of CFD-Informed Models for the Advanced Subchannel Code CTF." (2017).

[39] Gonzalez-Amoros, Jorge, et al. “Capability extension of a high-resolution thermal-hydraulics code ESCOT for hexagonal geometry core multiphysics analysis.” Nuclear Science and Engineering.

[40] Lee, Deokjung, Thomas J. Downar, and Yonghee Kim. "Convergence analysis of the nonlinear coarse-mesh finite difference method for one-dimensional fixed-source neutron diffusion problem." Nuclear science and engineering

147.2 (2004): 127-147.
[41] Lee, Hyun Chul, Deokjung Lee, and Thomas J. Downar. "Iterative two-and one-dimensional methods for three-dimensional neutron diffusion calculations." Nuclear science and engineering 151.1 (2005): 46-54.
[42] Lee, Hyun Chul, et al. "Fourier convergence analysis of two-dimensional/one-dimensional coupling methods for the three-dimensional neutron diffusion eigenvalue problems." Nuclear science and engineering 156.1 (2007): 74-85.
[43] PETSc Team, “PETSc users’ Manual - Rev. 3.10,” ANL-95/11, Argonne National Laboratory, Glen Forest, Illinois, USA (2018).
[44] Lee, Jae Jin. "Development of a Drift-Flux Model Based Pinwise Whole Core Thermal-Hydraulics Analysis Code Aiming at Highly Parallelized Execution." (2016).
[45] Lee, Jae Jin. "Development and Optimization of a Neutronics Coupled Refined Core Thermal-Hydraulics Analysis System Capable of Massive Parallel Execution." (2020).
[46] Todreas, Neil E., Mujid S. Kazimi, and Mahmoud Massoud. Nuclear systems Volume II: Elements of thermal hydraulic design. CRC Press, 2021.
[47] Todreas, Neil E., and Mujid S. Kazimi. Nuclear systems volume I: Thermal hydraulic fundamentals. CRC press, 2021.
[48] Chexal, B., et al. "A void fraction correlation for generalized applications." Progress in nuclear energy 27.4 (1992): 255-295.
[49] Armand, Aleksandr Aleksandrovich. "The resistance during the movement of a two-phase system in horizontal pipes." Izvestiia Vsesoiuznyi Teplotekhnicheskii Institut 1 (1946): 16-23.
[50] Rogers, J. T., and Robert G. Rosehart. "Mixing by Turbulent Interchange in Fuel Bundles-Correlations and Influences." MECHANICAL ENGINEERING. Vol. 94. No. 9. 345 E 47TH ST, NEW YORK, NY 10017: ASME-AMER SOC MECHANICAL ENG, 1972.
[51] Nuclear Regulatory Commission. RELAP5/MOD3 code manual. Volume 4, Models and correlations. No. NUREG/CR--5535-VOL. 4. Nuclear Regulatory Commission, 1995.
[52] Lahey Jr, Richard T. "A mechanistic subcooled boiling model." International Heat Transfer Conference Digital Library. Begel House Inc., 1978.
[53] Van Doormaal, Jeffrey P., and George D. Raithby. "Enhancements of the SIMPLE method for predicting incompressible fluid flows." Numerical heat transfer 7.2 (1984): 147-163.
[54] Stewart, C. W., et al. COBRA-IV: The model and the method. No. BNWL-2214. Pacific Northwest Lab., Richland, WA (USA), 1977.

[55] Geelhood, K. J., et al. "A Computer Code for the Calculation of Steady-State, Thermal-Mechanical Behavior of Oxide Fuel Rods for High Burnup." Pacific Northwest. National Laboratory Richland, Washington, 2015.

[56] Hales, J. D., et al. BISON theory manual the equations behind nuclear fuel analysis. No. INL/EXT-13-29930. Idaho National Lab.(INL), Idaho Falls, ID (United States), 2016.

[57] Dittus, F. W., and L. M. K. Boelter. "Heat transfer in automobile radiators of the tubular type." International communications in heat and mass transfer 12.1 (1985): 3-22.

[58] Sparrow, Ephraim M., Albert L. Loeffler Jr, and H. A. Hubbard. "Heat transfer to longitudinal laminar flow between cylinders." (1961): 415-422.

[59] Facchini, Alberto. and Lee, Jaejin. “ESCOT Theory Manual,” SNURPL-TR-050-Rev.2(18), Seoul National University, Rep. of Korea (2019).

[60] Rehme, K. (1973). Pressure drop correlations for fuel element spacers. Nuclear Technology, 17, 15-23.

[61] Fang, Haw-ren, and Yousef Saad. "Two classes of multisecant methods for nonlinear acceleration." Numerical linear algebra with applications 16.3 (2009): 197-221.

[62] Walker, Homer F., and Peng Ni. "Anderson acceleration for fixed-point iterations." SIAM Journal on Numerical Analysis 49.4 (2011): 1715-1735.

[63] Walker, Homer F. "Anderson acceleration: Algorithms and implementations." WPI Math. Sciences Dept. Report MS-6-15-50 (2011).

APPENDIX A. Conservation Equations in Discretized Form

In section 2.4.1, the discretized forms of conservation equations are presented but the details about the coefficients are omitted, so those are described in this appendix. In below equations, '*rnb*' denotes neighbors in radial direction and '*wnb*' means whole neighbors.

Mixture mass continuity in subchannel form:

$$\frac{\rho_{m,I,J}^{n+1}-\rho_{m,I,J}^{n}}{\Delta t}A_{c,I,J}\Delta z_J+\sum_{ic=1}^{rnb}\left[\rho_m^{\bar{n}}\left(\vec{u}_m^{n+1}\cdot\vec{s}\right)_{ic}\Delta z_J\right]_{ic,J}$$
$$+\left[\rho_m^{\bar{n}}w_m^{n+1}A_c\right]_{I,j}-\left[\rho_m^{\bar{n}}w_m^{n+1}A_c\right]_{I,j-1}=\sum_{ic=1}^{rnb}\left[TM_m\right]_{ic}^{n}$$

where

$$\sum_{ic=1}^{rnb}\left[TM\right]_{ic}^{n}=\sum_{ic=1}^{rnb}\left[\Theta_{ic}s_{ic}\left(\frac{\varepsilon}{z_{ic}}\right)\right]_J^n\left\{\left[\left(\rho_m\right)_{ic,J}-\left(\rho_m\right)_{I,J}\right]\right.$$
$$\left.-K_M\frac{G_{ic,J}-G_{I,J}}{G_{I,J}+G_{ic,J}}\left[\left(\alpha\rho_v-\alpha\rho_l\right)_{I,J}+\left(\alpha\rho_v-\alpha\rho_l\right)_{ic,J}\right]\right\}^n\Delta z_J$$

Vapor mass continuity in subchannel form:

$$\left[\alpha_{I,J}^{n}\frac{\rho_{v,I,J}^{n+1}-\rho_{v,I,J}^{n}}{\Delta t}+\rho_{v,I,J}^{n}\frac{\alpha_{I,J}^{n+1}-\alpha_{I,J}^{n}}{\Delta t}\right]A_{c,I,J}\Delta z_J$$
$$+\sum_{ic=1}^{rnb}\left[\left(\alpha\rho_v\right)^{\bar{n}}\left(\vec{u}_m^{n+1}\cdot\vec{s}\right)\Delta z_J\right]_{ic,J}+\left[\left(\alpha\rho_v\right)^{\bar{n}}w_m^{n+1}A_c\right]_{I,j}-\left[\left(\alpha\rho_v\right)^{\bar{n}}w_m^{n+1}A_c\right]_{I,j-1}\quad(5.4)$$
$$=\frac{H_{il}^{n}(T_l^{n+1}-T_{sat}^{n+1})}{h_{v,sat}^{n}-h_{li}^{n}}A_{c,I,J}\Delta z_J+\Gamma_w^{n}A_{c,I,J}\Delta z_J-\sum_{wnb}\left[CV\right]_{wnb}^{n}+\sum_{rnb}\left[TM_v\right]_{hnb}^{n}$$

where

$$\sum_{wnb}[CV]_{wnb}^{n} = \sum_{ic=1}^{wnb}\left[\left(\frac{\alpha\rho_l\rho_v}{\rho_m}\right)^{n}\left(\vec{V}'_{gj}\cdot\vec{s}\right)^{n}\Delta z_J\right]_{ic,J}$$
$$+\left(\frac{\alpha\rho_l\rho_v}{\rho_m}V'_{gjz}A_c\right)_{I,j}^{n}-\left(\frac{\alpha\rho_l\rho_v}{\rho_m}V'_{gjz}A_c\right)_{I,j-1}^{n}$$

$$\sum_{rnb}[TM_v]_{rnb}^{n} = \sum_{ic=1}^{rnb}\left[\Theta_{ic}s_{ic}\left(\frac{\varepsilon}{z_{ic}}\right)\right]_{J}^{n}\left\{\left[\left(\alpha\rho_v\right)_{ic,J}-\left(\alpha\rho_v\right)_{I,J}\right]\right.$$
$$\left.-K_M\frac{G_{ic,J}-G_{I,J}}{G_{I,J}+G_{ic,J}}\left[\left(\alpha\rho_v\right)_{I,J}+\left(\alpha\rho_v\right)_{I,J}\right]\right\}^{n}\Delta z_J$$

Axial momentum equation in subchannel form:

$$a_{z,P}w_{m,I,j}^{n+1}-\sum_{ic=1}^{rnb}a_{z,ic}w_{m,\langle ic\rangle,j}^{n+1}-a_{z,DW}w_{m,I,j-1}^{n+1}-a_{z,UP}w_{m,I,j+1}^{n+1}$$
$$=\left[P_{I,J-1}^{n+1}-P_{I,J}^{n+1}\right]A_{c,I,j}+S_{z,I,j}$$

where

$$a_{z,UP}=\max\left[-\left(\rho_m w_m\right)_{I,J+1}^{n}A_c,0\right]=\max\left[-F_{z,up}^{n},0\right]$$

$$a_{z,DW}=\max\left[\left(\rho_m w_m\right)_{I,J}^{n}A_c,0\right]=\max\left[F_{z,dw}^{n},0\right]$$

$$a_{z,ic}=\max\left[-\left(\rho_m\vec{u}_m\right)^{n}s_{ic,j}\Delta z_j\cdot\vec{n},0\right]$$
$$+\Theta_{I,IC}^{n}s_{I,IC}\left(\frac{\varepsilon}{z}\right)_{I,IC}^{n}\left[\left(\rho_m\right)_{IC,j}^{n}+\left(\alpha\rho_v-\alpha\rho_l\right)_{IC,j}^{n}\right]\Delta z_j$$
$$=\max\left[-\vec{F}_{z,ic}^{n}\cdot\vec{n},0\right]+\Theta_{I,IC}^{n}s_{I,IC}\left(\frac{\varepsilon}{z}\right)_{I,IC}^{n}\left[\left(\rho_m\right)_{IC,j}^{n}+\left(\alpha\rho_v-\alpha\rho_l\right)_{IC,j}^{n}\right]\Delta z_j$$

$$a_{z,P}=a_{z,UP}+a_{z,DW}+\frac{\left(\rho_m\right)_{I,j}^{n}}{\Delta t}A_{c,I,j}\Delta z_j$$
$$+\sum_{ic=1}^{rnb}\left\{\max[-\vec{F}_{z,ic}^{n}\cdot\vec{n},0]+\Theta_{I,ic}^{n}s_{I,\langle ic\rangle}\left(\frac{\varepsilon}{z}\right)_{I,\langle ic\rangle}^{n}\left[\left(\rho_m\right)_{I,j}^{n}+\left(\alpha\rho_l-\alpha\rho_v\right)_{I,j}^{n}\right]\Delta z_j\right\}$$

$$S_{z,I,j} = -\Phi^n \left[\sum \frac{f}{2D_h} \frac{\left(G_k\right)^2}{\rho_k} + \frac{K_z}{2\Delta z_j} \rho_m w_m \left| w_m \right| \right]_{I,j}^n \Delta V_{I,j}$$

$$- \sum_{wnb} \left[CM \right]_{z,wnb}^n + \frac{\left(\rho_m\right)_{I,j}^n \left(w_m\right)_{I,j}^n}{\Delta t} A_{c,I,j} \Delta z_j - \rho_m g \Delta V_{I,j} + \sum_{rnb} \left[VD_s \right]_{z,rnb}^n$$

$$\sum_{wnb} \left[CM \right]_{z,wnb}^n = \sum_{ic=1}^{rnb} \left[\frac{\alpha}{1-\alpha} \frac{\rho_v \rho_l}{\rho_m} V'_{gjz} \left(\vec{V}'_{gj} \cdot \vec{n} \right) s \Delta z \right]_{ic,j}$$

$$+ \left(\frac{\alpha}{1-\alpha} \frac{\rho_v \rho_l}{\rho_m} V'_{gjz} V'_{gjz} A_c \right)_{I,J+1}^n - \left(\frac{\alpha}{1-\alpha} \frac{\rho_v \rho_l}{\rho_m} V'_{gjz} V'_{gjy} A_c \right)_{I,J}^n$$

$$\sum_{rnb} \left[VD_s \right]_{z,rnb}^n = -\sum_{IC=1}^{rnb} \left[\Theta_{I,IC} s_{I,IC} \left(\frac{\varepsilon}{z} \right)_{I,IC}^n K_M \frac{G_{IC,j} - G_{I,j}}{G_{IC,j} + G_{I,j}} \right.$$

$$\left. \left\{ \left[\left(\frac{\alpha}{1-\alpha} \frac{\rho_l \rho_v}{\rho_m} V'_{gj} \right)_{IC,J} + \left(\frac{\alpha}{1-\alpha} \frac{\rho_l \rho_v}{\rho_m} V'_{gj} \right)_{I,j} \right] \right\} \Delta z \right]$$

Lateral momentum equation in subchannel form:

$$a_{x,P} u_{m,i,J}^{n+1} - a_{x,W} u_{m,i-1,J}^{n+1} - a_{x,E} u_{m,i+1,J}^{n+1} - a_{x,DW} u_{m,i,J-1}^{n+1} - a_{x,UP} u_{m,i,J+1}^{n+1}$$
$$= \left[P_{IA,J}^{n+1} - P_{IB,J}^{n+1} \right] s_i \Delta z_J + S_{x,i,J}$$

where

$$a_{x,E} = \max\left[-\left(\rho_m u_m\right)_e^n s_i \Delta z_J, 0 \right] = \max\left[-F_{x,e}^n, 0 \right]$$

$$a_{x,W} = \max\left[\left(\rho_m u_m\right)_w^n s_i \Delta z_J, 0 \right] = \max\left[F_{x,w}^n, 0 \right]$$

$$a_{x,UP} = \max\left[-\left(\rho_m w_m\right)_{i,j}^n s_i l_i, 0 \right] = \max\left[-F_{x,up}^n, 0 \right]$$

$$a_{x,DW} = \max\left[\left(\rho_m w_m\right)_{i,j-1}^n s_i l_i, 0 \right] = \max\left[F_{x,dw}^n, 0 \right]$$

$$a_{x,P} = \sum_{wnb} a_{x,wnb} + \frac{\left(\rho_m\right)_{i,J}^n}{\Delta t} s_i l_i \Delta z_J$$

$$S_{x,i,J} = -\left[\frac{K_x}{2}\rho_m u_m \left|u_m\right|\right]_{i,J}^n s_i \Delta z_J - \sum_{wnb}\left[CM\right]_{x,wnb}^n + \frac{\left(\rho_m\right)_{i,J}^n \left(u_m\right)_{i,J}^n}{\Delta t} s_i l_i \Delta z_J$$

$$\sum_{wnb}\left[CM\right]_{x,wnb}^n = \left[\left(\frac{\alpha}{1-\alpha}\frac{\rho_v\rho_l}{\rho_m}V'_{gjx}V'_{gjx}\right)_{IB,J}^n - \left(\frac{\alpha}{1-\alpha}\frac{\rho_v\rho_l}{\rho_m}V'_{gjx}V'_{gjx}\right)_{IA,J}^n\right] s_i \Delta z_J$$
$$+\left[\left(\frac{\alpha}{1-\alpha}\frac{\rho_v\rho_l}{\rho_m}V'_{gjx}V'_{gjz}\right)_{i,j}^n - \left(\frac{\alpha}{1-\alpha}\frac{\rho_v\rho_l}{\rho_m}V'_{gjx}V'_{gjz}\right)_{i,j-1}^n\right] s_i l_i$$

Mixture energy equation in subchannel form:

$$\frac{\left(\rho_m h_m\right)_{I,J}^{n+1} - \left(\rho_m h_m\right)_{I,J}^n}{\Delta t} A_{c,I,J}\Delta z_J + \sum_{ic=1}^{rnb}\left[\left(\rho_m h_m\right)^{\bar{n}}\left(\vec{u}_m^{n+1}\cdot\vec{s}\right)\Delta z_J\right]_{ic,J}$$
$$+\left[\left(\rho_m h_m\right)^{\bar{n}}\left(w_m\right)^{n+1}A_c\right]_{I,j} - \left[\left(\rho_m h_m\right)^{\bar{n}}\left(w_m\right)^{n+1}A_c\right]_{I,j-1}$$
$$= \sum_{rnb}\left[TM_{en}\right]_{rnb}^n + \frac{P_{I,J}^{n+1} - P_{I,J}^n}{\Delta t}A_{c,I,J}\Delta z_J + q''_w \xi_c \Delta z_J + q'''_v A_{c,I,J}\Delta z_J - \sum_{wnb}\left[CE\right]_{wnb}^n$$

where

$$\sum_{rnb}\left[TM_{en}\right]_{rnb}^n = \sum_{ic=1}^{rnb}\left[\Theta_{ic}s_{ic}\left(\frac{\varepsilon}{z_{ic}}\right)\right]_j^n \left[\left(\rho_m h_m\right)_{ic,J}^n - \left(\rho_m h_m\right)_{I,J}^n\right.$$
$$\left. -\left[K_M\frac{G_{ic,J} - G_{I,J}}{G_{I,J} + G_{ic,J}}\right]^n \left\{\left[\alpha\left(\rho_v h_v - \rho_l h_l\right)\right]_{ic,J} + \left[\alpha\left(\rho_v h_v - \rho_l h_l\right)\right]_{I,J}\right\}^n \Delta z_J\right]$$

$$\sum_{wnb}\left[CE\right]_{wnb}^n = \sum_{ic}\left[\frac{\alpha\rho_v\rho_l}{\rho_m}\left(h_v - h_l\right)\left(\vec{V}'_{jg}\cdot\vec{n}\right)\right]_{ic,J}^n s_{ic}\Delta z_J$$
$$+\left[\frac{\alpha\rho_v\rho_l}{\rho_m}\left(h_v - h_l\right)V'_{jgz}\right]_{I,j}^n A_{c,I,j} - \left[\frac{\alpha\rho_v\rho_l}{\rho_m}\left(h_v - h_l\right)V'_{jgz}\right]_{I,j-1}^n A_{c,I,j-1}$$

APPENDIX B. Coupled Linear System of Scalar Equations

In section 2.4.2, the pressure equation is derived from coupled linear system of scalar equations as below:

$$\begin{bmatrix} a_{11} & a_{12} & a_{13} \\ a_{21} & a_{22} & a_{23} \\ a_{31} & a_{32} & a_{33} \end{bmatrix} \begin{bmatrix} h_{l,I,J}^{n+1} \\ \alpha_{I,J}^{n+1} \\ P_{I,J}^{n+1} \end{bmatrix} = \begin{bmatrix} s_1 \\ s_2 \\ s_3 \end{bmatrix} - \begin{bmatrix} b_{11} & b_{12} & b_{13} & b_{14} & b_{15} & b_{16} \\ b_{21} & b_{22} & b_{23} & b_{24} & b_{25} & b_{26} \\ b_{31} & b_{32} & b_{33} & b_{23} & b_{35} & b_{36} \end{bmatrix} \begin{bmatrix} u_{ie,J}^{n+1} \\ -u_{iw,J}^{n+1} \\ v_{is,J}^{n+1} \\ -v_{in,J}^{n+1} \\ w_{I,j}^{n+1} \\ -w_{I,j-1}^{n+1} \end{bmatrix} .(2.52)$$

However, the details related with coefficients are omitted, so those are presented in this appendix.

Linearized mixture continuity equation:

$$\begin{aligned} & a_{11} h_{l,I,J}^{n+1} + a_{12} \alpha_{I,J}^{n+1} + a_{13} P_{I,J}^{n+1} \\ & = - \left[\sum_{ic=1}^{rnb} \left[\rho_m^{\bar{n}} \left(\vec{u}_m^{n+1} \cdot \vec{s} \right)_{ic} \Delta z_J \right]_{ic,J} + \left[\rho_m^{\bar{n}} w_m^{n+1} A_c \right]_{I,j} - \left[\rho_m^{\bar{n}} w_m^{n+1} A_c \right]_{I,j-1} \right] + s_1 \end{aligned}$$

where

$$a_{11} = \left(\frac{\partial \rho_l}{\partial h_l} \right)_{I,J}^{n} \left(1 - \alpha_{I,J}^{n} \right) \left(\frac{A_{c,I,J} \Delta z_J}{\Delta t} \right)$$

$$a_{12} = \left(\rho_{v,I,J}^{n} - \rho_{l,I,J}^{n} \right) \left(\frac{A_{c,I,J} \Delta z_K}{\Delta t} \right)$$

$$a_{13} = \left(\left(\frac{\partial \rho_v}{\partial P} \right)_{I,J}^{n} \alpha_{I,J}^{n} + \left(\frac{\partial \rho_l}{\partial P} \right)_{I,J}^{n} \left(1 - \alpha_{I,J}^{n} \right) \right) \left(\frac{A_{c,I,J} \Delta z_J}{\Delta t} \right)$$

$$s_1 = a_{11} h_{l,I,J}^n + a_{12} \alpha_{I,J}^n + a_{13} P_{I,J}^n + \sum_{rnb} \left[TM_m \right]_{rnb}^n .$$

Linearized vapor continuity equation:

$$a_{21} h_{I,J}^{n+1} + a_{22} \alpha_{I,J}^{n+1} + a_{23} P_{I,J}^{n+1} = - \left[\begin{array}{l} \sum_{ic=1}^{rnb} \left[\left(\alpha \rho_v \right)^{\bar{n}} \left(\vec{u}_m^{n+1} \cdot \vec{s} \right) \Delta z_J \right]_{ic,J} + \\ \left[\left(\alpha \rho_v \right)^{\bar{n}} w_m^{n+1} A_c \right]_{I,j} - \left[\left(\alpha \rho_v \right)^{\bar{n}} w_m^{n+1} A_c \right]_{I,j-1} \end{array} \right] + s_2$$

where

$$a_{21} = - \frac{H_{il}^n}{h_{v,sat}^n - h_{il}^n} \left(\frac{\partial T_l}{\partial h_l} \right)_{I,J}^n A_{c,I,J} \Delta z_J$$

$$a_{22} = \rho_{v,I,J}^n \left(\frac{A_{c,I,J} \Delta z_J}{\Delta t} \right)$$

$$a_{23} = \alpha_{I,J}^n \left(\frac{\partial \rho_v}{\partial P} \right)_{I,J}^n \left(\frac{A_{c,I,J} \Delta z_J}{\Delta t} \right) + \frac{H_{il}^n}{h_{v,sat}^n - h_{il}^n} \left[\left(\frac{\partial T_{v,sat}}{\partial P} \right)_{I,J}^n - \left(\frac{\partial T_l}{\partial P} \right)_{I,J}^n \right] A_{c,I,J} \Delta z_J$$

$$s_2 = \left(\frac{H_{il}^n (T_l^n - T_{v,sat}^n)}{h_{v,sat}^n - h_{li}^n} + \Gamma_w \right)_{I,J} A_{c,I,J} \Delta z_J - \sum_{wnb} \left[CV \right]_{wnb}^n + a_{21} h_{l,I,J}^n + a_{22} \alpha_{I,J}^n + a_{23} P_{I,J}^n + \sum_{rnb} \left[TM_v \right]_{rnb}^n .$$

Linearized mixture enthalpy equation:

$$
\begin{aligned}
& a_{31} h_{l,I,J}^{n+1} + a_{32} \alpha_{I,J}^{n+1} + a_{33} P_{I,J}^{n+1} \\
& = - \left[\begin{array}{l} \sum_{ic=1}^{rnb} \left[\left(\rho_m h_m \right)^{\bar{n}} \left(\vec{u}_m^{n+1} \cdot \vec{s} \right) \Delta z_J \right]_{ic,J} + \left[\left(\rho_m h_m \right)^{\bar{n}} \left(w_m \right)^{n+1} A_c \right]_{I,j} \\ - \left[\left(\rho_m h_m \right)^{\bar{n}} \left(w_m \right)^{n+1} A_c \right]_{I,j-1} \end{array} \right] + s_3
\end{aligned}
$$

where

$$
a_{31} = \left(1 - \alpha_{I,J}^n \right) \left(\left(\frac{\partial \rho_l}{\partial h_l} \right)_{I,J}^n h_{l,I,J}^n + \rho_{l,I,J}^n \right) \frac{A_{c,I,J} \Delta z_J}{\Delta t}
$$

$$
a_{32} = \left(\left(\rho_v h_v \right)_{I,J}^n - \left(\rho_l h_l \right)_{I,J}^n \right) \frac{A_{c,I,J} \Delta z_J}{\Delta t}
$$

$$
\begin{aligned}
a_{33} = \Bigg(& h_{l,I,J}^n \left(1 - \alpha_{I,J}^n \right) \left(\frac{\partial \rho_l}{\partial P} \right)_{I,J}^n \\
& + \left(\frac{\partial \rho_v}{\partial P} \right)_{I,J}^n \left(\alpha h_v \right)_{I,J}^n + \left(\frac{\partial h_v}{\partial P} \right)_{I,J}^n \left(\alpha \rho_v \right)_{I,J}^n - 1 \Bigg) \left(\frac{A_{c,I,J} \Delta z_J}{\Delta t} \right)
\end{aligned}
$$

$$
\begin{aligned}
s_3 = & \sum_{rnb} \left[TM_{en} \right]_{rnb}^n + q_w'' \xi_c \Delta z_J + q_v''' A_{c,I,J} \Delta z_J \\
& - \sum_{wnb} \left[CE \right]_{wnb}^n + a_{31} h_{l,I,J}^n + a_{32} \alpha_{I,J}^n + a_{33} P_{I,J}^n
\end{aligned}
.
$$

초 록

봉단위 노심 열수력 해석 부수로 코드인 ESCOT을 확장하여 육각 기하 노심 처리능을 탑재하고, 특히 VVER 노심을 해석할 수 있도록 하였다. ESCOT의 전처리기는 육각 기하구조에서의 부수로-간극-연료봉의 관계식을 생산할 수 있도록 개선하였. 해당 코드의 알고리즘은 새로운 기하 구조에 대해 맞게 조정하였다. 구체적으로는 측면 운동량의 반경방향 항을 제거하고, 난류 혼합 계수의 고정값을 재계산하고, 중공 연료봉 형태의 계산을 위한 핵연료봉 열전도 풀이법을 조정하였다. 축방향의 압력 강하, 열전달 계수의 개선, 난류 혼합 증가에 대한 지지격자의 효과를 고려하기 위한 보다 정교한 상관관계 모델이 적용하였다. 고스트 셀의 정의와 문제 단위 프로세스 할당으로 병렬 처리를 위한 두 방향의 영역분할 기법 또한 조정하였다. ESCOT 코드는 전노심 직접해석 코드인 nTRACER의 육각 기하 솔버와 연계시켰다. 독립 계산과 연계 계산 모두 CTF 결과와 비교하여검증하였다. 참조해는 PSI에서 개발한 nTRACER/CTF 코드 연계 시스템으로부터 확보하였다. 독립계산 결과는 참조해와 비슷한 결과를 보였고, CTF 코드와 비교하여 1.35배 빠른 것으로 나타났다. 연계 계산 또한 서로잘 일치하는 결과를 보여준다. 전노심 계산의 경우 wrapper 기반 병렬화를 통한 ESCOT과 연계 시 CTF 코드 연계와 비교해 7배 가량 더 빠른 결과를 보여주었다.

이후 열수력 궤환 효과와 제논 궤환 효과가 혼합된 연소계산에서 나타나는 수렴 불안정성을 해결하기 위한 연구를 수행하였다. 먼저 단일군-일차원으로 단순화된 문제를 통해 열수력 관련 변수들 외에 제논 및 붕산농도의 궤환효과등의 확장된 물리현상을 고려하는 고정점 반복 연계 체계에 대해 분석하였다. Power iteration의 최적의 수렴을 위한 인자를 찾기 위해 해석적인 식을 정의하는 것은 실용적이지 않기 때문에, 기존의 Anderson 가속법을 수정하여 수렴성을 개선시켰다. 해당 기법을 열

수력 관련 변수들에 적용하는 대신 중성자속 변수에 적용함으로써 과도하게 진동하는 수렴거동을 효과적으로 완화할 수 있었고, 결과적으로 고정점 반복 계산의 수렴거동이 눈에 띄게 개선되는 것을 확인하였다. 고정점 반복 계산 방법의 변화는 반복 계산의 횟수를 1.5배 가량 줄이는 효과를 보였다. 수정된 Anderson 가속법은 nTRACER에도 적용시켜 연소 계산을 안정시키는 성능을 확인했다. nTRACER에서의 power iteration 동안의 불필요한 CMFD 반복계산을 피하기 위한 수렴 조건을 평가하였고, 잔차절대값에대한수렴조건을추가함으로써총 계산 시간을 11.5 % 가량 줄일 수 있었다. 마지막으로, 연구성과 및 계산성능 개선효과 등을 보여주기 위해 nTRACER/ESCOT 연계 체계를 통한 VVER 노심의 연소 계산을 수행하였다. 이 연구에 제시한 방법과 개발한 코드 모듈을 통해 육각 기하노심에 대한 봉단위 열수력 연계 고신뢰도 직접 전노심 연소 계산이 현 실적인 시간안에 안정적으로 수행이 가능함을 입증하였다.

주 요 어 : nTRACER, ESCOT, 육각 기하 구조 노심, 제논 궤환, Fourier 분석, Anderson 가속법

학 번 : 2017-35073